# Apport de l'analyse paléopiézométrique des macles de la calcite et des stylolites à la compréhension de l'histoire tectonique et d'enfouissement des bassins sédimentaires de la marge ouest-africaine de l'Atlantique Sud

Boubacar Bah

# Sorbonne Université

Ecole doctorale 398 : Géosciences, Ressources Naturelles et Environnement

Institut des Sciences de la Terre de Paris (ISTeP)

# Apport de l'analyse paléopiézométrique des macles de la calcite et des stylolites à la compréhension de l'histoire tectonique et d'enfouissement des bassins sédimentaires de la marge ouest-africaine de l'Atlantique Sud

Par M. Boubacar BAH

Pour obtenir le grade de

**Docteur de Sorbonne Université**

Présentée et soutenue publiquement le 12 Mai 2023

**Devant un jury composé de :**

M. Damien Delvaux de Fenffe, Géologue sénior - Musée Royal de l'Afrique Centrale, Belgique (Rapporteur)

M. Khalid Amrouch, Professeur associé – Université Mohammed VI, Maroc (Rapporteur)

Mme. Juliette Lamarche, Maître de conférences (HDR) – Université Aix-Marseille (Examinatrice)

M. Loïc Labrousse, Professeur – Sorbonne Université (Président du jury)

Mme. Catherine Homberg, Maître de conférences (HDR) – Sorbonne Université (Examinatrice)

M. Olivier Lacombe, Professeur – Sorbonne Université (Directeur de thèse)

M. Nicolas Beaudoin, Maître de conférences (HDR) – Université de Pau et des Pays de l'Adour (Co-directeur de thèse)

M. Pierre-Alexandre Teboul, Géologue – TotalEnergies (Co-encadrant)

**Invités :**

M. Claude Gout, Chercheur associé - Université de Pau et des Pays de l'Adour (UPPA)

M. Jean-Pierre Girard, Expert géochimie inorganique – TotalEnergies

# Remerciements

Je voudrais introduire brièvement le contexte dans lequel s'est réalisé cette thèse ainsi que les différentes personnes qui ont permis de mettre "le petit au bout". Je souhaite remercier les membres du Jury, Damien Delvaux (Musée Royal de l'Afrique Centrale, Belgique, rapporteur), Khalid Amrouch (Université Mohammed VI, Maroc, rapporteur), Juliette Lamarche (Université Aix-Marseille, examinatrice), Catherine Homberg (Sorbonne Université, examinatrice), Loïc Labrousse (Sorbonne Université, Président du jury), Pierre-Alexandre Teboul (TotalEnergies Pau, co-encadrant de thèse) et mes deux directeurs de thèse pour leur remarques et critiques qui m'ont permis de progresser.

Je tiens tout d'abord à rendre hommage à mes directeurs de thèse et mes promoteurs chez TotalEnergies. Merci à Olivier Lacombe (directeur de thèse) et Nicolas Beaudoin (co-directeur de thèse) dont la vision, l'expertise et l'engagement ont été d'une valeur inestimable. Votre passion pour la recherche, votre perspicacité et votre dévouement ont été une source d'inspiration constante. Grâce à votre guidance éclairée, vos conseils avisés et votre disponibilité sans faille, j'ai pu repousser mes limites intellectuelles et repenser mes approches méthodologiques. Vos enseignements précieux ont façonné ma pensée critique et ont contribué à faire de cette thèse un travail solide et rigoureux.

Merci Olivier pour m’avoir fait confiance et m’avoir donné cette opportunité unique d’apprendre ce qu’est la recherche. Tu m’as pris sous ton aile depuis le Master et tu ne m’as jamais lâché depuis. Merci d’avoir été présent à tout moment, que ce soit pour m’encourager à avancer ou, de temps à autre, me pousser un peu plus dans mes retranchements; merci de m’avoir recadré dès que je partais un peu dans tous les sens. Et surtout merci d’avoir été là dans les moments les plus difficiles au cours de ses dernières années qui n’ont pas été facile pour moi de point de vue personnel et sanitaire.

Bien évidemment, je suis très reconnaissant envers Claude Gout qui a initié ce projet et sans qui cette thèse n’aurait jamais eu lieu pour sa confiance et son soutien tout au long de ces trois années. Il m’a transmis une partie de son énorme expérience en matière de géologie. Ses vastes connaissances m'ont permis, en particulier sur le contexte régional et la modélisation, d'élargir la vision de ma problématique scientifique et pétrolière. Lors de mes déplacements au CSTJF de TotalEnergies à Pau, j'ai rencontré de nombreuses personnes que je tenais aussi à mettre en valeur. Tout d'abord, je voulais remercier Jean-Pierre Girard qui m’a beaucoup appris sur la géochimie minérale et la diagénèse dans les carbonates qui a beaucoup enrichi mon travail. Je

tiens à remercier Olivier Chailan, Sébastien Déhez et Pierre-Alexandre Teboul qui se sont relayés successivement au co-encadrement cette thèse pour leur soutien et leur disponibilité car ils m'ont beaucoup appris. Merci également à Philippe Marchina, Jean-Yves Leroy pour les discussions sur la géomécanique et enfin Lionel Martinez et toute l'équipe à la carothèque avec qui j'ai developpé des liens étroits pour leur aide et leur soutien technique.

Merci à l'ISTeP de m'avoir accueilli pendant 4 ans maintenant et particulièrement à tous les thésards pour les moments de détente, salvateurs au cours de ces années de travail. À mes collègues et camarades, je veux adresser mes remerciements chaleureux. Votre esprit de camaraderie et votre volonté de partager vos connaissances ont créé une atmosphère d'apprentissage inspirante et bienveillante. Un spécial clin d'oeil à Aniès Zeboudj avec qui j'ai collaboré depuis son Master et qui partage avec moi le burau pour son aide, sa gentillesse et sa joie de vivre débordante. La relève de la team « calcite twin » est assurée.

D'un point de vue plus personnel je tiens à exprimer ma reconnaissance envers mes amis et ma famille, qui ont été une source inépuisable de soutien, d'amour et de motivation tout au long de cette aventure. Votre présence constante, vos encouragements inconditionnels et votre croyance en mes capacités ont été des facteurs clés dans l'accomplissement de ce projet. Votre soutien moral, vos gestes d'attention et vos mots d'encouragement ont nourri ma détermination, même dans les moments de doute et de difficulté. Je suis profondément reconnaissant pour le soutien indéfectible que vous m'avez apporté.

Enfin, je tiens à exprimer ma gratitude envers le programme de R&D Frontier Exploration de TotalEnergies, l'organisme de financement et Sorbonne Université qui ont rendu cette thèse possible. Leurs ressources, leur soutien logistique et leurs opportunités de collaboration ont été des éléments clés dans la réalisation de ce travail. Leur engagement en faveur de la recherche et de l'éducation a joué un rôle fondamental dans la poursuite de mes objectifs académiques.

En résumé, je suis profondément reconnaissant envers toutes les personnes qui ont contribué de près ou de loin à la réalisation de cette thèse de doctorat. Leurs encouragements, leurs idées, leur soutien et leur confiance ont été des moteurs essentiels pour mener à bien ce travail de recherche. Je suis conscient que ce projet n'aurait pas été possible sans leur précieuse contribution, et je les remercie du fond du cœur pour leur engagement et leur impact positif sur mon parcours académique et professionnel.

# Résumé

La présente thèse a pour objectif d'éprouver des méthodologies permettant de reconstituer l'évolution des propriétés reservoirs et de la pression subit par un réservoir. Ce manuscrit présente (1) une caractérisation pétrologique des roches réservoirs avec une estimation du calendrier de l'évolution de la porosité, (2) les résultats d'une étude paléopiézométrique, et (3) une évolution des contraintes effectives et potentielles (sur)pressions de fluides ayant prévalu dans le réservoir carbonaté au cours de son évolution. Ces éléments permettent de reconstituer l'histoire d'enfouissement et des paléocontraintes subies par des réservoirs carbonatés dans un contexte de marge passive. Pour cela ce travail s'est basé sur une approche couplée de deux outils paléopiézométriques complémentaires combinant l'inversion des macles de la calcite et l'inversion de la rugosité des stylolites. Cette approche a été combinée avec des analyses pétrographiques, géochimiques, géomécaniques et géochronologiques pour bien caractériser le réservoir. Le matériel étudié lors de cette thèse consiste en des carottes de forage offshore récupérées de puits profonds fournis par TotalEnergies situés dans les bassins du Bas Congo et de Kwanza sur la marge ouest africaine de l'océan Atlantique Sud. Ces bassins ont subi un épisode de rifting au Crétacé inférieur (145,5-112 Ma).

L'étude de la destruction de la porosité des réservoirs pré-sel de la formation TOCA syn-rift d'âge Barrémien (130-125 Ma) à partir de carottes prélevées dans le bassin du Bas Congo a révélé que la porosité initiale avait été réduite à sa valeur actuelle de 4-8% au cours des 35 premiers Ma de son histoire d'enfouissement, atteignant ~10% après seulement 10 Ma, i.e. dans les 400-500 premiers mètres d'enfouissement et que la porosité actuelle n'avait pas évolué de manière significative depuis 95 Ma (fin de la stylolitisation). Cette étude a ainsi montré que les propriétés des réservoirs dans les formations carbonatées bioclastiques telles que la formation TOCA peuvent être largement contrôlés par des processus diagénétiques précoces et très superficiels plutôt que par des réactions mésogénétiques qui se produisent ultérieurement en profondeur dans l'histoire de l'enfouissement.

Une étude paléopiézométrique a été réalisée dans le but de reconstituer l'histoire d'enfouissement et des paléocontraintes des formations carbonatées de la TOCA (syn-rift) du Barrémien et Sendji (post-rift) de l'Albien sur la marge ouest africaine. La paléopiézométrie basée sur l'inversion de la rugosité des stylolites et l'inversion des macles de la calcite a été combinée à l'analyse de la fracturation, à la datation géochronologique U-Pb du ciment calcitique et à la modélisation de l'enfouissement des deux formations pour reconstruire les orientations et les grandeurs des contraintes horizontales et verticales ayant affecté les deux

formations au cours du temps. L'inversion des macles de la calcite réalisée sur des ciments précoces a révélé que les carbonates syn-rift et post-rift avaient enregistré une histoire des paléocontraintes polyphasée, incluant (1) des régimes de contraintes extensifs liés à l'ouverture l'océan Atlantique Sud (145,5-112 Ma), avec un $\sigma_3$ orienté NE-SW à E-W, et à l'échelle du bassin des failles normales orientées N-S et NE-SW. Cette phase d'extension n'est observée que dans les formations syn-rift. (2) des régimes de contraintes extensifs associés à une tectonique salifère locale affectant les formations post sel, trouvés uniquement dans la formation Sendji (101 à 80 Ma) avec un $\sigma_3$ orienté ~N-S et ~E-W. (3) Des régimes de contraintes compressifs et décrochants avec un $\sigma_1$ horizontal orienté ~N-S à NE-SW probablement liés à la collision Afrique-Eurasie. (4) Des régimes de contraintes compressifs et décrochants avec un $\sigma_1$ horizontal orienté ~E-W que nous avons proposé d'atrribuer à la poussée à la ride médio-Atlantique et qui prévalent depuis ~15-10 Ma.

## Abstract

This thesis aims to test methodologies allowing the reconstruction of the evolution of reservoir properties and their pressure. This manuscript presents (1) a petrological characterization of the reservoir rocks with an estimation of the timing of porosity evolution, (2) the results of a paleopiezometric study, and (3) an evolution of effective stresses and potential fluid (over)pressures that prevailed in the carbonate reservoir during its evolution. These tools allow the reconstruction of the burial history and the paleostresses experienced by carbonate reservoirs in a passive margin. For this purpose, this work was based on a coupled approach of two complementary paleopiezometric tools combining the inversion of calcite twin data and stylolite roughness data. This approach was combined with petrographic, geochemical, geomechanical and geochronological analyses to fully characterize the reservoir. The studied material during this thesis consists of offshore cores recovered from deep wells provided by TotalEnergies located in the Lower Congo and Kwanza basins on the West African margin of the South Atlantic Ocean. These basins underwent a rifting event in the early Cretaceous times (145.5-112 Ma).

The study of the porosity destruction of the pre-salt reservoirs of the syn-rift TOCA formation of Barremian age (130-125 Ma) from offshore core located in the Lower Congo basin revealed that the initial porosity was reduced to its current value of 4-8% during the first 35 Ma of its burial history, reaching ~10% after only 10 Ma, i.e. in the first 400-500 meters of burial and that the current porosity has not evolved significantly since 95 Ma (end of stylolitization). This study has shown that the outcome of reservoir properties in bioclastic carbonate formations such as the TOCA formation may be largely controlled by early and very shallow diagenetic processes rather than by mesogenetic reactions that occur later in the burial history.

A paleopiezometric study was carried out in order to reconstruct the burial and paleostress history of the TOCA (syn-rift) Barremian and Sendji (post-rift) Albian carbonate formations on the West African margin. Paleopiezometry based on stylolite roughness inversion and calcite twins inversion was combined with fracture analysis, U-Pb geochronological dating of the calcite cement and burial modelling of the both formations to unravel the orientations and magnitudes of horizontal and vertical stresses that affected the TOCA and Sendji formations over time. The inversion of calcite twins on early diagenetic cements revealed that syn-rift and post-rift carbonates recorded a complex, polyphase paleostress history, (1) extensional stress regimes related to the opening of the South Atlantic ocean (145.5-112 Ma), with a $\sigma_3$ oriented NE-SW to E-W, and at the basin scale N-S and NE-SW oriented normal faults. This extensional

phase is only recorded by the TOCA syn-rift formation. (2) Extensional stress regimes associated with local salt tectonics that affect the post-salt formations, only found in the Sendji formation (101 to 80 Ma) with a $\sigma_3$ oriented ~N-S and ~E-W. (3) Compressional and strike-slip stress regimes with horizontal $\sigma_1$ oriented ~N-S to NE-SW probably related to the Africa-Eurasia collision at ~67-60 Ma. (4) Compressional stress regimes with horizontal $\sigma_1$ oriented ~E-W that we proposed to attribute to the mid-Atlantic ridge push and that have prevailed since 15-10 Ma onwards.

# Table des matières

# Chapitre I : Introduction générale : problématique, contexte régional et méthodologie adoptée

# 1. Thématique de la thèse

L'hétérogénéité des propriétés pétrophysiques des carbonates est liée aux microstructures héritées à la fois des conditions de dépôt et de la diagenèse des sédiments, de l'histoire des contraintes subies par la roche et de l'histoire des interactions fluides roches. (Regnet et al., 2019). Ces roches représentant environ 40 % des zones exploitées dans l'industrie pétrolière et gazière ce qui fait d'elles d'importantes cibles pour l'exploration (Ehrenberg et al., 2009a). Les propriétés pétrophysiques des roches réservoir jouent un rôle fondamental dans la viabilité économique d'un gisement de pétrole et/ou de gaz (Worden et al., 2018), et plus récemment un élément majeur de la transition énergétique, via le stockage des gaz à effet de serre et des déchets issus de l'activité anthropique (Wang et al., 2020). La porosité d'un réservoir affecte le volume d'hydrocarbures en place et la perméabilité affecte la vitesse à laquelle les hydrocarbures s'écoulent du réservoir vers les puits de forage (Gluyas and Swarbrick, 2004). Ces propriétés doivent être quantifiées afin de définir la qualité du réservoir et de réduire les risques exploratoires ou de minimiser les coûts de production. De ce fait la prédiction de la qualité des réservoirs, est donc une question primordiale pour l'exploration-production des hydrocarbures; notamment car celle-ci tend à se faire dans des environnements de plus en plus difficiles d'accès et en ciblant des réservoirs moins conventionnels (c'est-à-dire plus complexes). La porosité et la perméabilité actuelles sont mesurées ponctuellement à l'aide de techniques d'analyse sur carotte ou de diagraphie de puits, mais ces outils seuls ne permettent pas de faire des prédictions valide sur la qualité du réservoir loin du puits. Pour une meilleure prédiction via des modèles de bassin élaborés, il est essentiel de définir les facteurs de contrôle de cette qualité des réservoirs. Cela passe par plusieurs paramètres tels que les caractéristiques texturales du réservoir, telles que les types de grains et leur minéralogie, la granulométrie et le classement, le volume intergranulaire (indicateur de la compaction), le type et la quantité de la0 matrice, la minéralogie, la morphologie du ciment et le types de pores, leur origine et leur proportion, afin de pouvoir établir les principaux paramètres de contrôle de la qualité des réservoirs (Primmer et al., 1997). Il est également essentiel de quantifier l'histoire post-dépôt du réservoir, et notamment l'impact de la diagenèse, en reconstruisant l'historique des contraintes et des (sur)pression de fluides, de température et de nature des fluides qui ont caractérisé l'évolution de la roche depuis son dépôt jusqu'à son enfouissement et à son éventuel soulèvement, pour arriver à une compréhension globale et établir un modèle prédictif fiable sur la qualité des réservoirs (Worden et al., 2018). En intégrant d'autres disciplines telles que la sédimentologie, la géologie structurale, la géomodélisation et l'ingénierie des réservoirs, il est

possible que les modèles diagénétiques qui prennent en considération ces caractéristiques de l'histoire du dépôt et de l'enfouissement fournissent des informations plus pertinentes sur les mécanismes de contrôle de la qualité des réservoirs et constituent de puissants outils de prédiction. Il y a lieu de préciser qu'il existe des controverses concernant la compréhension des mécanismes de contrôle des qualités réservoirs (Morad et al., 2012). Parmi ces questions on compte par exemple l'effet inhibiteur du chargement en hydrocarbures sur la croissance minérale et la digenèse, également si c'est la contrainte effective ou la température qui contrôle la pression-solution (compaction chimique) et enfin le degré d'ouverture des systèmes géochimiques (ouvert, semi-ouvert ou fermé) pendant la diagenèse dans les réservoirs.

La contrainte effective est la contrainte qui s'exerce sur la partie solide du sédiment dans une masse rocheuse, par opposition à la pression de fluide hydrostatique présente dans les pores dans la roche. Le concept de contrainte effective a été introduit par Terzaghi, en 1923, et est défini par la différence entre la pression lithostatique et la pression de fluide. En terme de contrainte verticale, cette relation s'exprime comme suit (équation 1) :

$$\sigma v_{effective} = \sigma v_{litho} - P_f \quad (1)$$

avec $P_f$ – la pression de fluide ; $\sigma v_{litho}$ –la contrainte verticale liée au poids des sédiments. La pression de fluide hydrostatique ($P_f$) est définie par la pression exercée par le poids de l'eau dans le sédiment.

$$P_f = \rho_f g h \quad (2)$$

avec $\rho_f$ la densité du fluide ($g.cm^{-3}$), g l'accélération du champ gravitationnel ($m.s^{-2}$) et h la hauteur de la colonne d'eau (m).

La contrainte verticale lithostatique ($\sigma v_{litho}$) quant à elle represente la pression exercée sur la roche à une profondeur donnée due au poids des roches sus-jacentes.

$$\sigma v_{litho} = \rho_f g h \quad (3)$$

avec $\rho$ la densité des roches ($g.cm^{-3}$), g l'accélération du champ gravitationnel ($m.s^{-2}$) et h la profonduer considérée (m).

Des études (Lade et al., 1996; Chuhan et al., 2002; Makowitz and Milliken, 2003) ont montré que dans les réservoirs silicoclastiques, la contrainte effective représente le moteur de la compaction physique et le facteur le plus important de la perte de qualité des réservoirs.

De ce fait il est important pour l'exploration de connaitre la valeur de la contrainte effective et son évolution au cours de l'enfouissement.

Un autre paramètre important à prendre en compte dans l'étude des réservoirs en général est l'occurrence de surpressions de fluides dans le réservoir pendant son évolution. La surpression de fluide peut être définie comme un état de pression de fluide dans le réservoir supérieur à la pression de fluide hydrostatique (Li et al., 2022). Elle correspond à la différence entre la contrainte effective verticale et la pression de fluide hydrostatique (Fig. 1).

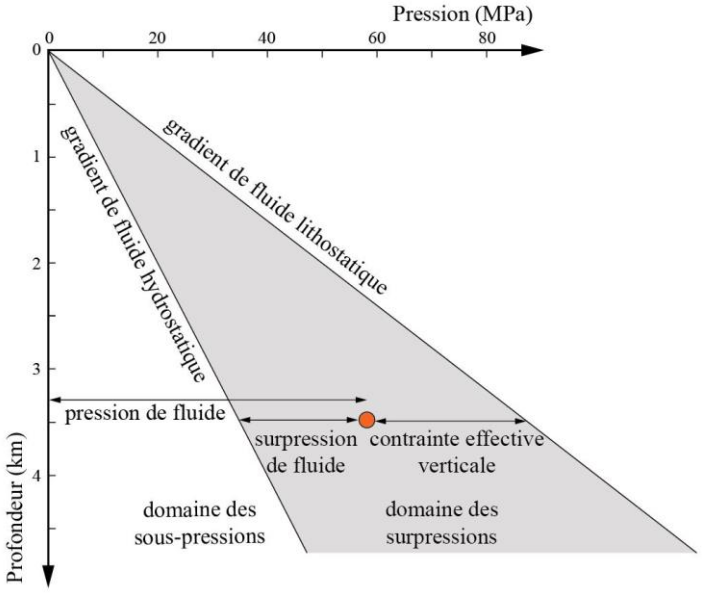


**Figure 1:** Définition de la contrainte effective et du domaine des surpressions de fluide.

Le maintien des surpressions à plus ou moins long terme dans le réservoir dépend de deux paramètres : (1) de la perméabilité globale du réservoir (partiellement controlé par les pores et les fractures) qui va définir la capacité d'expulsion des fluides des espaces interstitiels du réservoir (Green and Wang, 1986), (2) du mécanisme et de la vitesse de génération des surpressions de fluides dans le réservoir (Swarbrick et al., 2002). La surpression de fluide est l'un des facteurs de contrôle le plus important de l'accumulation et de la distribution de pétrole et de gaz dans le réservoir (Frazer et al., 2014; Sakhaee-Pour and Bryant, 2014; and Jones, 2016; Duan et al., 2018). Elle a un effet positif direct primordial qui est de retarder et réduire les effets de la compaction mécanique avec l'enfouissement. Elle a aussi un effet secondaire indirect de réduction des processus de cimentation/dissolution car elle limite/réduit les circulations de fluides à l'intérieur du réservoir. Cet effet-là peut être négatif ou positif selon les cas : un effet négatif en limitant la dissolution (porosité secondaire) lors de la diagénèse qui améliore les propriétés réservoir (Duan et al., 2018) ou un effet positif en limitant la cimentation qui détruit la porosité primaire ou en favorisant la réouverture/extension de fractures fermées préexistantes (Bian et al., 2011). Il est par conséquent crucial pour l'exploration de pouvoir estimer les surpressions de fluides et surtout le calendrier du développement des surpressions

par rapport au chargement en hydrocarbures du réservoir. Il y a lieu de souligner que la reconstruction de la surpression de fluide passée d'un réservoir carbonaté reste un défi à cause des processus diagénétiques variés et divers pouvant modifier les propriétés réservoirs des carbonates au cours du temps (Liu et al., 2021).

Les origines des surpressions de fluide dans les réservoirs carbonatés peuvent être diverses, parmi lesquelles les plus courantes sont :

- Le chargement vertical ou le déséquilibre de compaction (i.e. sous-compaction) : Il correspond à l'enfouissement d'une roche sédimentaire sous l'effet d'une sédimentation rapide ou lors de son charriage sous une nappe (Wang et al., 1990 ; Smith and Wiltschko, 1996 ; Mark et al., 2009). Dans cette situation, le fluide interstitiel n'a pas le temps de s'échapper dans les niveaux sus-jacents au réservoir et la pression fluide augmente jusqu'à dépasser la pression hydrostatique. Cette surpression peut provoquer des fractures ou des failles dans les roches réservoirs.
- Le chargement horizontal ou la compression tectonique : Le mécanisme est le même que dans la compaction verticale, la différence réside dans l'orientation des contraintes (Balen and Cloetingh, 1995). La compression latérale résultante peut entraîner le tassement et la compaction des roches réservoir. Cela peut conduire à une augmentation de la pression et à une surpression (Yielding and Freeman, 2011 ; Guo et al., 2016).
- La migration d'hydrocarbures: La migration d'hydrocarbures au sein du réservoir peut conduire à une surpression (Bredehoeft et al., 1994, Tian et al., 2008, Guo et al., 2010, 2011). Lorsque la matière organique est enfouie et soumise à une température et une pression élevée, elle peut libérer des hydrocarbures qui migrent vers les réservoirs et qui s'accumulent dans les pores. L'accumulation d'hydrocarbures peut provoquer une surpression dans le réservoir, notamment dans le cas des hydrocarbures gazeux en raison du « boyancy effect ». D'une manière générale, le transfert latéral de fluides (y compris eaux, saumures…) depuis des réservoirs plus profonds très pressurisés jusqu'à des réservoirs moins enfouis et moins pressurisés par advection peut générer des surpressions.
- Le dépôt et le déplacement du sel : Lorsque les structures salines se déforment et se déplacent, elles peuvent générer une pression au sein des roches réservoirs. Cette surpression peut provoquer des fractures ou des failles dans les roches.

Comprendre l'origine et les mécanismes de développement de la surpression dans un réservoir carbonaté est essentiel pour la prédiction de la pression et la compréhension de

l'accumulation des hydrocarcarbures dans le réservoir. Il est communément admis que le déséquilibre de compaction est la principale cause de surpression.

L'objectif de cette thèse est d'une part de réaliser une étude paléopiézométrique couplée macles de la calcite-rugosité des stylolites permettant de reconstituer l'histoire d'enfouissement et des paléocontraintes subies par des réservoirs carbonatés dans un contexte de marge passive, et d'autre part de proposer une méthodologie permettant de déterminer les contraintes effectives et les potentielles (sur)pressions de fluides ayant prévalu dans le réservoir carbonaté au cours de son évolution.

Au-delà de l'histoire des pressions de fluides d'un réservoir, la taille et la géométrie du piège pétrolier, le calendrier et les chemins de la migration des fluides résultent en partie de l'histoire des contraintes subies par les roches sédimentaires (Tveranger et al., 2018; Zhang et al., 2019 ; Wang et al., 2019). Pourtant à ce jour très peu d'outils existent pour reconstituer l'histoire des paléocontraintes dans les réservoirs carbonatés, qui restent une donnée absente des modèles de bassin intégrés et prédictifs.

Ces modèles sont communément utilisés dans l'industrie pétrolière pour reconstruire l'histoire d'enfouissement, mais ces outils ont l'inconvénient notamment d'être dépendants du gradient géothermique qui est variable au cours du temps (Tissot et al., 1987 ; Allen and Allen, 2013).

Des outils paléopiézométriques fondées sur l'étude des mécanismes de déformation ont été développés afin de reconstituer en totalité ou en partie les orientations et magnitudes des paléocontraintes subies par les roches au cours de leur histoire d'enfouissement ou d'exhumation. Ces outils paléopiézométriques sont basés sur des procédés d'inversion liant la déformation à la contrainte par un modèle physique.

Le terme paléopiézométrie désigne ainsi l'ensemble des méthodes permettant d'accéder aux grandeurs des paléocontraintes dans la croûte terrestre sur de longues périodes de temps (Beaudoin et Lacombe, 2018). La paléopiézométrie basée sur l'inversion des macles de la calcite et la paléopiezométrie basée sur l'inversion de la rugosité des stylolites ont été choisies pour cette étude. Cette section résume l'utilisation des méthodes paléopiézométriques et l'approche combinant plusieurs méthodes (multi-proxies) pour mieux contraindre l'histoire de l'enfouissement et des paléocontraintes dans les carbonates. Les méthodes abordées ici sont détaillées dans les différents articles qui forment le corps de ce manuscrit de thèse.

L'inversion des macles de la calcite a montré un fort potentiel pour déterminer l'évolution du tenseur des contraintes déviatoriques (orientations des contraintes principales et magnitudes des différentielles de contraintes) au cours de l'histoire d'un bassin sédimentaire en enregistrant les événements tectoniques majeurs (voir la revue de Lacombe et al., 2021a pour plus de détails). Cet outil paléopiézométrique a été appliqué jusqu'alors principalement dans des chaînes plissées d'avant-pays (voir synthèses de Lacombe, 2010; Lacombe et al., 2021a), à l'exception des études réalisées sur des carottes orientées de TotalEnergies du bassin de Paris (Lacombe et al., 1994) et dans le bassin Aquitain (Rocher et al., 2000), et plus récemment en Australie dans les bassins de Cooper (Kulikowski and Amrouch, 2017, 2018) et d'Otway (Burgin et al., 2018). Le développement récent d'un autre paléopiézomètre, l'inversion de la rugosité des stylolites (Schmittbuhl et al., 2004), offre une méthodologie complémentaire permettant de reconstruire les contraintes verticales lorsqu'elle est appliquée aux stylolites sédimentaires (Ebner et al., 2009a), donc d'approcher la profondeur d'enfouissement des couches indépendamment de toute considération sur le gradient géothermique et la pression de fluide, ou de reconstruire les contraintes horizontales lorsqu'elle est appliquée aux stylolites tectoniques (Ebner et al., 2010b). Au-delà de l'inversion de la rugosité des stylolites, des études ont montré que les stylolites pouvaient être utilisés pour quantifier au premier ordre le taux de compaction chimique (Toussaint et al., 2018; Koehn et al., 2016, 2022). Beaudoin et al., (2016) ont montré pour la première fois l'intérêt d'une approche couplée de deux méthodes paléopiézométrique (l'inversion des macles de la calcite et l'inversion de la rugosité) pour la reconstitution plus complète des paléocontraintes.

L'objectif de ce travail de thèse est de s'appuyer sur les travaux antérieurs sur les paléopiézomètres cités ci-dessus afin d'avoir un outil robuste permettant d'estimer les paléocontraintes effectives en lien avec la fracturation méso-échelle dans les réservoirs carbonatés. Des études récentes ont montré qu'en adoptant une approche multi-proxies combinant l'inversion de la rugosité des stylolites sédimentaires, la datation absolue du ciment, la fracturation et un modèle d'enfouissement, il était possible de déterminer la profondeur d'enfouissement maximale pendant la période où la contrainte principale maximale $\sigma_1$ était verticale, le calendrier de l'activité de la pression-solution et enfin de contraindre l'histoire tectonique complète d'un bassin sédimentaire (Labeur et al., 2021; Lacombe et al., 2021b). La datation absolue des ciments maclés (Fig. 2B) permet de donner un âge maximum pour le début du maclage, tandis que les profondeurs déduites de l'inversion de la rugosité des stylolites sédimentaires (Fig. 2C & 2D) reportées sur un modèle d'enfouissement permettent de donner

un âge à la période de dissolution le long des stylolites sous une contrainte principale maximale $\sigma_1$ verticale (Fig. 2G). Cela permet ainsi de contraindre, en l'absence de toute autre information, le calendrier des régimes de contraintes extensifs ($\sigma_1$ vertical) enregistrés par les macles aux périodes où l'on sait d'après les stylolites que $\sigma_1$ est vertical, et celui des régimes de contraintes compressives ($\sigma_1$ horizontal) en dehors de ces périodes (Fig. 2G). La combinaison de la méthode paléopiézométrique basée sur l'inversion des macles de la calcite avec l'étude de la fracturation permet d'approximer les (sur)pressions de fluides via un digramme de Mohr-Coulomb (avec l'enveloppe de la rupture du matériau) (Amrouch et al., 2011 ; Beaudoin et al., 2014).

L'objectif à moyen/long terme est de mettre à la disposition de l'Exploration-Production de TotalEnergies un outil et une méthodologie fiables pour aider à la reconstruction des historiques de développement des (sur)pressions de fluides dans les zones prospectives. A cet effet le projet de thèse a été conçu comme un projet de recherche appliqué (avec un cas d'application et un cas de validation de la méthode) pour répondre le plus efficacement possible aux besoins de l'industrie.

Une étude précédente a été financée par TotalEnergies dans le but de développer un outil permettant d'estimer la contrainte effective et les surpressions de fluide dans les réservoirs silicoclastiques à partir de la fracturation des grains de quartz (Mehrkian, 2016).

Cette nouvelle approche combine (1) l'inversion des macles de la calcite effectuée dans des ciments datés par géochronologie U-Pb, (2) la paléopiézométrie de la rugosité des stylolites sédimentaires combinée à l'histoire d'enfouissement modélisées, et (3) l'analyse de la fracturation afin de reconstruire l'histoire complète des paléocontraintes sur la marge ouest africaine.

Cette approche est appliquée à des carottes de forage offshore récupérées de puits profonds fournis par TotalEnergies situés dans les bassins du Bas Congo (étude de référence) et de Kwanza (benchmark validation de la méthode). Avoir un outil qui permet de reconstruire l'histoire des paléocontraintes en orientation et en grandeur sur de petit volume de roche comme les carottes est un atout majeur dans la compréhension globale de l'histoire tectonique de la marge où les seules données disponibles reposent en majeure partie sur l'interprétation sismique et les données de paléocontraintes collectées sur la partie continentale à partir de l'inversion des failles striées.

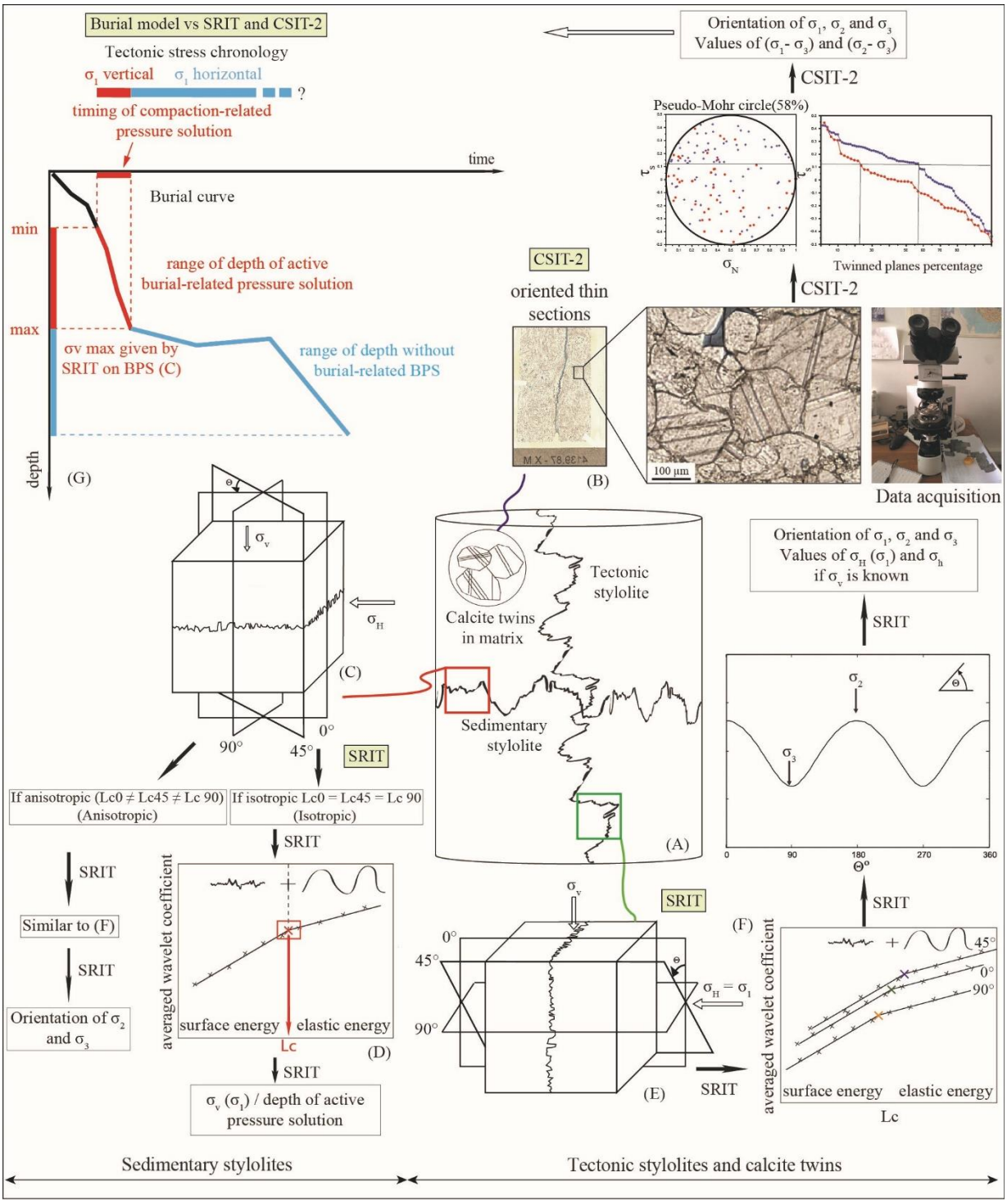


**Figure 2:** Workflow de l'approche multi-proxy utilisée dans cette thèse. (A) Schéma illustrant sur une carotte les éléments étudiés (stylolites et macles de la calcite). (B) Illustation de l'inversion des macles de la calcite: de l'acquisition des données aux résultats. (C - D) Schéma des coupes et principe d'inversion de la rugosité des stylolites sédimentaires. (E – F) Principe d'inversion de la rugosirté des stylolites tectoniques. (G) Représentation de la méthode de conversion en temps pour les paléo-enfouissement obtenues par l'inversion de la rugosité des stylolites à l'aide du modèle d'enfouissement.

Cette opportunité unique de reconstruire l'histoire locale complète de l'histoire d'enfouissement et des paléocontraintes de réservoirs offshore profond nous permet d'aborder la question de l'origine des contraintes qui ont affecté la marge passive ouest africaine au cours de son histoire.

## 2. Problématique de la thèse

Cette thèse intitulée : « **Apport de l'analyse paléopiézométrique des macles de la calcite et des stylolites à la compréhension de l'histoire tectonique et d'enfouissement des bassins sédimentaires de la marge ouest-africaine de l'Atlantique sud** » a été initiée par la R&D de TotalEnergies dans le but de tester l'applicabilité des méthodes paléopiézométriques existantes pour remonter aux contraintes effectives dans les réservoirs carbonatés et d'évaluer comment elles pourraient être utilisées pour améliorer les modèles de bassin. Ce besoin vient de l'absence d'outil permettant de déterminer les contraintes effectives subit par un réservoir carbonaté au cours du temps.

Cette thèse aborde les sujets suivants: (1) l'apport d'une approche multi-proxies pour la reconstitution de l'histoire d'enfouissement et d'évolution des propriétés réservoirs d'un réservoir carbonaté très enfoui, permettant de déterminer le calendrier de la précipitation des ciments dans lesquels les macles se développent et celui du développement des stylolites, permettant de reconstruire l'histoire de la destruction de la porosité, (2) l'application de la méthode paléopiézométrique basée sur l'inversion des macles de la calcite pour la reconstruction de l'histoire des paléocontraintes (orientation des contraintes principales et grandeur des différentiels de contraintes) enregistré par les réservoirs carbonatés au cours de leur histoire, (3) l'approche paléopiézométrique couplée macles de la calcite-inversion de la rugosité des stylolites combiné avec l'étude des données de la fracturation et des tests géomécaniques pour la quantification des contraintes effectives et la formulation d'hypothèses sur les (sur)pressions de fluides ayant prévalu dans le réservoir au cours de son enfouissement et la prédiction du développement des fractures dans les réservoirs carbonatés.

- **Problématique 1 : Comment estimer à la fois le calendrier et la proportion de la destruction de la porosité dans des réservoirs carbonatés pré-sel enfouis ? Quelles sont les leçons à tirer pour le schéma d'exploration des carbonates ?**

L'étude porte sur les carbonates lacustres syn-rift d'âge Barrémien de la formation TOCA ou équivalent (TOCA pour TOp CArbonates ; Fig. 3). Ces carbonates qui constituent d'importants réservoirs de pétrole et de gaz de la marge ouest africaine, ont des propriétés

réservoirs très variées et sont néanmoins assez peu étudiés (Harris, 2000). Plusieurs questions restent en suspens sur les processus diagénétiques dont dépend la préservation/destruction des propriétés réservoirs.

Nous proposons ici une approche combinant plusieurs techniques pour définir avec précision et valider la chronologie de l'évolution de la porosité dans ces carbonates pré-sel. Le résultat de cette étude est présenté sous la forme d'un article (Bah et al.) publié en 2023 dans le journal Marine and Petroleum Geology.

- **Problématique 2 : Quel état de contraintes peut être enregistré dans un réservoir carbonaté supra-sel très enfoui ?**

La formation cible de cette étude sont les carbonates post-rift d'âge Albien inférieur de la formation Sendji supra-salifère (Fig. 3). Cette formation est très répandue et représente l'un des plus grands réservoirs d'hydrocarbures dans la zone d'étude.

Cette étude a permis de contraindre l'histoire d'enfouissement et des paléocontraintes des carbonates supra-sel de la formation Sendji par l'approche méthodologique multi-proxy appliquée dans cette thèse. Les résultats ont été valorisés sous la forme d'un article (Zeboudj, Bah et al.) publié en 2023 dans le journal Marine and Petroleum Geology.

- **Problématique 3 : Quel état de contraintes peut être enregistré dans un réservoir carbonaté infra-sel très enfoui ? Quelle implication dans l'histoire tectonique du bassin ?**

Cette étude a pour but de reconstruire l'histoire des paléocontraintes de la formation TOCA d'âge Barrémien (130-125 Ma), profondément enfouie dans le bassin du Bas Congo (marge passive ouest africaine), en utilisant l'inversion des macles de la calcite pour les paléocontraintes pour déchiffrer les différents tenseurs de contraintes qui ont affecté la formation au cours du temps. Une comparaison des tenseurs issus de l'inversion des macles de la calcite dans la formation Sendji supra-sel et ceux de la TOCA infra-sel est faite dans cette étude pour voir s'il y a une différence sur l'histoire des paléocontraintes enregistrée par les deux formations. Cette comparaison nous a permis de discuter de l'influence des dépôts salifères aptiens sur l'évolution des contraintes sur la marge. Les résultats de l'étude paléopiézométrique dans la formation Sendji ont permis de contraindre le calendrier de l'histoire complète des paléocontraintes enregistré par la formation. Ces résultats ont servi par la suite à contraindre l'histoire post-rift

enregistrés dans la TOCA sur la base des similitudes des tenseurs de contrainte enregistrés dans les deux formations.

Les résultats de cette étude ont été valorisés sous forme d'un article (Bah et al.) actuellement en cours de révisions (modérées) pour le journal Tectonophysics.

# 3. Contexte géologique régional

### 2.1.3.1. Cadre géodynamique

L'ouverture de l'océan Atlantique Sud a démarré à la fin du Trias. Cette période est marquée par la dislocation du méga-continent Pangée le long d'anciennes lignes de sutures héritées de l'amalgamation des supercontinents Gondwana et Laurasia (Moulin et al., 2010).

Dès le Jurassique inférieur, la séparation entre le Gondwana et la Laurasia entraîne la mise en place de grandes provinces ignées dont le volcanisme de Karoo le long de la ligne de suture des deux continents. Ensuite l'ouverture stricte s'initie au Crétacé inférieur avec la création d'une zone amincie avec des systèmes de failles normales et de détachement entre les futurs continents Afrique et Amérique du Sud. L'océan Atlantique Sud est à un stade embryonnaire à 125 Ma (anomalie magnétique M0, Gradstein et al., 2004). L'évolution du rifting de l'océan Atlantique Sud peut être décomposé en plusieurs phases tectoniques qui ont été identifiées dans les architectures tectono-sédimentaires des marges de l'Atlantique Sud (voir: Karner et al., 2003; Contrucci et al., 2004; Moulin et al., 2005). Cependant, étant donné l'absence de forages profonds dans ces domaines, le timing précis de ces différentes phases reste difficile à déterminer et sujet à des interprétations contrastées.

Du point de vue structural, l'Atlantique Sud peut être subdivisé en quatre segments majeurs du nord au sud (Torsvik et al., 2009; Moulin et al., 2010) (Fig. 3):

- Le segment Equatorial situé dans la partie septentrionale de l'Atlantique Sud,
- Le segment Central situé entre les zones transformantes de l'Ascension (Ascension FZ) et du Rio Grande (Rio Grande FZ),
- Le segment Austral situé entre les zones transformantes du Rio Grande et du Falkland-Agulhas,
- Le segment Falkland faisant la jonction avec la ride indienne SW.

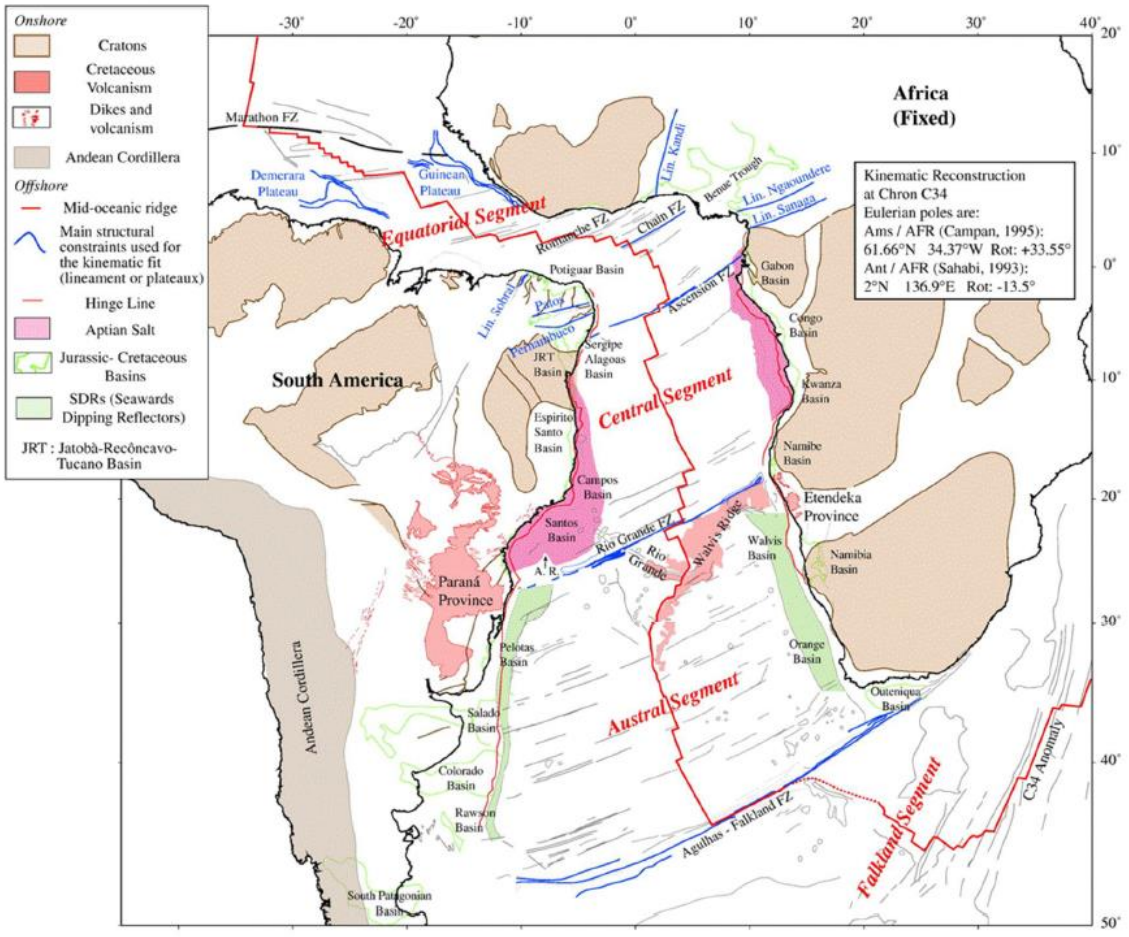


**Figure 3:** Carte structurale de l'océan Atlantique Sud montrant les différents (Moulin et al., 2010).

### 2.2.3.2. Cadre tectonique et sédimentaire du segment central de l'Atlantique Sud

Cette étude se concentre tout particulièrement sur le segment Central, qui héberge les bassins de Douala, de Gabon, du Bas Congo, de Kwanza, de Benguela et de Namibie situés entre le Cameroun au nord et la Namibie au sud (Fig. 3). Les bassins cités ci-dessus forment ensemble le bassin salin aptien (Beglinger et al., 2012). Ces bassins partagent des caractéristiques structurales et stratigraphiques communes (Brownfield et al., 2006).

Selon Reston (2010), le segment Central est considéré comme non-volcanique. La présence d'un manteau exhumé serpentinisé soutient le modèle de marge pauvre en magma. On trouve peu de données dans la littérature sur les roches magmatiques anté-salifères profondément enfouies, ce qui contraste clairement avec la vaste littérature consacrée à l'expression magmatique du Crétacé précoce au large de l'Angola (Cainelli and Mohriak, 1999; Torsvik et al., 2009).

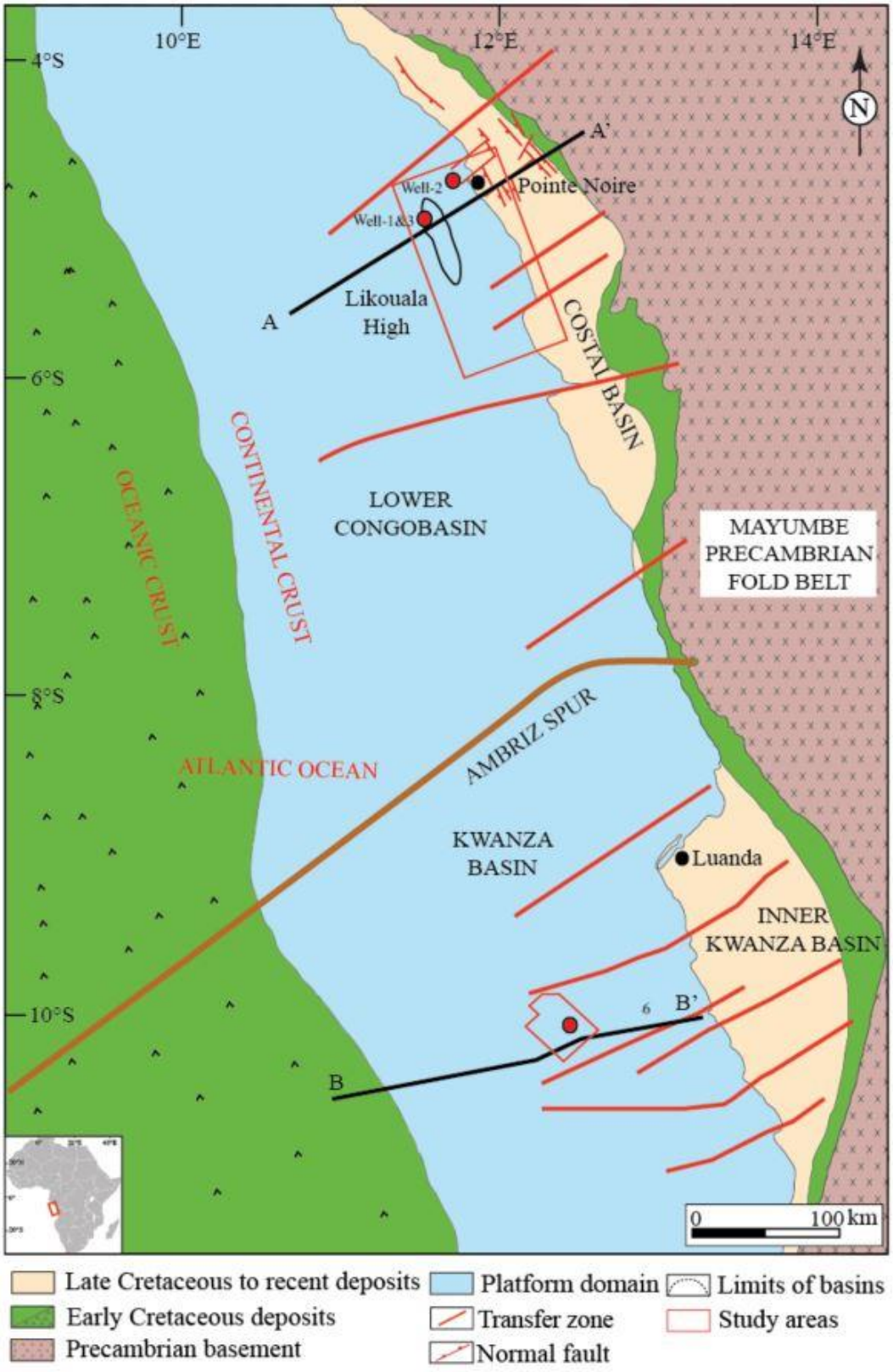


**Figure 4:** Carte structurale de l'Afrique le long de l'Atlantique Sud du sud du Gabon à l'Angola avec localisation des zones d'études dans les bassins du Bas Congo et de Kwanza. La couleur verte dans le domaine marin représente la croûte océanique du Crétacé. L'insert montre la localisation de la zone d'étude sur la marge ouest africaine de l'Atlantique Sud.

Deux événements magmatiques majeurs, qui ont influencé le bassin de Kwanza, ont été mis en évidence et datées par la géochronologie $^{40}Ar/^{39}Ar$ avec un âge plateau de 131,9 ± 1,6 Ma et 131,6 ± 1,4 Ma pour l'évènement principal et 126,1 ± 1,4 Ma pour le second évènement (Marzoli et al., 1999).

L'histoire tectono-sédimentaire du segment Central de l'Atlantique Sud peut être subdivisée comme suit (Fig. 5):

1) La période pré-rift correspond à des roches d'âge Précambrien à Jurassique qui sont observées dans le bassin intérieur du Gabon et qui existent aussi dans la partie orientale du bassin du Bas Congo (Brownfield et al., 2006 ; Delvaux et al., 2021). Cette phase est caractérisée par des failles intracratoniques et des dépôts clastiques continentaux d'âge Carbonifère-Jurassique (Fig. 5 & 6) dans les bassins intérieurs du Gabon et du Congo (Teisserenc and Villemin, 1990). La partie onshore du bassin de Kwanza contient des roches pré-rift d'âge jurassique potentiellement, constituées des séries continentales Red Beds et Red Basal (Burwood, 1999; Fig. 5). Les roches pré-rift n'ont pas été atteintes par les forages dans la partie offshore du basin (Brownfield and Charpentier, 2006). Dans le bassin du Bas Congo, la série syn-rift (Crétacé inférieur) repose directement sur le socle Précambrien (Fig. 5 & 6) formé de grès micacé quartzeux (Brice et al., 1982; Schoellkopf and Patterson, 2000). Le socle englobe à la fois la partie cristalline du craton du Congo et les sédiments précambriens pré-rift sus-jacents (Delpomdor et al., 2008; Mbina Mounguengui et Guiraud, 2009; Préat et al., 2010; Delvaux et al., 2021).
2) La première étape syn-rift entre le Berriasien et le Barrémien moyen (~144-127 Ma) correspond au développement et au fonctionnement des failles normales générant des blocs basculés et des bassins (Brownfield and Charpentier, 2006) progressivement remplis par un apport sédimentaires continental important composé de conglomérats, argiles et grès (Beglinger et al., 2012; Fig. 5). Une seconde étape du Barrémien moyen à l'Aptien (~127-117 Ma) correspond à des séquences sédimentaires très peu faillées (Uncini et al., 1998; Beglinger et al., 2012) avec des conditions environnementales de dépôt lacustres à marin peu profond (Beglinger et al., 2012). L'ensemble de la séquence sédimentaire associée à ces deux étapes du rifting est communément appelée « pré-sel »et/ou appartenant au « bassin sag » (Fig. 5 & 6).

3) Une phase tardi-syn-rift (phase de transition) qui est associée à des dépôts de sel et/ou d'évaporites (Lehner and De Ruiter, 1977; Teisserenc and Villemin, 1989; Aslanian et al., 2009) vers la fin de l'Aptien (117-112 Ma) (Fig. 5 & 6). Plusieurs études ont montré que l'apparition du sel est probablement liée à des transgressions marines progressives dans le proto-Atlantique Sud (Asmus and Ponte, 1973; Beglinger et al. 2011) et à des conditions plus arides (Bate, 1999; Karner and Gambôa, 2007). La rupture continentale est supposée être atteint vers ~112-110 Ma (Torsvik et al., 2009; Moulin et al., 2010).
4) Ces dépôts salifères sont ensuite recouverts par une plateforme carbonatée déposée au cours de l'Albien inférieur (Beglinger et al., 2012; Fig. 5). Le sel subit par la suite une déformation gravitaire à partir de la fin de l'Albien inférieur quand la plateforme carbonatée albienne sus-jacente commence à se développer de façon conséquente. Cette déformation gravitaire se fait en trois étapes : (1) l'initiation de diapirs de sel pendant l'Albien inférieur, (2) la création de structures locales de radeaux délimitées par des failles listriques (Rouby et al., 2002; Wonham et al., 2010) et (3) le développement de failles normales listriques N-S. Ensuite, au cours de l'accrétion océanique, la sédimentation post-rift s'installe sur la marge. De l'Albien à l'Eocène, des séquences sédimentaires marines se déposent en aggradation sur l'intervalle évaporitique et la plateforme carbonatée Albienne (Baudoy and Legorjus, 1991). Des séries marines peu épaisses déposées au cours du Cénomanien et Turonien (Séranne and Anka, 2005; Torsvik et al., 2009; Anka et al., 2010). Une phase d'uplift affecte ensuite la séquence sédimentaire à partir de l'Eocène (Kounov et al., 2009), et un nouveau système progradant se met en place à partir du Miocène en liaison avec le développement du dépôcentre tertiaire du Zaïre.

## 4. Présentation du matériel d'étude

Toutes les observations ont été faites et les données ont été acquises à partir de carottes offshore profondément enfouies sur la marge ouest africaine de l'Atlantique Sud (Fig. 4). Dans les puits où des carottes ont été prelevées, nous avons eu accès à plusieurs mètres de carottes, provenant de divers endroits dans le bassin (Fig. 4). Cependant, les intervalles de carottes étudiés comprennent toutes les textures sédimentaires significatives représentatives de l'ensemble de chaque carotte (Fig. 7).

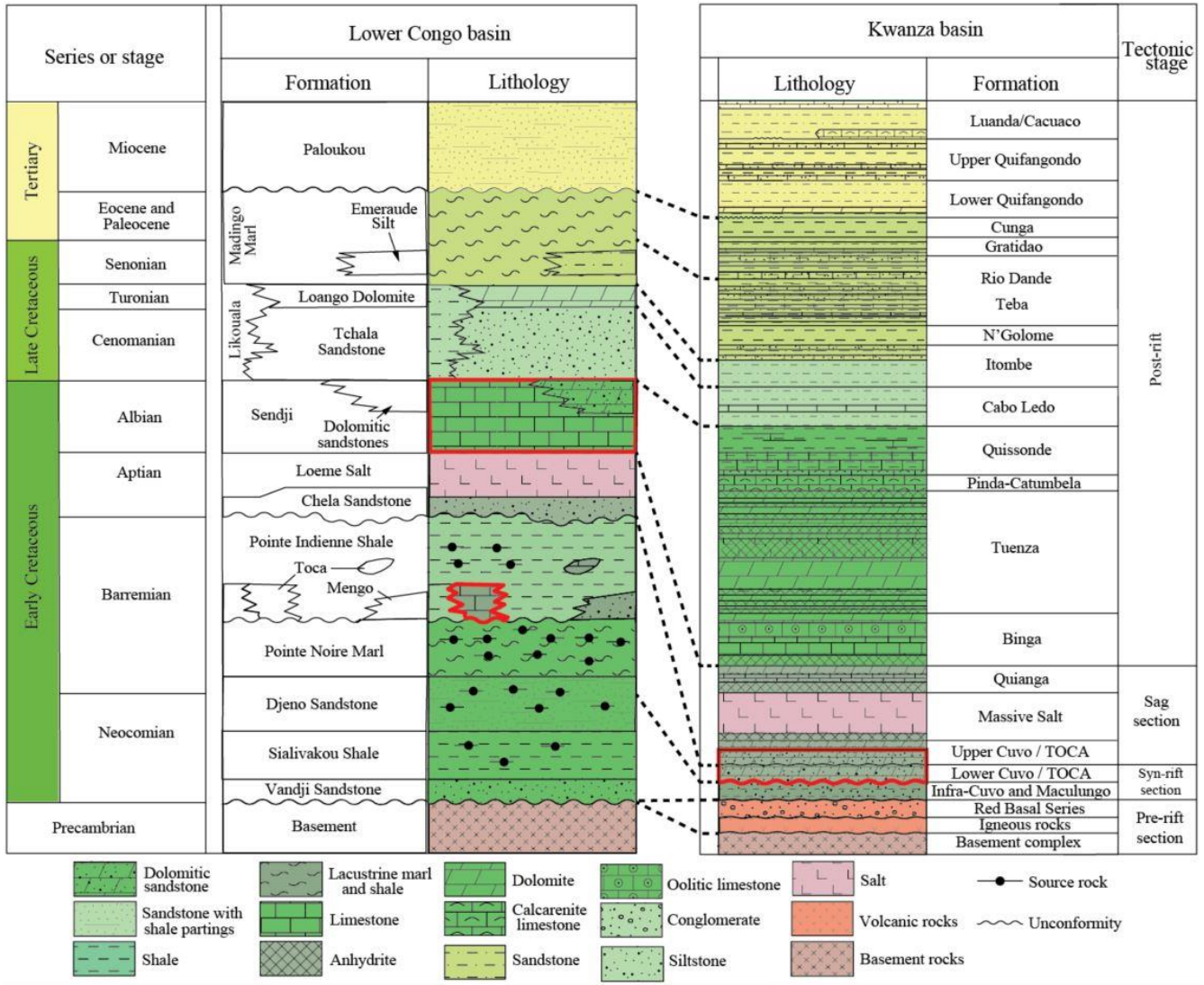


**Figure 5:** Charte stratigraphique des bassins du Bas-Congo et de Kwanza. Modifié d'après Brownfield et al., (2006). Les formations étudiées dans cettes thèse sont ceux avec un contour en rouge.

## 5. Principe et limites des méthodes employées dans la thèse

L'analyse des carottes provenant de forages est par définition ponctuelle car limité par les horizons accessibles sur des diamètres decimétriques. Il est donc important de privilégié des méthodes microstructurales qui ne nécessitent que peu de matériel, tel que les macles de la calcite, ou l'étude des stylolites. Un bref rappel des principes des méthodes paléopiézométriques est apporté dans cette section.

#### 2.3.5.1. Inversion des macles de la calcite (CSIT-2)

Plusieurs méthodes d'inversion des macles de la calcite ont été proposées (e.g., Laurent et al., 1981; Etchecopar 1984; Laurent et al., 1990; Yamaji, 2015; Parlangeau et al., 2018; voir la revue dans Lacombe et al., 2021a). Ces méthodes reposent sur des principes différents mais partagent les mêmes conditions d'application, à savoir une faible déformation, ce qui justifie la coaxialité entre la contrainte et la déformation, et un champ de contrainte homogène à l'échelle du grain/agrégat. Le maclage dans la calcite est considéré comme irréversible, et se produit si la contrainte cisaillante résolue appliquée $\tau s$ est supérieure ou égale à la contrainte cisaillante résolue critique pour le maclage (CRSS) $\tau a$ (voir la revue et la discussion sur la signification de la CRSS dans Lacombe et al., 2021a). Pour les plans maclés (4): $\tau s \geq \tau a$ et pour les plans non maclés (5): $\tau s < \tau a$. Le développement des macles dans la calcite est fortement dépendant de la taille des grains (Rowe and Rutter, 1990) et de la quantité de déformation intra cristalline (Turner, 1953; Turner et al. 1954; Laurent et al., 2000): le maclage est plus facile, c'est-à-dire que le CRSS est plus faible, dans les gros grains et plus difficile, c'est-à-dire que le CRSS est plus élevé, lorsque la déformation par maclage est plus importante car la calcite durcit une fois maclée (Lacombe, 2010; Parlangeau et al., 2019; Lacombe et al., 2021a).

Dans cette étude, la méthode d'inversion des macles de la calcite pour reconstituer les contraintes (CSIT-2; Fig. 2A & 2B) développée par Parlangeau et al., (2018) a été utilisée pour déterminer les tenseurs des paléocontraintes successifs. Le principe de l'inversion est de trouver un tenseur de contraintes (ou plusieurs tenseurs de contraintes) qui vérifie les inégalités (4) et (5) ci-dessus pour le plus grand nombre de plans maclés et l'ensemble des plans non maclés.

La solution a la forme d'un tenseur de contraintes réduit avec 4 paramètres : les orientations des axes des contraintes principales ($\sigma_1$, $\sigma_2$, $\sigma_3$) et le rapport des différentiels de contraintes ($\Phi$) : $1 \geq \Phi = \frac{\sigma 2 - \sigma 3}{\sigma 1 - \sigma 3} \geq 0$ avec $\sigma_1 \geq \sigma_2 \geq \sigma_3$ (6)

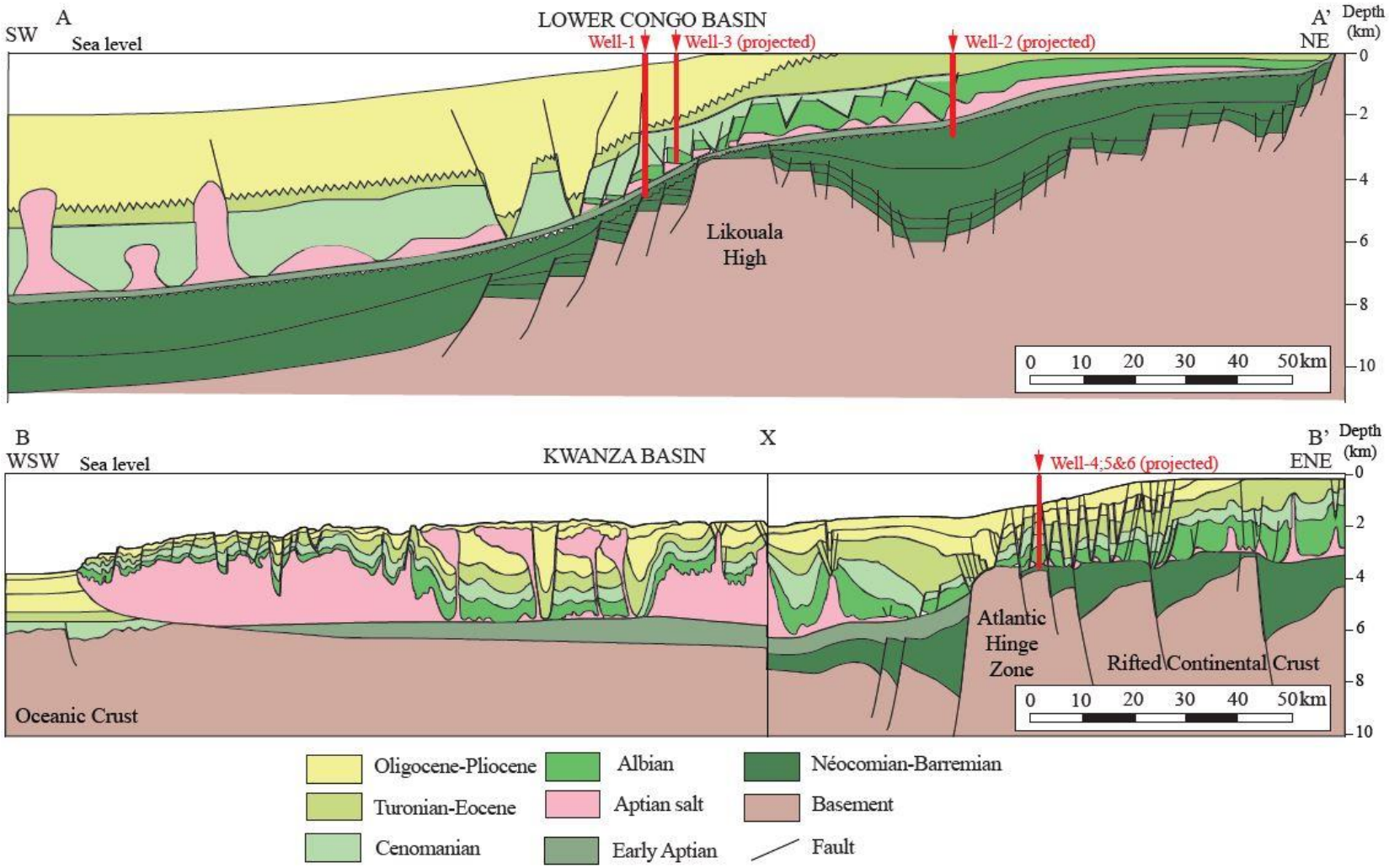


**Figure 6:** Coupes géologiques régionales à travers (A) la marge congolaise (modifiée d'après Vernet et al., 1996) et (B) la marge angolaise (modifiée d'après Erdi and Jackson, 2021). La position approximative des puits étudiés a été projetée sur chacune des coupes.

La méthode CSIT-2 permet de détecter automatiquement la présence d'un ou plusieurs tenseurs. Le nombre de tenseurs total testés par la méthode CSIT-2 est de 5832. Cette méthode d'inversion permet de couvrir systématiquement l'espace avec un intervalle régulier de 10° pour les trois angles d'Euler (définissant l'orientation des axes du tenseur de contrainte) et un rapport des différentiels de contraintes (Φ) fixe de 0,5 sur l'ensemble des plans maclés et non maclés, et sélectionne les tenseurs qui représentent au moins 20% de l'ensemble des plans maclés. Pour chacun de ces tenseurs, une fonction de pénalisation f est définie:

$$f = \sum_{j=1}^{j=n} (\tau_s^j - \tau_s^{min}) \quad (7)$$

avec $\tau_s^j$ la contrainte cisaillante résolue appliquée sur les plans non maclés j telle que $\tau_s^j \geq \tau_s^{min}$ et $\tau_s^{min}$ la plus petite contrainte cisaillante résolue appliquée sur les plans maclés compatibles avec le tenseur.

Théoriquement, la fonction de pénalisation devrait être égale à 0 pour un jeu de données idéal et augmenter au fur et à mesure si des plans non maclés incompatibles sont incorporés dans la solution. Après cette étape, seul les tenseurs de contraintes dont la fonction de pénalisation est inférieure à 0.5 sont retenus et chacun d'entre eux est alors pondéré par le nombre de ses plus proches voisins en fonction d'un critère de similarité (i.e. la distance angulaire entre les tenseurs telle que définie par Yamaji et Sato, 2006). Cela permet de détecter simultanément et de façon automatique différents groupes de tenseurs qui partagent un pourcentage de plans maclés compatibles élevé et qui sont associés à de faibles valeurs de la fonction de pénalisation (pour plus de détails, voir Parlangeau et al., 2018). Le tenseur de contraintes réduit de référence de chaque groupe est ensuite appliqué à l'ensemble des plans maclés et non maclés tandis que les pourcentages de plans maclés à expliquer sont progressivement augmentés. Le tenseur optimal est obtenu lorsque 1) le nombre maximal de plans maclés est pris en compte; 2) le nombre minimal de plans non maclés est pris en compte; 3) la valeur de la fonction de pénalisation est minimale.

Cette méthode d'inversion donne pour chaque tenseur l'orientation des axes principaux des contraintes ($\sigma_1$, $\sigma_2$, $\sigma_3$), le rapport des différentiels des contraintes Φ et un différentiel des contraintes adimensionné $\frac{(\sigma_1 - \sigma_3)}{\tau a}$ qui est liée à la valeur finale de $\tau s^{min}$: $\frac{(\sigma_1 - \sigma_3)}{\tau a} = \frac{1}{\tau s^{min}}$ (8)

Dans la continuité de Rocher et al., (2004) et Amrouch et al., (2010), Parlangeau et al., (2019) et Lacombe et al., 2021a ont proposé des courbes empiriques reflétant l'évolution de la valeur du seuil de maclage (CRSS) en fonction de la taille des grains (règle de Hall-Petch) et

de la quantité de déformation, à partir desquelles nous avons estimé la valeur appropriée du CRSS ($\tau$a) pour nos échantillons. En utilisant la valeur $\tau s^{min}$ obtenue de l'inversion, nous avons déterminé les valeurs des contraintes différentielles ($\sigma_1$-$\sigma_3$) et ($\sigma_2$-$\sigma_3$) en utilisant l'équation (8), qui donne les 5 paramètres du tenseur des contraintes déviatoriques.

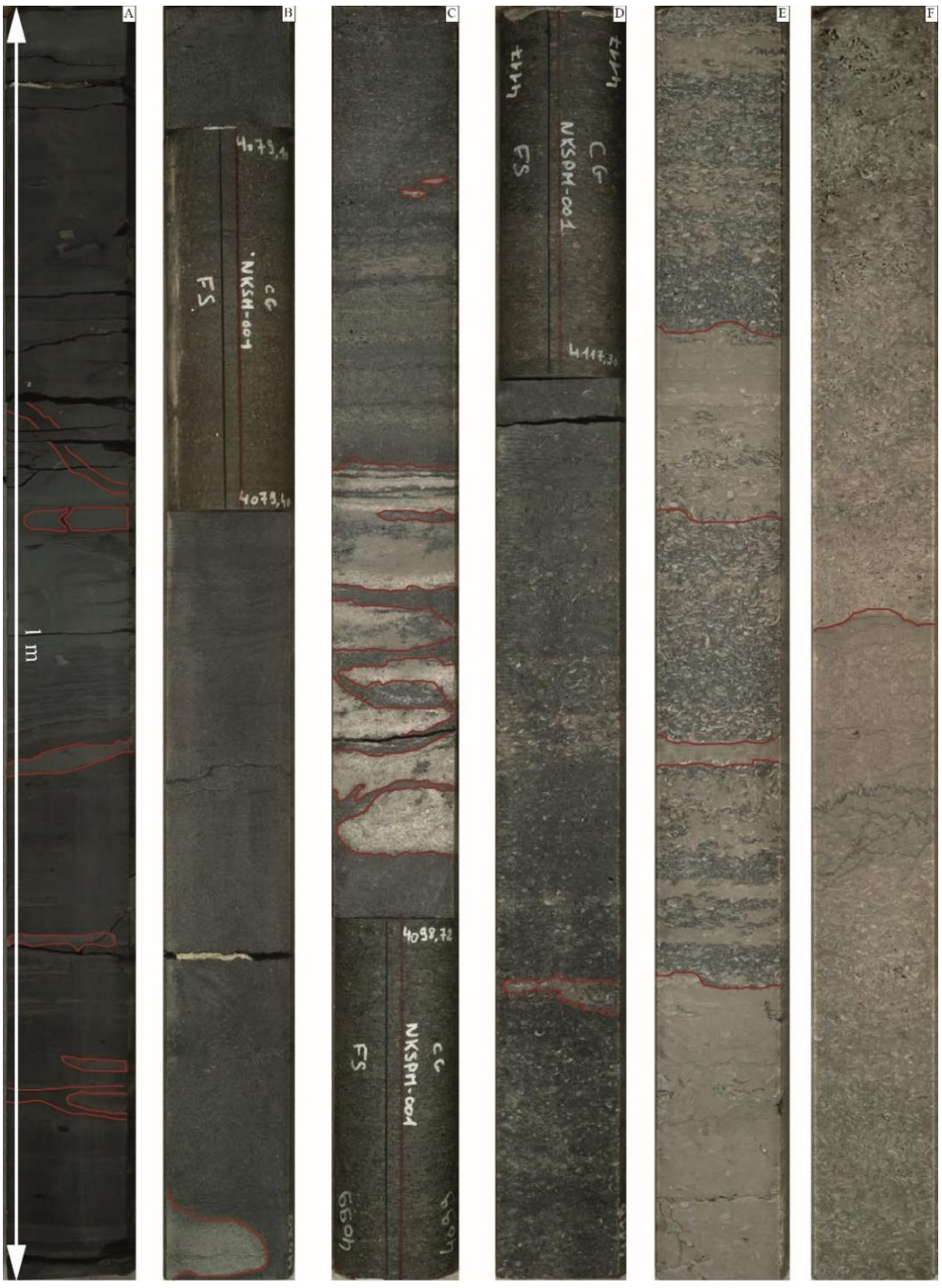


**Figure 7:** Exemple de photos de carottes utilisées montrant différents faciès sédimentaires des carbonates lacustres syn-rift de la formation TOCA. (A) Faciès de black shales lités avec quelques niveaux de green shales. (B) Faciès mudstones; (C) Faciès wackestone avec un niveau lessivé. (D à F) Faciès packstone avec des figures de pression-solution (stylolites).

La capacité de la méthode à détecter, séparer et déterminer les tenseurs de contraintes à partir d'un ensemble de données de macles monophasées et polyphasées, y compris les erreurs de mesure ou les différences de taille de grain, a été démontrée par de multiples tests sur des ensembles de données de macle générés numériquement ainsi que sur des échantillons polyphasés déformés naturellement (Parlangeau et al., 2018). L'incertitude méthodologique lors de la détermination des orientations des contraintes principales par la méthode CSIT-2 est de ± 10°, l'incertitude maximale est de ± 0,1 pour le rapport des différentiels de contraintes (Φ) et l'incertitude méthodologique maximale sur les valeurs du différentiel de contraintes est de l'ordre de ± 30 % (Parlangeau et al., 2018).

#### 2.4.5.2. Inversion de la rugosité des stylolites (SRIT)

L'analyse du signal des traces de stylolites 2-D a montré que la rugosité des stylolites (c'est-à-dire la différence de hauteur entre des points consécutifs séparés par une distance donnée) présente deux régimes avec des propriétés auto-affines (Renard et al., 2004). Les régimes sont chacun définis par une loi de puissance avec un coefficient de rugosité spécifique (exposant de Hurst). À grande échelle, typiquement au-dessus de 1 mm, l'exposant de Hurst est égal à 0,5, régime associé à l'énergie élastique (régime mécanique). A petite échelle, typiquement en dessous de 1 mm, le coefficient de rugosité associé est ~1.1, régime associé à l'énergie de surface (régime Laplacien). À partir de cette observation, Schmittbuhl et al., (2004) ont déduit une longueur caractéristique à laquelle le régime mécanique passe au régime Laplacien, définie comme suit:

$$L_c = \frac{\gamma E}{\beta \sigma_m \sigma_d} \quad (9)$$

où Lc est la longueur de coupure (m), définie graphiquement avec une incertitude de ± 23 % relative à la méthode de régression non linéaire (Rolland et al., 2014) ; E le module de Young (Pa) ; γ l'énergie de l'interface solide-fluide ($J.m^{-2}$) et $\beta = \upsilon\ (1 - 2\upsilon)\ /\pi$, une constante sans dimension, ν étant le coefficient de Poisson. La contrainte moyenne ($\sigma_m$, en Pa) et la contrainte différentielle ($\sigma_d$, en Pa) sont définies comme suit:

$$\sigma_m = \frac{\sigma_1 + \sigma 2 + \sigma 3}{3} \quad (10)$$

$$\sigma_d = \sigma_1 - \sigma_3 \quad (11)$$

L'équation (9) démontre que la rugosité des stylolites est un enregistreur de contraintes passées indépendant de toute hypothèse sur le gradient géothermique et la pression des fluide (Toussaint et al., 2018 ; Beaudoin et Lacombe, 2018).

Le processus d'inversion allant de la Lc aux estimations de la magnitude de la contrainte principale diffère selon qu'il est appliqué sur des stylolites sédimentaires ou sur des stylolites tectoniques.

Dans le cas des stylolites sédimentaires (Fig. 2A, 2C, 2D), il est possible de considérer la contrainte sur le plan horizontal comme isotrope ($\sigma_1 = \sigma_v > \sigma_H \approx \sigma_h$, avec $\sigma_H$ et $\sigma_h$ les valeurs maximale et minimale des contraintes principales horizontales, respectivement, et $\sigma_v$ la contrainte principale verticale), ce qui conduit à une simplification de l'équation (6) comme:

$$\sigma_v^2 = \frac{\gamma E}{\alpha L_C} \quad (12)$$

avec $\alpha = \frac{(1-2\nu)(1+\nu)^2}{30\pi(1-\nu)^2}$ (Ebner et al, 2009b). Afin de s'assurer que les contraintes dans le plan horizontal $\sigma_H$ et $\sigma_h$ peuvent être considérées comme égales, et donc pour tester la validité de l'hypothèse de la déformation uniaxiale, trois coupes obliques sont effectuées perpendiculairement au plan du stylolite (Fig. 2C) et sont traitées en suivant la même méthode d'inversion (Schmittbuhl et al, 2004; Ebner et al, 2009b) (Fig. 2D). Si les valeurs de Lc résultantes des différentes coupes sont identiques dans les limites de l'incertitude, l'hypothèse est considérée comme valide. Au contraire, les stylolites qui présentent une anisotropie de contraintes sont traités de manière plus approfondie en suivant le même processus d'inversion que les stylolites tectoniques (Fig. 2E & 2F).

Il est alors possible de convertir la valeur de $\sigma_v$ (en Pa) en profondeur h (m) en utilisant l'équation suivante : $\sigma_v = \rho g h$ (13)

avec $\rho$ la densité de la roche hôte (2600 $kg.m^{-3}$) et g l'accélération du champ gravitationnel (9,81 $m.s^{-2}$).

D'après Beaudoin and Lacombe, (2018), le modèle chimico-mécanique admis pour le SRIT considère que la dissolution se produit sur un plan pressurisé à l'interface fluide-roche, ce qui fait que ce paléopiézomètre est indépendant de la pression de fluide environnant et par conséquent est incapable de contraindre le tenseur de contrainte effectif complet. Malgré le fait que le modèle de croissance soit indépendant de la cinétique de dissolution et de la température

(Schmittbuhl et al., 2004), le SRIT se fonde sur des hypothèses mécaniques fortes dont le module de Young (E) qui peut varier au cours de la diagénèse.

### *5.2.1. La méthode SRIT appliquée aux stylolites tectoniques*

Les stylolites tectoniques (Fig. 2A et 2E) ne se forment pas en réponse à l'enfouissement, mais résultent plutôt de la déformation ou de la contrainte tectonique affectant le bassin. Contrairement aux stylolites sédimentaires, ils sont rarement parallèles aux couches et ne se forment pas sous l'influence d'une contrainte verticale maximale, sauf possiblement dans des contextes extensifs et à proximité des failles normales. Contrairement aux stylolites sédimentaires, les contraintes dans le plan du stylolite tectonique sont anisotropes, avec $\sigma_H > \sigma_v \neq \sigma_h$. En raison de cette anisotropie dans le plan horizontal, la valeur de la Lc résultante de l'analyse du signal 2-D dépend de l'orientation du plan de coupe à travers le stylolite (Ebner et al., 2010b). La relation entre $L_h$ et $L_v$ (les valeurs maximales des Lc dans les directions horizontale et verticale du plan du stylolite au moment de sa formation, respectivement) et les magnitudes des contraintes principales $\sigma_H$, $\sigma_v$ et $\sigma_h$ sont les suivantes (Ebner et al., 2010b):

$$\frac{L_h}{L_v} = \frac{\sigma_H - \sigma_v}{\sigma_H - \sigma_h} \quad (14)$$

$$\sigma_h = \sigma_H - \frac{L_v}{L_h}(\sigma_H - \sigma_v) \quad (15)$$

$$\sigma_H{}^2 + \sigma_H\left(\frac{2\sigma_v\left(\frac{L_v}{L_h}\right)^2 - \sigma_v\frac{L_v}{L_h}}{2\frac{L_v}{L_h} - \left(\frac{L_v}{L_h}\right)^2}\right) - \frac{\sigma_v{}^2\frac{L_v}{L_h} - \sigma_v{}^2\left(\frac{L_v}{L_h}\right)^2 - 3\frac{\gamma E}{\beta L_h}}{2\frac{L_v}{L_h} - \left(\frac{L_v}{L_h}\right)^2} = 0 \quad (16)$$

Il faut noter que l'équation (14) se résoud comme un système d'équation (14) et (15) qui nécessite une estimation indépendante de $\sigma_v$ (Ebner et al., 2010b).

Afin de déterminer les valeurs de $L_v$ et $L_h$, nous avons analysé le signal 2-D dans trois plans/coupes perpendiculaires au plan du stylolite (Beaudoin et al., 2016) (Fig. 2E & 2F) et nous avons reconstruit une distribution périodique des valeurs de Lc (Ebner et al., 2010b). La relation entre la Lc et l'angle θ entre chaque coupe et le plan vertical une fois le stylolite remis à la verticale est définie par une fonction sinusoïdale dont les extrema sont séparés de 90° (Fig. 2F), et dont la période a été estimée à 180° par Ebner et al., (2010b).

$$L_{c(\theta)} = a + b\sin(2\theta + c) \quad (17)$$

Les paramètres a, b et c dépendent des longueurs de coupure définies à partir de chaque surface de coupe et des angles θ. Ces paramètres peuvent être calculés à partir des équations ci-dessous (Beaudoin et al, 2016):

$$a = L_{c1} + b\sin(2\theta_1 + c) \quad (17.1)$$

$$b = \frac{L_{c_2} - Lc_1}{\sin(2\theta_2 + c) - \sin(2\theta_1 + c)} \quad (17.2)$$

$$c = \tan^{-1}\left(-\frac{\Delta L\,(\sin(2\theta_3 - \sin 2\theta_1) - (\sin(2\theta_2 - \sin 2\theta_1)}{\Delta L\,(\cos 2\theta_3 - \cos 2\theta_1) - (\cos 2\theta_2 - \cos 2\theta_1)}\right) \quad (17.3)$$

avec $\Delta L = \frac{L_{c_2} - Lc_1}{L_{c_3} - Lc_1}$. Trois surfaces normales au plan du stylolite (θ = 0°/45°/90°) ont été numérisées et la Lc a été calculée à partir de l'analyse du signal pour chaque coupe. Les trois valeurs différentes de la Lc ont ensuite été utilisées dans l'équation (15) pour construire une fonction sinusoïdale reliant l'angle d'orientation des coupes 2-D à la longueur de coupure (Fig. 2F).

Les valeurs maximale et minimale de Lc parmi les coupes correspondent aux extrema des différentiels de contraintes calculées par rapport à la contrainte principale horizontale $\sigma_1$ initiant le développement du stylolite. La longueur de coupure maximale correspond au différentiel de contrainte ($\sigma_1$-$\sigma_2$), et la valeur minimale de la longueur de coupure au différentiel de contrainte ($\sigma_1$-$\sigma_3$) (Fig. 2F ; Ebner et al., 2010b). La courbe sinusoïdale sur laquelle est reporté la Lc des trois coupes nous permet d'obtenir l'orientation de $\sigma_2$ et $\sigma_3$. Le plan passant par le Lc minimum de la courbe contient la direction de $\sigma_3$ et le plan passant par le Lc maximum contient la direction de $\sigma_2$. Ceci nous permet de définir le régime de contrainte (compressif - $\sigma_v = \sigma_3$, $\sigma_h = \sigma_2$ ou décrochant - $\sigma_v = \sigma_2$, $\sigma_h = \sigma_3$) sous lequel le stylolite tectonique s'est formé.

Notons que l'approche adoptée n'est valable que lorsqu'un régime de contrainte andersonien prévaut (au moins une des contraintes principales est verticale), sinon l'inversion n'est pas possible (Ebner et al., 2010b ; Beaudoin et al., 2016).

En résumé, l'inversion de la rugosité des stylolites (SRIT) donne l'orientation des contraintes principales ($\sigma_1$, $\sigma_2$, $\sigma_3$) et les magnitudes des contraintes principales horizontales maximale $\sigma_H$ ($\sigma_1$) et minimale $\sigma_h$ à condition que la valeur de la contrainte verticale soit connue.

## 6. Plan de la thèse

Les résultats de recherche réalisés dans cette thèse ont donné lieu à la rédaction de trois articles publiés ou soumis. Ce présent manuscrit est composé de 6 chapitres incluant cette introduction et une discussion générale revenant sur les apports de ce travail de thèse. Les chapitres qui suivent s'organisent comme suit:

- **Chapitre II**

**Article 1:** Multi-proxy reconstruction of the burial history and porosity evolution of the TOCA carbonate formation in the Lower Congo basin (South West Africa). Bah et al., (2023)

- **Chapitre III**

**Article 2:** Depicting past stress history at passive margins: A combination of calcite twinning and stylolite roughness paleopiezometry in supra-salt Sendji deep carbonates, Lower Congo basin, west Africa. Zeboudj, Bah et al., (2023)

- **Chapitre IV**

**Article 3:** Paleostress evolution of the Western Africa passive margin: new insights from calcite twinning paleopiezometry in the deeply buried syn-rift TOCA formation (Lowe Congo basin). Bah et al., (submitted)

- **Chapitre V**

Ce chapitre résume les derniers résultats acquis en fin de thèse sur le bassin de Kwanza choisi pour valider l'approche multi-proxy utilisée dans cette thèse. Une comparaison avec les similitudes et les différences avec le bassin du Bas Congo est réalisé.

- **Chapitre VI**

Ce chapitre constitue (1) une discussion à la fois méthodologique et régionale. L'histoire des paléocontraintes enregistrée dans le bassin du Bas Congo est comparé à celui du bassin de Kwanza et (2) les perspectives futures.

# Chapitre II : Reconstitution de l'histoire d'enfouissement et d'évolution de la porosité des réservoirs carbonatés syn-rift de la formation TOCA dans le bassin du Bas Congo

Ce chapitre est constitué par un article publié dans Marine and Petroleum Geology début 2023. Cette étude se concentre sur l'investigation de la destruction de la porosité de la formation TOCA syn-rift d'âge Barrémien (130-125 Ma) à partir de la carotte de forage offshore du puits Well-1 situé dans le bassin du Bas Congo foré en 2012.

Le défi scientifique de cette étude est de quantifier l'évolution de la porosité dans les carbonates lacustres syn-rift du Barrémien de la formation TOCA (Bassin du Bas Congo), ainsi que de déterminer le calendrier de cette évolution. La formation TOCA présente des porosités actuelles extrêmement variables à l'échelle régionale, avec des valeurs de porosité allant de 1% à 30% selon les textures de dépôt, l'emplacement dans le bassin et l'intensité de la diagenèse (voir détails dans Harris, 2000). Du fait de cette variabilité, il est particulièrement important de comprendre et de quantifier les processus diagénétiques, qui ont été les plus défavorables à la qualité des réservoirs, conduisant à des porosités inférieures à 10% (c'est-à-dire le seuil généralement admis pour une production économiquement viable).

Dans cet article, nous avons déterminé la part relative des phénomènes qui ont entrainé la destruction de la porosité, ainsi que leur chronologie pendant l'enfouissement de la formation. En confirmant une séquence diagénétique existante, la destruction de la porosité liée à (1) la compaction mécanique a été déterminée en utilisant un modèle de bassin (TemisFlow™), (2) celle liée à la précipitation de ciment diagénétique dans les pores, par l'analyse d'images en lame mince, la datation géochronologique U-Pb et la microthermométrie des inclusions fluides, et (3) celle liée à la pression-solution basée sur la quantification de la compaction chimique le long des stylolites couplée à un modèle d'enfouissement. Chacune de ces estimations comporte sa propre incertitude mais nous considérons que la combinaison de méthodes semi-quantitatives réduit l'incertitude globale sur la chronologie des événements mécano-chimiques qui en résulte. Cette approche multi-proxy illustre notamment la valeur ajoutée des informations fournies par le SRIT dans la compréhension de l'évolution de la porosité dans les roches carbonatées et dans les réservoirs.

Marine and Petroleum Geology 148 (2023) 106018

Contents lists available at ScienceDirect

Marine and Petroleum Geology

journal homepage: www.elsevier.com/locate/marpetgeo

# Multi-proxy reconstruction of the burial history and porosity evolution of the TOCA carbonate formation in the Lower Congo basin (South West Africa)

Boubacar Bah [a,*], Nicolas E. Beaudoin [b], Olivier Lacombe [a], Jean-Pierre Girard [b,c], Claude Gout [b,c], Nicolas Godeau [d], Pierre Deschamps [d]

[a] Sorbonne Université, Institut des Sciences de La Terre de Paris (ISTeP), CNRS-INSU, 75005, Paris, France
[b] Universite de Pau et des Pays de L'Adour, Laboratoire des Fluides Complexes et Leurs Réservoirs (LFCR), E2S UPPA, CNRS, TotalEnergies, 64000, Pau, France
[c] TotalEnergies, Centre Scientifique et Technique Jean Féger (CSTJF), 64000, Pau, France
[d] Aix Marseille Univ, CNRS, IRD, INRAE, CEREGE, Aix-en-Provence, France

A B S T R A C T

The timing of porosity destruction in reservoir rock is key for hydrocarbon exploration. This study constrains the porosity destruction of the syn-rift Barremian (130-125 Ma) TOCA Fm. from one drill core located in the Lower Congo basin (West African passive margin). We apply an unprecedented multi-proxy approach to reconstruct the absolute timing of mechanical compaction, pressure-solution and cementation as well as their relative contribution to porosity destruction. LA-ICP-MS U–Pb geochronology combined with petrological observations suggest that the main interstitial diagenetic cement C1 filling the porosity of the packstones and dated 127.4 ± 2.2 to 119.4 ± 6.4 Ma predates pressure-solution. The quantification of the cement distribution by image analysis indicates that C1 clogged ~30% of the initial porosity before the strata were buried at 400 m. We assume that the early cementation limited the effect of mechanical compaction on porosity reduction which is estimated to ~2% in the first 100 m of burial. In contrast, a first order estimate of the chemical compaction-reprecipitation can account for up to ~6% of the initial porosity destruction, as estimated by the inversion of sedimentary stylolite roughness. This technique also documents that the burial-related pressure-solution in the TOCA Fm. occurred in the 550–1750 m burial depth range corresponding to a time spanning from 117 to 95 Ma considering the burial-time model of the TOCA Fm. Our study reveals that the initial porosity of carbonates was reduced down to its current value of 4–8% within the first 35 Ma of its burial history, reaching ~10% after only 10 Ma, i.e. in the first 400–500 m of burial. This case study indicates that the fate of reservoir properties in bioclastic carbonate formations such as the TOCA Fm. may be largely controlled by early, very shallow diagenetic processes rather than subsequent deep-burial mesogenetic reactions.

## 1. Introduction

Carbonate sedimentary rocks are prime targets for the oil and gas industry, representing 40% of exploited plays (Ehrenberg et al., 2009), despite intrinsic reservoir properties (porosity and permeability) that are notoriously highly variable, heterogeneous and difficult to predict (Regnet et al., 2019). In addition to the large variability related to depositional environments, reservoir properties are further altered by diagenetic and structural processes including compaction, pressure-solution, fracture development and dissolution/cementation, which may take place from early burial to exhumation (Choquette and Pray, 1970; Schoeder, 1988; Moore, 1989; Tucker and Wright, 1990; Tucker, 2001; Booler and Tucker, 2002; Moore and Wade, 2013; Humphrey et al., 2019). As a consequence, the distribution of porosity and permeability, in space and in time, is a major challenge for the modelling of such reservoirs in hydrocarbon and ore exploration/exploitation, as well as greenhouse gas storage operations (Guo et al., 2006; Salem and Shedid, 2013; Wang et al., 2020). While most diagenetic studies focus on characterizing the origin and relative chronology of cements filling the porosity (e.g. Barbier et al., 2012), it is essential to be able to reconstruct the calendar and proportion of porosity destruction/enhancement during the burial and diagenetic history of the rock (Moore and Wade, 2013). Such calendar can be assessed thanks to the recent development of in situ U–Pb geochronology of carbonates (Roberts et al., 2020) which provides a way to determine the absolute age of porosity-reducing cements occurring in fractures (e.g. Beaudoin et al., 2018), or in intergranular/intercrystalline pores (e.g. Godeau et al., 2018; Li et al., 2014).

Among the other processes affecting the porosity in carbonate rocks, pressure-solution might be one of the most overlooked (Croize et al., 2013). Stylolites, i.e. serrated pressure-solution planes developed under stress (Alvarez et al., 1978; Koehn et al., 2007; Toussaint et al., 2018) are

* Corresponding author.
*E-mail address:* boubacar.bah@sorbonne-universite.fr (B. Bah).

https://doi.org/10.1016/j.marpetgeo.2022.106018
Received 19 July 2022; Received in revised form 17 October 2022; Accepted 7 November 2022
Available online 17 November 2022

ubiquitous in carbonates and accommodate vertical compaction or horizontal shortening very early during burial and tectonic contraction, respectively (Andrews and Railsback, 1997; Ben-Itzhak et al., 2014; Toussaint et al., 2018; Beaudoin et al., 2020a; Gomez-Rivas et al., 2022; Xu et al., 2022). A number of recent studies (Baud et al., 2016; Koehn et al., 2016; Martin-Martin et al., 2018; Heap et al., 2014, 2018; Bruna et al., 2019; Humphrey et al., 2019) demonstrated how stylolites development and morphology impact fluid flow and alter the reservoir properties of carbonate rocks following reprecipitation of the dissolved material in adjacent pores or farther in the rock volume. It occurs that the roughness of stylolites (i.e. the difference in height between two points along a 1D track) can be used as a stress gauge (Schmittbuhl et al., 2004; Ebner et al., 2009b, 2010b; Rolland et al., 2012, 2014; Toussaint et al., 2018). This tool was developed as the so-called Stylolite Roughness Inversion Technique (SRIT, Beaudoin and Lacombe, 2018) and has been successfully applied to a number of geological problems (Renard et al., 2004; Schmittbuhl et al., 2004; Koehn et al., 2007, 2012; Ebner et al., 2010a, 2010b; Rolland et al., 2012, 2014; Bertotti et al., 2017; Beaudoin et al., 2016, 2019, 2020a,b,c; Beaudoin and Lacombe, 2018; Labeur et al., 2021). In particular, the recent combination of SRIT applied to bedding-parallel stylolites with burial models allows estimation of the timing at which burial-related pressure-solution was active, granting valuable insights into the timing of subsequent tectonic phases (i.e. Beaudoin et al., 2020c; Lacombe et al., 2021) and past fluid migration (Beaudoin et al., 2020c; Labeur et al., 2021).

The scientific challenge of this study is to effectively combine latest techniques to accurately define and validate the chronology of porosity evolution in the early Cretaceous lacustrine carbonates of the TOCA Fm. in the Lower Congo basin, West African passive margin (Harris, 2000). The Lower Congo basin holds important oil and gas resources in offshore carbonate reservoirs, including the TOCA Fm. The syn-rift Barremian (130-125 Ma) carbonates of the TOCA Fm. exhibit extremely variable present-day porosities at a regional scale, with porosity values ranging from 1% to 30% depending on depositional textures, location within the basin and intensity of diagenesis (see details in Harris, 2000). In such a situation, it is of particular importance to understand and quantify the diagenetic processes, which have been most detrimental to reservoir quality, leading to porosities below 10% (i.e. generally admitted threshold for economic production). In this study, we investigated a well in which the TOCA Fm. exhibits present-day porosities of only 4–8% at 4069–4150 m burial depth in order to best demonstrate the added value of our new methodology and the relevance of our results to address the scientific challenge stated above. In this paper, we report an unprecedented multi-proxy approach which combine semi-quantitative estimates of the proportion and timing of porosity destruction related to (1) mechanical compaction by using a basin model (TemisFlow™), (2) diagenetic cement precipitation in pores, by means of thin-section image analysis, U–Pb ages and fluid inclusion microthermometry, and (3) pressure-solution based on quantification of chemical compaction along stylolites coupled with burial model. Each of these techniques embeds its own uncertainty but we consider that the combination of semi-quantitative methods reduces the global uncertainty on the resulting chronology of mechano-chemical events. This multi-proxy approach illustrates notably the added value of the information provided by SRIT in the understanding of porosity evolution in carbonate rocks and reservoirs.

## 2. Geological setting

### 2.1. Geodynamical history of the South Atlantic basins

The break-up of the supercontinent Pangea in Neocomian times (145-130 Ma) led to the separation of the African from the South American continents and the formation of the South Atlantic Ocean as a progressive northward opening of new oceanic domains (Mohriak et al., 2008; Matton and Jébrak, 2009; Pletsch et al., 2001; Szatmari and Milani, 2016). More specifically, concerning the evolution of rifting of the South Atlantic Ocean, several tectonic phases have been identified in the tectono-sedimentary architecture of the margins (Karner et al., 2003; Contrucci et al., 2004; Moulin et al., 2005). Nowadays, the South Atlantic can be divided into four segments from north to south (Torsvik et al., 2009; Moulin et al., 2010): the equatorial segment, the southern segment, the Falkland segment and the central segment, the latter being the focus of this study. The central segment is characterized by the presence of a thick salt layer approximately 1–2 km thick (Brognon and Verrier, 1966; Masson, 1972; Brice et al., 1982; Giresse, 1982; Teisserenc and Villemin, 1989; Aslanian et al., 2009), overlying a mainly continental sedimentary series (145-116 Ma). These series (pre-salt and salt) are overlain by marine clastics and carbonates (112 Ma to present-day) (Burk and Dewey, 1974; Doyle et al., 1982; Mussard, 1996). The history of the central segment can be divided into three main phases from the onset of rifting to the present day (below) (Da Costa et al., 1999; Aslanian et al., 2009; Beglinger et al., 2012; Chaboureau et al., 2013).

1) The syn-rift phase (Neocomian to mid-Aptian) marked by deposition of lacustrine and alluvial formations within graben and half-graben-like structural basins (Lehner and De Ruiter, 1977; Schoellkopf and Patterson, 2000; Beglinger et al., 2012). According to Brownfield and Charpentier (2006), the syn-rift basins are separated by basement highs and are internally organized as a series of asymmetrical horsts and grabens parallel to the present-day coastline.
2) The transition phase corresponds to a transitional cycle from active rifting to thermally-induced lithospheric subsidence affecting the South Atlantic basins (Gabon, Lower Congo and Kwanza basins; Fig. 1a) in the Aptian times, i.e., after crustal stretching, rifting and basement fault activity stopped (Uncini et al., 1998; Beglinger et al., 2012). This transient subsidence is marked by the "break-up unconformity" (BUU), when basin dynamics was controlled by thermal subsidence (Beglinger et al., 2012) and by 1–2 km thick evaporite deposition (Lehner and De Ruiter, 1977; Teisserenc and Villemin, 1989; Aslanian et al., 2009). Following Mohriak (2003), the BUU is linked to a period of peneplanation leading to a low residual topography. Early Aptian siliciclastic deposits from reworked uplifted and tilted Neocomian rift blocks mark this peneplanation episode. Late Aptian evaporites overly the clastic deposits (Burwood, 1999). Several studies have shown that the onset of salt deposition is probably linked to progressive marine transgressions in the proto-South Atlantic (Asmus and Ponte, 1973; Beglinger et al., 2012) and to more arid conditions (Bate, 1999; Karner and Gambôa, 2007).
3) The post-rift phase started at Albian times, and encompasses the separation of the two continents by continental break-up and subsequent oceanization (Aslanian et al., 2009; Guiraud et al., 2010; Beglinger et al., 2012). The post-rift phase is marked by a thermal subsidence (Guiraud and Maurin, 1991), a major regional marine transgression to the north and gravity driven salt tectonics (Lehner and De Ruiter, 1977; Dingle, 1999; Karner and Driscoll, 1999). Post-rift deposits are composed of ramp or shelf carbonates (deposited in shallow water), deep marine clastic, organic-rich black shales and local deltaic deposits (Séranne and Anka, 2005; Torsvik et al., 2009).

### 2.2. The Lower Congo basin: location and structural setting

The Lower Congo basin is located in the eastern margin of the central segment of the South Atlantic, between Gabon and Angola (Vernet et al., 1996; Harris, 2000; Aslanian et al., 2009). Two zones of low subsidence delimit the Lower Congo basin, referred to in the regional literature as "arches" and corresponding to oceanic fracture zones (Asmus and Ponte, 1973; Beglinger et al., 2012): the Mayumbe arch to the north and the Ambriz arch to the south. To the east, the basin rests unconformably on the Mayumbe Precambrian basement (Fig. 1a). The Congo margin part

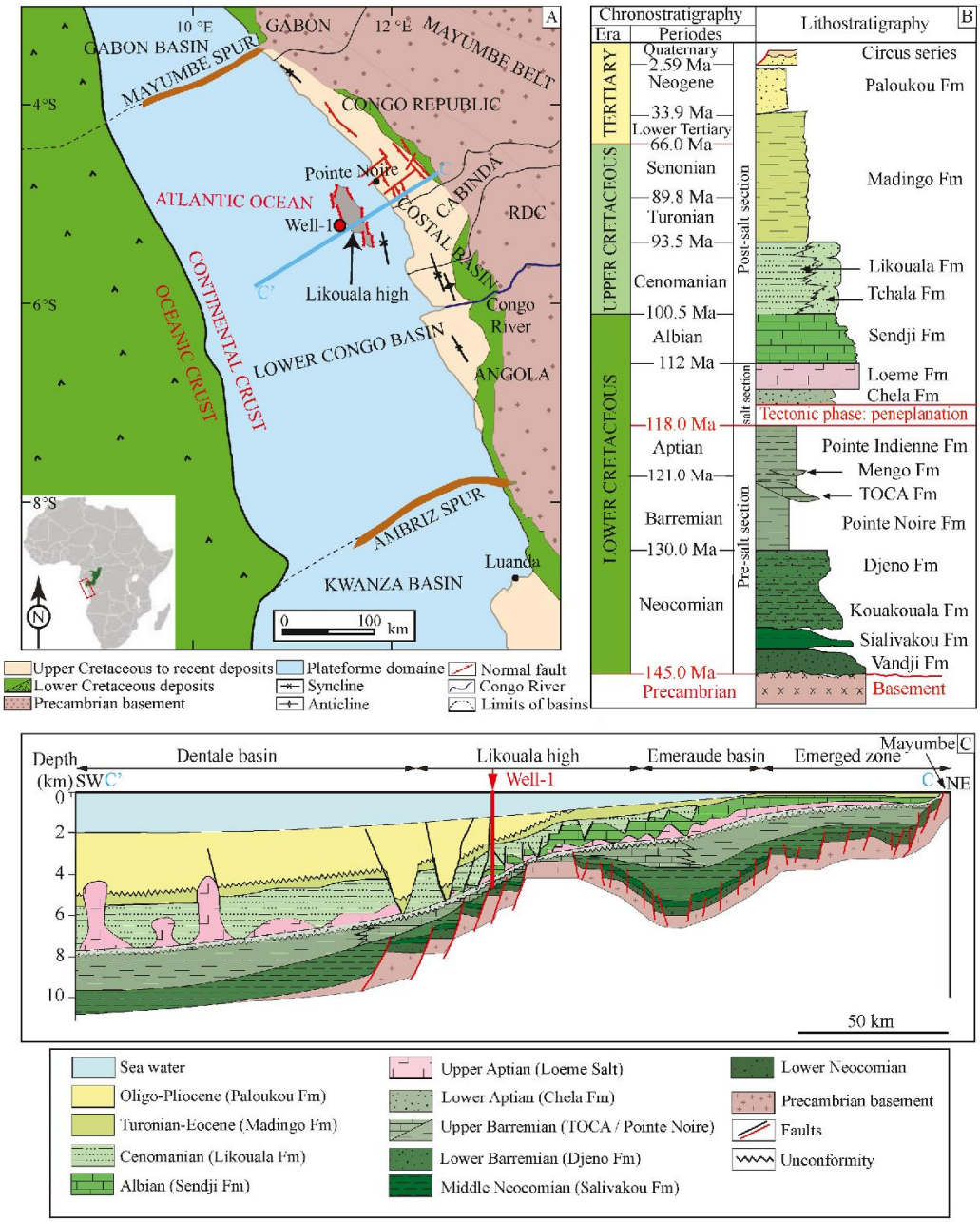


**Fig. 1.** (A) Structural map of Africa along the South Atlantic from Gabon to Angola with basins location. The green color in the marine domain represents the Cretaceous oceanic crust. (B) Stratigraphic chart of Lower Congo basin. (C) Regional geological cross-section through the Congolese margin. Modified after Vernet et al. (1996) (see 1a for section location). (For interpretation of the references to color in this figure legend, the reader is referred to the Web version of this article.)

of the Lower Congo basin extends from the SW of Gabon to the NE of Cabinda Province (Angola). The coastal basin, a vast (17 000 km$^2$, Desthieux, 1993) flat area of low elevation, is bounded to the east by the Mayumbe belt composed of terraced and levelled surfaces (Guillocheau et al., 2015) with an average elevation of 500 m and with peaks reaching 700–800 m. The Congolese margin is the offshore part of the coastal basin in the northern part of the Lower Congo basin. In the central Lower Congo basin (offshore Pointe Noire region; Fig. 1a), the syn-rift sediments are present in two zones: a proximal depocenter in the Emeraude basin and a distal depocenter in the Dentale basin, separated by the horst of Likouala (Fig. 1a & c) where the data analyzed in this paper were collected.

### 2.3. The Lower Congo basin: stratigraphy and sedimentology

The stratigraphy of the Lower Congo basin can be subdivided into

three main intervals from rifting to the present-day (Fig. 1b): (1) the pre-salt section (145-118 Ma), which consists of continental syn-rift sequence, (2) the salt section (118-112 Ma), which marks the major incursion of the South Atlantic Ocean into the rift (transition phase), and (3) the post-salt section (112 to present-day), which essentially consists of marine sequences deposited on the subsiding passive margin of West Africa (McHargue, 1990). Because Jurassic, Triassic and Palaeozoic series are missing (Bidiet et al., 1998), the Cretaceous-Cenozoic sedimentary series rests directly on the so-called Precambrian 'basement' (Fig. 1b & c), which comprises both the crystalline part of the Congo craton and the overlying Precambrian pre-rift sediments (Delpomdor et al., 2008; Mbina Mounguengui and Guiraud, 2009; Préat et al., 2010). Fluvial and lacustrine deposits dominate the syn-rift filling of the pre-salt basins (Guiraud et al., 2010), and were dated using ostracods, pollens and spores biozones (Grosdidier, 1967; Chaboureau et al., 2013). This study focuses on the Barremian lacustrine carbonates

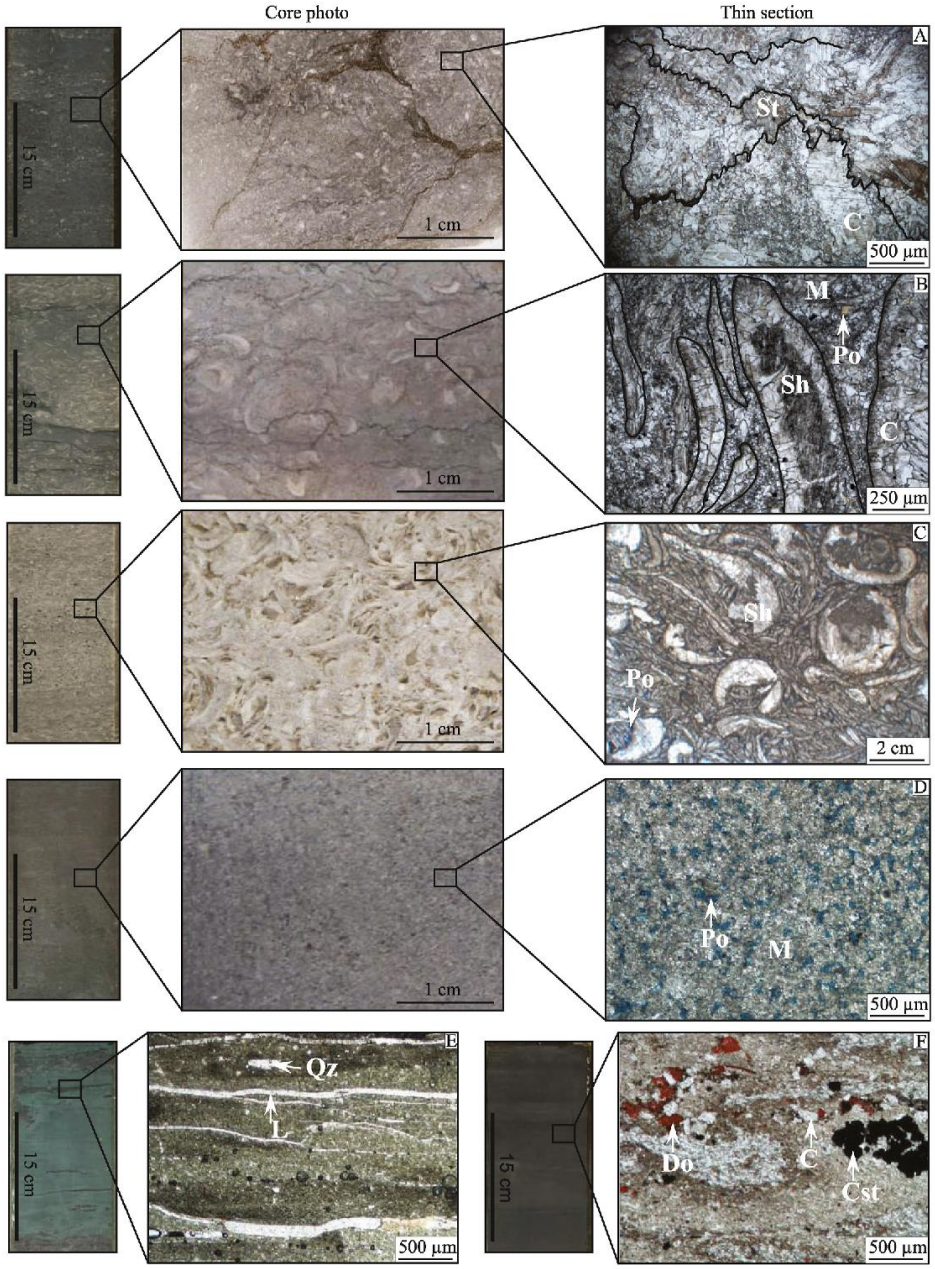


**Fig. 2.** Photographs of the Well-1 core showing different carbonate textures. (A) Wackestone to packstone texture; (B) matrix-supported coquina; (C) grain-supported coquina; (D) mudstone to wackestone texture; (E) green shales and (F) black shales. Po - pore; Sh – shells; C -Calcite cement; St – Stylolite; M – matrix; Do – dolomite; L – lamination; Cst – Clastic undefined fragment; Qz – Quartz fragment. (For interpretation of the references to color in this figure legend, the reader is referred to the Web version of this article.)

of the TOCA Fm. (TOCA for TOp CArbonates), a member of the pre-salt, syn-rift interval. The pre-salt interval starts with the Neocomian sandstones and clay of the Vandji, Sialivakou, Kouakouala and Djeno formations, which are overlain by the lower Barremian clay of the Pointe Noire Fm. (PN) (Fig. 1b) and the studied lacustrine carbonates of the TOCA Fm., deposited during the terminal phase of rifting. The late Barremian clay deposits of the Pointe Indienne Fm. overlie the PN and TOCA formations and are themselves unconformably overlain by the early Aptian sandstones of the Chela Fm. (Harris, 2000).

### 2.4. The studied area: The Likouala high

The Likouala high is located in the central part of the Lower Congo basin, at the border between Congo and Angola (Cabinda province) (Fig. 1a). The Likouala high (Fig. 1a & c) is one of the horsts formed in response to rifting. It has a submeridian orientation, is 50 km long and 20 km wide and is intersected by a series of troughs oriented between N40 and N180. The high separates two domains: the Emeraude basin to the northeast and the Dentale basin to the southwest (Fig. 1c). The Likouala high was a long-lived topographic high since the time of deposition of the Djeno Fm. until the end of the rifting period, with an intense erosion at the top of the high so that the Chela Fm. rests locally unconformably on the Berriasian Vandji Fm. (145–140 Ma, Chaboureau et al., 2013). The Likouala horst allowed the preservation of a low bathymetry environment and the development of the TOCA carbonates (Fig. 1c) (Unpublished data from TotalEnergies internal report).

E-W oriented seismic lines constrain the regional structure. Seismic data of the top of the horst reveal that the structure is a set of tilted blocks oriented NW-SE bounding a monocline. On this high, towards the NE, the carbonates of the TOCA Fm. wedge out under the Chela, either due to erosion or to a lack of deposition (Fig. 1c).

## 3. Materials and methods

### 3.1. Studied material

All observations were made and data were acquired from an 81 m long core within the TOCA Fm. sampled between 4069 and 4150 m depth in one offshore well (Well-1 in Fig. 1). Within this interval, we were granted access to a total length of 51 m (63%) of the cored section, distributed at various places along the entire core length. However, the core intervals we studied include all significant sedimentary textures representative of the entire core.

#### 3.1.1. Core description

The carbonates of the TOCA Fm. exhibit several recrystallized sedimentary textures (Fig. 2). The TOCA Fm. was deposited in a shallow, lacustrine environment showing cyclical variation in water depth and a tendency to water stratification and oxygenation fluctuations (Unpublished data from Totalenergies internal report). It can be divided into three units based on biological features (Harris et al., 1994; Harris, 2000), from bottom to top: (i) TOCA 1 characterized by microbialites; (ii) TOCA 2 hosting microbial encrustations of shells, microbial mats and thrombolites; and (iii) TOCA 3 consisting in a substantial accumulation of granular and coquina texture, i.e. where constitutive elements consist mainly of freshwater lamellibranch tests belonging to the Unionidae group (Grosdidier et al., 1996). This study focuses on the TOCA 3 unit, which is characterized by the lowest porosity values encountered in the TOCA Fm. regionally (Harris, 2000). The identification of the AS9 Ostracod biozone (AS9 base ~130 Ma, AS9 top ~125 Ma) constrain the deposition age to the Barremian (Grosdidier et al., 1996; Bate, 1999; Gradstein et al., 2004). In addition to the diversity of textures, the TOCA Fm. shows numerous stylolites on the studied Well-1 core.

#### 3.1.2. Stylolites

Stylolites are rough dissolution surfaces developing under the stress resulting from either burial compaction or tectonic shortening. In the former case, they are referred to as sedimentary stylolites and in the latter case to as tectonic stylolites. They are frequently observed in sedimentary rocks, namely carbonates (Stockdale, 1922, 1926, 1936, 1943; Dunnington, 1954; Bushinskiy, 1961; Park and Schot, 1968; Bathurst, 1972; Buxton and Sibley, 1981; Railsback, 1993). Stylolites are observed at different scales, from microscopic (grains, veins) to macroscopic (outcrop or core). A stylolite (Fig. 3) can be physically described by the amplitude, wavelength, and frequency of the peaks, parameters of which regularity permits to classify the stylolite based on its morphology, itself related to the growth rate of the stylolite (Koehn et al., 2016). The more recent morphological classification, which accounts for the effect of the stylolite on the local fluid flow, has been proposed by Koehn et al. (2016). For the sake of clarity, stylolite morphology distinguishes the shape of the base (greater-than mm) from infra-mm-scale peaks. Class 1 (rectangular) consists of a large rectangular base with low-amplitude peaks on the flat top of the rectangle. Class 2 (seismogram) is characterized by a narrow top-hat shaped base with low-amplitude peaks. Class 3 (suture and sharp peak) includes all stylolites with a flat or wavy base with locally high-amplitude peaks. Class 4 (wave) stylolites have a wavy base with scattered small peaks. Two other characteristics of stylolites have also been considered and further analyzed in this study: (1) the height of the biggest tooth with respect to an average baseline, which is a proxy for estimating compaction by dissolution along a 1D profile (Toussaint et al., 2018); and (2) the roughness (Renard et al., 2004), defined as the difference in height (dh) between two points, separated by a defined horizontal distance (dx) along the stylolite track (Fig. 3). The final stylolite roughness is acquired at the end of the stylolite development in a quasi-instantaneous process, independent of time and strain rate (Rolland et al., 2014).

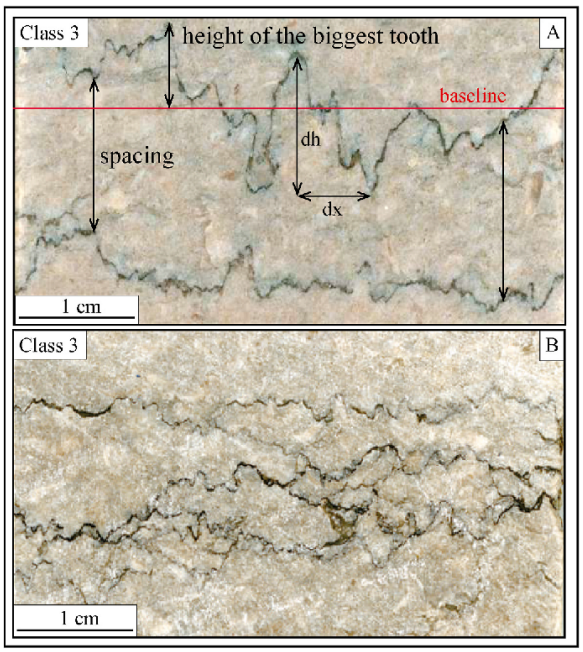


**Fig. 3.** Core photographs showing examples of class 3 stylolites: (A) – single, well-spaced stylolites and (B) – anastomosed stylolites. The stylolite roughness is defined as the difference in height (dh) between two points, separated by a defined horizontal distance (dx) along the stylolite track.

### 3.2. Methods

This section presents the different methods used to characterize the TOCA carbonates (petrography, fluid inclusion microthermometry, U–Pb dating) and to estimate the porosity destruction over time (mechanical compaction, cementation, chemical compaction).

#### 3.2.1. Optical and cathodoluminescence microscopy

The petro-diagenetic study of the TOCA Fm. is based on the petrographic analysis of 57 thin-sections under a Zeiss Axioplot polarising microscope equipped with a Nikon Digital sight DS_U2/Ds_Fi1 camera. The diagenetic state of carbonates was further investigated under cathodoluminescence on a NewTec scientific Cathodyne model CATHOD-SP01 equipped with an IDS UI-3850CP-C-GL R camera (vacuum of 90 mTorr, 12–15 kV voltage and 200 μA intensity). All microscopic work was carried out at the laboratory facilities of the TotalEnergies technical and scientific center (CSTJF, Pau, France).

#### 3.2.2. Elastic parameters of the TOCA textures from mechanical tests

In order to determine the mechanical properties of the studied carbonates, multitriaxial tests were conducted on two samples. A multitriaxial or multi-stage test is a triaxial revolution test during which the confinement is set to a given value, then the sample is brought close to failure, then the confinement is increased again. The cycle is repeated 3–4 times. This type of test allows several triaxial tests to be simulated with a single sample. The tests were carried out at TotalEnergies Geomechanical Laboratory (CSTJF, Pau, France). Two plug samples (38 mm diameter ×76 mm height) were carefully selected to ensure that the carbonate texture has not been deformed during burial history, and then were cut along the vertical axis of the core. The two selected samples include a wackestone and a packstone, i.e., the two carbonate textures most commonly encountered in the core.

Two multitriaxal tests were performed to evaluate the elastic properties of the rock: Young modulus and Poisson ratio. Three cycles were done per sample. Each plug was tested at 10, 30 and 50 MPa of confining stress. For each confining stress, an axial stress ramp was applied with a displacement rate of 0.01 mm/min until the yield point was reached, and then the deviatoric stress was unloaded with the same displacement rate at 0.01 mm/min to finalize the cycle. Axial and radial gauges measured deformations.

#### 3.2.3. Stylolite distribution

The stylolite dataset comes from the 51 m studied from Well-1 core over a depth range between 4069 m and 4149 m (see section 3.1). In order to better understand the spatial distribution of stylolites along the entire core length, we conducted a statistical study of the stylolite density and their spacing. Only stylolites with a total visible length of at least 2 cm were considered in this study. Stylolite density was obtained by counting the number of visible stylolites along the core (for each sedimentary texture). Interpreted density values were obtained by normalizing the total number of stylolites in a given texture per meter length of this texture.

To measure the spacing, we drew two scanlines parallel to the core axis on the photos that intersect perpendicularly the tracks of the stylolites. Then we measured the spacing between the stylolites along these lines, stopping the measurement at each texture transition. The spacing was discontinuously measured along the core, in zones of stylolite clusters of maximum 30 cm thickness. The spacing between stylolite clusters exceeding 30 cm and the core sections devoid of stylolites were not considered. Statistical distribution of both stylolite density and spacing values were calculated considering the sedimentary texture.

#### 3.2.4. Estimates of burial–related chemical compaction

The minimum amount of chemical compaction that stylolites accommodated was estimated from the height of the highest tooth along the 1-D profile (Koehn et al., 2016; Toussaint et al., 2018).

Digitized stylolite tracks were used with Matlab scripts modified after Ebner et al. (2009a). We first define the baseline position by calculating the average trend of the track, correcting it from the dip, and placing the extremities of the signal to 0. The height of all peaks (teeth) from the baseline is measured along the track, and the maximum absolute value is considered as representative of the minimal compaction accommodated along the plane, making the assumption that dissolution was evenly distributed. It is noteworthy that this approach is bound to be a rough underestimate of the true compaction, as (1) the maximum height on a tooth in a 1-D signal can miss bigger teeth on the 3-D plane, (2) this approach neglects the effect of the growth rate highlighted in Koehn et al. (2016); and (3) recent work shows that stylolite can dissolve without changing the morphology (Koehn et al., 2022). However, the latter study also states that the biggest tooth, if preserving the full dissolution, was a good estimate of the dissolution. On top of it, this approach, when applied on a large population of stylolites, yields results that are comparable at the first order to the loss of matter estimated by chemical mass balances (Toussaint et al., 2018).

Cumulating chemical compaction estimates along each stylolite plane of the entire population yields a rough minimal estimate of the total volume of dissolved rocks during burial. This is expressed as a percentage value of compaction with respect to a given texture as follows:

$$\%\ \text{compaction} = \frac{\sum (BPS) * \text{Amean}}{h} * 100 \quad (1)$$

where h is the thickness of the sedimentary texture considered (m), $A_{mean}$ is the mean value of the highest teeth for all stylolites identified in the carbonate texture (m) and ∑(BPS) is the number of stylolites in the carbonate texture.

#### 3.2.5. Stylolite roughness inversion technique (SRIT) applied to sedimentary stylolites

The empirical study of single-track stylolites has shown that their roughness displays two regimes with self-affine properties, according to the scale of observation: one dominated by the surface energy at small-scale < 1 mm and the other by the elastic energy at large-scale > 1 mm (Renard et al., 2004; Schmittbuhl et al., 2004). By treating a stylolite track as a signal, signal analysis method such as Fourier transform returns two slopes, each defined by a specific roughness coefficient (Hurst coefficient). When the roughness is > 1 mm, the Hurst exponent equals 0.5, a value typical of elastic energy. When the roughness is < 1 mm, the related roughness coefficient is ~1.1, a value typical of surface energy (Ebner et al., 2009a, b, 2010b; Rolland et al., 2012, 2014).

From this observation, Schmittbuhl et al. (2004) derived a characteristic length at which the growth regime switches from being dominated by surface energy to being dominated by elastic energy. This cross-over length is defined as follows:

$$L_c = \frac{\gamma E}{\beta \sigma_m \sigma_d} \quad (2)$$

where Lc is the cross-over length (m); E the Young modulus (Pa); $\gamma$ the solid-fluid interface energy (J.m$^{-2}$) and $\beta = \nu(1-2\nu)/\pi$, a dimensionless constant with $\nu$ being the Poisson ratio. For $\gamma$, we used the known value for calcite, $\gamma = 0.32$ J m$^{-2}$ (Wright et al., 2001). The mean stress ($\sigma_m$, in Pa) and differential stress ($\sigma_d$, in Pa) are defined as:

$$\sigma_m = \frac{\sigma_1 + \sigma 2 + \sigma 3}{3} \quad (3)$$

$$\sigma_d = \sigma_1 - \sigma_3 \quad (4)$$

In the specific case of sedimentary stylolites, it is possible to consider the stress on the horizontal plane as isotropic ($\sigma 1 > \sigma 2 = \sigma 3$), leading to a simplified equation as:

$$\sigma_v^2 = \frac{\gamma E}{\alpha L_C} \quad (5)$$

with $\alpha = \frac{(1-2\nu)(1+\nu)^2}{30\pi(1-\nu)^2}$ (Ebner et al., 2009b).

The appropriate values of each parameter are needed to derive the vertical stress. The mechanical parameters (Young modulus and Poisson ratio) are derived from the mechanical tests.

Then it is possible to convert the value of $\sigma_v$ (in Pa) into depth (m) using the following formula:

$$\sigma_v = \rho g h \quad (6)$$

with ρ the density of the host rock (2600 kg m $^{3}$) and g the gravitational field acceleration (9.81 m s $^{2}$), regardless of any assumption on the past geothermal gradient and fluid pressure (Toussaint et al., 2018; Beaudoin et al., 2019, 2020; Beaudoin and Lacombe, 2018).

In order to ensure that the in-plane stresses (i.e., the stresses in the plane of the stylolite) are equal, hence to test of the validity of the uniaxial strain hypothesis which allows the derivation of equation (5), three mutually oblique sections were cut perpendicular to the stylolites and were treated following the same inversion method (Schmittbuhl et al., 2004; Ebner et al., 2009b). If the resulting Lc values from the three cuts were found to be identical within uncertainty, the assumption was considered to be valid. On the contrary, the stylolites were not considered as sedimentary stylolites and were discarded from the dataset.

### 3.2.6. *Burial-time model*

We have built a burial-time model to reconstruct the burial evolution of the TOCA Fm. over time using TemisFlow™ basin modelling software. The present-day geometry to be simulated is based on the formation top-base depths, as measured in Well-1 data. We defined the properties of each lithology (porosity, permeability) from the Well-1 and the geological events (erosion) described from the seismic interpretation (TotalEnergies internal maps). Two erosional events are described in the field: (1) early Aptian (~75 m) related to the peneplanation of the Likouala high and (2) early Tertiary (~100 m) related to the global uplift of the margin. The ages of these two erosional events were estimated on the basis of unpublished seismic interpretations from TotalEnergies. The chronostratigraphic column (Table 1) shows the list of the 14 layers considered for this study, each of those being characterized by the age at which deposition begun and ended, by a thickness and by a lithology. Restored geometries can be edited further by entering an estimate of erosion (in m) and paleo topography or paleo-bathymetry maps. The physical properties of each layer (initial porosity, solid density; Table 1), as well as the constitutive laws (compaction) are defined with respect to the ratio of the different sedimentary textures (limestone, shale, sandstone) described in the layer.

The backstripping process allows for the inversion of the evolution of the basin geometry through time using a 1-D backward modelling (Perrier and Quiblier, 1974). The simulation begins in the present day and ends when only the substratum remains. In this case, the simulation is finished at −145.5 Ma, which corresponds to the age of the basement top.

For each period defined in the chronostratigraphic column (Table 1), we removed what has been deposited and added what has been eroded as defined from the seismic data. After sedimentation and erosion have been accounted for, the remaining sedimentary formations are decompacted, or compacted (in the case of erosion), by using porosity vs depth curves calibrated empirically for each lithology. The porosity vs depth curve for the carbonates used in the TemisFlow™ software is taken from literature data for conventional endmembers: Schmoker and Halley (1982) for micritic carbonate of the mudstone to wackestone type; Bebout (1974) for grainstone type carbonates with no fine fraction and with early diagenesis and Scholle (1977) for chalk.

For modelling the evolution of the porosity, the key controlling factors are the compaction parameters. The calibrated porosity vs depth empirical law used in the simulation represents porosity evolution controlled by both mechanical compaction (grain framework tightening) and early chemical compaction (bioclast dissolution along grain-to-grain contacts due to pressure-solution). For the sake of simplicity, we will describe hereinafter the mechanical tightening and the early chemical micro-seams developing at grain contacts altogether as mechanical compaction, and the mesoscale stylolitization as chemical compaction. The backstripping is performed considering the hydrostatic pressure regime and the porosity vs depth law.

The forward modelling provides access to the evolution of the geometry of the 1-D column, and to the associated porosity in each layer.

### 3.2.7. *Fluid inclusion petrography and microthermometry*

Fluid inclusions are sealed cavities filled with water, oil, gas and/or solid phases occurring in minerals. They can form during/soon after crystal growth (primary inclusions or pseudo-secondary inclusions) or later as a result of crystal microfracturing and healing (secondary inclusions) in the presence of a fluid. They constitute a microsample of the paleo-fluid present in the pore space at the time of their formation (Roedder, 1984). The aim of our fluid inclusion work was to identify the different populations of fluid inclusions present in the samples, to analyze their distribution and abundance, and to determine their melting and homogenization temperatures ($T_{m\ (ice)}$ and $T_h$) in order to constrain the nature of the mineralizing fluid.

Four samples were prepared as double polished 150 μm thick sections glued on a petrographic glass slide using acetone-dissolvable superglue. For microthermometric analysis, the rock wafer must be removed from the glass slide in order to fit on a 6 mm quartz disc within

**Table 1**
Chronostratigraphic column used for the study presented here. The simulation begins at 145.5 Ma and ends at the present day. The basin model input parameters such as age; present-day thickness and initial porosity of each formation are indicated.

| Event | | Age (Ma) | | Thickness (m) | Initial porosity (%) | Solid density (kg/m3) |
|---|---|---|---|---|---|---|
| Lithology/Event | Number | From | To | | | |
| Paloukou | 14 | 33,9 | 0,0 | 1833,9 | 59,6 | 2,65 |
| Erosion | 13 | 65,5 | 33,9 | | | |
| Lower Tertiary | 12 | 65,5 | 33,9 | | | |
| Madingo | 11 | 93,5 | 65,5 | 207,0 | 59,6 | 2,65 |
| Likouala | 10 | 99,6 | 93,5 | 605,8 | 48,1 | 2,70 |
| Upper Sendji | 9 | 103,0 | 99,6 | 417,2 | 56,4 | 2,68 |
| Lower Sendji | 8 | 112,0 | 103,0 | 527,9 | 54,2 | 2,66 |
| Loeme | 7 | 116,0 | 112,0 | 60,0 | 9,4 | 2,20 |
| Chela | 6 | 118,0 | 116,0 | 45,0 | 62,3 | 2,65 |
| Erosion | 5 | 118,0 | 117,0 | | | |
| Pointe Indienne | 4 | 123,0 | 118,0 | 90,0 | 62,3 | 2,10 |
| TOCA/Pointe Noire | 3 | 130,0 | 123,0 | 129,0 | 51,5 | 2,69 |
| Djeno | 2 | 141,0 | 130,0 | 117,0 | 51,5 | 2,65 |
| Basal sandstones | 1 | 145,5 | 141,0 | 90,0 | 51,5 | 2,65 |

the heating/cooling stage. The rock wafers were separated from the glass slides by dissolving in acetone for one night. Each wafer was then carefully cleaned.

The fluid inclusion microthermometry study was performed by H-Expertise Services (HES), Nancy, France. The petrographic study, based on optical observations by polarized light and epi-UV fluorescence, was performed with the goal to describe the different fluid inclusion populations within a petrographic context (host cement, limit grain-overgrowth, overgrowth, and fracture cement), their petrographic origin (primary fluid inclusion, intragranular or transgranular fluid inclusion planes), the content and abundance of each phase (water, gas or oil) and the relative timing relationships (contemporaneous versus not contemporaneous aqueous and oil inclusions). Only fluid inclusion populations showing the petrographic characteristics of primary fluid inclusions (following Goldstein and Reynolds, 1994) were selected for microthermometric measurements.

The epi-UV fluorescence observations were conducted using a Zeiss AxioImager.A1m microscope with an excitation filter centered at 365 ± 5 nm and an emission filter long pass around 400 nm. Phase transitions observed in two-phase fluid inclusions were recorded over a LINKAM MDS 600 heating-freezing stage (min. −170 °C, max. 400 °C) equipped with a Sony Exwave HAD3 color video camera mounted on an Olympus BX 51 microscope at GeoRessources, Vandœuvre-lès-Nancy. The microthermometric stage was thermally calibrated using CO2 synthetic fluid inclusions standards for melting temperature $T_{m\ (CO2)}$, H2O synthetic fluid inclusions standards for $T_{m\ (ice)}$ and cross-calibrated natural alpine fluid inclusions ("home" standard) for $T_h$. The accuracy of measurements is estimated at ± 0.2 °C for $T_{m\ (ice)}$ (heating at 0.5–1 °C/min) and ±0.5 °C for $T_h$ (heating at 1–5 °C/min). To avoid stretching problems related to freezing, the measurements of the homogenization temperatures were done prior to the measurements of ice melting temperature on the same sample.

#### 3.2.8. U − Pb dating of the calcite cement

The U–Pb dating of the interstitial calcite cements was carried out at Center Européen de Recherche et d'Enseignement des Géosciences de l'Environnement (CEREGE), Aix-en-Provence, France using a LA-ICP-MS-HR. The equipment consists of an ArF 193 nm, 4 ns excimer laser: (ESI, Elemental Scientific Industries) and an HR-ICP-MS with magnetic sector (Element XR, Thermo fisher). Measurements were performed following a methodology analogous to Godeau et al. (2018).

Analyses were conducted on five thick (~100 μm) polished sections exhibiting large areas of the sparitic cement of interest. The samples were placed in the sample cell and scanned (3200 dpi resolution) for easy navigation from one piece to another on the instrument software.

A screening phase was first conducted to investigate U and Pb concentrations and U/Pb ratio variation over the entire thick section in order to select the best areas for the final measurements (Roberts et al., 2020). Analyses were done with a laser spot size of 150 μm. The ablation speed is of the order of 1–1.5 μm/s under standard conditions, it is preceded by a pre-ablation phase of a few seconds to clean the sample surface. Samples were measured by a standard bracketing approach, using the NIST-614 glass standard for instrumental drift and lead isotope composition (Woodhead and Hergt, 2001) and the WC-1 natural calcite standard for inter-elemental fractionation (reference age = 254.4 ± 6.4 Ma; Roberts et al., 2017). A total of 24–48 ablation spots were performed for each microsite analyzed. Detailed spot-by-spot assessment was carried out afterwards by examining ablation pits under CL microscopy.

The U–Pb isochrone ages were calculated in a Tera-Wasserburg diagram using the Isotplot 4.15 add-on (Excel).

#### 3.2.9. Phase estimates by image analysis

Eight thin-sections were cut perpendicularly to the bedding in the core. In order to quantify the amount of the various diagenetic cements observed in the samples, we conducted a 2-D image analysis based on interpretations from optical (PPL) and cathodoluminescence (CL) microscopy observations. Thin-section wide photomosaics of the most representative texture, i.e., packstone, were assembled for eight samples located at different depths along the core. The pictures were performed under the same exposure conditions for all thin-sections to ensure the representativeness and comparability of data. We used the Fiji software for performing a manual picking based on combination of the luminescence of each pixel on the CL image and on the color of the minerals on the corresponding PPL image. Emphasis was put on quantifying the most important calcite cements (C1 and C2, see below) which fill the interbioclast and intrabioclast (bivalve shell filling) porosity. The very minor occurrence of aragonite shell cement was not quantified.

## 4. Results

### 4.1. Macroscopic and microscopic observations and sedimentary texture description

#### 4.1.1. Petrogenetic description

Following observations on core and thin-section, five different sedimentary facies were identified, referred to as F1a, F1b, F1c, F2a and F2b described below, and grouped into two main types: bioclastic facies (F1) and mudstone facies (F2). They are characterized by their mineralogical and paleontological content and their sedimentological characteristics (texture, grain size, etc.). The latter mainly comprises Lamellibranchs of the Unionidae family (freshwater characteristics), and Ostracods (Grosdidier et al., 1996; Bate, 1999; Gradstein et al., 2004). It is notable that in all the observed facies, the amount of clayish mineral is negligible.

Facies F1a (Fig. 2a) consists in bioclastic limestone composed of broken shells of Ostracods and Pelecypods (rare ooids) in a micritic matrix, occurring as grainstones to rudstones. Shells are generally composed of macrosparitic calcite while the matrix is microsparitic. F1a is highly stylolitized and tight.

Facies F1b (Fig. 2b) consists in bioclastic limestone composed of poorly sorted Unio shells and Gastropods in a microsparitic matrix, occurring as wackestones to floatstones. This facies is highly stylolitized and mainly tight. One plug porosity measurement (total Phi) has been performed on this texture and shows a porosity of <2%.

Facies F1c (Fig. 2c) consists in bioclastic limestone composed of brocken or preserved Unio shells, Gastropods and rare Oncoids in a microsparitic matrix, occurring as packstones to rudstones according to the abundance of the shells. Most of the shells are recrystallized either into a macrosparite or into a microsparite. This facies exhibits intergranular and intercrystalline macroporosity visible in thin-sections. Plug measurements yielded total porosity ranging from 4 to 8% and averaging 6% (n = 14) porosity.

Facies F1b and F1c are overwhelmingly predominant representing about 90% of the cored section. They are mainly composed of packstones. Facies F1c (packstones) accounts for 70% of the studied section in Well-1 core.

Facies 2a (Fig. 2d) consists in microsparitic calcareous mudstone (mudstones to wackestones), with rare scattered debris of Gastropods and Ostracods. The matrix is a homogeneous microsparite. This facies occurs in very low amount along the Well-1 core.

Facies 2b (Fig. 2e and f) consists in microsparitic calcareous mudstone, with scattered crystals of pyrite crystals, and rare quartz grains (silt) and dolomite rhombs, occurring as green shales or black shales.

#### 4.1.2. Diagenetic description

Thin-section examination by optical (LPNA) and cathodoluminescence (CL) microscopy allowed identification of several diagenetic events (Fig. 4 & Fig. 5). These diagenetic events include, in chronological order, shell micritization, aragonite to calcite neomorphism, precipitation of blocky calcite C1, mechanical compaction, precipitation of blocky calcite C2, and chemical compaction. In

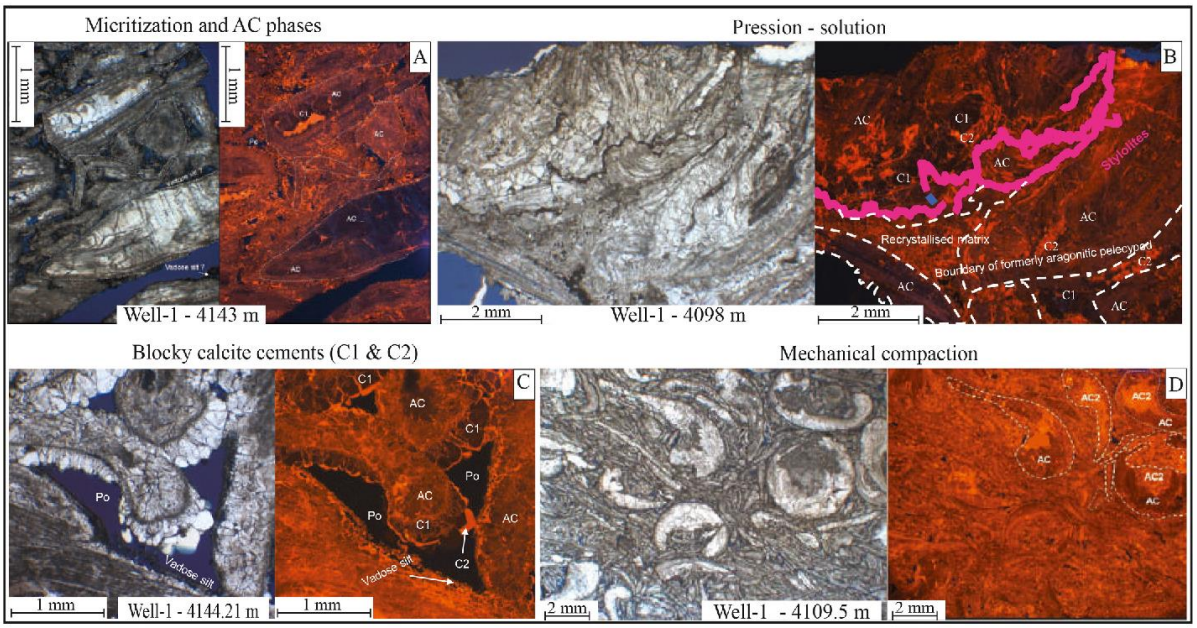


**Fig. 4.** Examples of diagenetic events of the TOCA Fm. (A) Eogenetic phase (AC) and vadose silt in F1a facies; (B) pressure-solution (stylolite) in F1b facies; (C) early and late cementation in F1b facies; (D) mechanical compaction expressed by broken shells in F1c facies. AC – aragonite to calcite; C1 & C2 - blocky calcite cement and Po – pore.

| Diagenetic event | Paragenetic sequence: Oldest → Youngest |
|---|---|
| Micritization | |
| Aragonite to calcite neophormism | |
| Mechanical compaction | |
| Early blocky calcite (C1) | |
| Late blocky calcite (C2) | |
| Stylolitization | |

**Fig. 5.** Diagenetic sequence of the TOCA Fm. at Well-1- core.

accordance with data reported by Harris (2000), our samples of the TOCA 3 interval show very little visible secondary porosity limited to rare residual dissolution voids within aragonite bioclasts (that were not entirely filled by blocky calcite cement C1) and very minor leaching of C1 calcite crystals locally. The remaining secondary dissolution was not precisely quantified but is estimated to represent on the order 0.5% at most (see Fig. 11c for illustration). Consequently, the main diagenetic transformations observed in thin sections appear to have either no effect (micritization, neomorphism) or a negative effect (compaction, cementation) on reservoir properties.

The micritization is common in the grainstone facies and is the earliest stage of the paragenetic sequence. Micrite mostly developed around bivalve shells and ooids. The diagenetic phase AC (Fig. 4) corresponds to the neomorphism of the aragonite of gastropod and pelecypod shells into calcite. It shows a black to dark brown cloudy luminescence under cathodoluminescence. The blocky calcite cement C1 (Fig. 4a, b & 4d) develops inside and around the bioclasts, i.e., as intrabioclast and interstitial cement. Under cathodoluminescence, C1 is non-luminescent (dull to dark brownish color). The mechanical compaction is expressed by the breaking (Fig. 4c) and microfracturing of bioclasts and is not homogeneous in intensity along the core; it is more developed and visible in grain-supported facies. The mechanical compaction affects the early cement (AC and C1). The calcite C2 cement postdates calcite C1 and is characterized by a rather bright orange cathodoluminescence (Fig. 4a, b & 4d). Mesoscale stylolites developed in these intervals affect all the calcite cements (Fig. 4b), indicating that stylolitization prevailed/continued after C1 and C2 precipitation.

The compaction-related pressure-solution appears to have been active throughout a large part of the diagenetic history (Fig. 5). It developed first along discrete pressure-solution seams and micro-stylolites along contacts between bioclasts as a result of stress increase during mechanical compaction. As previously mentioned, the process encompassing both the mechanical and the early grain-contact-limited chemical compaction (micro-stylolites and seams), which prevailed before and slightly after early C1 cementation, will be referred to as 'mechanical compaction' hereinafter. In contrast, the compaction-

related pressure-solution occurring along widespread mesoscale stylolites and affecting both the bioclastic material and the cements C1 and C2 will be referred to as 'chemical compaction'.

In summary, three main significant mechanisms operated during the diagenetic history (Fig. 5) to control the evolution of the reservoir porosity, all in a negative way: (1) mechanical compaction, expectedly mostly efficient during early burial; (2) (early) precipitation of intra-bioclast and interstitial cement (e.g., C1 and C2) and (3) chemical compaction through the mesoscale stylolitization and the likely precipitation of the dissolved material in the vicinity of the stylolites (eventually filling the remaining porosity). Although, these mechanisms developed in sequence they likely overlapped significantly and may have affected each other to some extent. For instance, the early calcite cementation (C1) may have delayed/limited the subsequent mechanical compaction by increasing framework rigidity.

### 4.2. Sedimentary stylolite distribution

In the investigated 51 m depth interval, a total of 615 stylolites was counted in the different carbonate textures. The distribution of stylolites in relation to sedimentary texture (Fig. 6a) shows that stylolite density (number of stylolites per m length) is greater in wackestones (median = 20) than in mudstones (median = 13) and packstones (median = 8). The complete statistical data are shown in Table 2.

### 4.3. Chemical compaction along stylolites

As already reported, a minimum estimate of the dissolution due to chemical compaction along a stylolite track is provided by the height of the highest tooth with respect to the baseline (Fig. 3a; Beaudoin et al., 2016; Koehn et al., 2016). It is noteworthy that the distribution of tooth heights (Fig. 6b) shows a first-order correlation with sedimentary textures. The lowest heights are found in mudstones, with a median value of 2.5 mm, while the wackestones and packstones show similar distributions, with median values of ~4.4 mm.

**Table 2**
Statistics of the density of stylolites along the Well-1 core.

| Statistics of the density of stylolites (number/m) | | | |
|---|---|---|---|
| | Mudstone | Wackestone | Packstone |
| minimum | 0 | 0 | 0 |
| median | 13 | 20 | 8 |
| maximum | 80 | 175 | 90 |
| mean | 22 | 31 | 9 |
| mode | 20 | 0 | 0 |
| standard deviation | 21 | 48 | 16 |

The cumulated linear thickness of the different carbonate textures along the 51 m core investigated is 4 m, 8 m and 28 m for mudstone, wackestone and packstone, respectively, for a total length of 40 m. The other textures covering the remaining 11 m were not investigated due to the very low number of stylolites (grainstones) or the absence of stylolites (black/green shales). The percentages of chemical compaction (equation (1)) in the different carbonate textures are as follows: 5.4% for mudstones (over 4 m), 4.1% for packstones (over 28 m) and 13.6% in wackestones (over 8 m) (Fig. 6c). Considering the 40 m interval investigated by SRIT, the total percentage of chemical compaction is around 6.1% (i.e. ~2.5 m linear). Because of the limited number of maximum tooth heights measured (analysis performed on 44 stylolites considered representative of the 615 stylolites identified in the studied core section), we estimate that the uncertainty on the overall percentage of chemical compaction is ±30% (relative). Consequently, the minimum estimate for the total chemical compaction is considered to be between 4.3 and 7.9%.

### 4.4. Rock mechanics test

The results of the geomechanical tests (Table 3) show that the Young modulus E increases with confining pressure. E values are systematically

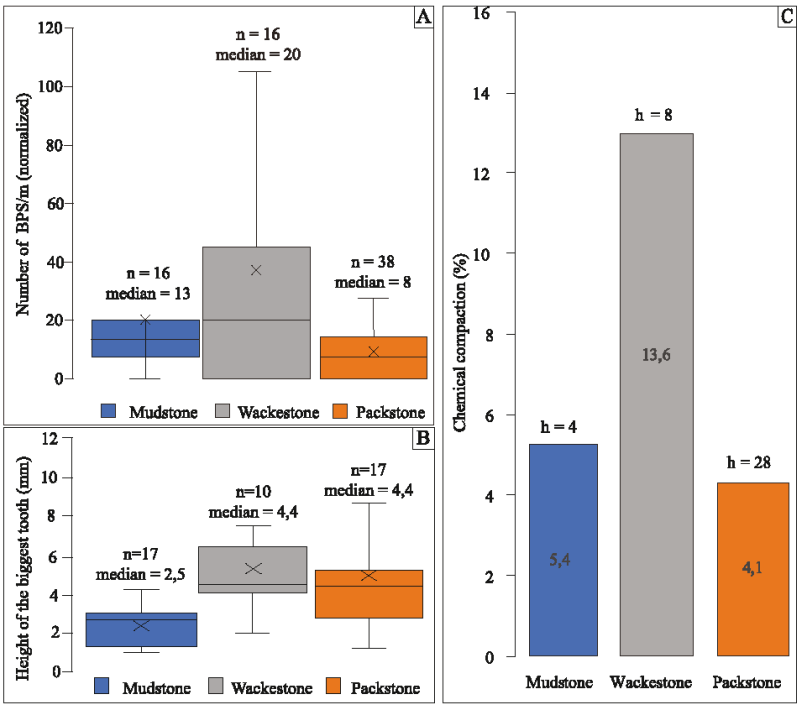


**Fig. 6.** Box-and-whiskers plots of the normalized number of Bedding-Parallel Stylolites (BPS) per meter (A) and the distribution of the height of the biggest tooth along a BPS track (B) as a function of the sedimentary texture. Distribution is reported from bottom to top: first decile, first quartile, median value, third quartile and ninth decile. (C) Percentage of chemical compaction calculated from eq. (1). The mean height of the biggest tooth are 2.3 mm; 4.9 mm and 4.9 mm for mudstone, wackestone and packstone textures, respectively. n- number of occurrences; h - thickness of each carbonate texture observed and measured on the core (in m).

**Table 3**
Elastic properties of the wackestone and packstone of the TOCA Fm. determined from rock mechanics tests.

| Sample depth (m) | Core sedimentary facies | Young Modulus (GPa) | | | Poisson ratio | | |
|---|---|---|---|---|---|---|---|
| | | Cycle 1 | Cycle 2 | Cycle 3 | Cycle 1 | Cycle 2 | Cycle 3 |
| 4086,66 | Pelecypod Wackestone | 21,4 | 27,9 | 33,3 | 0,30 | 0,22 | 0,19 |
| 4135,00 | Pelecypod Packstone | 28,1 | 31,4 | 35,2 | 0,30 | 0,25 | 0,21 |

higher in packstone than in wackestone textures. The Poisson ratio $\nu$ does not show any significant variation except for cycle 1, for which the determination of the ratio was difficult due to poor data quality.

The mean values of the elastic parameters determined from the tests are E = 30 GPa and $\nu = 0.23$. The uncertainty on the determination of E and $\nu$ is ±10% and ±20%, respectively.

### 4.5. Results of stylolite roughness inversion

Thirty samples were studied, in which 44 sedimentary stylolites (mainly class 3 and few class 4) were analyzed using the Fourier Power Spectrum (FPS) method. Only 27 stylolites (class 3) displayed two self-affine regimes with the expected Hurst coefficients, corresponding to a success rate of 61% (Table 4).

Fig. 7a shows four examples of processing. Three (Fig. 7 a1, a2 & a3) are acceptable because the inversion provides a trend showing two well-marked slopes with Hurst coefficients consistent with those predicted by the growth model. In contrast, Fig. 7 a4 shows a case of non-acceptable data because the inversion provides a monotonic trend with no change in slope.

For the stylolite roughness inversion, we used the mean values of the elastic parameters determined from the geomechanical tests (Table 3): E = 30 GPa and $\nu = 0.23$. The cross-over length (Lc) is given within ±23% uncertainty (Rolland et al., 2014).

After calculating the value of the vertical principal stress at the time pressure-solution along the considered stylolite stopped (equation (5)), the corresponding maximum depth was calculated (equation (6)). The 14–43 MPa range of $\sigma 1$ values obtained for the 27 stylolites converts into a depth range of 550–1750 m. This information is presented as a violin plot in Fig. 7b, which is similar to a conventional box plot but takes into account the data distribution and the probability density (Hintze and Nelson, 1998 and references therein). Fig. 7b shows that the dissolution along 90% of the stylolites halted between 800 and 1600 m.

We also investigated if the carbonate texture may have an impact on the SRIT reliability for class 3. The results show that the highest Lc values are associated with the packstone texture, with a median value of 1.2 mm, while the mudstones and wackestones show much lower median values of 0.46 mm and 0.54 mm, respectively (Fig. 7c). This result reflects a significant effect of the sedimentary texture on the reconstructed Lc. Packstones appear to better record stylolites formed at medium depths, while mudstones and wackestones record a wider range of Lc values reflecting stylolites formed over the first burial phase.

### 4.6. Burial-time model

The burial-time model shows three phases of burial evolution over time (Fig. 8): (1) 130 Ma to 95 Ma, a first phase of rapid burial (~63 m/Ma) associated with the early Cretaceous rifting episode and an erosion phase. This major erosional event observed at 118-117 Ma, represents a margin uplift with a peneplanation event (as seen in Fig. 1b). The estimated subsidence of 63 m/Ma is an average value between the moderate burial rates of the first 500 m and the abrupt increase in the following ~2000 m. (2) 95 Ma to 35 Ma, a plateau with a low burial rate (~5 m/Ma) ending with an erosional phase in the Lower Tertiary; (3) 35 Ma to present-day, a second phase of rapid burial (~42 m/Ma) before reaching the present-day depth. Fig. 8 also shows the histogram plot of the maximum depths of active pressure-solution along bedding-parallel stylolites obtained from the roughness inversion.

**Table 4**
Results of stylolite roughness inversion for stress, applied to bedding-parallel stylolites in the TOCA Fm. The Lc value was calculated with an uncertainty of 23%. σv is calculated with values of E 30 GPa and $\nu$ 0.23 determined from rock mechanics tests.

| Samples | Textures | Class | Cross-over length (mm) | σv (MPa) | Depth (m) |
|---|---|---|---|---|---|
| 4069,09-1.2 A | Mudstone | 3 | 0,46 | 38 | 1550 |
| 4069,92-2 B | Mudstone | 3 | 0,46 | 38 | 1550 |
| 4069,92-3 A | Mudstone | 3 | 1,72 | 19 | 750 |
| 4074,30-1.1 A | Mudstone | 3 | 0,69 | 31 | 1250 |
| 4074,30-1.1 B | Mudstone | 3 | 0,58 | 33 | 1350 |
| 4074,30-1.2 A | Mudstone | 3 | 0,37 | 42 | 1700 |
| 4074,30-1.2 B | Mudstone | 3 | 0,38 | 41 | 1650 |
| 4074,30-2.2 B | Mudstone | 3 | 0,44 | 38 | 1550 |
| 4074,30-3.2 B | Mudstone | 3 | 0,64 | 32 | 1300 |
| 4074.30–4.2 B | Mudstone | 3 | 0,63 | 32 | 1300 |
| 4074,30-2.1 A | Mudstone | 3 | 0,78 | 29 | 1200 |
| 4074,30-2.3 A | Mudstone | 3 | 0,43 | 39 | 1600 |
| 4079,40-1 A | Packestone | 3 | 1,19 | 23 | 950 |
| 4079,40-1 B | Packestone | 3 | 0,99 | 26 | 1050 |
| 4079,40-2.1 A | Packestone | 3 | 1,29 | 22 | 900 |
| 4079,90-2 A | Packestone | 3 | 1,05 | 25 | 1000 |
| 4079,40-2 B | Packestone | 3 | 0,53 | 35 | 1450 |
| 4079,90-2 B | Packestone | 3 | 1,20 | 23 | 950 |
| 4087,52-B1 | Packestone | 3 | 1,57 | 20 | 800 |
| 4097,54-2 A | Wackestone | 3 | 0,54 | 35 | 1450 |
| 4112,27-1 B | Packestone | 2 | 1,27 | 23 | 950 |
| 4113-1.1 A | Packestone | 3 | 3,10 | 14 | 550 |
| 4131,14-A1 | Wackestone | 3 | 1,05 | 25 | 1000 |
| 4131,14-A2 | Wackestone | 3 | 0,47 | 37 | 1500 |
| 4137,09-1.1 B | Wackestone | 3 | 1,13 | 24 | 1000 |
| 4137,09-1.2 B | Wackestone | 3 | 0,36 | 43 | 1750 |
| 4148,59-A | Packestone | 2 | 0,66 | 31 | 1250 |

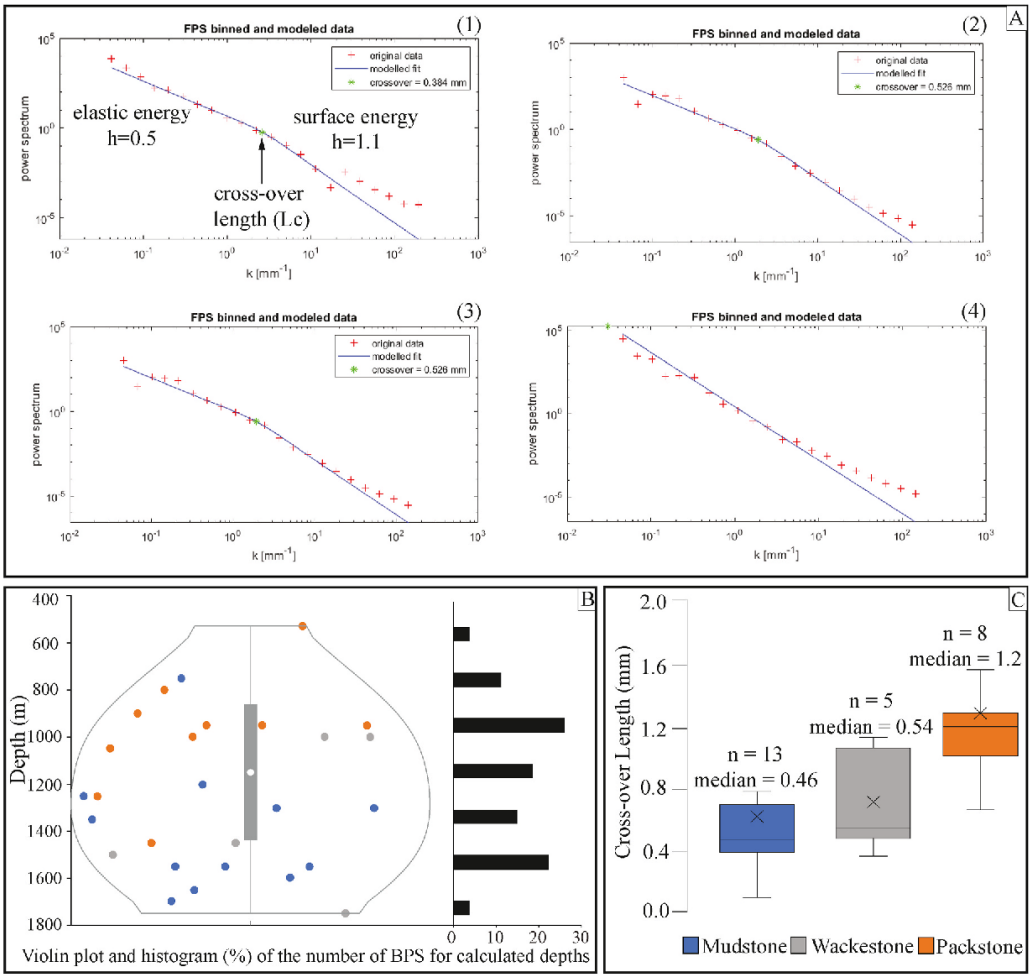


**Fig. 7.** (A) Definition of the Hurst exponent and cross-over length on a log-log plot of the Fourier Power Spectrum method (1) and examples of sedimentary stylolite roughness inversion for some samples, either successful (2 and 3) or failed (4). (B) Violin plots of the maximum depth of active pressure-solution derived from magnitude of vertical stress from stylolite roughness inversion and associated histogram (in %) of the data used for the violin plot. The blue, grey and orange circles represent class 3 stylolites in mudstone, wackestone and packstone textures respectively. (C) Box-and-whiskers plots reporting the value of the cross-over length obtained from the stylolite roughness inversion technique applied to the bedding-parallel stylolites versus carbonate texture for class 3 stylolites. n-number of occurrences. (For interpretation of the references to color in this figure legend, the reader is referred to the Web version of this article.)

### *4.7. Fluid inclusion microthermometry*

Fluid inclusion microthermometry measurements could only be done on small to medium-size aqueous two-phase fluid inclusions (±5–25 μm) in calcite C1 cement. No oil inclusion was observed in the samples. $T_h$ temperatures range from 80 to 160 °C and salinities from 300 to 360 g/l ($T_{m\ (ice)}$ range between −25.9 and −21.7 °C). All the measured $T_h$ values are lower or close to the bottom-hole present-day temperature for the TOCA Fm. (~157–164 °C). The $T_h$ data (Fig. 9a) illustrate a well-marked mode around ~120 °C, which may represent the main period of carbonate cementation. The measured salinities are well grouped at very high values of 300–360 g/l. The plot of salinity versus $T_h$ (Fig. 9b) shows a large variation in $T_h$ values with little or no variation in salinity, suggesting trapping of the same pore water over a wide temperature range. This data distribution brings up the question of a possible resetting of $T_h$ values during subsequent burial, in particular in light of the U–Pb ages which indicate that the calcite C1 cement formed sub-syn-depositional (section 4.8). We note however the following observations: (1) the $T_h$ histogram is well defined and rather symmetrical around a mode at 110–130 °C; (2) the mode is rather large ("flat") and 30–40 °C lower than present-day temperature; (3) the overall range of $T_h$ values is very large, i.e., 67–158 °C; (4) only the very highest $T_h$ value (158 °C) approaches present-day temperature (164 °C); (5) there is no evidence of heterogeneous trapping phenomena, i.e. boiling or two-phase fluid, in particular no report of vapor-rich inclusions eventually homogenizing to vapor; (6) there is no spatial control on the distribution of $T_h$ values within calcite crystals. Consequently, the FI data are compatible with precipitation of the C1 calcite from a highly saline brine at variable temperatures, with a major phase around 110–130 °C. Alternatively, it cannot be totally excluded at this time that C1 formed at lower temperature (possibly as low as 70–80 °C) and that fluid inclusion were largely but not completely reset during subsequent burial by stretching (120 °C corresponding to the temperature prevailing during the long late Cretaceous-early Tertiary burial plateau).

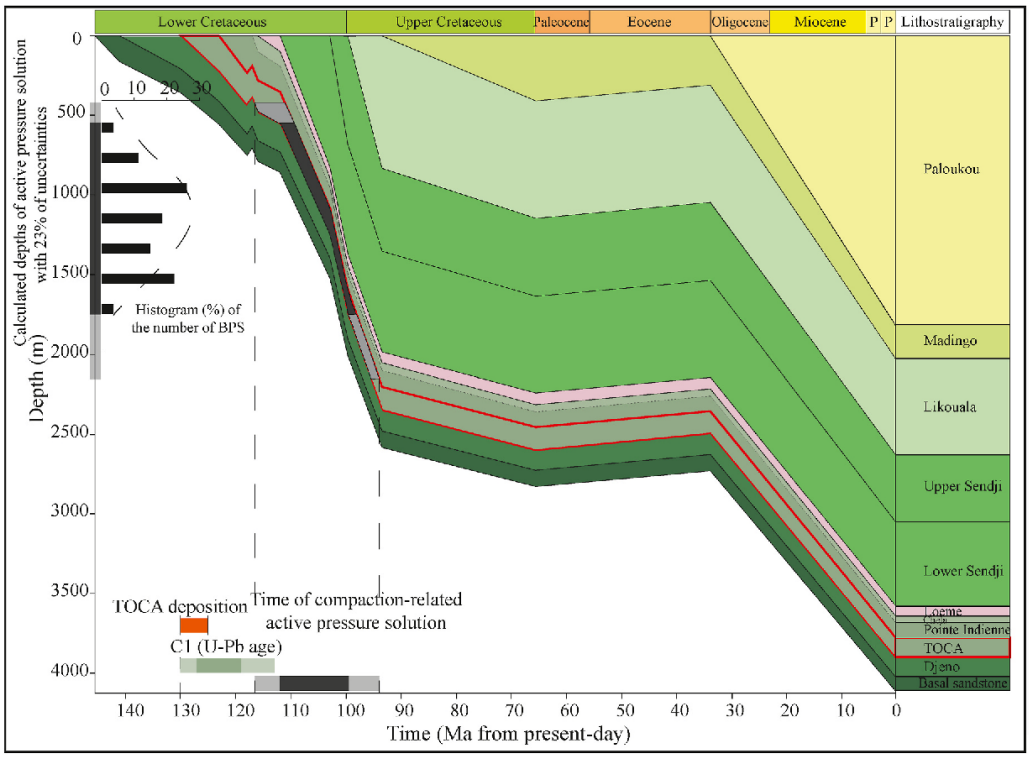


**Fig. 8.** Burial model constructed from Well-1 data corrected for mechanical compaction. The depth on the model is counted from the sea-bed. The calculated depth range of active pressure-solution from bedding-parallel stylolite inversion is reported for the TOCA Fm. as grey levels on the y-axis. The corresponding timing (with uncertainties in light grey) is reported on the x-axis.

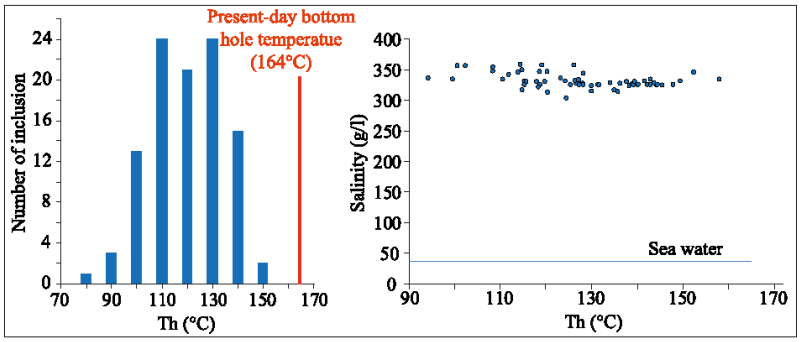


**Fig. 9.** Histograms of homogenization temperatures and salinity data from fluid inclusions.

### *4.8. U–Pb dating of the calcite cement*

Only the early calcite C1 cement provided reliable U–Pb ages (Fig. 10). The late C2 cement could not be dated because of a low U–Pb signal. Two ages measured on the intrabioclast C1 cement yielded 127.4 ± 2.2 Ma and 123.13 ± 7.7 Ma (Fig. 10 a, b). Three ages measured on the intergranular C1 cement gave 125.7 ± 5.0 Ma, 123.35 ± 10.4 Ma and 119.4 ± 6.4 Ma (Fig. 10 c, d, e). All these ages are indistinguishable from each other within error, yielding an average age of 125 Ma basically identical to the upper age limit for the TOCA Fm. deposition.

The Tera-Wasserburg diagrams for the C1 cement displayed in Fig. 10 show an excellent alignment of individual data points, providing a very precise isochron age. Some minor data scatter is observed in the less radiogenic samples (Fig. 10c, d, and 10e). The isochron in Fig. 10c being the most affected by scatter (highest MSWD), it may be considered as providing a somewhat less accurate age than other samples, although indistinguishable within analytical error.

The U–Pb ages indicate that the C1 cement precipitated syn-depositionally or extremely early in the TOCA diagenetic history (considering TOCA Fm. deposition between 130 and 125 Ma). The complete dataset is available in the supplementary material.

### *4.9. Cement distribution estimates*

Image analysis reveals that C1 calcite represents 25–30% (average 28%) of the thin-section surface depending on the sample, and C2 calcite

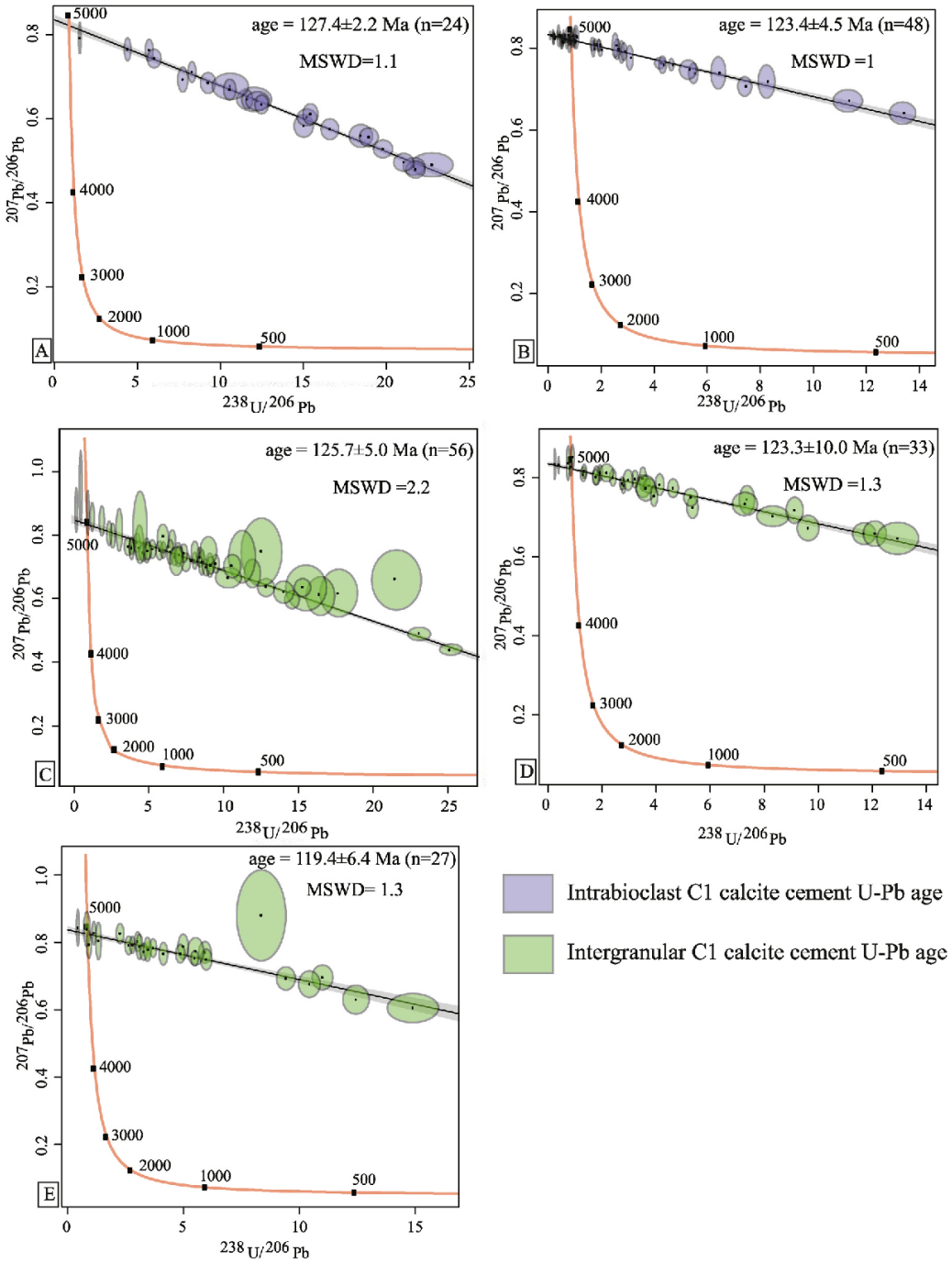


**Fig. 10.** Examples of the Tera-Wasserburg Concordia plots with the dated calcitic phase from TOCA carbonate formation. Intrabioclast C1 calcite cement U–Pb age (A and B) and intergranular C1 calcite cement U–Pb age (C, D and E). n – number of spots; MSWD - mean square of weighted deviates.

15–20% (average 17%) (Table 5). Fig. 11 shows that the intergranular C1 cement (~29%) is significantly more abundant than the intergranular C2 cement (~15%).

In order to assess repeatability and to reduce uncertainty in the results, we performed 3 different color calibration of the Fiji software for each of the eight thin-sections. However, because of the potential errors associated with picking C1 and C2 cements, and considering that the selected thin-sections may not be fully representative of the entire core, we estimate the uncertainty on the image-analyzed surfaces to be ±25%. This leads to an overall range of 19–38% (average 21–35%) for

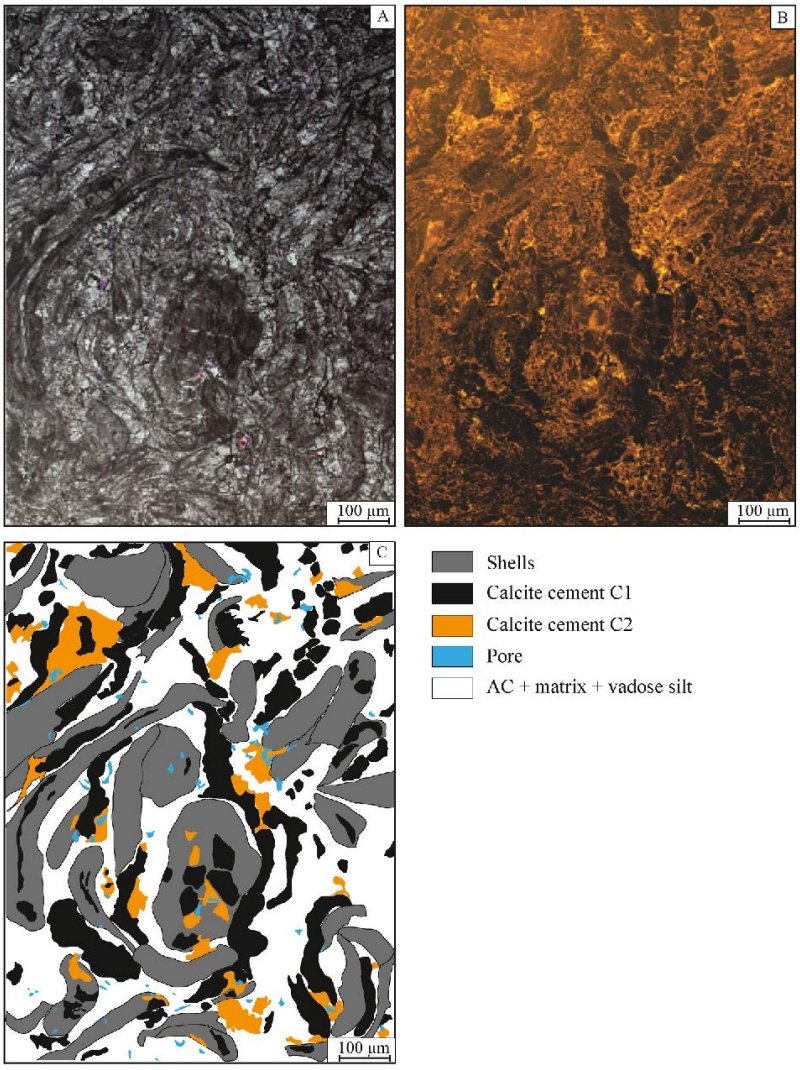


**Fig. 11.** Example of thin-section showing the different diagenetic phases. LPNA (A) and CL (B) image of the thin-section. (C) Line drawing underlining early calcite C1 (black), late calcite C2 (orange), shells (grey); residual porosity (blue) and other diagenetic processes/features (AC, matrix, micrite, microporosity; in white). (For interpretation of the references to color in this figure legend, the reader is referred to the Web version of this article.)

**Table 5**
Estimates of abundance of diagenetic cementation phase. The values represent the percentage of surface area of each phase in the considered thin-section.

| Depth (m) | C1 (%) | C2 (%) |
|---|---|---|
| 4126,92 | 26 | 20 |
| 4130,09 | 30 | 17 |
| 4132,05 | 29 | 15 |
| 4132,87 | 25 | 20 |
| 4139,87 | 29 | 15 |
| 4141,90 | 30 | 15 |
| 4145,90 | 25 | 20 |
| 4148,08 | 30 | 15 |

the C1 calcite and 11–25% (average 13–21%) for the C2 calcite.

Note that the porosity derived from image analysis of packstones (see Fig. 11c) reflects the visible macro-porosity only. It differs from the present-day total porosity (4–8%) determined on plugs for the packstone texture, because the micro-porosity associated to the microsparitic matrix cannot be quantified from Fiji image analysis.

## 5. Interpretation of results

### 5.1. Paragenetic sequence of the TOCA Fm. on the Well-1 core

The TOCA Fm. carbonates have been interpreted as lacustrine deposits presenting two distinct depositional environments: (1) a shoreline dominated by waves and rich in coquinas and (2) a palustrine system with episodic storm deposits. From the core and thin-sections, we established the paragenetic sequence that affected the TOCA Fm. since its deposition. The main diagenetic events that affected the TOCA Fm.

and had an impact on the reservoir quality are summarized below. Five major diagenetic processes are identified (Fig. 5):

1 Diagenesis started with a phase of partial to total calcification of the aragonite of the shells of bivalves in an eogenetic environment. This aragonite to calcite neomorphism AC resulted in the formation of shell replacive sparitic calcite crystals (Fig. 4a). The replacement of aragonite occurred rapidly and very early. In cathodoluminescence, neomorphic AC calcite is readily recognized by its brown to dark orange luminescence with a cloudy aspect. The aragonitic parts not replaced by AC have been dissolved later and are now either empty (as rare residual dissolution voids) or more generally cemented by the lately formed diagenetic calcites as described below. The occasional diagenetic micrite observed around the bivalve shells is more specifically common in grainstones and is the earliest stage of the paragenetic sequence. This micritization is attributed to microorganisms living near the sediment-water interface. These two phenomena (AC neomorphism and biogenic micritization) had no significant impact on the evolution of porosity.
2 The diagenetic cementation phase started with the precipitation of the first blocky calcite cement (C1) in the pores, resulting in a significant reduction of the interstitial porosity (both intergranular and intrabioclast). C1 precipitated in the voids (intergranular pores) and around AC (Fig. 4c), but textural relationships suggest that AC and C1 calcites may have developed partly synchronously. Cement C1 is affected by microfractures due to mechanical compaction (described below) and shows some minor dissolution affecting crystal outlines locally. C1 blocky calcite precipitated shortly after (or during) the dissolution phase of the biogenic aragonite not replaced by AC. The very high salinity (300–360 g/l) of the fluid inclusions in C1 indicates precipitation from hyper-saline water. This contrasts with the presence of freshwater fossils (Lamellibranchs (Unionidae group), Ostracods) in the TOCA Fm. which indicates that the lake water was not very salty. The U–Pb age (~125 Ma) indicates that C1 cementation occurred syn-depositionally or extremely early after deposition (130-125 Ma). The precipitation of C1 cement has an important impact on porosity reduction estimated to be in the range of ~25–30% (based on image analysis data). The relative volumes of C1 cement filling intrabioclast secondary porosity after shell dissolution (see event 1) and C1 cement filling original primary intergranular porosity are not known.
3 The mechanical compaction is expressed by microfracturing and breaking of bioclast shells that develop from the grain boundaries and propagate into the AC and C1 (Fig. 4d). The mechanical compaction is responsible for most of the poronecrosis observed in the intervals not affected by early calcite cementation. Mechanical compaction in the core parts where C1 is present appears to be very minor, suggesting that the framework rigidification resulting from extensive C1 cementation may have significantly inhibited mechanical compaction in these intervals.
4 The late blocky calcite cement (C2) precipitated after mechanical compaction during burial. The calcite crystals are orange under cathodoluminescence (Fig. 4c). The C2 cement is observed all along the studied depth interval with variable ratios. C2 often developed as overgrowths over C1 in the intergranular porosity and after all biogenic aragonite has been dissolved (or replaced by AC). The small amount of microfractures occurring in C2 suggests that burial was still moderate when C2 formed, which is consistent with precipitation either shortly after C1 in a slightly different diagenetic context or a somewhat later at the very beginning of burial diagenesis. The blocky calcite C2 represents ~15–20% of porosity loss in volume (based on image analysis).
5 The chemical compaction (117-95 Ma) is expressed by pressure-solution (mesoscale stylolites) which is best developed within those intervals that were not affected by the early cementation event (C1). The chemical compaction mainly postdates C1 and C2 cements, and represents a volume loss estimated to be on the order of 6%.

Petrographic and cathodoluminescence observations provide no evidence of any late corrosion-dissolution of the early calcite cements that could have produced secondary porosity and rejuvenated some reservoir quality.

Noteworthy, all the diagenetic processes described above took place prior to about 95 Ma (or 2500 m depth), in other words, during the first phase of burial preceding the late Cretaceous to early Tertiary subsidence idling (see above and Fig. 8).

### 5.2. Porosity evolution during burial

In this section, we estimate the contribution of each diagenetic event to the destruction of the porosity in the Barremian TOCA Fm. during burial, by quantifying the porosity reduction associated to mechanical compaction, early diagenetic cementation (C1 and C2) and pressure-solution reprecipitation (117-95 Ma). Moving back in time from the present-day porosity value, we then further propose a rough estimate of the initial porosity of the TOCA Fm., taking as an example the packstone texture.

Starting from a present-day average porosity value of 6% (average value obtained from geomechanical tests on 14 plugs of packstones ranging from 4% to 8% porosity) and assuming that 100% of the carbonate dissolved following chemical compaction by stylolitization (6 ± 2%) has reprecipitated in the intergranular porosity, we estimate that the porosity was 12 ± 2% before chemical compaction (Fig. 12). The reduction of the porosity by pressure-solution is of about 50%, which is in line with conservative estimates of Koehn et al. (2016). As cements C1 and C2 together represent 45 ± 11% of the rock volume, this implies that the porosity before calcite cement precipitation was 57 ± 13%, i.e. between 44 and 70% (Fig. 12).

The calculation above needs to be considered as a first order semi-quantitative estimate. It takes into consideration global uncertainties associated to some of the parameters (i.e., range of porosity values, amount of dissolution along stylolites, image analysis quantification of C1 and C2). However, other uncertainties exist that cannot be evaluated from current data. First, the calculation does not take into account that part of the C1 calcite has filled secondary pores after shell dissolution. Second, the use of the bigger teeth of stylolites to estimate chemical compaction leads to a minimum estimate of the carbonate volume dissolved along stylolites. Third, 100% of the material dissolved along stylolites has probably not precipitated on site. The underestimate of dissolution related to chemical compaction may to some extent be counterbalanced by the overestimate of reprecipitation of the dissolved carbonate material, but this cannot be ascertained. Our study does not permit to provide a more accurate quantification of the cumulative error on the reconstructed path of porosity evolution at this time, but this does not impair the importance of our results and the value of our methodology as discussed below.

To estimate the contribution of mechanical compaction to early porosity reduction, we used the total porosity-depth curve for packstone to grainstone as accounted for in the basin model TemisFlow™ and used for the burial-time model (Fig. 8). Considering an oldest depositional age of 130 Ma and that the major early cementation event (C1) occurred at 125 Ma, we can estimate the contribution of the early mechanical compaction to porosity reduction during the first ~5 Ma before C1 precipitated and prevented further significant mechanical compaction. This corresponds to a porosity reduction of ~2% (much of which might have affected preferentially the matrix microporosity), so the initial porosity was at about 59 ± 13% (i.e., between 46 and 72%; Fig. 12).

In spite of the methodological uncertainties associated with the estimates of mechanical and chemical compaction as well as with the amounts of C1 and C2 cements, this initial porosity estimate appears to be reasonable for a packstone carbonate depositional texture (Choquette

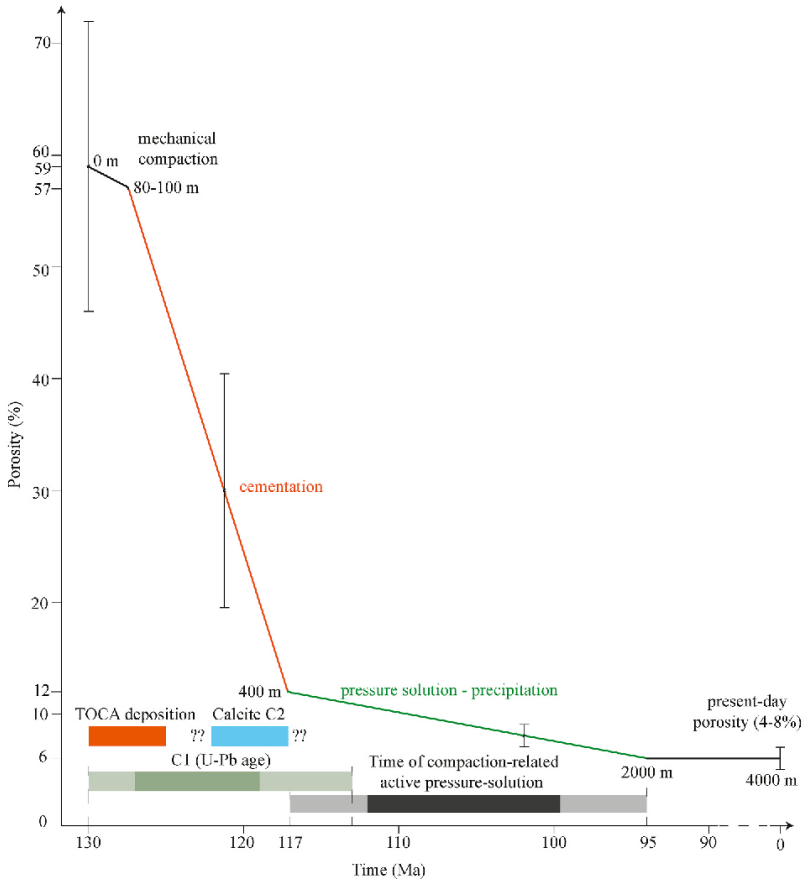


**Fig. 12.** Porosity evolution over time of TOCA Fm. Vertical lines in each part of the curve indicate the range of possible porosity values according to the estimated uncertainties.

and Pray, 1970; Schmocker et Halley 1982) and overall, falls within the range of initial porosities of 40–70% for carbonate sediments reported in the literature (Choquette and Pray, 1970). They are also consistent with the initial porosity values reconstructed by the TemisFlow™ software (Table 1).

Beyond this estimate of the porosity reduction, the important information from the above calculations is that the porosity has been drastically reduced over the first 10 Ma, primarily by cementation rather than by mechanical/chemical compaction. Porosity loss due to C1–C2 cementation alone represents about 75% of the depositional porosity (Fig. 12). The pressure-solution process then additionally reduced the residual porosity by ~50% to reach its current value at the end of the chemical compaction at about 95 Ma and 2500 m burial depth. This implies that the reservoir quality did not significantly evolve during the last ~100 Ma despite continuing burial to nearly 4000 m depth.

## 6. Discussion

### *6.1. Impact of carbonate textures on stylolite distribution and paleopiezometry*

The distribution of the stylolite population in the studied core reveals that in term of density, mudstones are more prone to develop a dense network of stylolites compared to packstones and wackestones. Yet, the greater density of stylolites is documented in mud-supported, grain-rich wackestone, an observation in line with the ones of Xu et al. (2022). The relationship between stylolite initiation and texture is supported by the role of muddy-carbonate interface on the initiation of dissolution (Aharonov and Katsman, 2009). That role complements the known facilitating role of the clayish minerals on the initiation of dissolution under pressure (Carozzi and Bergen, 1987; Renard et al., 1997). While the stylolite initiation and density are seemingly affected by the texture, the amount of chemical compaction on a single stylolite is relatively stable with respect to textures (2.5 mm–4.4 mm, Fig. 6b). When considering the whole population, we estimated a minimum compaction of ~6%, which is consistent with the results of Vandeginste and John (2013) (7–12%), Koehn et al. (2016) (3–5.6%) and Ehrenberg et al. (2016) (5–9%). This consistency suggests that the amount of chemical compaction accommodated by pressure solution is about 10% in carbonate rocks, regardless of the context. At a closer look, in the case of the TOCA Fm., the wackestone texture is more efficient in accommodating vertical shortening by pressure solution.

The results from stylolite roughness inversion highlight an effect of the sedimentary texture on the reconstructed Lc values (Fig. 7c). Indeed, it is striking that the class 3 stylolites Lc values are significantly different between mud-supported textures (mudstones and wackestones) for which the Lc value is lower (median = 0.5 mm), and grain-supported textures (packstones) for which the Lc value is significantly higher (median = 1.2 mm). We can tentatively link this result to the role of grain size in the stylolite development. Koehn et al. (2016) demonstrated that the amount of dissolution was inversely proportional to the grain size of the material undergoing dissolution. In other words, the

smaller the grains, the greater the chemical compaction, because smaller grains offer a larger reaction surface in the rock. Consequently, in mud-supported carbonates where the average grain size is smaller than in grain-supported carbonates, the dissolution might last longer, and SRIT may return greater depths of active pressure solution.

This new dataset suggests that a reliable estimate of the maximum burial depth at which compaction-related pressure solution was still active using class 3 stylolites would require the analysis of these stylolites within mudstone. We believe this novel indication will help establish the application of this developing method.

### 6.2. Origin of fluids associated with early cementation of the TOCA Fm

Fluid inclusions indicate that C1 calcite cement precipitated from hot (or moderately hot if resetting occurred) highly saline fluid. The age of the C1 cement (~125 Ma) indicates a very early precipitation in the burial history, certainly before the formation reached 200–300 m burial. Considering a sea-bed temperature of 13 °C based on paleo bathymetric map (Unpublished data from TotalEnergies internal report) and a paleo geothermal gradient documented for the early Cretaceous times of 27–30 °C/km (Robert and Yapaudjian, 1990; Baudino et al., 2018; Macgregor, 2020) would result in a burial temperature of ~25 °C at 400–500 m depth, i.e., much lower that the range of 80–160 °C suggested by fluid inclusion thermometry (Fig. 9). Consequently, we infer that the parent waters of the C1 cement were most likely of hydrothermal origin. The $T_h$ values should therefore not be interpreted as reflecting the burial depth of the TOCA Fm. at the time of C1 formation. A possible origin of the hydrothermal and hypersaline fluids could be the Neoproterozoic evaporite formations (Schisto-Calcaire Subgroup) which have been documented in the underlying pre-rift basement by field studies conducted in the continental part of the Lower Congo basin (Delpomdor et al., 2008; Préat et al., 2010). Such occurrence of Neoproterozoic evaporites has also been proposed by Kadima et al. (2011) based on well and geophysical data. In such a scenario the hypersaline hydrothermal fluids would have migrated upward along major basement-rooted syn-rift normal faults, invaded the porous carbonates at shallow depth and probably partially reached the lake water locally.

### 6.3. Evolution of porosity in the TOCA tight carbonate reservoir and implication for hydrocarbon exploration

In the coquina facies studied in Well-1 core, the macroscopic porosity is diverse in nature, being interparticular, intercrystalline, moldic and vuggy. This porosity is largely cemented by the C1 calcite cement. Together with the eogenetic AC phase, this early cementation has limited mechanical compaction and pressure-solution, and possibly later fluid-rock interactions during burial. In contrast, in other core sections where early diagenetic events (AC and C1) were less important, numerous stylolites are observed and the interparticle porosity was mainly destroyed by mechanical compaction. In the studied core section, porosity was further reduced by later precipitation of blocky calcite C2 as well as by the likely precipitation of the material dissolved along bedding-parallel stylolites. Although not observed in the studied section bitumen occurring as pore-fillings has been reported in other sections of the Well-1 core, and would constitute an additional cause of poronecrosis in the TOCA limestone (Unpublished data from TotalEnergies internal report).

Our results show that early cementation governed the evolution of porosity in the TOCA (Fig. 12). This is consistent with the results of Xu et al. (2022) on bioclastic limestones from the Middle East which support that early cementation is the controlling factor for compaction and subsequent dissolution under pressure in the reduction of porosity. Our results show that the present-day porosity of the TOCA carbonates (~4–8%) in the studied well was acquired very early during the diagenetic and burial histories and has probably not evolved much since the end of pressure-solution at 95 Ma, i.e., since the formation has reached 2500 m depth (Fig. 12). This is supported by the absence of evidence of any significant corrosion-dissolution of the early calcite cements in the core that could have produced secondary porosity and rejuvenated some reservoir quality (the minor secondary porosity formed by very early dissolution of parts of the aragonite shells was rapidly filled by C1 cementation). This suggests that fluid-rock interactions in the reservoir were strongly limited due to the low (connected) porosity remaining after the massive early cementation. Early diagenetic cementation therefore appears to be the main controlling factor of the evolution of reservoir porosity in the packstone carbonates of the TOCA Fm. This conclusion is in line with the observations made by Harris (2000) in the coquina facies of the upper part of the TOCA Fm. from offshore cores provided by Elf Congo and Chevron. The sedimentological observations of Harris (2000) showed that the upper TOCA unit (TOCA 3: coquina facies, which is the TOCA unit investigated in this study in the Well-1 core) shows poor reservoir qualities. Harris (2000) reports that the best TOCA reservoirs regionally are primarily found in TOCA 1 (microbialites) and TOCA 2 (microbial encrustations of shells, microbial mats and thrombolites) facies units. Our results provide an explanation for the generally poor quality of TOCA 3 reservoirs in the studied area of the Lower Congo basin (Well-1 is located within the regional perimeter considered by Harris, 2000). Our observations from Well-1 indicate that the initial porosity in the TOCA 3 unit (coquina facies) was largely destroyed during early burial, well before hydrocarbon migration in the TOCA Fm. (see more discussion below), resulting in making the TOCA 3 unit a regionally poor reservoir. Note that this steady and fast decrease in porosity during burial (Fig. 12) suggests that the creation of porosity by dissolution is far less important than porosity occlusion during burial diagenesis. The major role played by early cementation in the reduction of porosity in the TOCA carbonates support the results of other studies (Ehrenberg and Nadeau, 2005; Xu et al., 2022).

It is well known that the relative timing of the hydrocarbon migration into the reservoir and of the mechanisms that preserve/create or destroy porosity is key for the appraisal of the petroleum system. When early cementation remains limited, mechanical compaction may reduce the porosity progressively during burial, allowing some residual porosity to be available at the time of potential hydrocarbon charge. In contrast, despite its delaying/inhibiting effect on mechanical compaction, massive early diagenetic cementation may reduce most (>78% relative) of the porosity even during shallow burial (first 500 m), thereby strongly limiting the amount of porosity available later at the time of hydrocarbon migration into the reservoir. The hydrocarbon migration in the TOCA reservoirs in the Lower Congo basin is mainly dated from the Cenomanian to the Paleocene (i.e. after 95 Ma) (Schoellkopf and Patterson, 2000; Brownfield and Charpentier, 2006; Beglinger et al., 2012). The hydrocarbon migration into the TOCA reservoir therefore occurred after the initial porosity had been largely destroyed, resulting in the tight nature of the TOCA reservoir in Well-1. This hydrocarbon migration is also concomitant with the end of the development of the population of bedding-parallel stylolites, hence the role of the increase of the local (i.e. at the dissolution interface scale) fluid pressure by the hydrocarbons can be questioned in the halting of the development of the stylolites.

## 7. Conclusions

This study unravels the history of porosity destruction over time in the tight, deeply buried early Cretaceous (130-125 Ma) lacustrine carbonates of the syn-rift TOCA Fm. in the Lower Congo basin (West Africa passive margin). The main conclusion are summarized below:

- An original multi-proxy approach was adopted to unravel the burial and diagenetic history of the TOCA Fm. This approach includes simulation of a burial model, U–Pb dating and fluid inclusion thermometry of diagenetic cements and inversion of the roughness of the

sedimentary stylolites for maximum burial depth of active chemical compaction.

- The absolute age of the key paragenetic events controlling reservoir properties of the TOCA Fm. have been constrained: mechanical compaction (~130-127 Ma based on TemisFlow™), early cementation (~125 ± 5 Ma based on U–Pb dating on calcite diagenetic cement), and chemical compaction (~117-95 Ma based on stylolite roughness inversion). This provides new constraints on the diagenetic sequence of the TOCA Fm. and a better understanding of the diagenetic processes and their absolute timing, which is a key information for a better prediction of the reservoir properties in exploration.
- All diagenetic processes occurred early in the TOCA Fm. burial history, so that the TOCA Fm. acquired its reservoir properties during the first 35 Ma following its deposition. Especially, the current porosity of the TOCA Fm. was acquired during early diagenesis and has not significantly evolved since 95 Ma. Early cementation and chemical compaction by stylolitization followed by reprecipitation of the dissolved material in the residual porosity were quantitatively the main factors controlling the destruction of the reservoir properties in this tight carbonate reservoir.
- U–Pb dating and fluid inclusion microthermometry of calcite cement revealed that the early mineralizing fluids were hot (80–160 °C) highly saline (300–360 g/l) brines, not in thermal equilibrium with the host rocks buried at a maximum depth at 400–500 m at the time of cementation. These hydrothermal fluids likely originated from the pre-rift Precambrian rocks along syn-rift normal faults. These results (combined age and fluid inclusions) illustrate that $T_h$ recorded in the C1 cement cannot be used to infer precipitation depth.

Beyond regional implications, this study demonstrates the potential of our new multi-proxy approach combining stylolite inversion paleopiezometry, fluid inclusion microthermometry, calcite cement U–Pb dating, burial modelling and cement phase petrography image analysis to reconstruct both the timing and amount of porosity destruction in deeply buried tight carbonates reservoirs. In addition, our results illustrate the potential of stylolite roughness inversion to constrain part of the burial history of a carbonate strata, and to grant indirect timing information on the diagenetic evolution of this strata. We show that carbonate texture impacts the overall distribution and development of stylolites, and that considering a given morphology of stylolite, the paleoburial it records seems to be dependent on the texture, being higher in mud-supported rocks. Last but not least, our results also illustrate that the reservoir quality of bioclastic carbonates may be primarily controlled and set as a result of early, very shallow diagenetic processes, leaving only minor potential of impact to the subsequent deep-burial mesogenetic diagenesis.

The original multi-proxy methodology described in this paper is expected to be most useful for application to the reconstruction of diagenetic processes and concomitant porosity evolution in carbonate reservoirs, as shown here. It may also provide valuable information for the calibration of basin models, in particular when dealing with extensively stylolitized carbonates which original thickness may have been significantly reduced by stylolitization.

## Declaration of competing interest

The authors declare that they have no known competing financial interests or personal relationships that could have appeared to influence the work reported in this paper.

## Data availability

Data will be made available on request.

## Acknowledgments

The authors are very grateful to TotalEnergies for complete financial support of this research, for providing the cores and for permission to publish. We would like to thank Philippe Marchina for his help in carrying out the geomechanical tests and for the discussions on the results. Nicolas E. Beaudoin is funded through the isite-E2S, supported by the ANR PIA and the Région Nouvelle-Aquitaine. The laser U–Pb dating analyses were carried out as part of the CEREGE-TotalEnergies collaborative R&D project DATCARB (2018–2021), co-funded by the "Excellence Initiative" program of Aix Marseille University A*MIDEX, TotalEnergies, and Sud region. Abel Guihou is thanked for its technical support in the U–Pb analyses by LA-ICPMS. The authors would also like to thank the editor Bo Liu and three anonymous reviewers for their useful comments and suggestions that improved the quality of the paper.

## Appendix A. Supplementary data

Supplementary data to this article can be found online at https://doi.org/10.1016/j.marpetgeo.2022.106018.

## References

Aharonov, E., Katsman, R., 2009. Interaction between pressure-solution and clays in stylolite development: insights from modeling. Am. J. Sci. 309 (7), 607–632.
Alvarez, W., Engelder, T., Geiser, P.A., 1978. Classification of solution cleavage in pelagic limestones. Geology 6 (5), 263–266.
Andrews, L.M., Railsback, L.B., 1997. Controls on stylolite development: morphologic, lithologic, and temporal evidence from bedding-parallel and transverse stylolites from the US Appalachians. J. Geol. 105 (1), 59–73.
Aslanian, D., Moulin, M., Olivet, J.L., Unternehr, P., Matias, L., Bache, F., Rabineau, M., Klingelheofer, F., Contrucci, I., Labails, C., 2009. Brazilian and african passive margins of the central segment of the South Atlantic ocean: kinematic constraints. Tectonophysics 468 (1–4), 98–112.
Asmus, H.E., Ponte, F.C., 1973. The Brazilian marginal basins. In: The South Atlantic. Springer, Boston, MA, pp. 87–133.
Bate, R.H., 1999. Non-marine ostracod assemblages of the Pre-Salt rift basins of West Africa and their role in sequence stratigraphy. Geological Society, London, Special Publications 153 (1), 283–292.
Barbier, M., Hamon, Y., Callot, J.P., Floquet, M., Daniel, J.M., 2012. Sedimentary and diagenetic controls on the multiscale fracturing pattern of a carbonate reservoir: the Madison Formation (Sheep Mountain, Wyoming, USA). Mar. Petrol. Geol. 29 (1), 50–67.
Bathurst, R.G., 1972. Carbonate Sediments and Their Diagenesis. Elsevier, pp. 459–475.
Baud, P., Rolland, A., Heap, M., Xu, T., Nicolé, M., Ferrand, T., Reuschlé, T., Toussaint, R., Conil, N., 2016. Impact of stylolites on the mechanical strength of limestone. Tectonophysics 690, 4–20.
Baudino, R., Pontet, M., Manas, M., Herra, A., Sanders, C., Badali, M., Tocco, R., Martinez, S., Tritlla, J., Loma, R., Carrasco, A., Padron, S., Mora, S., 2018. Modelling petroleum systems of hyperextended margins: the Angola case study. In: Global Analogues for the Atlantic Margin. AAPG European Regional Conference, Abstracts.
Beaudoin, N., Lacombe, O., Koehn, D., David, M.E., Farrell, N., Healy, D., 2020a. Vertical stress history and paleoburial in foreland basins unravelled by stylolite roughness paleopiezometry: insights from bedding-parallel stylolites in the Bighorn Basin, Wyoming, USA. J. Struct. Geol. 136, 104061.
Beaudoin, N., Lacombe, O., David, M.E., Koehn, D., 2020b. Does stress transmission in forelands depend on structural style? Distinctive stress magnitudes during Sevier thin-skinned and Laramide thick-skinned layer-parallel shortening in the Bighorn Basin (USA) revealed by stylolite and calcite twinning paleopiezometry. Terra. Nova 32 (3), 225–233.
Beaudoin, N.E., Labeur, A., Lacombe, O., Koehn, D., Billi, A., Hoareau, G., Boyce, A., John, C.M., Marchegiano, M., Robert, N.M., Millar, I.L., Clavery, F., Pecheyran, C., Callot, J.P., 2020c. Regional-scale paleofluid system across the Tuscan Nappe–Umbria–Marche Apennine Ridge (northern Apennines) as revealed by mesostructural and isotopic analyses of stylolite–vein networks. Solid Earth 11 (4), 1617–1641.
Beaudoin, N., Gasparrini, M., David, M.E., Lacombe, O., Koehn, D., 2019. Bedding-parallel stylolites as a tool to unravel maximum burial depth in sedimentary basins: application to Middle Jurassic carbonate reservoirs in the Paris basin. Geol. Soc. Am. Bull. 131 (7/8), 1239–1254.
Beaudoin, N., Lacombe, O., Roberts, N.M., Koehn, D., 2018. U-Pb dating of calcite veins reveals complex stress evolution and thrust sequence in the Bighorn Basin, Wyoming, USA. Geology 46 (11), 1015–1018.
Beaudoin, N., Lacombe, O., 2018. Recent and future trends in paleopiezometry in the diagenetic domain: insights into the tectonic paleostress and burial depth history of fold-and-thrust belts and sedimentary basins. J. Struct. Geol. 114, 357–365.
Beaudoin, N., Koehn, D., Lacombe, O., Lecouty, A., Billi, A., Aharonov, E., Parlangeau, C., 2016. Fingerprinting stress: stylolite and calcite twinning paleopiezometry revealing the complexity of progressive stress patterns during

folding—the case of the Monte Nero anticline in the Apennines, Italy. Tectonics 35 (7), 1687–1712.
Bebout, D.G., 1974. Stuart City Trend, Lower Cretaceous, South Texas: a Carbonate Shelf-Margin Model for Hydrocarbon Exploration. Virtual Landscapes of Texas.
Beglinger, S.E., Doust, H., Cloetingh, S., 2012. Relating petroleum system and play development to basin evolution: west African South Atlantic basins. Mar. Petrol. Geol. 30 (1), 1–25.
Ben-Itzhak, L.L., Aharonov, E., Karcz, Z., Kaduri, M., Toussaint, R., 2014. Sedimentary stylolite networks and connectivity in limestone: large-scale field observations and implications for structure evolution. J. Struct. Geol. 63, 106–123.
Bertotti, G., de Graaf, S., Bisdom, K., Oskam, B., Vonhof, H.B., Bezerra, F.H.R., Reijmer, J.J.G., Cazarin, C.L., 2017. Fracturing and fluid-flow during post-rift subsidence in carbonates of the jandaíra formation, potiguar basin, NE Brazil. Basin Res. 29 (6), 836–853.
Bidiet, J., Kinga, A., Loemba, C., Assoua-Wande, C., Hossie, G., Mahoukou-Sounga, A., 1998. Aperçu géologique et pétrolier des bassins du congo. Rapport de l'association des producteurs de pétrole africains, Hydro-Congo, Elf-Congo, AGIP Congo. Ministère des Mines et de l'Energie, p. RF11904.
Booler, J., Tucker, M.E., 2002. Distribution and geometry of texture and early diagenesis: the key to accommodation space variation and sequence stratigraphy: upper Cretaceous Congost Carbonate platform, Spanish Pyrenees. Sediment. Geol. 146 (3–4), 225–247.
Brice, S.E., Cochran, M.D., Pardo, G., Edwards, A.D., 1982. Tectonics and sedimentation of the South Atlantic Rift Sequence: Cabinda, Angola: rifted margins: field investigations of margin structure and stratigraphy. In: Studies in Continental Margin Geology. AAPG Special Volumes, pp. 5–18.
Brognon, G.P., Verrier, G.R., 1966. Oil and geology in cuanza basin of Angola. AAPG (Am. Assoc. Pet. Geol.) Bull. 50 (1), 108–158.
Brownfield, M.E., Charpentier, R.R., 2006. Geology and Total Petroleum Systems of the West-Central Coastal Province (7203), West Africa (No. 2207-B). US Geological Survey.
Bruna, P.O., Lavenu, A.P., Matonti, C., Bertotti, G., 2019. Are stylolites fluid-flow efficient features? J. Struct. Geol. 125, 270–277.
Burk, K., Dewey, J.F., 1974. Two plates in Africa during the cretaceous? Nature 249 (5455), 313–316.
Burwood, R., 1999. Angola: source rock control for Lower Congo Coastal and Kwanza Basin petroleum systems. Geological Society, London, Special Publications 153 (1), 181–194.
Bushinskiy, G.I., 1961. Stylolites. Izv. Akad. Nauk. SSSR, Ser. Fiz 8, 31–46.
Buxton, T.M., Sibley, D.F., 1981. Pressure-solution features in a shallow buried limestone. J. Sediment. Res. 51 (1), 19–26.
Carozzi, A.V., Bergen, D.V., 1987. Stylolitic porosity in carbonates: a critical factor for deep hydrocarbon production. J. Petrol. Geol. 10 (3), 267–282.
Chaboureau, A.C., Guillocheau, F., Robin, C., Rohais, S., Moulin, M., Aslanian, D., 2013. Paleogeographic evolution of the central segment of the South Atlantic during Early Cretaceous times: paleotopographic and geodynamic implications. Tectonophysics 604, 191–223.
Choquette, P.W., Pray, L.C., 1970. Geologic nomenclature and classification of porosity in sedimentary carbonates. AAPG Bull. 54 (2), 207–250.
Contrucci, I., Matias, L., Moulin, M., Géli, L., Klingelhofer, F., Nouzé, H., Aslanian, D., Olivet, J.L., Réhault, J.P., Sibuet, J.C., 2004. Deep structure of the West African continental margin (Congo, Zaïre, Angola), between 5 S and 8 S, from reflection/refraction seismics and gravity data. Geophys. J. Int. 158 (2), 529–553.
Croize, D., Renard, F., Gratier, J.P., 2013. Compaction and porosity reduction in carbonates: a review of observations, theory, and experiments. Adv. Geophys. 54, 181–238.
Da Costa, J.L., Schirmer, T.W., Laws, B.R., 1999. Lower Congo basin, deepwater exploration province. offshore West Afri~ AAPG Bulletin 83 (12).
Delpomdor, F., Préat, A., Tack, L., 2008. Paleoenvironments of the neoproterozoic carbonates in the schisto-calcaire Subgroup (C2 and C3) in democratic republic of Congo: lithostratigraphy and diagenesis. In: 22nd Colloquium of African Geology (CAG22) & 13th Conference of the. Geological Society of Africa (GSAf13) (109).
Desthieux, F., 1993. Notice explicative de la carte géologique de la République du Congo au 1/1.000. 000. Ministère des mines et de l'énergie, vol. 27. Direction Générale des Mines. Brazzaville.
Dingle, R.V., 1999. Walvis Ridge barrier: its influence on palaeoenvironments and source rock generation deduced from ostracod distributions in the early South Atlantic Ocean. Geological Society, London, Special Publications 153 (1), 293–302.
Doyle, J.A., Jardiné, S., Doerenkamp, A., 1982. Afropollis, un nouveau genre de pollen d'Angiosperme précoce, avec de données sur la palynostratigraphie et les paléoenvironnements du Crétacé du Nord-Gondwana. Bulletin des Centres de Recherche et d'Exploration-Production Elf-Aquitaine 6, 39–117.
Dunnington, H.V., 1954. Stylolite development post-dates rock induration. J. Sediment. Res. 24 (1), 27–49.
Ebner, M., Piazolo, S., Renard, F., Koehn, D., 2010a. Stylolite interfaces and surrounding matrix material: nature and role of heterogeneities in roughness and microstructural development. J. Struct. Geol. 32 (8), 1070–1084.
Ebner, M., Toussaint, R., Schmittbuhl, J., Koehn, D., Bons, P., 2010b. Anisotropic scaling of tectonic stylolites: a fossilized signature of the stress field? J. Geophys. Res. Solid Earth 115 (B6).
Ebner, M., Koehn, D., Toussaint, R., Renard, F., 2009a. The influence of rock heterogeneity on the scaling properties of simulated and natural stylolites. J. Struct. Geol. 31 (1), 72–82.
Ebner, M., Koehn, D., Toussaint, R., Renard, F., Schmittbuhl, J., 2009b. Stress sensitivity of stylolite morphology. Earth Planet Sci. Lett. 277 (3–4), 394–398.
Ehrenberg, S.N., Morad, S., Yaxin, L., Chen, R., 2016. Stylolites and porosity in a lower cretaceous limestone reservoir, onshore abu dhabi, UAE. J. Sediment. Res. 86 (10), 1228–1247.
Ehrenberg, S.N., Nadeau, P.H., Steen, Ø., 2009. Petroleum reservoir porosity versus depth: influence of geological age. AAPG Bull. 93 (10), 1281–1296.
Ehrenberg, S.N., Nadeau, P.H., 2005. Sandstone vs. carbonate petroleum reservoirs: a global perspective on porosity-depth and porosity-permeability relationships. AAPG Bull. 89 (4), 435–445.
Giresse, P., 1982. La succession des sédiments dans les bassins marins et continentaux du Congo depuis le début du Mésozoïque. Sciences Géologiques, bulletins et mémoires 35 (4), 183–206.
Godeau, N., Deschamps, P., Guihou, A., Leonide, P., Tendil, A., Gerdes, A., Hamelin, B., Girard, J.P., 2018. U-Pb dating of calcite cement and diagenetic history in microporous carbonate reservoirs: case of the Urgonian Limestone. France. Geology 46 (3), 247–250.
Goldstein, R.H., Reynolds, T.J., 1994. Systematics of Fluid Inclusions in Diagenetic Minerals. SEPM Short Course No. 31. SEPM Society for Sedimentary Geology.
Gomez-Rivas, E., Martín-Martín, J.D., Bons, P.D., Koehn, D., Griera, A., Travé, A., Llorens, M.G., Humphrey, E., Neilson, J., 2022. Stylolites and stylolite networks as primary controls on the geometry and distribution of carbonate diagenetic alterations. Mar. Petrol. Geol. 136, 105444.
Gradstein, F.M., Ogg, J.G., Smith, A.G., Bleeker, W., Lourens, L.J., 2004. A new geologic time scale, with special reference to Precambrian and Neogene. Episodes 27 (2), 83–100.
Grosdidier, E., Braccini, E., Dupont, G., Moron, J.M., 1996. Biozonation du Crétacé Inférieur non marin des bassins du Gabon et du Congo. Bulletin des Centres de recherches exploration-production Elf-Aquitaine. Memoir (16), 67–82.
Grosdidier, E., 1967. Quelques ostracodes nouveaux de la Série anté–salifère ("Wealdienne") des bassins côtiers du Gabon et du Congo. Rev. Micropaleontol. 10 (2), 107–118.
Guillocheau, F., Chelalou, R., Linol, B., Dauteuil, O., Robin, C., Mvondo, F., Callec, Y., Colin, J.P., 2015. Cenozoic landscape evolution in and around the Congo Basin: constraints from sediments and planation surfaces. In: Geology and Resource Potential of the Congo Basin. Springer, Berlin, Heidelberg, pp. 271–313.
Guiraud, M., Buta-Neto, A., Quesne, D., 2010. Segmentation and differential post-rift uplift at the Angola margin as recorded by the transform-rifted Benguela and oblique-to-orthogonal-rifted Kwanza basins. Mar. Petrol. Geol. 27 (5), 1040–1068.
Guiraud, R., Maurin, J.C., 1991. Le Rifting en Afrique au Cretace inferieur; synthese structurale, mise en evidence de deux etapes dans la genese des bassins, relations avec les ouvertures oceaniques peri-africaines. Bull. Soc. Geol. Fr. 162 (5), 811–823.
Guo, X., Dong, F., Du, Z., 2006. Design and demonstration of creating underground gas storage in a fractured oil depleted carbonate reservoir. In: SPE Russian Oil and Gas Technical Conference and Exhibition. OnePetro.
Harris, N.B., 2000. Toca Carbonate, Congo Basin: response to an evolving rift lake. In: Mello, M.R., Katz, B.J. (Eds.), Petroleum systems of South Atlantic margins: AAPG Memoir 73, pp. 341–360.
Heap, M., Reuschlé, T., Baud, P., Renard, F., Iezzi, G., 2018. The permeability of stylolite-bearing limestone. J. Struct. Geol. 116, 81–93.
Harris, N.B., Sorriaux, P., Toomey, D.F., 1994. Geology of the Lower Cretaceous Viodo Carbonate, Congo Basin: a lacustrine carbonate in the South Atlantic rift. in A. J. Lomando, B. C. Schreiber, and P. M. Harris, eds., Lacustrine reservoirs and depositional systems: SEPM Core Workshop No. 19, 143–172.
Heap, M.J., Baud, P., Reuschlé, T., Meredith, P.G., 2014. Stylolites in limestones: barriers to fluid flow? Geology 42 (1), 51–54.
Hintze, J.L., Nelson, R.D., 1998. Violin plots: a box plot-density trace synergism. Am. Statistician 52 (2), 181–184.
Humphrey, E., Gomez-Rivas, E., Koehn, D., Bons, P.D., Neilson, J., Martín-Martín, J.D., Schoenherr, J., 2019. Stylolite-controlled diagenesis of a mudstone carbonate reservoir: a case study from the Zechstein_2_Carbonate (Central European Basin, NW Germany). Mar. Petrol. Geol. 109, 88–107.
Kadima, E., Delvaux, D., Sebagenzi, S.N., Tack, L., Kabeya, S.M., 2011. Structure and geological history of the Congo Basin: an integrated interpretation of gravity, magnetic and reflection seismic data. Basin Res. 23 (5), 499–527.
Karner, G.D., Gambôa, L.A.P., 2007. Timing and origin of the South Atlantic pre-salt sag basins and their capping evaporites. Geological Society, London, Special Publications 285 (1), 15–35.
Karner, G.D., Driscoll, N.W., Barker, D.H.N., 2003. Syn-rift regional subsidence across the West African continental margin: the role of lower plate ductile extension. Geological Society, London, Special Publications 207 (1), 105–129.
Karner, G.D., Driscoll, N.W., 1999. Tectonic and stratigraphic development of the West African and eastern Brazilian Margins: insights from quantitative basin modelling. Geological Society, London, Special Publications 153 (1), 11–40.
Koehn, D., Koehler, S., Toussaint, R., Ghani, I., Stollhofen, H., 2022. Scaling analysis, correlation length and compaction estimates of natural and simulated stylolites. J. Struct. Geol., 104670
Koehn, D., Rood, M.P., Beaudoin, N., Chung, P., Bons, P.D., Gomez-Rivas, E., 2016. A new stylolite classification scheme to estimate compaction and local permeability variations. Sediment. Geol. 346, 60–71.
Koehn, D., Ebner, M., Renard, F., Toussaint, R., Passchier, C.W., 2012. Modelling of stylolite geometries and stress scaling. Earth Planet Sci. Lett. 341, 104–113.
Koehn, D., Renard, F., Toussaint, R., Passchier, C.W., 2007. Growth of stylolite teeth patterns depending on normal stress and finite compaction. Earth Planet Sci. Lett. 257 (3–4), 582–595.
Labeur, A., Beaudoin, N.E., Lacombe, O., Emmanuel, L., Petracchini, L., Daëron, M., Klimowicz, S., Callot, J.P., 2021. Burial-deformation history of folded rocks unraveled by fracture analysis, stylolite paleopiezometry and vein cement

geochemistry: a case study in the Cingoli Anticline (Umbria-Marche, Northern Apennines). Geosciences 11 (3), 135.
Lacombe, O., Beaudoin, N.E., Hoareau, G., Labeur, A., Pecheyran, C., Callot, J.P., 2021. Dating folding beyond folding, from layer-parallel shortening to fold tightening, using mesostructures: lessons from the Apennines, Pyrenees, and Rocky Mountains. Solid Earth 12 (10), 2145–2157.
Lehner, P., De Ruiter, P.A.C., 1977. Structural history of the atlantic margin of Africa. AAPG (Am. Assoc. Pet. Geol.) Bull. 61 (7), 961–981.
Li, Q., Parrish, R.R., Horstwood, M.S.A., McArthur, J.M., 2014. U–Pb dating of cements in Mesozoic ammonites. Chem. Geol. 376, 76–83.
Macgregor, D.S., 2020. Regional variations in geothermal gradient and heat flow across the African plate. J. Aft. Earth Sci. 171, 103950.
Martin-Martin, J.D., Gomez-Rivas, E., Gomez-Gras, D., Travé, A., Ameneiro, R., Koehn, D., Bons, P.D., 2018. Activation of stylolites as conduits for overpressured fluid flow in dolomitized platform carbonates. Geological Society, London, Special Publications 459 (1), 157–176.
Masson, M.P., 1972. L'exploration pétrolière en Angola. Revue de l'Association Française des Techniciens du Pétrole, p. 212.
Matton, G., Jébrak, M., 2009. The Cretaceous Peri-Atlantic Alkaline Pulse (PAAP): deep mantle plume origin or shallow lithospheric break-up? Tectonophysics 469 (1–4), 1–12.
Mbina Mounguengui, M., Guiraud, M., 2009. Neocomian to early aptian syn-rift evolution of the normal to oblique-rifted north Gabon margin (interior and n'komi basins). Mar. Petrol. Geol. 26 (6), 1000–1017.
McHargue, T.R., 1990. Stratigraphic Development of Proto-South Atlantic Rifting in Cabinda, Angola–A Petroliferous Lake Basin (Chapter 19).
Mohriak, W., Nemčok, M., Enciso, G., 2008. South Atlantic divergent margin evolution: rift-border uplift and salt tectonics in the basins of SE Brazil. Geological Society, London, Special Publications 294 (1), 365–398.
Mohriak, W.U., 2003. Sedimentary basins of the Brazilian continental margin. In: Bizzi, L.A., Schobbenhaus, C., Vidotti, R.M., Goncalves, J.H. (Eds.), Geologia, Tectonica e Recursos Minerais do Brasil. CPRM, Brasilia, pp. 87–165 (Chapter 3).
Moore, C.H., Wade, W.J., 2013. Carbonate Reservoirs: Porosity and Diagenesis in a Sequence Stratigraphic Framework. Newnes, pp. 3–20.
Moore, C.H., 1989. Carbonate Diagenesis and Porosity. Elsevier, pp. 43–71.
Moulin, M., Aslanian, D., Unternehr, P., 2010. A new starting point for the South and equatorial Atlantic Ocean. Earth Sci. Rev. 98 (1–2), 1–37.
Moulin, M., Aslanian, D., Olivet, J.L., Contrucci, I., Matias, L., Géli, L., Klingelhoefer, F., Nouzé, H., Unternehr, P., 2005. Geological constraints on the evolution of the Angolan margin based on reflection and refraction seismic data (ZaïAngo project). Geophys. J. Int. 162 (3), 793–810.
Mussard, J.M., 1996. Les palynomorphes, indicateurs des variations du niveau marin relatif: analyses quantitatives dans l'Albien supérieur de la République du Congo. In: Jardiné, S., de Klasz, I., Debenay, J.-P. (Eds.), Géologie de l'Afrique et de l'Atlantique Sud, Compte Rendus des Colloques de géologie d'Angers, 16–24 juillet 1994, Mémoires du Bulletin des Centres de Recherche et d'Exploration-Production d'Elf, vol. 16, pp. 57–66, 1996.
Park, W.C., Schot, E.H., 1968. Stylolites; their nature and origin. J. Sediment. Res. 38 (1), 175–191.
Perrier, R., Quiblier, J., 1974. Thickness changes in sedimentary layers during compaction history; methods for quantitative evaluation. AAPG Bull. 58 (3), 507–520.
Pletsch, T., Erbacher, J., Holbourn, A.E., Kuhnt, W., Moullade, M., Oboh-Ikuenobede, F. E., Söding, E., Wagner, T., 2001. Cretaceous separation of Africa and south America: the view from the West African margin (ODP leg 159). J. S. Am. Earth Sci. 14 (2), 147–174.
Préat, A., Kolo, K., Prian, J.P., Delpomdor, F., 2010. A peritidal evaporite environment in the neoproterozoic of south Gabon (Schisto-Calcaire Subgroup, nyanga basin). Precambrian Res. 177 (3–4), 253–265.
Railsback, L.B., 1993. Lithologic controls on morphology of pressure-dissolution surfaces (stylolites and dissolution seams) in Paleozoic carbonate rocks from the mideastern United States. J. Sediment. Res. 63 (3), 513–522.
Regnet, J.B., David, C., Robion, P., Menéndez, B., 2019. Microstructures and physical properties in carbonate rocks: a comprehensive review. Mar. Petrol. Geol. 103, 366–376.
Renard, F., Schmittbuhl, J., Gratier, J.P., Meakin, P., Merino, E., 2004. Three-dimensional roughness of stylolites in limestones. J. Geophys. Res. Solid Earth 109 (B3).
Renard, F., Ortoleva, P., Gratier, J.P., 1997. Pressure solution in sandstones: influence of clays and dependence on temperature and stress. Tectonophysics 280 (3–4), 257–266.
Robert, P., Yapaudjian, L., 1990. Early Cretaceous rift sediments of the Gabon-Congo margin: lithology and organic matter; tectonic and paleogeothermal evolution. J. Aft. Earth Sci. 10 (1–2), 319–330.
Roberts, N.M., Lee, J.K., Holdsworth, R.E., Jeans, C., Farrant, A.R., Haslam, R., 2020. Near-surface Palaeocene fluid flow, mineralisation and faulting at Flamborough Head, UK: new field observations and U–Pb calcite dating constraints. Solid Earth 11 (5), 1931–1945.
Roberts, N.M., Rasbury, E.T., Parrish, R.R., Smith, C.J., Horstwood, M.S., Condon, D.J., 2017. A calcite reference material for LA-ICP-MS U-Pb geochronology. G-cubed 18 (7), 2807–2814.
Roedder, E., 1984. Volume 12: fluid inclusions. Rev. Mineral. 12.
Rolland, A., Toussaint, R., Baud, P., Conil, N., Landrein, P., 2014. Morphological analysis of stylolites for paleostress estimation in limestones. Int. J. Rock Mech. Min. Sci. 67, 212–225.
Rolland, A., Toussaint, R., Baud, P., Schmittbuhl, J., Conil, N., Koehn, D., Renard, F., Gratier, J.P., 2012. Modeling the Growth of Stylolites in Sedimentary.
Salem, A.M., Shedid, S.A., 2013. Variation of petrophysical properties due to carbon dioxide (CO2) storage in carbonate reservoirs. J. Petrol. Gas Eng. 4 (4), 91–102.
Schmittbuhl, J., Renard, F., Gratier, J.P., Toussaint, R., 2004. Roughness of stylolites: implications of 3D high resolution topography measurements. Phys. Rev. Lett. 93 (23), 238501.
Schmoker, J.W., Halley, R.B., 1982. Carbonate porosity versus depth: a predictable relation for south Florida. AAPG (Am. Assoc. Pet. Geol.) Bull. 66 (12), 2561–2570, 9.
Schoellkopf, N.B., Patterson, B.A., 2000. AAPG Memoir 73, (Chapter 25): Petroleum Systems of Offshore Cabinda (Angola).
Scholle, P.A., 1977. Chalk diagenesis and its relation to petroleum exploration: oil from chalks, a modern miracle? AAPG (Am. Assoc. Pet. Geol.) Bull. 61 (7), 982–1009.
Schroeder, J.H., 1988. Spatial variations in the porosity development of carbonate sediments and rocks. Texture 18 (1), 181–204.
Séranne, M., Anka, Z., 2005. South Atlantic continental margins of Africa: a comparison of the tectonic vs climate interplay on the evolution of equatorial west Africa and SW Africa margins. J. Afr. Earth Sci. 43 (1–3), 283–300.
Stockdale, P.B., 1943. Stylolites, primary or secondary? J. Sediment. Res. 13 (1), 3–12.
Stockdale, P.B., 1936. Rare stylolites. Am. J. Sci. 5 (188), 129–133.
Stockdale, P.B., 1926. The stratigraphic significance of solution in rocks. J. Geol. 34 (5), 399–414.
Stockdale, P.B., 1922. Stylolites: their nature and origin. Indiana Univ. Stud. 9 (55), 1–97.
Szatmari, P., Milani, E.J., 2016. Tectonic control of the oil-rich large igneous-carbonate-salt province of the South Atlantic rift. Mar. Petrol. Geol. 77, 567–596.
Teisserenc, P., Villemin, J., 1989. Sedimentary basin of Gabon–geology and oil systems. In: Edwards, J.D., Santogrossi, P.A. (Eds.), Divergent/passive Margins Basins, vol. 48. AAPG, pp. 117–199, 1990.
Torsvik, T.H., Rousse, S., Labails, C., Smethurst, M.A., 2009. A new scheme for the opening of the South Atlantic Ocean and the dissection of an Aptian salt basin. Geophys. J. Int. 177 (3), 1315–1333.
Toussaint, R., Aharonov, E., Koehn, D., Gratier, J.P., Ebner, M., Baud, P., Rolland, A., Renard, F., 2018. Stylolites: a review. J. Struct. Geol. 114, 163–195.
Tucker, M., 2001. Carbonate reservoirs: porosity evolution and diagenesis in sequence stratigraphic framework-by clyde Moore, published by elsevier, amsterdam, developments in sedimentology volume 55, 2001, 444. Org. Geochem. 11 (32), 1373.
Tucker, M.E., Wright, V.P., 1990. Diagenetic processes, products and environments. Carbonate sedimentology 314, 364.
Uncini, G., Brandao, M., Giovannelli, A., 1998. In: ABGP/AAPG International Conference and Exhibition November 8-11, 1998. Neocomian-Upper Aptian Pre-Salt sequence of southern Kwanza Basin: a regional view, Rio de Janeiro, Brazil.
Vandeginste, V., John, C.M., 2013. Diagenetic implications of stylolitization in pelagic carbonates, Canterbury Basin, offshore New Zealand. J. Sediment. Res. 83, 226–240.
Vernet, R., Assoua-Wande, C., Massamba, L., Sorriaux, P., 1996. Paléogéographie du Crétacé (Albien-Maastrichtien) du bassin côtier congolais. Bull. Cent. Rech. Explor.-Prod. Elf-Aquitaine - Mem. (16), 39–55.
Wang, L., He, Y., Peng, X., Deng, H., Liu, Y., Xu, W., 2020. Pore structure characteristics of an ultradeep carbonate gas reservoir and their effects on gas storage and percolation capacities in the Deng IV member, Gaoshiti-Moxi Area, Sichuan Basin, SW China. Mar. Petrol. Geol. 111, 44–65.
Woodhead, J.D., Hergt, J.M., 2001. Strontium, neodymium and lead isotope analyses of NIST glass certified reference materials: srm 610, 612, 614. Geostand. Newsl. 25 (2–3), 261–266.
Wright, K., Cygan, R.T., Slater, B., 2001. Structure of the (1014) surfaces of calcite, dolomite and magnesite under wet and dry conditions. Phys. Chem. Chem. Phys. 3 (5), 839–844.
Xu, J., Deng, Y., Fu, M., Guo, R., Chen, P., Duan, G., Ma, R., 2022. The nonuniform distribution of stylolite in bioclastic limestones and its influence on reservoir petrophysical properties—a case study of the mishrif formation from the ah oilfield. Energies 15 (9), 3032.

# Chapitre III : Reconstitution des paléocontraintes dans un réservoir supra-salifère : le cas de la formation post-rift Sendji

Ce chapitre se présente sous la forme d'un article publié dans Marine and Petroleum Geology début 2023. Le travail a été réalisé dans le cadre d'un stage de Master 2 (Anies Zeboudj) que j'ai co-encadré activement et dont l'objectif était de mener une étude paléopiézométrique couplée macles de la calcite – inversion de la rugosité des stylolites sur les carbonates de la formation Sendji. Mon travail d'encadrement a consisté à la préparation en amont des échantillons (choix de la carotte adaptée, préparation des lames minces et des slabs pour les stylolites), la formation d'Aniès à la technique d'acquisition et de traitement des données de macles à Paris et la participation à la réflexion sur les résultats de l'inversion et leurs interprétations. J'ai effectué par la suite après la fin du stage 1 mois supplémentaire de mesures de macles pour augmenter le nombre d'échantillons de macles acquis par Aniès au cours de son stage qui passent de 6 à 14 échantillons (Well-3).

Ce chapitre résume les principaux résultats obtenus sur l'histoire d'enfouissement et des paléocontraintes dans la formation albienne Sendji située dans le bassin du Bas Congo (marge ouest africaine). La paléopiézométrie basée sur l'inversion de la rugosité des stylolites et l'inversion des macles de la calcite a été combinée à l'analyse de la fracturation, à la datation géochronologie U-Pb du ciment calcitique et à la modélisation de l'enfouissement pour reconstruire les orientations et les grandeurs des contraintes horizontales et verticales ayant affecté la formation Sendji au cours du temps. L'objectif était de caractériser l'évolution de l'enfouissement et des paléocontraintes des réservoirs carbonatés profondément enfouis sur la marge proximale offshore. En plus de fournir des informations importantes sur les régimes de paléocontraintes à l'échelle du réservoir, cette étude alimentera également le débat sur la façon dont les contraintes lithosphériques tectoniques et gravitaires engendrées en champ lointains sont transférées depuis les limites de plaques actives ont pu jouer un rôle dans l'évolution de la marge passive ouest-africaine.

Marine and Petroleum Geology 152 (2023) 106219

Contents lists available at ScienceDirect

Marine and Petroleum Geology

journal homepage: www.elsevier.com/locate/marpetgeo

# Depicting past stress history at passive margins: A combination of calcite twinning and stylolite roughness paleopiezometry in supra-salt Sendji deep carbonates, Lower Congo Basin, west Africa

Aniès Zeboudj [a,b,*], Boubacar Bah [a], Olivier Lacombe [a], Nicolas E. Beaudoin [b], Claude Gout [c,b], Nicolas Godeau [d], Jean-Pierre Girard [c], Pierre Deschamps [d]

[a] Institut des Sciences de La Terre de Paris (ISTeP), Sorbonne Université, CNRS-INSU, 75005, Paris, France
[b] Universite de Pau et des Pays de L'Adour, E2S UPPA, TotalEnergies, CNRS, LFCR, Pau, France
[c] TotalEnergies, Centre Scientifique et Technique Jean Féger-CSTJF, Pau, France
[d] Aix Marseille Univ, CNRS, IRD, INRAE, CEREGE, Aix-en-Provence, France

ARTICLE INFO

Keywords:
Stress
Paleopiezometry
Calcite twins
Stylolites
Passive margin
Salt

ABSTRACT

The paleostress history and associated deformation mechanisms affecting passive margins are seldom studied, as access to offshore parts is rather limited. We analyze an offshore wellbore core of the Albian, post-rift carbonates of the Sendji Fm which directly overlies the salt of the Aptian Loeme Fm in the Lower Congo Basin. Paleopiezometry based on stylolite roughness inversion (SRIT) and calcite twin inversion (CSIT) was combined with fracture analysis, U–Pb geochronology of calcite cement and burial modeling to unravel the orientations and magnitudes of horizontal and vertical stresses affecting the Sendji Fm over time, with a focus on the impact of salt tectonics on stress records. The results of SRIT on bedding-parallel stylolites constrain the range of depths over which the Sendji Fm strata deformed under a vertical principal stress σ1 to 650–2800 m (median ~1300 m). Once projected onto the burial model derived from TemisFlow ™ software, the range of depths converts to a period of pressure solution activity, from 101 to 15 Ma. Calcite twin measurements within the early diagenetic cement (U–Pb age = 101 ± 1 Ma) reveal three main types of stress regimes: (1) extensional stress regimes with σ3 trending ~ N–S and ~E-W associated with local, thin-skinned salt tectonics (101–80 Ma), (2) strike-slip stress regimes with σ1 trending ~ NW-SE to NNE-SSW and a compressional stress regime with σ1 trending NNW-SSE, reflecting possible intraplate stress transfer from the distant Africa-Eurasia plate boundary (67–60 Ma); (3) a strike-slip and a compressional stress regime with σ1 trending E-W likely related to the mid-Atlantic ridge push possibly combined with effects of variations in elevation and density of the lithosphere and sedimentary flexural loading (15 Ma to present). The paleostress sequence suggests that the sedimentary cover was decoupled from the crust during salt tectonics and then recoupled from the late Cretaceous onwards.

## 1. Introduction

Divergent passive margins are diverse in their geometry and structural evolution owing to their segmentation, geodynamic history, and pre-rift inheritance (see review in Sapin et al., 2021). As a response to continental breakup, they are formed through a process of first rifting and then drifting. Extensional stress prevails during the rifting stage and originates from tectonic forces linked to plate motion, frictional forces exerted by the convecting mantle on the base of the lithosphere (e.g., Ziegler et al., 1995), asthenospheric flow, basal drag and, to a lesser extent, from stresses developing in the lithosphere above mantle plumes (Bott, 1993).

In contrast, the present-day stress field at passive margins is often dominated by a reverse or strike-slip stress regime with maximum horizontal principal stress $S_H$ roughly perpendicular to both the trend of the margin and the oceanic ridge (Zoback, 1992; Heidbach et al., 2016). This supports the idea that the ridge push may be a possibly significant source of the present-day stress at passive margins (e.g., Pascal and Cloetingh, 2009). However, the contribution of other gravitational forces should not be neglected. These forces include flexural loading of

* Corresponding author.
E-mail address: anies.zeboudj@sorbonne-universite.fr (A. Zeboudj).

https://doi.org/10.1016/j.marpetgeo.2023.106219
Received 1 August 2022; Received in revised form 8 March 2023; Accepted 9 March 2023
Available online 21 March 2023

the lithosphere in response to sedimentation or differences in elevation and associated gravitational potential energy differences between the continent and the margin (e.g., Pascal and Cloetingh, 2009), as well as lateral density differences within the lithosphere (e.g., Artyushkov, 1973; Zhou and Sandiford, 1992). Finally, when considering the long-lasting post-rift history of passive margins, far-field tectonic stress transfer from distant active plate boundaries may likely have, at least transiently, also played some role (Ziegler et al., 1995; Withjack et al., 1995; Vågnes et al., 1998).

In the framework of oil exploration, numerous deep supra-salt carbonate reservoirs have been investigated so far along the Atlantic margins (Brice et al., 1982; Marton et al., 2000; Brownfield and Charpentier, 2006). To date, however, our knowledge on the tectonic and stress evolution of these reservoirs remains limited, especially in poorly accessible offshore domains where well-established paleopiezometry techniques such as calcite twinning paleopiezometry have, to the best of our knowledge, never been applied. The Congolese segment of the Atlantic passive margin of SW Africa exhibits a post-rift salt sequence deposited during the mid-Cretaceous marine transgression associated with slow subsidence (Moulin, 2003), which triggered gravity-induced thin-skinned extensional salt tectonics and the development of associated structures (Duval et al., 1992, Gaullier et al., 1993; Penge et al., 1999, Rowan et al., 2022), and therefore significantly increased the structural complexity.

In the proximal margin sequences of the lower Congo basin, the Cretaceous Sendji carbonate formation (Wonham et al., 2010) presumably recorded the tectonic complexity that can be expected for a supra-salt reservoir. However, the paleoburial and paleostress evolution of this formation remains unconstrained despite being of prime importance for a reliable prediction of its reservoir properties.

In this contribution, we characterize the paleoburial and paleostress evolution of the post-rift, supra-salt Sendji deep carbonate reservoir using a multi-proxy approach. Our method combines calcite twinning and sedimentary stylolite roughness paleopiezometry with fracture analysis, geomechanical tests, U–Pb dating of host rock calcite cement, and burial modeling. We applied this approach to a core recovered from a deep well drilled by Totalenergies in the lower Congo basin. This unique opportunity to better constrain the local paleoburial and paleostress history of a deep offshore reservoir enables us to tackle the question of the origin of stresses that affected the west African passive margin during its long-lasting post-rift geological evolution. Our dataset is also used to illustrate the impact of halokinesis on the stress distribution in a supra-salt reservoir. Beyond the reservoir scale, this study also provides new constraints on the way shallow and deep gravitational and tectonic forces interplay and control the evolution of divergent passive margins.

## 2. Geodynamic and geological settings

### 2.1. Geodynamic evolution of the South Atlantic Ocean

The opening history of the South Atlantic Ocean is commonly divided into four major phases: the pre-rift, syn-rift, transitional and post-rift (or drift) phases (Cainelli and Mohriak, 1999; Beglinger et al., 2012). In the Gondwana supercontinent, from the Late Palaeozoic to the Jurassic, the pre-rift phase was characterized by the development of intracratonic basins and regional sag basins (Beglinger et al., 2012). During this phase, southwestern Gondwanaland (currently South Africa) was affected by the subduction of the palaeo-Pacific plate beneath the supercontinent (Lock, 1980; Catuneanu et al., 2005). This compressional regime led to the formation of the PanGondwanian fold-and-thrust belt, now preserved as the Cape Fold Belt in South Africa (Catuneanu et al., 2005). From the Late Jurassic to the Early Cretaceous, the divergent movement between the future African (Nubian) and South American plates generated the breakup of Western Gondwana. The counter-clockwise rotation of Africa away from South America led to the progressive northward opening of the South Atlantic (Heine et al., 2013). The transition phase, starting at the Aptian and ending by the Early Albian, represents a quiescent period when the stretching of the continental crust and related basement-involved fault activity stopped (Unternehr et al., 2010), starting with an erosional peneplanation period (Lehner and De Ruiter, 1977). The beginning of the post-rift phase is linked to the onset of the spreading floor between the future African and South-American plates being dated ~112 Ma between latitudes 10°S-27°S (Angola, Congo, and Gabon areas) (Torsvik et al., 2009). This period was marked by breakup unconformity (Beglinger et al., 2012). From the Early Albian to the present day, the post-rift phase was characterized by the thermal subsidence of the oceanic lithosphere and the progressive drift apart of the African and South American continents from ~112 to 110 Ma onwards (Moulin et al., 2010). Noticeably, the Africa motion with respect to Eurasia changed from ENE-directed to NNE-directed during the Campanian then to NNW during the Oligocene (Guiraud and Bosworth, 1997; Rosenbaum et al., 2002; Jolivet et al., 2016).

### 2.2. Paleostress and contemporary stress orientations in western Africa

As a consequence of the above described geodynamic evolution, Western Africa underwent a complex tectonic and paleostress history. Stress orientations reported hereafter from the literature refer to the current African plate position.

During the pre-rift phase (280-215 Ma), the southwestern subduction of Gondwana induced an NW-SE compressional stress related to the Gondwanide orogeny (Johnston, 2000). This was inferred in the Paleozoic Inkisi Group, South West Congo (Nkodia et al., 2020; Tack et al., 2008; Kadima et al., 2011). From the Late Jurassic to the Early Cretaceous, i.e. during the syn-rift phase, the West African margin experienced a NE-SW oriented extension related to the opening of the Atlantic Ocean (Rabinowitz and LaBrecque, 1979; Nürnberg and Müller, 1991 and Salomon et al., 2015), also highlighted by Viola et al. (2012) as an ENE-WSW extension.

During the post-rift phase, a major tectonic uplift event took place from Albian to Turonian times (115-90 Ma) on the western coast of South Africa (Kounov et al., 2009). This uplift induced erosional denudation of up to 2.5–3 km and has been tentatively related to an E-W-oriented extension, recorded on the western coast of South Africa (Viola et al., 2012). Viola et al. (2012) also recognized two subsequent compressional events, with $\sigma_1$ oriented NW-SE and NNE-SSW, respectively, as well as a NE-SW oriented extension in between.

A strike-slip stress regime associated with NW-SE-oriented compression was recognized in Namibia by Salomon et al. (2015) and in continental Congo by Nkodia et al. (2020). In the absence of stratigraphic constraints, these stress regimes could not be precisely dated but were tentatively correlated, based on consistent stress orientations, to the compressional and extensional tectonic events described in Central and North Africa by Guiraud and Bosworth (1997), namely the late Santonian N–S to NW-SE compression, the mid-Campanian-Maastrichtian NE-SW extension and the late Maastrichtian-early Paleocene N–S to NW-SE compression. The authors related these tectonic events to the shift in opening directions of the Atlantic oceanic spreading centers and the subsequent counterclockwise rotational northward drift of Africa–Arabia into Eurasia during the so-called "End Cretaceous event" (Guiraud and Bosworth, 1997; Guiraud et al., 2005).

From the Miocene onward, Nkodia et al. (2020) reported a consistent ENE-WSW-oriented compression in onshore Congo using inversion of fault-slip data from the Paleozoic Inkisi Group. Although this compression could not be dated, the authors speculated that this ~ E-W compression started in the Miocene and would possibly be related to some degree to the Atlantic ridge push associated with variations of the lithospheric structure and gravitational energy. The overall E-W compressional stress field still prevails in the present-day as established

in the World Stress Map Project (Heidbach et al., 2016) and by inversion of earthquake focal mechanisms in Congo (Delvaux and Barth, 2010).

### 2.3. Geology of the offshore lower Congo basin

Amid the several rift basins located in the West African passive margin (Fig. 1A), the Lower Congo Basin covers approximately 115,000 $km^2$ distributed between Congo and Angola. It is bounded to the north by the South Gabon basin and to the south by the Kwanza basin. The Lower Congo basin is characterized by a succession of stratigraphic mega-sequences as described hereinafter. For the following, we gather under the term 'basement' both the crystalline part of the Congo craton and the overlying Precambrian pre-rift sediments (Delpomdor et al., 2008; Mbina Mounguengui and Guiraud, 2009), so the Cretaceous-Cenozoic sedimentary series rests directly on the so-called Precambrian 'basement' (Fig. 1B and C). The younger pre-rift sedimentary sequences are missing in the basin (Brownfield and Charpentier, 2006).

The syn-rift megasequence is characterized by two main continental lithofacies: lacustrine black shales and deltaic/fluvial sediments (Baudouy and LeGorjus, 1991; Harris, 2000). The syn-rift sedimentary succession (Fig. 1B) begins with the fluvial and alluvial deposits of the Vandji-Lucula Fm (Bracken, 1994), followed by the lacustrine shale of Sialivakou Fm until about 141 Ma, and by the Djeno sandstone until 130 Ma for a total thickness between 200 and 600 m. The Pointe Noire and Toca formations correspond to lacustrine deposits (clays and limestones respectively) that were deposited until 125 Ma (Chaboureau et al., 2013). The syn-rift phase ends with the deposition until 118 Ma of the Pointe Indienne Fm./Tchibola Fm made of at least ~270 m thick lacustrine siliciclastic shales. The overall pre-salt sequence - including pre-rift and syn-rift sequences - can reach 5000 m in thickness near Angola (Lehner and De Ruiter, 1977). The transition phase is associated with a megasequence starting with a peneplanation phase followed by ~60 m thick Aptian sandstones of the Chela Fm (Lehner and De Ruiter, 1977) and ends with the massive Aptian evaporite Loeme Fm comprising interbedded anhydrite, halite, and potash salts. The Aptian salt basin spreads along 2000 km from southern Angola to the Cameroon shores and extends up to 250 km offshore. The thickness is very variable, estimated at ~300 m at the basin scale (Ala and Selley, 1997) but can reach locally 1000 m (Lehner and De Ruiter, 1977; Brice et al., 1982). This Aptian salt episode marks the transition between the rifting phase and the subsequent thermal subsidence due to lithosphere cooling following the breakup and oceanic accretion (Brognon and Verrier, 1966; Cainelli and Mohriak, 1999).

The Loeme Fm is overlain by the marine post-rift megasequence, characterized by three supersequences: (1) the restricted marine supersequence made of high energy, shallow-water carbonates, tidal sandstone deposits, and silts ( Baudouy and LeGorjus, 1991) followed by shallow and deep marine clastic deposition (Séranne and Anka, 2005; Anka et al., 2010) topped with organic-rich black shales. (2) the open marine supersequence comprises sandstones, shelly limestones, and siltstone, characteristic of the transgression phase during oceanic deposition. (3) the deltaic supersequence is marked by a major submarine erosion of the ramp (McGinnis et al., 1993; Séranne and Anka, 2005).

In summary, the post-rift sedimentary succession (Fig. 1B) started with the ~1000 m thick Sendji Fm limestone, dolomite, sandstone and silts that were deposited between 112 and 99.6 Ma (Fig. 2). This Albian layer was overlain by Cenomanian deposits with an age up to 93.5 Ma, consisting either of the Tchala sandstones that were deposited in a continental to marginal litoral environment in the eastern part of the basin, or of the ~600 m thick Likouala siltstone that was deposited in a marginal littoral environment in the rest of the basin. These Cenomanian formations were covered by the ~200 m thick Madingo marls, with an age up to 34 Ma. The megasequence ended with the ~1800 m thick sandstone and shales of the Paloukou Fm.

### 2.4. The N'Kossa oil field and the Sendji Formation

#### 2.4.1. Structure

The N'Kossa field is located in the Lower Congo Basin, 60 km off the Congolese coast (Fig. 1A, C). The general structure of the N'Kossa field originated from salt tectonics, defining a major raft structure bounded by compensation normal faults and by long-lasting gravity-related listric normal faults on the western side. Three main stages of structural evolution can be described: (1) the initiation of salt diapirs during the Early Albian, (2) the formation of the local raft structures bounded in the East by N–S to NNW-SSE striking normal faults (Fig. 3) (Rouby et al., 2002; Wonham et al., 2010) and (3) the development of N–S striking listric normal faults (Fig. 3) in response to local E-W extension triggered by the collapse and lateral creep of the underlying salt. The geometries of the post-rift, post-salt formations in the area of the N'Kossa raft are shown on the interpreted seismic profile in Fig. 4 (TotalEnergies internal report). The area of interest comprises a raft structure bounded by two listric faults separating the Albian limestone deposits from the Cenomanian deposits (Fig. 4), with the remaining salt in the footwall of the bounding faults (Rouby et al., 2002). Gravity-related extensional salt tectonics were initiated during Late Albian and intensified due to the increased sediment loading (TotalEnergies internal report).

The salt-related raft tectonics that took place in the N'Kossa field area is widespread recognized along the South Atlantic margin (Duval et al., 1992). Fig. 3 illustrates the structural setting of the top Lower Sendji Fm. Large, multi-kilometer-long, broadly N–S striking normal faults affect the lower Sendji Fm and delineate the Nkossa field (Fig. 3). Smaller NW-SE-oriented normal faults link these large listric normal faults. This complex fault pattern results from the translation of a raft over a non-planar substrate (in this case, the Loeme Fm).

#### 2.4.2. Stratigraphic succession of the Sendji Formation

The Albian Sendji Fm corresponds to the first stage of the post-salt restricted marine supersequence, and can be divided into two layers (TotalEnergies internal report, Wonham et al., 2010): (1) the Lower Sendji (Early Albian), which corresponds to the reservoir level of the N'Kossa field, and (2) the Upper Sendji (Late Albian). The Lower Sendji comprises shelf and litoral deposits mainly composed of limestones and dolomites, whereas dominant lithologies in the Upper Sendji are sandstones and shales (Wonham et al., 2010). In the N'Kossa field area, four sequences can be recognized in the drill core (Fig. 2) from a reference well located at the top of the N'Kossa raft. At the top of the N'Kossa raft, the first sequence (S1) is characterized by 108 m of dolomite and anhydrite confined deposits. The second sequence (S2), is made up of 114 m of more detrital deposits with a dolomitic front. The third sequence (S3) is a 68 m thick succession marked by flooding, characterized by a strong lithological variation of sandstone, dolomitic sandstone, limestone, dolomite alternation, and very fine clay levels. This sequence corresponds to the hydrocarbon reservoir section of the Sendji Fm. Opening and deepening of the depositional environment are characterized by the last sequence (S4), a sequence of alternating limestones, sandstones, and minor silty clays, forming the reservoir seal.

From base to top, the depositional environments evolved as follows: an upper infralittoral environment marked by the presence of arenaceous foraminifera in a predominantly wackestone series, a supralittoral stage characterized by a siltic-dolomitic series with anhydrite that becomes more dolomitic upward the core, a lower infralittoral to an upper infralittoral environment characterized by a wackestone series followed by an upper circalittoral stage. The depositional environment analyses indicate a bathymetric deepening with time during Albian. All the analyzed facies indicate an internal platform deposit environment (TotalEnergies internal report). Gravelly facies indicate an upper subtidal environment with low porosity (0–5%), while the oolitic facies indicate a lower subtidal environment with greater porosity (5–10%).

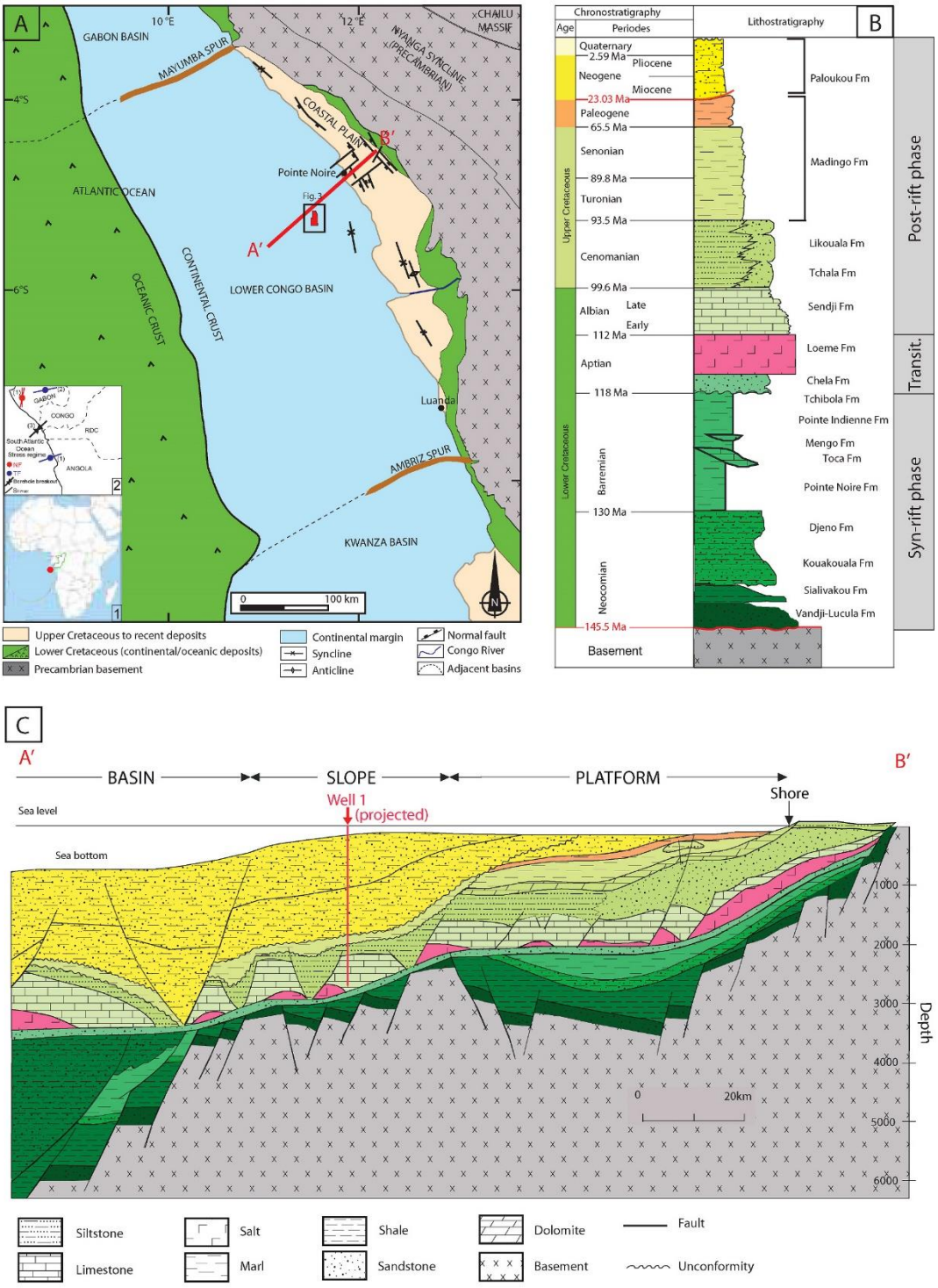


Fig. 1. A. Simplified geological map of the Lower Congo Basin area, offshore Republic of Congo. B. Stratigraphic column of the Lower Congo Basin (modified from TotalEnergies internal report). C. Cross section of the Lower Congo Basin with the horizontal projection of well 1 (modified from Brownfield and Charpentier, 2006).

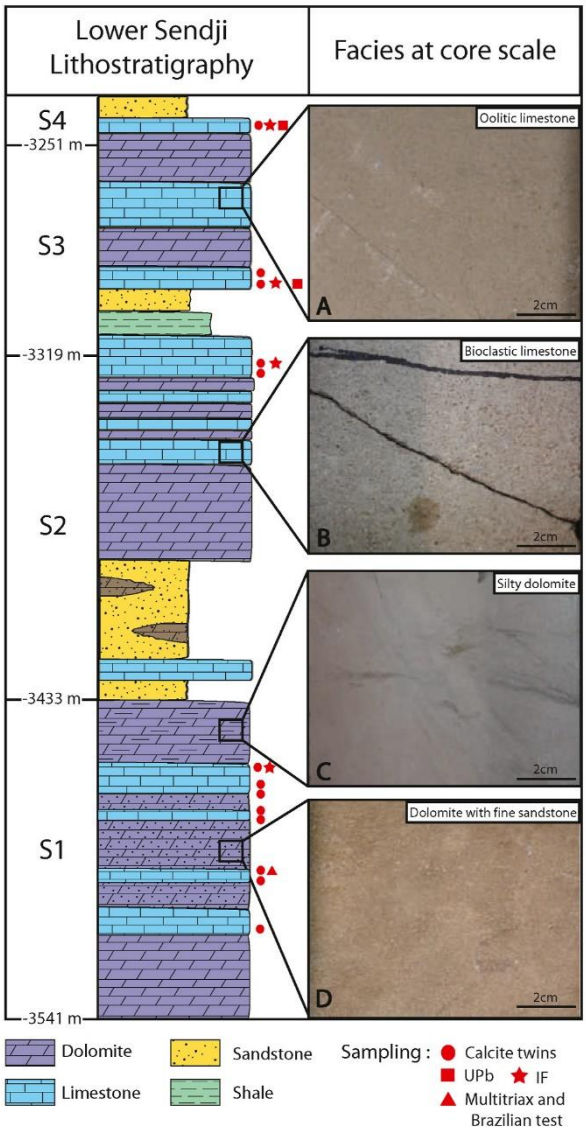


Fig. 2. Lithostratigraphy of the Lower Sendji formation with successive sequences and the associated facies from discontinuous core sections analyses completed by the TotalEnergies database. A. Oolitic limestone. B. Bioclastic limestone. C. Silty dolomite. D. Dolomite with fine sandstone.

## 3. Material

This study is based on the analysis of a continuous core of 306 m (−3235 to −3541 m BSW) of the Lower Sendji Fm recovered from Well 1 in the N'Kossa raft (Fig. 3). The core is slightly deviated with respect to the vertical axis, up to 5° in places. The orientation of the drill core was determined after drilling by comparing the FMS (Formation MicroScanner) imagery recorded on the borehole with the core images. It was thus possible to find the orientation of fractures or bedding of the non-oriented core by comparing the same fractures and bedding oriented by FMS present in the well.

The cored interval of the Sendji Fm represents the reservoir part and internal platform deposits (dolomite, sandstone, and limestone). The main facies in the core are shown in Fig. 2, such as oolitic limestone, bioclastic limestone, silty dolomite, and dolomite with fine sandstone. Limestone levels are particularly rich in stylolites and display sparry crystals suitable for calcite twin analysis. The investigation, therefore, focused on the gravelly and bioclastic-oolitic limestone facies. It is noteworthy that Well 1 is located close to the intersection between two normal faults above the top Sendji Fm (Fig. 3).

## 4. Methods

We adopted an original combination of methods to constrain the burial and paleostress history of the Sendji Fm. First, petrographic studies and U–Pb geochronology were used to identify the nature and to constrain the absolute age of the main calcite cement, respectively. Fluid inclusion microthermometry applied on these cements reveals the minimum temperature of the fluid from which it precipitated. Second, the inversion of sedimentary stylolite roughness combined with the elastic parameters of the carbonates derived from mechanical tests constrains the depth of active, compaction-related pressure solution under a vertical σ1. Third, the inversion of calcite mechanical twins from the main cement is used to determine the orientations and the magnitudes of the stresses that were recorded by the Sendji Fm since its deposition. Then the time periods of prevailing either compaction-dominated or salt tectonics-related vertical σ1 on the one hand, and of prevailing tectonic-related horizontal σ1 on the other hand, can be determined by combining the above stress results with time-burial modeling. Results of calcite twin inversion are finally further combined with the rock strength envelope derived from the mechanical tests to interpret and predict fracture occurrence in the Sendji Fm.

### 4.1. Petrographic analyses of calcite cement

To establish the paragenesis and diagenetic sequences of the Well 1 samples, a petro-diagenetic study was carried out on 39 thin sections. Optical petrography was conducted using a Zeiss Axiophot polarizing microscope equipped with a Nikon Digital sight DS_U2/Ds_Fi1 camera at the CSTJF TotalEnergies in Pau. The petrographic phases were identified in LPNA (unanalyzed polarized light) and LPA (analyzed polarized light), then the diagenetic sequence was investigated using cathodoluminescence on a NewTec scientific Cathodyne model CATHOD-SP01 equipped with a cold cathode and an IDS camera UI-3850CP-C-GL. These analyses were performed with replicable parameters, 90 mTorr vacuum, 12–15 kV voltage, and 200 μA electron beam.

### 4.2. U–Pb geochronology of calcite cement

The absolute dating of the main calcite cement was carried out at Centre Européen de Recherche et d'Enseignement des Géosciences de l'Environnement (CEREGE), Aix-en-Provence, France. The equipment consists of an ArF 193 nm excimer laser (ESI, Elemental Scientific Industries) coupled to an HR-ICP-MS (High Resolution Inductively Coupled Plasma Mass Spectrometry) with magnetic sector (Element XR, Thermo fisher). Measurements were performed following a methodology analogous to Godeau et al. (2018). Analyses were carried out directly on polished 100 μm thick sections. Samples were first scanned with a resolution of 3200 dpi to pre-select the areas of interest, i.e. consisting of calcite cement from the same diagenetic phase. The samples were first screened to assess the quality of the U–Pb signal (U and Pb intensity, variability of the U–Pb ratio) and to identify the best spots to perform the analysis (Roberts et al., 2020). The ESI laser beam was configured as follows: 150 μm spot-size, 193 μm wavelength, and 10 Hz firing rate. The energy of the laser was adapted to carbonates, i.e. with a density of the photon emitted per surface density of 1–1.3 J/cm$^2$. To obtain good statistics and a robust age, we usually performed ~30 spots per mineral phase to be dated. During analysis, the ablation speed was of the order of 1–1.5 μm/s under standard conditions, following a pre-ablation phase of a few seconds to clean the sample surface.

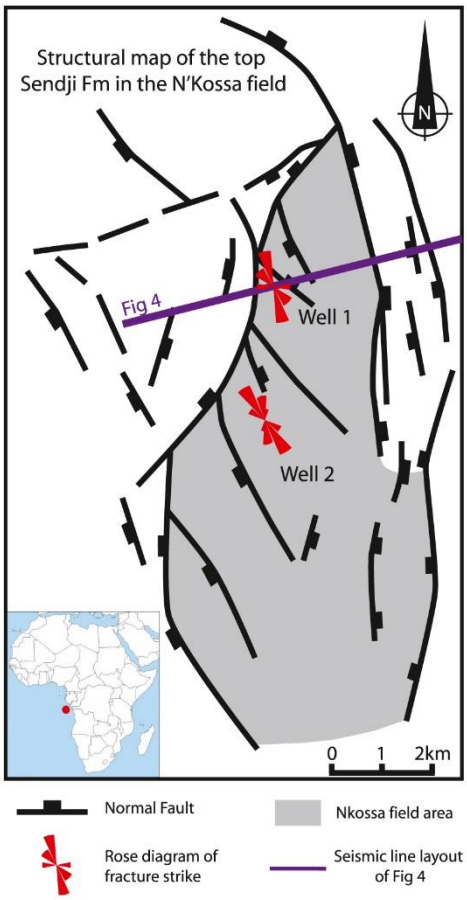


Fig. 3. Structural map of the top of the Sendji Fm in the N'kossa field (modified from TotalEnergies internal report).

Correction of the instrumental bias was done using the WC-1 natural calcite standard for inter-elemental fractionation (reference age = 254.4 ± 6.4 Ma; Roberts et al., 2020). The U–Pb isochron age was established from Tera-Wasserburg plots constructed using the Isotplot 4.15 add-on (Excel ™ ).

### 4.3. Fluid inclusion microthermometry

Four double-polished 150 µm thick wafers, distributed along the drill core, were used for microthermometric analysis of fluid inclusions. Fluid inclusions are small cavities or pores, typically ranging from micrometer to millimeter size, filled with fluid, ubiquitously found in minerals, which can provide information on the nature and the trapping temperature of the mineralizing fluid (Goldstein and Reynolds, 1994). The micro thermometric study was performed by H-Expertise services, Nancy France. The selection of aqueous primary fluid inclusions was based on a petrographic study based on optical observations by polarized light and epi-UV fluorescence. The epi-UV fluorescence observations were conducted using a Zeiss Axiolmager.A1m microscope with an excitation filter centered at 365 ± 5 nm and an emission filter long pass around 400 nm.

Samples were first heated to reach their homogenization temperature, i.e. $T_h$, then they were cooled down to ice freezing and heated up again to reach the final melting temperature of ice, i.e. $T_{m(ice)}$. These phase transitions were measured at temperatures between −170 °C and 400 °C using a LINKAM MDS 600 heating-freezing stage equipped with a Sony Exwave HAD3 color video camera mounted on an Olympus BX 51 microscope at GeoRessources laboratory (Nancy, France). The microthermometric stage was thermally calibrated using $CO_2$ synthetic fluid inclusions standards for $T_{m(CO2)}$, $H_2O$ synthetic fluid inclusions standards for the final melting temperature of ice, $T_{m(ice)}$, and cross-calibrated natural alpine fluid inclusions (Georessources standard) for the bulk homogenization temperature $T_h$. The accuracy of measurements is estimated at ±0.2 °C for $T_{m(ice)}$ (heating at 0.5–1 °C/min) and ±0.5 °C for $T_h$ (heating at 1–5 °C/min).

### 4.4. Rock mechanical properties

Mechanical properties of the limestone levels of the Sendji Fm were characterized by multitriax tests and Brazilian tests. The multitriax, or

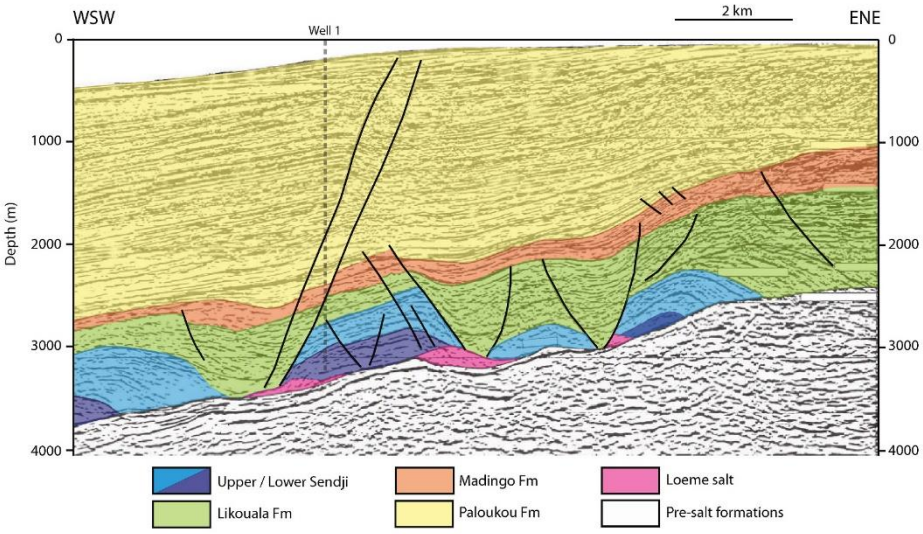


Fig. 4. Interpreted seismic profile of the N'kossa field area (modified from TotalEnergies internal report).

multi-stage test, consists of a triaxial revolution test during which confining pressure is fixed and the sample is brought close to failure. Soon before failure occurs, the confining pressure is increased so it precludes failure. The cycle is repeated 3–4 times, which enables to simulate a maximum of triaxial tests with a single sample. The tests were carried out at the Geomechanical Laboratory located at the Total-Energies CSTJF (Pau, France). Two plugs (38 mm diameter x76 mm height) were selected to be representative of stylolite-bearing lithologies, i. e limestone then were cut along the vertical axis of the core. Each plug was loaded at 10, 30, and 50 MPa of confining pressure. For each confining pressure value, an axial stress ramp was applied with a displacement rate of 0.01 mm/min until the yield point was reached, then the deviatoric stress was unloaded with the same displacement rate at 0.01 mm/min to finalize the cycle.

The values of the maximum principal stress (σ1) at 10 MPa and 30 MPa have been used to build the Mohr circles. For that, the yield stress, also known as the applied stress at which irreversible plastic deformation is first observed and the end of the elastic behavior, was multiplied by the ratio between the yield stress at 50 MPa and the maximum stress at 50 MPa. Following the Mohr-Coulomb criterion, Mohr circles associated with each loading enabled us to build the failure envelope that was approximated by a straight line in the domain of positive normal stress, characterized by the following equation:

$$|\tau| = S_0 + \mu\sigma_n$$

with the shear stress component τ, the cohesion of the material $S_0$, the coefficient of internal friction, μ, and the normal stress component σn. Deformation was measured by axial and radial gauges, and the elastic parameters (Young modulus, Poisson ratio) were determined along with the friction angle, cohesion, and maximum strength of the rock sample.

The diametral compression (or Brazilian) tests were performed to evaluate the indirect tensile strength of the rock. A thin disc sample was placed in a specially designed cell consisting of two steel parts assembled with the sample in the middle. The load was continuously increased at a constant rate until the failure of the sample occurs.

### 4.5. Sedimentary stylolite analysis

#### 4.5.1. Morphology and distribution of stylolites

Stylolites are localized rough dissolution surfaces common in carbonate formations. Stylolites form as a result of pressure-solution related to either vertical, compaction-related stress (sedimentary stylolites) or tectonic stress (tectonic stylolites). Stylolites affect the petrophysics of the reservoir by reducing porosity (Raynaud and Carrio-Schaffhauser, 1992; Ehrenberg, 2006) and permeability when insoluble material such as clays plays a sealing role (e.g. Koehn et al., 2016), albeit stylolites can also be localized conduits for fluids (Martín-Martín et al., 2018; Koehn et al., 2016; Gomez-Rivas et al., 2022). Stylolites can be classified into four types of morphologies (Koehn et al., 2016, Fig. 5): (1) class 1 (rectangular layer) is characterized by a rectangular baseline with peaks on the rectangle flat top. (2) Class 2 (Seismogram pinning) is characterized by small-scale pics on top of narrow rectangle large-scale teeth. (3) Class 3 (Suture/sharp peak) is characterized by a flat or wavy baseline and locally tall peaks. (4) Class 4 (Simple wave-like) is characterized by a simple wave baseline. The minimum value of the compaction (or vertical displacement) accommodated by a stylolite can be estimated in the first order by measuring the maximum amplitude of the teeth (Koehn et al., 2016; Toussaint et al., 2018). A statistical analysis of the distribution of these stylolite classes was carried out to reveal a possible lithological control and to study their density in order to highlight isolated stylolites or clusters. For each stylolite, we have reported the depth in the core and the class the stylolite belongs to. These data were completed with data previously collected by Total-Energies for the core intervals we did not have direct access.

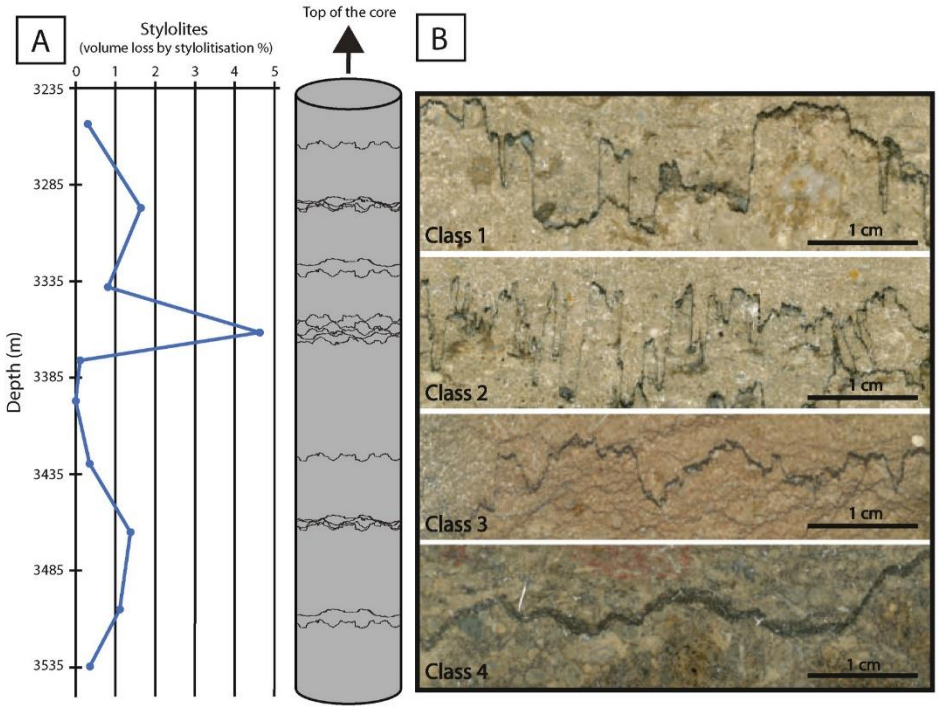


Fig. 5. A. Volume loss by stylolitisation showing the distribution of bedding-parallel (sedimentary) stylolites along the drill core (analyses completed by the TotalEnergies database). B. Stylolite morphology classes.

#### 4.5.2. Stress inversion of sedimentary stylolite roughness

The recent development of stress inversion based on stylolite roughness signal offers a new opportunity to reconstruct the history of vertical stress regardless of the past geothermal gradient and fluid pressure (Schmittbuhl et al., 2004; Ebner et al., 2009, 2010; Toussaint et al., 2018; Beaudoin and Lacombe, 2018; Beaudoin et al., 2019, 2020b). The principle of the inversion of stylolite roughness for stress is based on the idea that the final roughness of a stylolite, i.e. the difference in height between two consecutive points separated by a set length of observation, is directly related to stress. Bedding-parallel (sedimentary) stylolites (BPS, hereinafter) have been used as paleopiezometers to constrain the maximum depth of active compaction-related pressure-solution in carbonate rocks (Schmittbuhl et al., 2004; Rolland et al., 2012; Koehn et al., 2012; Bertotti et al., 2017; Beaudoin et al. 2019, 2020a; Labeur et al., 2021; Koehn et al., 2022; Bah et al., 2023), leading to recent attempts to time the period at which the vertical stress became lower than the horizontal stress (Beaudoin et al., 2020a, 2020b; Labeur et al., 2021; Lacombe et al., 2021b). This approach relies on the assumption that in a contractional setting, the prime reason that makes a population of BPS stops their development is that the maximum principal stress becomes horizontal. Such an assumption leads to estimating an absolute age that can be attributed to the onset of layer parallel shortening (LPS). In published studies, the obtained age was compared to e.g. U–Pb absolute ages of the LPS-related vein cement, supporting that no BPS developed after the formation of the oldest LPS-related vein (Beaudoin et al., 2020a).

SRIT is a paleopiezometric technique developed by Schmittbuhl et al. (2004) that relies on the self-affine properties of the stylolite final roughness, acquired quasi instantaneously with regard to the geological time scale (~200 years, Aharonov and Katsman, 2009). Indeed, the spatial transform of the signal defined by the roughness of a stylolite along its track can be defined by a power law characterized by a roughness coefficient, the so-called Hurst exponent (Barabási and Stanley, 1995), that is a constant for a given process. For example, considering a Fourier Power Spectrum (FPS) transform, the power law is defined by $P(k) \propto k^{-1-2H}$ (1) with P(k) the power, H is the Hurst coefficient, and k the wavenumber ($mm^{-1}$) (Renard et al., 2004). For stylolites, the roughness can be defined by two self-affine regimes, hence by two different Hurst exponents (Schmittbuhl et al., 2004): the Hurst exponent equals 0.5 at the large scale (typically > 1 mm), a value typical of the elastic energy, while it equals 1.1 at a smaller scale (typically < 1 mm), suggesting an effect of the surface energy (Schmittbuhl et al., 2004).

Sample preparation consists in cutting the stylolite along two orthogonal faces, both perpendicular to the stylolite plane. Each face is then polished and scanned in 2D with a 12,800 dpi resolution, the 2D track is digitized, then its average trend is set horizontally and to a value of 0. A nonlinear regression with two set slopes corresponding to the Hurst exponents (0.5 and 1.1) is used with regularly binned FPS data to find the Lc value, with an intrinsic uncertainty of ~23% (Rolland et al., 2014).

In the specific case of sedimentary stylolites, i.e., when the magnitude of the in-plane stress can be considered isotropic and smaller than the magnitude of the vertical stress (uniaxial strain hypothesis), the relationship between the cross-over length (noted Lc in m) and vertical stress magnitudes are expressed as:

$$\sigma_v^2 = \frac{\gamma E}{\alpha L_c} \quad (2)$$

with γ the energy of the solid-fluid interface ($Jm^{-2}$), E young's modulus (Pa), and $\alpha = \frac{(1-2\nu)(1+\nu)^2}{30\pi(1-\nu)^2}$, a dimensionless constant with ν being the Poisson ratio (Ebner et al., 2009). It is noteworthy that the validity of the uniaxial strain hypothesis ($\sigma V > \sigma H = \sigma h$) can be tested by comparing the Lc obtained from the 2 perpendicular cuts, which should be similar within methodological uncertainty. The uncertainty for γ is negligible and the one for α is very low considering the limited range of variations of the Poisson ratio in carbonates. However, the value of E can be very different among carbonates, and it weighs more than the other parameters in equation (2). Its calibration by mechanical tests, therefore, allows for reducing considerably this uncertainty, which can be considered then as negligible. Then, the 23% uncertainty on the value of Lc is the main source of uncertainty in the calculation of σV. Considering equation (2) that links σV to the square root of Lc, the final uncertainty on the calculated magnitude of σV amounts to 12% (Rolland et al., 2014).

The maximum depth at which the stylolite stopped being active is obtained by the following equation:

$$\sigma_v = \rho g h \quad (3)$$

with ρ the density of the rock column above the stylolite ($g.m^{-3}$), g the gravitational field acceleration ($m.s^{-2}$), and h the depth at which the dissolution along the stylolite halted (m). Noticeably, since the chemo-mechanical model assumed for SRIT considers that the dissolution occurs on a pressurized plane at the fluid-rock interface (Toussaint et al., 2018), the conversion of σv into depth is independent on surrounding fluid pressure, then it is sound to consider the dry density of the rock column for the value of ρ (Ebner et al., 2009). When applied to a population of BPS, SRIT yields the range of depths in which compaction-induced pressure solution was active under a vertical maximum principal stress (e.g. Beaudoin et al., 2019; Labeur et al., 2021) even though some local fluid pressure effect might also halt pressure solution at depth (e.g. Bah et al., 2023).

### 4.6. Calcite twin analysis

#### 4.6.1. Calcite twin data acquisition

From each sample, three mutually perpendicular thin sections of well-defined orientation in the core (X axis parallel to the generator of the oriented core, Y the dip of the core and Z the normal to the XY plane) were analyzed. For each crystal, the strike and dip of the twinned and untwinned planes were measured using an optical microscope equipped with a Universal stage and with the help of the software of Tourneret and Laurent, 1990). About 30 crystals were measured on average in each of the 3 thin sections, for a given sample. Moreover, orientations of optical axes and poles to twinned and untwinned planes were projected into the geographical referential to ensure a random spatial distribution within each sample. We also ensured that calcite twins were collected from grains belonging to the same diagenetic phase based on cathodoluminescence images.

In order to have a rough estimate of the strain accommodated by twinning, we summed the width of each twin lamella of a given twin set in grain and divided this value by the width of the grain measured perpendicular to the twins. The grain size was determined as (long-axis + short axis)/2 in 2D (thin sections) for each grain and the representative range of grain sizes for each sample was determined from a grain size histogram by eliminating the smallest and/or largest crystals, which are under-represented. The mean grain size and internal strain were further used to constrain the value of the Critical Resolved Shear Stress for twinning (Parlangeau et al., 2019) to be used in the inversion process (Lacombe et al., 2021a).

#### 4.6.2. Stress inversion of calcite twins

Calcite twins (e.g., Jamison and Spang, 1976; Lacombe and Laurent, 1992; Lacombe, 2007) are a well-established paleopiezometer that has been successfully applied to quantify paleostresses in intracratonic and foreland sedimentary basins as well as in fold-and-thrust belts (e.g., Lacombe et al., 1990, 1993, 2007; Rocher et al., 1996, 2000; Craddock et al., 1993; Kulikowski and Amrouch, 2017; Beaudoin et al., 2022. See Lacombe, 2010 and Lacombe et al., 2021a for reviews). Mechanical twinning is a common mechanism of plastic deformation in calcite

crystals (Fig. 6A) at low pressure and temperature (Tourneret and Laurent, 1990; Lacombe et al., 1990; Burkhard, 1993 Ferrill et al., 2004; Lacombe et al., 2021a). Twinning occurs by an approximation to simple shear in a particular direction and sense along specific crystallographic e planes (Fig. 6B). The effect of strain rate, temperature, and confining pressure is negligible on twinning activation, the latter being mainly dependent on differential stress, grain size and strain (Rowe and Rutter, 1990; Lacombe et al., 2021a). Twinning occurs if the resolved shear stress τs exceeds or equals the critical resolved shear stress τa (or CRSS) (Jamison and Spang, 1976; Tullis, 1980; Lacombe and Laurent, 1996; Lacombe, 2010; Lacombe et al., 2021a): the e-twin plane is twinned if and only if τs ≥ τa, and remains untwinned if τs < τa. τa decreases with increasing grain size and increases with the amount of accommodated strain since calcite hardens once twinned (Turner et al., 1954; Rowe and Rutter, 1990; Laurent et al., 2000; Lacombe, 2010; Parlangeau et al., 2019; Lacombe et al., 2021a).

In order to determine the successive paleostress tensors from the measured twin dataset, we used the stress inversion technique (CSIT-2) developed by Parlangeau et al. (2018). The principle of the inversion is to find the different stress tensors which theoretically satisfy the inequalities between τs and τa for several measured twinned planes and the whole set of untwinned planes. Each stress tensor solution has the form of a reduced stress tensor with 4 parameters: the orientation of the principal stress axes (σ1, σ2, σ3), and the stress ratio φ.

$$1 \geq \varphi = \frac{\sigma 2 - \sigma 3}{\sigma 1 - \sigma 3} \geq 0 \quad \text{with} \quad \sigma_1 \geq \sigma_2 \geq \sigma_3 \tag{4}$$

CSIT-2 first applies several thousands of reduced stress tensors determined by the systematic scanning of the 3D orientation space (with the 3 Euler's angles being sampled every 10°) and with a stress ratio of 0.5 on the set of twinned and untwinned planes, and selects those tensors which account for at least 20% of the set of twinned planes. For each of these tensors, a penalization function is defined as:

$$f = \sum_{j=1}^{j=n} \left(\tau_s^j - \tau_s^{min}\right) \tag{5}$$

with $\tau_s^j$ the resolved shear stress applied on the j untwinned planes such as $\tau_s^j \geq \tau_s^{min}$ and $\tau_s^{min}$ the smallest resolved shear stress applied on the twinned planes compatible with the tensor. The penalization function should theoretically equal 0 for a perfect dataset and increases if incompatible untwinned planes are incorporated into the solution. The stress tensors with a penalization function lower than 0.5 were retained and each of them was weighted by the number of its nearest neighbors based on a similarity criterion. This allows the simultaneous and automatic detection of the few different clusters of tensors that share a high percentage of accounted twinned planes and which are associated with low values of the penalization function. The reference reduced stress tensor of each cluster is then applied to the set of twinned and untwinned planes while the percentage of twinned planes to be explained is progressively increased. The final solution tensor is the one for which the number of compatible twinned and untwinned planes is maximum, while the value of the penalization function remains low (ideally less than 1) (see Parlangeau et al., 2018 for details).

For each stress tensor, the inversion process yields the orientation of the principal stress axes, the stress ratio, and non-dimensional differential stress $\frac{(\sigma_1-\sigma_3)}{\tau a}$ which is related to the final value of $\tau s^{min}$:

$$\frac{(\sigma_1 - \sigma_3)}{\tau a} = \frac{1}{\tau s^{min}} \tag{6}$$

The suitable value of the CRSS $\tau_a$ is determined as a function of grain size (Newman, 1994; Covey-Crump et al., 2017; Meyers et al., 2001) and strain (Turner et al., 1954; Laurent et al., 2000; Lacombe, 2010) using the curves reported in Lacombe et al. (2021a). Knowing the value of $\tau_a$ (in Pa) and $\tau s^{min}$, the actual differential stress value (σ1 − σ3) can be determined using equation (6). The methodological uncertainties are ±10° for the principal stress orientations, ±0.1 for the stress ratio and ±30% for (σ1 − σ3). The ability of this technique to detect, separate and determine stress tensors from monophase and polyphase twin datasets, including measurement errors or various grain sizes, has been demonstrated by multiple tests on numerically generated twin datasets as well as naturally deformed polyphase samples (Parlangeau et al., 2018).

### 4.7. Fracture analysis

Fracture orientation data were collected from the cored Sendji interval. Fractures were either reoriented using fracture picking on Formation Micro-Scanner (FMS) or directly measured on the core. For the first method, the FMS processing and high-resolution core images were compared to reorient the fractures. The second method consisted of measuring the fractures directly on the core with a compass equipped with a dipmeter, positioning the generator to the North, then correcting from the actual orientation of the generator. When possible, the deformation mode of fractures (opening or shearing) was determined to ensure that the opening mode corresponds to an opening perpendicular to the vein (or fracture) and the shearing mode corresponds to a lateral displacement of the matrix. These observations are made in 2D therefore we remain careful about the attribution of these deformation modes. Depending on their orientation and deformation mode, the formation and the kinematics of the fracture sets were related to the activity of the major faults and/or to the stress regimes reconstructed from calcite twins.

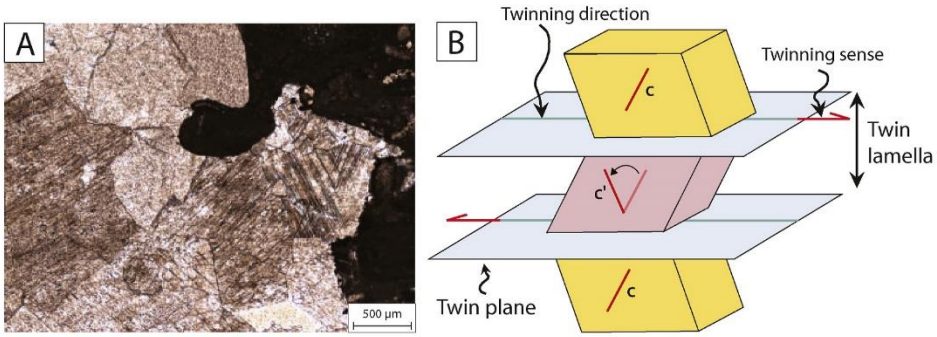


Fig. 6. A. Photograph in natural light of twinned calcite grains. B. Schematic representation of calcite twinning with C the optical axis of the host and C° the optical axis of the twinned portion of the crystal (Lacombe et al., 2021a).

### 4.8. Construction of a burial model

Petroleum system modeling software TemisFlow ™ was used to generate a burial model applying a backstripping process (Perrier and Quiblier, 1974). Backstripping consists in removing the successive sedimentary layers and decompacting the remaining layers to reconstruct the thickness of the strata at each time step since they are deposited.

Lithological data and depths of the top and bottom of each formation we obtained from a nearby well (located 1 km from well-1). This well includes more complete information than well-1 and the geological events (erosion) was described from the seismic reflection image interpretation (TotalEnergies unpublished maps). The chronostratigraphic column (Table 1) is composed of a list of layers (14 for this study, corresponding to the main formations), each of these layers being characterized by a number, a beginning age, and an ending age. Restored geometries can be edited by defining erosion thickness and paleo topography or paleo bathymetry at each time step. Each layer was defined by the ratio of the different sedimentary facies (limestone, shale, sandstone) from which petrophysical parameters such as initial porosity, solid density, and permeability are defined.

The backstripping process was based on the input data described above. This step begins with the computation from present-day to −145.5 Ma when only the substratum remains. For each event (deposition or erosion) every formation is progressively removed or eroded layers are added. Once sedimentation and erosion are accounted for, the remaining sediments are decompacted, or compacted (if eroded or not), using the porosity/depth relationships for each lithology that make up the 1D block through the forward modeling. Porosity is a variable parameter during burial and is related to the conventional hydrostatic exponential compaction laws for each lithology.

## 5. Results

### 5.1. Sedimentologicand diagenetic evolution

Four main sedimentary facies were recognized in the studied core interval (Fig. 7). The first facies corresponds to a grainstone-packstone with oolites and bioclasts (Fig. 7A) which is interpreted to have been deposited in a tidal flat of upper infralittoral to supralittoral environment with episodic emersion. These facies are characterized by cemented shells as is the case for the second facies, a micritic matrix wackestone with bioclasts (Fig. 7B). This limestone was deposited in the internal part of the oolite-dominated tidal bars of the upper infralittoral environment. Fig. 7C shows a silt-rich dolomite with calcitic and dolomitic cementation from a border of estuarine channels of a restricted domain. The last facies is silto-bioclastic dolomite with clay stringers (in blue in Fig. 7D) and corresponds to a tidal flat of upper infralittoral environment. The diagenetic evolution of the carbonate layers includes three main episodes: dolomitization, grain leaching, and calcite cementation. The latter episode consists mainly of the precipitation of a single sparry calcite cement that fills and/or replaces bioclast shells, which is the carbonate phase focused on in this work. (Fig. 7E and F). This cement exhibits a characteristic bright yellow cathodoluminescence, in strong contrast with the surrounding matrix showing dull orange luminescence (See Fig. 7F).

Table 1
Input data used in the burial model construction (using TemisFlow). Parameters such as age, thickness, and initial porosity of each syn-rift and post-rift formations are indicated.

| Event | | Age (Ma) | | Thickness (m) | Initial Porosity % |
|---|---|---|---|---|---|
| Name | Number | From | To | | |
| Paloukou | 14 | 33.9 | 0.0 | 1833.9 | 60 |
| Erosion | 13 | 65.5 | 33.9 | | |
| Lower Tertiary | 12 | 65.5 | 33.9 | | |
| Madingo | 11 | 93.5 | 65.5 | 207.0 | 60 |
| Likouala | 10 | 99.6 | 93.5 | 605.8 | 48 |
| Upper Sendji | 9 | 103.0 | 99.6 | 417.2 | 56 |
| Lower Sendji | 8 | 112.0 | 103.0 | 527.9 | 54 |
| Loeme | 7 | 116.0 | 112.0 | 60.0 | 9 |
| Chela sandstones | 6 | 118.0 | 116.0 | 45.0 | 62 |
| Erosion | 5 | 118.0 | 117.0 | | |
| Pointe Indienne shales | 4 | 123.0 | 118.0 | 90.0 | 62 |
| Toca/Pointe-Noire marls | 3 | 130.0 | 123.0 | 129.0 | 51 |
| Djeno sandstones | 2 | 141.0 | 130.0 | 117.0 | 51 |
| Basal sandstones | 1 | 145.5 | 141.0 | 90.0 | 51 |

### 5.2. Absolute U–Pb age dating

Five samples of the sparitic cement filling the micro-shells were selected at depths between 3245.9 and 3469.75 m for U–Pb absolute dating (see location on Fig. 2). Three of these samples could not be dated because the volume of the calcite phase of interest was not sufficient (3469.75 m) or because the U concentration was too low (3454.69 m; 3323.52 m). The two samples collected at 3294.35 m and 3245.9 m depth yielded reliable ages of 100.4 Ma ± 1.6 and 101.4 Ma ± 0.6, respectively (Fig. 8).

### 5.3. Fluid inclusion microthermometry

The ice melting and/or the homogenization temperatures were measured in 112 primary aqueous fluid inclusions in the calci-sparite cement at 3245.90 m, 3294.35 m, 3323.52 m, and 3454.69 m depth (see Fig. 2). All samples showed primary aqueous inclusions that are small to medium in size (± 3–20 μm), mostly two-phase (Lw > V). Homogenization temperatures of all samples are plotted together in a single histogram in Fig. 9A because the different samples show very similar $T_h$ modes ($T_h$ = 95 °C at 3245 m and 3294 m and $T_h$ = 90 °C at 3323 m and 3454 m). The overall distribution of $T_h$ is unimodal with a median at 90 °C, well lower than the current temperature at sample depths (about 3300 m) (ca. 145 °C, TotalEnergies internal report) indicating no resetting of the fluid inclusions. Ice melting temperature $T_{m(ice)}$ ranges from −23.2 °C to −18.6 °C corresponding to high salinities, around 300–320 g/L (range is 21.6 – 24.5 wt % NaCl eq) (Fig. 9B).

### 5.4. Rock mechanical properties

Mechanical tests yielded three measurements of the elastic parameters at increasing confining stress, i.e. values of 22.7 GPa, 25.2 GPa, and 27.5 GPa for the Young Modulus (E); and values of 0.23, 0.24, and 0.24 for the Poisson ratio (ν). Considering the uncertainties on the determination of the Young modulus and Poisson ratios, of 10% and 20%, respectively, all values were considered to be consistent and the elastic parameters were averaged such as follows: E = 25 GPa and ν = 0.24. For the studied sample, the yield stress is 110 MPa (Table 2), and the maximum stress is 130 MPa, so the ratio is 1.18. The calculated values of the rock mechanical parameters are then 20.5 ° for the friction angle and 9.8 MPa for the cohesion. In the domain of negative normal stress, we used the results of the Brazilian test which indicates that the rock tensile strength is ~3.1 MPa.

### 5.5. Stylolite distribution and inversion of stylolite roughnessfor stress

#### 5.5.1. Stylolite morphologyand distribution

A total of 52 stylolites were identified and measured over an interval from 3245 m to 3493 m. Observations of stylolite morphology reveal the predominance of class 3 (61% of the stylolites), then of class 2 (27% of the stylolites). Classes 1 and 4 are the least represented, they are associated with 7 and 5% of the stylolites, respectively. Overall, the distribution of stylolites is rather uniform with an average of 2 stylolites per

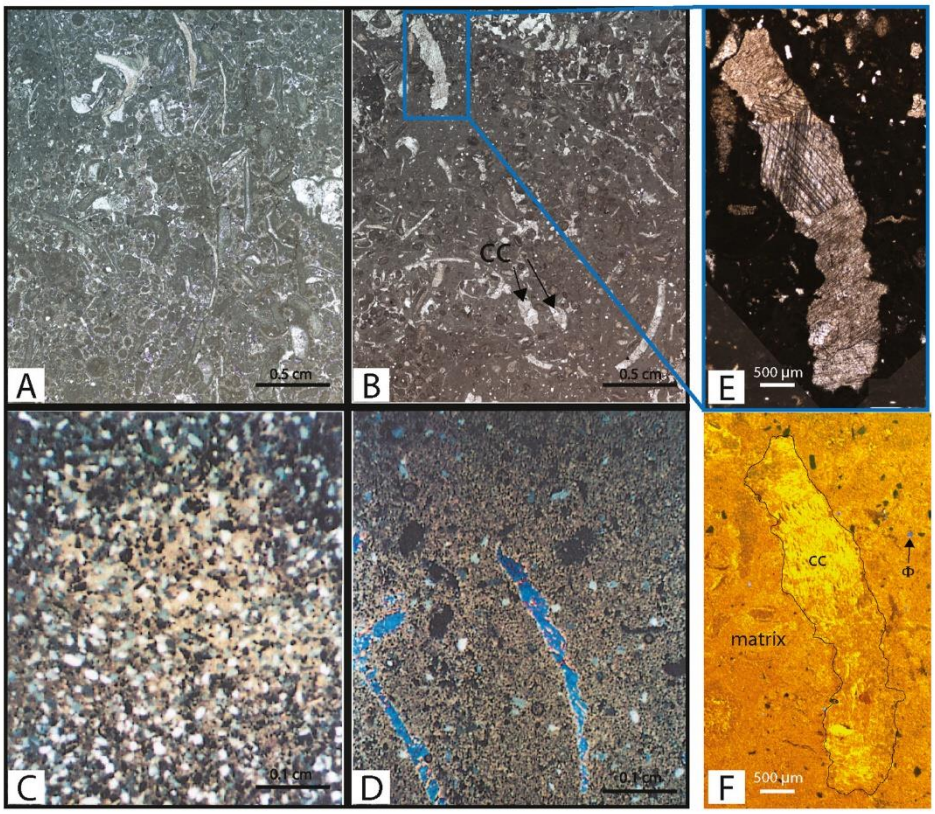


Fig. 7. Photographs in natural light of the representative facies in the drill core. A. Oolitic-bioclastic limestone. B. Gravelly bioclastic limestone. C. Fine sandstone. D. Silty-bioclastic dolomite. E. Close-up of a fossil-filled with a calcite cement in natural light and F. under cathodoluminescence.

meter with local stylolite clusters located at 3294.29 m, 3326 m, 3461.05 m, and 3487.08 m (Fig. 5A). The distribution of stylolite classes along the drill core indicates a predominance of class 3 stylolites between 3245 m and 3350 m while class 2 stylolites are mainly located near 3500 m. Classes 1 and 4 (Fig. 5B) are not sufficiently represented in the dataset to study their distribution statistically.

5.5.2. Stress inversion of stylolite roughness

52 stylolites were analyzed in the oolitic and bioclastic limestone facies and processed using SRIT (Table 3). For each stylolite, the binned Fourier power spectrum was plotted against the spectral frequency k (Fig. 10), and a nonlinear regression with fixed Hurst coefficients was modeled and fitted through the maximum of points. 41 stylolite profiles out of 52 showed a good fit to the curve (Fig. 10A and B), while 11 were not in accordance with the chemo-mechanical model (Fig. 10C and D) and were discarded. The final stylolite dataset comprises 3 class 1, 11 class 2, 25 class 3, and 2 class 4 stylolites (Fig. 5B).

We randomly checked the validity of the uniaxial strain hypothesis by obtaining Lc on 82 profiles cut orthogonal to the studied stylolite track. As all results show consistent Lc values along the two cuts (within the 23% uncertainty), we further used equation (2) to compute the vertical stress magnitude with the elastic coefficients of the Sendji limestone determined from mechanical tests (E = 25 GPa; ν = 0.24), and interfacial energy for calcite of 0.32 $Jm^{-2}$ (Wright et al., 2001). The roughness of the 41 selected stylolites showed Lc values from 0.085 to 2.427 mm, which correspond to magnitudes of the principal vertical stress σ1 between 65 and 15 MPa (Table 2).

Conversion of these vertical stress magnitudes into depths using equation (3) revealed that compaction-induced pressure solution along BPS in the Sendji Fm was active at burial depths between 650 m and 2800 m under a vertical principal stress σ1. The population of the calculated depths is represented in Fig. 10E as a violin plot (Hintze and Nelson, 1998). This plot shows local density estimates and provides a better visualization of the depth distribution than a traditional boxplot statistical representation. The distribution analysis shows that 47% of the stylolites exhibit a maximum burial depth between 1000 and 1300 m with a median located at about 1100 m.

We further investigated whether stylolite classes may have recorded specific maximum burial depth (e.g., Beaudoin et al., 2019) (Fig. 10E). Stylolite classes are shown here as a function of maximum burial depth revealed by signal analysis and inversion. Pressure solution along class 2 stylolites was continuous from 650 m to 2800 m whereas it mainly occurred between 1000 and 2000 m depth along class 3 stylolites. Classes 1 and 4 are too poorly represented (3 and 2 samples, respectively) in the dataset to study any relationship with depth.

5.6. Stress inversion of calcite twins

Stress inversion of calcite twins was carried out from 14 samples collected between 3245.90 m and 3510.88 m. As determined from the cathodoluminescence analysis, samples show only one twinned cement so all crystals could be processed together. Calcite grains were deformed in a thin-twin strain regime: the measured twins are thin (a fraction of µm) and straight and belong to Type I twins (Burkhard, 1993), which indicates that the temperature of deformation likely never exceeded ~170 °C (Ferrill et al., 2004; see discussion in Lacombe et al., 2021a).

Our samples show a nearly random spatial distribution of optical axes of grains (Fig. 11A), which is a prerequisite for the reliable

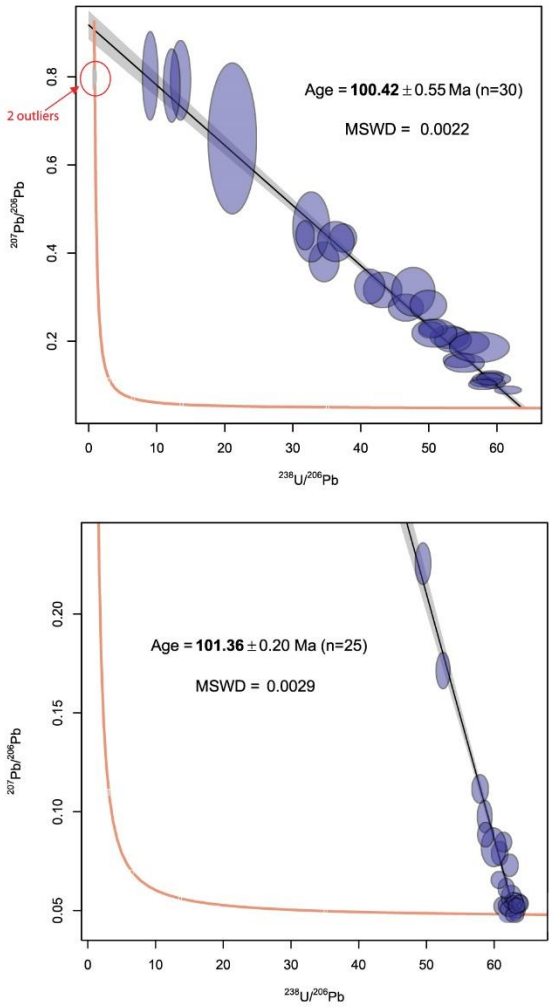


Fig. 8. Tera-Wasserburg Concordia plots showing 238U/206 Pb vs. 207Pb/206 Pb for calcite cement in samples 3294 (top) and 3245 (bottom) (n = 55). MSWD – mean square of weighted deviates.

inversion of calcite twin data for stress. Samples also highlight a modal distribution of calcite grain size ranging broadly from > 30 μm to < 350 μm (Table 4). Twinning strain was grossly estimated at 2%; this very small strain can be approximated by coaxial conditions so the orientation of twinning strain can be reliably correlated with paleostress orientation, which is also a prerequisite for the reliable inversion of calcite twin data for stress (Burkhard, 1993; Amrouch et al., 2010; Lacombe et al., 2021a). For each sample, this value was further considered along with the mean grain size of the size range (Fig. 11B) to define the CRSS used for the calculation of the differential stress (Table 4). Calcite twin inversion reveals that our samples are polyphase, i.e., the twin dataset results from superimposed stress tensors, each of them explaining part of the twinned planes and most of the untwinned planes. In our case, 77% of the samples yielded two or three superimposed stress tensors.

A first phase of selection was carried out to group stress tensors corresponding to similar principal stress orientations (within uncertainties) and stress regimes. Among the 26 stress tensors determined from the twinned cement of the 14 samples (see appendix), this selection revealed 7 main groups of stress tensors (Fig. 12): two extensional stress tensor groups (A and B), two compressional stress tensor groups (C and D), and three strike-slip stress tensor groups (E, F, and G). Regarding the extensional stress regimes (vertical σ1), tensor group A was identified in 4 samples and is characterized by a σ3 oriented ~ N–S and by mean differential stress magnitudes of 38 MPa (σ1 - σ3) and 17 MPa (σ2 - σ3). Tensor group B was recognized from 3 samples, with a σ3 oriented ~ N100 and mean differential stress magnitudes of 42 Ma (σ1- σ3) and 27 MPa (σ2- σ3) on average. Regarding the compressional stress regimes (vertical σ3), groups C and D were identified from 6 to 3 samples, respectively. Tensor group C is characterized by a σ1 oriented ~ N170 and mean differential stress magnitudes of 48 MPa (σ1- σ3) and 22 MPa (σ2- σ3). Tensor group D is characterized by a σ1 oriented ~ N100 and mean differential stress magnitudes of 59 MPa (σ1- σ3) and 31 MPa (σ2- σ3). Regarding the strike-slip stress regimes (vertical σ2), tensor groups E, F, and G were identified from 3, 5, and 2 samples, respectively, and are characterized by a σ1 oriented N143 (E), N020 (F), and N095 (G) and by mean differential stress magnitudes of 55 MPa (σ1- σ3) and 26 Ma (σ2- σ3) for E, 49 MPa (σ1- σ3) and 22 MPa (σ2- σ3) for F and 42 MPa (σ1- σ3) and 17 MPa (σ2- σ3) for G. Samples associated to these tensors are spatially distributed over the entire studied core interval. No evidence of tensor grouping was observed, suggesting that these tensors are post Lower Sendji deposition.

### 5.7. Fracture types and distribution

70 fractures (sealed and open fractures) were identified in the drill core within the Sendji formation (Fig. 13). These fractures are distributed throughout the reservoir, with a mean linear fracture density of about 0.5 fracture/meter for the complete core (TotalEnergies internal report; this work), but one depth interval, between 3400 m and 3541 m, appears to be more particularly fractured in sequence 1. In this interval, which corresponds to a dolomitic facies both large (decametric length) and small (centimetric length) sealed fractures are present. The fractures present a range of dips and show evidence for (1) a normal shearing mode (mode II) and (2) an undetermined opening mode. Despite scattering, the distribution of fracture directions indicates the predominance of two main sets: a set comprising fractures striking NNW-SSE (N140 ⊠ to N165 ⊠) and dipping ~50 –60⊠W (set 1) and a set comprising fractures striking N95 and with variable dips toward the North (set 2) (Fig. 13A and B).

### 5.8. Burial model

The burial model generated from well and seismic data describes the burial history of all N'Kossa field formations and, in particular, the burial history of the post-rift Sendji Fm. An erosional episode occurred around 118 Ma, represented by ~75 m of uplift affecting pre-salt formations only. This event also marks the beginning of the post-rift phase with the deposition of the Chela Fm. Three main phases of burial of the Sendji Fm can be distinguished based on contrasting burial rates: (1) a phase of rapid burial (about 100 m/Ma) between 113 Ma and 92 Ma, coeval with deposition of the Sendji Fm and the Likouala Fm; (2) a plateau-like phase (about 8 m/Ma) ending with a slight uplift between 66 Ma and 34 Ma (3.3 m/Ma) and (3) a last phase of rapid burial from 34 Ma onward (about 50 m/Ma) coeval with deposition of the Paloukou Fm.

## 6. Discussion: burial, structural and paleostress history of the Sendji Fm in the N'Kossa structure and implications for the post-rift evolution of the Congolese passive margin

### 6.1. Timing of salt tectonics, cementationand stylolitization in the Sendji Fm

The Sendji Fm experienced salt tectonics early during its burial history, between 110 and 80 Ma, which resulted in visible structural

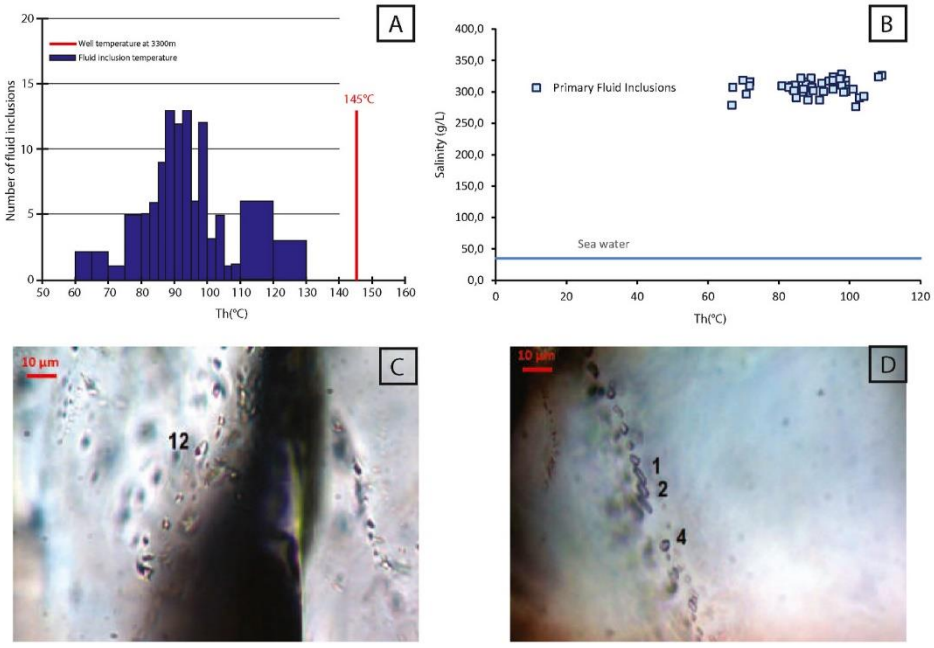


Fig. 9. A. Histogram of homogenization temperatures and B. plot of salinity against homogenization temperature determined from fluid inclusion microthermometry. C. Photographs of primary fluid inclusions in samples 3294 (left) and 3323 (right).

Table 2
Multitriax and Brazilian test results for two representative samples of the oolitic-bioclastic limestone facies, sampled in 3491 m depth in the drill cores. Samples for multitriax were tested at 10, 30, and 50 MPa confining pressure (Pconf).

| Multitriax test | | | | | | Brazilian test |
|---|---|---|---|---|---|---|
| Pconf | yield | rupture | estimated rupture | friction angle | cohesion | tensile strength |
| MPa | MPa | MPa | MPa | Degree | MPa | MPa |
| 10 | 40 | – | 47.2 | | | |
| 30 | 80 | – | 94.4 | 20.5 | 9.8 | 3.08 |
| 50 | 110 | 129.8 | – | | | |

remains as shown in Figs. 3 and 4. The structural map (Fig. 3) and the seismic section of the N'Kossa field (Fig. 4) illustrate the structural setting of Well 1 in the N'Kossa structure. Listric normal faults offsetting the post-rift formations reveal local extension and notably depict a raft structure, on top of which the Sendji Fm was sampled. The structure, laying on a thin salt pillow of Loeme Fm, is bounded by major N–S to NE-SW listric normal faults (Fig. 3). The gravity tectonics occurring mostly from Aptian to Cenomanian dismantled the first post-salt sediments into disjointed rafts, either cored by lower or upper Sendji sediments. The gravity-driven salt tectonics extended until the late Cretaceous with the Likouala Fm (Fig. 4) continuously filling the gaps between the divergent rafts. These thin-skinned tectonic processes were compensated by listric normal faults bounding rollover- or turtle-type structures. N'Kossa's fairly isopach Sendji sequences are bounded by listric faults and segmented by normal NW-SE to NE-SW faults (Figs. 3 and 4). Their activity is mostly Cenomanian, during the deposition of the Likouala Fm, with tens to hundreds of meters of vertical throw. Some of the bounding faults are interpreted to have had a continuous activity until Paleogene with a very low displacement of the Madingo Fm, mostly linked to sedimentary loading or differential compaction of the carbonaceous rafts vs the clayey inter-raft Likouala filling. The major western bounding normal fault remained active until recent times, with very low displacement reflecting likely late local accommodation within the sedimentary sequence rather than continuing salt-related extensional tectonics.

These major normal faults rooting within the Loeme salt Fm are roughly oriented N–S as indicated in Fig. 4 and therefore reflect roughly E-W oriented thin-skinned extensional deformation in the upslope domain of the margin. This extension is likely to be related to the gravitational movements of the salt of the Loeme Fm which progressively flowed downslope westward in response to sedimentary loading and accumulated several tens km further west, in the margin compressional domain. The structural style of the deformation of the post-rift sequences was therefore dominated by thin-skinned extensional tectonics (Wonham et al., 2010), mainly during the late Cretaceous. The structure of N'Kossa, therefore, recorded mostly a late Albian to Cenomanian gravity-driven extensional salt tectonics, followed by some sedimentary-driven slight gravity sliding effects rather localized to the main western bounding faults.

During the phase of salt tectonics, the Sendji Fm was progressively buried and underwent diagenesis marked by precipitation of the main calcite cement. U–Pb geochronology reveals an age of around 101 ± 1 Ma for this cement, pointing towards early cementation soon after the deposition of the Lower Sendji (between 112 and 104 Ma), during the deposition of the Upper Sendji (from ~104 to 99.6 Ma). Fluid inclusions microthermometry shows that this cement precipitated from a fluid with 10 times the salinity of seawater. This extremely high salinity could relate this fluid to the brines associated with the Loeme salt layer beneath, which was undergoing gravity-driven flow at that time. Yet the high temperature of precipitation (Th = 90 °C) is not compatible with the burial depth at which the studied strata were expected to be (950 m) at the time of precipitation (101 Ma), even considering the rather high geothermal gradient of 44°/km (TotalEnergies internal report). Thus, one can consider the contribution of high-temperature fluids of deep origin in the basin, possibly from the basement, and a rapid fluid ascent through the salt layer thanks to the normal faults related to the early salt tectonics. Note however that constraining the origin and migration

Table 3
Results of stylolite roughness inversion technique. σV is calculated with a value of E = 25 GPa and v = 0.24. Rounded up with an uncertainty of 12%.

| Stylolite characteristics (n = 41) | | | | | | | | | | | |
|---|---|---|---|---|---|---|---|---|---|---|---|
| Sample | Class | Insoluble Thickness (mm) | Crossover Length (mm) | $\sigma_V$ (MPa) | Depth (m) | Sample | Class | Insoluble Thickness (mm) | Crossover Length (mm | $\sigma_V$ (MPa) | Depth (m) |
| 3294.27_1 | 1 | 0.330 | 2.04 | 16 | 691 | 3245.75_6 | 3 | 0.06 | 0.607 | 30 | 1250 |
| 3294.27_3 | 3 | 0.047 | 0.56 | 31 | 1300 | 3245.75_5 | 3 | 0.113 | 0.393 | 37 | 1600 |
| 3294.27_4 | 3 | 0.044 | 0.26 | 44 | 1900 | 3294.14_3 | 3 | 0.1 | 1.077 | 22 | 950 |
| 3294.27_5 | 3 | 0.048 | 0.91 | 24 | 1050 | 3326.38_4 | 3 | 0.07 | 0.264 | 45 | 1900 |
| 3326.38_1 | 3 | 0.64 | 0.18 | 55 | 2300 | 3326.53_1 | 2 | 0.41 | 0.369 | 38 | 1600 |
| 3326.38_3 | 4 | 0.955 | 0.96 | 24 | 1000 | 3326.53_2 | 3 | 0.1 | 0.786 | 26 | 1100 |
| 3326.38_5 | 3 | 0.098 | 0.831 | 25 | 1080 | 3464.30_1 | 3 | 0.7 | 0.558 | 31 | 1300 |
| 3326.38_6 | 3 | 0.118 | 0.334 | 40 | 1700 | 3487.30_1 | 3 | 0.4 | 0.255 | 46 | 1950 |
| 3294.14_1 | 3 | 0.58 | 0.378 | 38 | 1600 | 3294.27_5 | 3 | 0.048 | 0.91 | 24 | 1050 |
| 3294.14_2 | 3 | 0.1 | 0.923 | 24 | 1000 | 3487.60_0 | 1 | 0.06 | 1.057 | 23 | 1000 |
| 3294.14_4 | 3 | 0.052 | 0.836 | 25 | 1100 | 3487.60_1 | 1 | 0.4 | 0.47 | 34 | 1450 |
| 3294.14_5 | 3 | 0.04 | 0.769 | 27 | 1150 | 3488.79_1 | 3 | 0.3 | 0.203 | 51 | 2150 |
| 3294.14_6 | 3 | 0.05 | 0.685 | 28 | 1200 | 3491.48_0 | 2 | 0.2 | 2.427 | 15 | 650 |
| 3294.14_7 | 4 | 0.19 | 0.896 | 25 | 1050 | 3491.88_1 | 2 | 0.48 | 1.026 | 23 | 1000 |
| 3245.75_1 | 2 | 0.5 | 0.331 | 40 | 1700 | 3491.88_2 | 2 | 0.48 | 0.927 | 24 | 1000 |
| 3294.43_1 | 3 | 0.99 | 0.392 | 37 | 1600 | 3492.27_1 | 2 | 0.21 | 0.127 | 65 | 2800 |
| 3326.27_1 | 3 | 0.176 | 1.069 | 53 | 955 | 3492.27_2 | 2 | 0.162 | 0.25 | 47 | 1970 |
| 3461.05_1 | 2 | 0.378 | 0.843 | 25 | 1050 | 3488.75_1 | 2 | 0.22 | 1.34 | 20 | 853 |
| 3245.75_2 | 3 | 0.05 | 0.399 | 37 | 1550 | 3487.60_2 | 2 | 0.28 | 0.209 | 51 | 2150 |
| 3245.75_4 | 3 | 0.07 | 0.331 | 40 | 1700 | 3461.05_4 | 2 | 0.085 | 0.085 | 55 | 2320 |
| 3245.75_7 | 3 | 0.029 | 0.954 | 24 | 1000 | | | | | | |

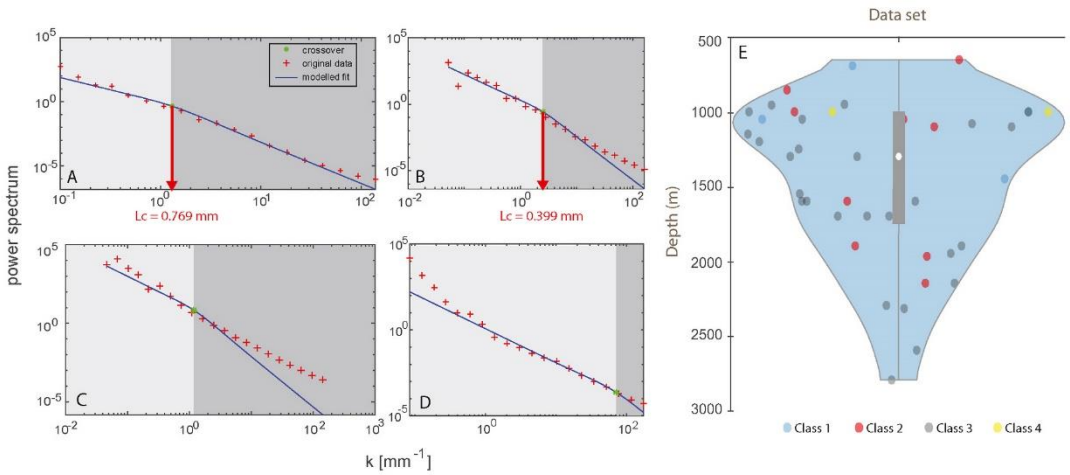


Fig. 10. Examples of Fourier power spectrum log-log plots. A. Successful inversion result for sample 3294.14_5 which is associated with a crossover length (Lc) of 0.769 mm. B. Successful inversion result for sample 3245.75_2 with an Lc of 0.399 mm. C, D. Failed inversion result where stylolite roughness inversion is missing large-scale data (C) and small-scale data (D). E. Violin plot of stylolite inversion results showing the heterogeneity of the depth distribution calculated from Lc values. The vertical bar represents the distribution of the data between the minimum and maximum values (at the extremities of the bar), the grey box plot displays the first quartile (at the top) and third quartile (at the bottom) whereas the white point displays the median.

pathways of the cementing fluids would require more geochemical proxies (e.g. Beaudoin et al., 2022), which is beyond the scope of this study.

The depth ranges of active stylolitization revealed by the inversion of the roughness of BPS projected onto the burial model indicate that the most superficial stylolite stopped its activity at 102 Ma (within uncertainties) (Fig. 14), so during the cementation. We can reasonably conclude that the (beginning of the) stylolitization was coeval with the (dated) cementation. From this point, the pressure-solution related to compaction continued at the first order until 15 Ma. In more detail however, 85% of the BPS ceased their development between 102 and 75 Ma (650–2000 m), and most of them between 1000 and 1600 m, as shown in Fig. 10. Only 15% of the studied population was still active at higher depths (between 2200 and 2800 m ± 12%). This bimodal distribution can be interpreted as a two-phase history of pressure solution, with a high activity below 1600 m of burial, and a lower activity between 2200 and 2800 m of burial. Interestingly, the period of time when burial stopped and the reservoir even uplifted (70–33 Ma, Fig. 14) corresponds to the depth range at which only a few stylolites halted (or none, if considering the uncertainty on each stylolite, Fig. 10). After 15 Ma, no BPS seems to have developed. The first phase of very active pressure-solution was also documented in the underlying pre-rift and pre-salt Toca Fm (Bah et al., 2023), and it coincides with the first burial phase characterized by the greatest burial rate (Fig. 14). That could suggest a potential correlation between the burial rate and the end of dissolution by stylolitization of the Sendji Fm, that we propose to relate to a higher saturation rate during the fast burial and associated sedimentary load increase. Our dataset does not allow us to discuss whether

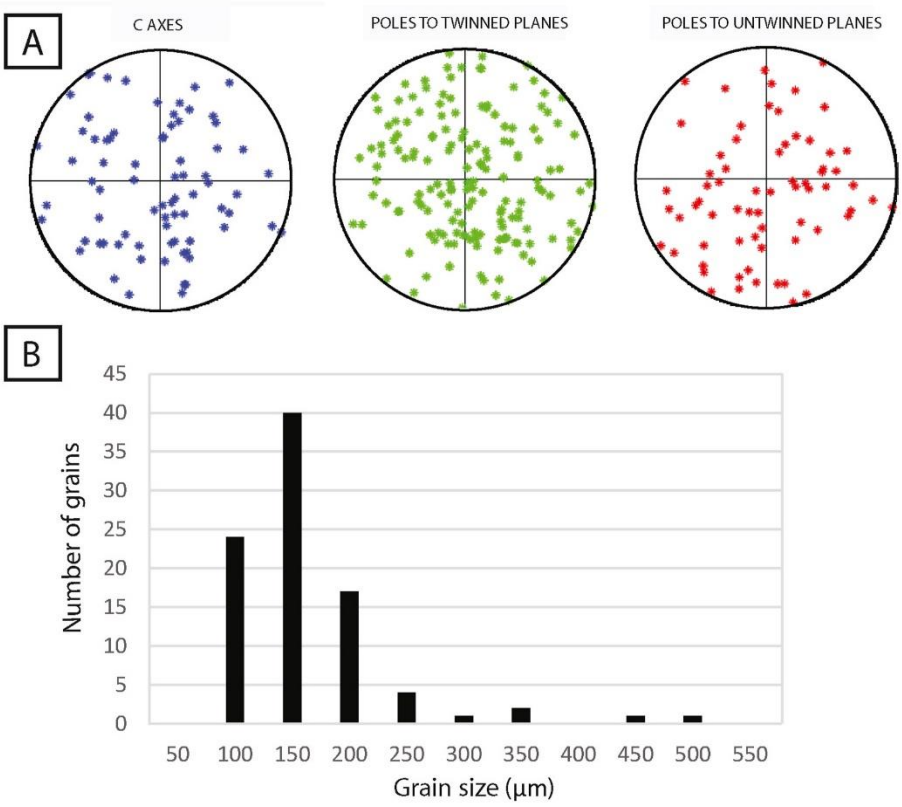


Fig. 11. A. Example of the spatial distribution of optical axes (blue) and poles to twinned (green) and untwinned (red) planes for a sample studied using CSIT-2 (sample 3454.69). B. Example of grain size distribution in the same sample.

all stylolites started their development at the same time and halted at variable depths for different local-scale reasons (sensu Beaudoin et al., 2019, e.g., local high fluid pressure, saturation of the dissolution plane, clogging of the surrounding porosity), or if stylolites that halted deeper started their development later during burial history (sensu Ebner et al., 2010). Also, we can discuss neither the impact of the sedimentary texture nor of the stylolite morphology on these inverted depths.

### 6.2. Timing and significance of successive paleostress regimes

The stress orientations discussed in this section are described in the present-day position of Africa.

#### 6.2.1. Timing of the reconstructed paleostress regimes

In order to establish the timing of the paleostress regimes revealed by calcite twinning, we adopted the following workflow (Fig. 15A). The Sendji deposition age together with the absolute age of the calcite cement yield time constraints at the very beginning of the story, i.e., early fluid circulation and cementation. The distribution of depth ranges of activity of BPS as revealed by SRIT projected onto the time-burial evolution curve for the Sendji Fm (Fig. 15B) defines the time periods of compaction-related pressure-solution, hence the periods dominated by a stress regime with a vertical σ1. Given the previously-advocated observation that BPS develops until σ1 is no longer vertical, one can derive the time at which σ1 switched from vertical to horizontal in response to the tectonic stress becoming high enough to overcome the burial stress (Beaudoin et al., 2019, 2020a; Labeur et al., 2021; Lacombe et al., 2021b). This constrains the time periods when the strike-slip and compressional stress regimes (horizontal σ1) recorded by calcite twins prevailed (Fig. 15B). These time constraints combined with published paleostress reconstructions in onshore western and southern Africa enable to depict a consistent scenario of the stress evolution during the burial history of the Sendji Fm.

The period of stylolitization between ~102 and 75 Ma was likely dominated by a stress regime with vertical σ1 (Fig. 14). It is therefore likely that the extensional stress tensors groups (A and B) recorded by calcite twinning prevailed within this time interval. Stress tensor groups E, C and F associated with σ1 trending NNW-SSE to NNE-SSW, recognized at other localities (Viola et al., 2012; Nkodia et al., 2020), hence of regional significance, can be assigned to the "End Cretaceous event" ~67-60 Ma (Guiraud and Bosworth, 1997), on the basis of consistent compressional trends. This timing fits with the onset of the 70-33 Ma time interval when burial stopped, the Sendji reservoir uplifted and few or no BPS were active (Fig. 14). Finally, because the current state of stress is dominated by ~ E-W compression (Heidbach et al., 2016), and because after ~15 Ma no BPS seems to have developed, which supports that σ1 has definitely switched from vertical to horizontal since then, we propose that the stress tensor groups G and D prevailed since ~15 Ma (15-10 Ma to be conservative taking into account uncertainties) onwards.

#### 6.2.2. Significance of the reconstructed paleostress regimes

6.2.2.1. Local extensional stresses related to salt tectonics in the N'Kossa field. Based on the location of the well from which the Sendji Fm was cored, the NNW-SSE striking, west-dipping fractures which display small extensional jogs filled with anhydrite (set 1 in Fig. 13A) are likely

Table 4
Paleostress tensors determined from calcite twin inversion (CSIT-2) for each sample (from −3510.88 m to −3245.90 m). The quality of each tensor is estimated based on several criteria such as the stability of principal stress orientations, the value of the penalization function and the number of incompatible untwinned planes (A: very good quality, B: good quality and C: poor quality).

| Depth (m) | Number of grains | Crystal size range (μm) | Total number of TP/UP | Number of compatible TP/UP | Tensors | σ1 trend-plunge(°) | σ2 trend-plunge(°) | σ3 trend-plunge(°) | Φ | Penalization Function | $\tau_s^{min}$ | % of explained twin planes | CRSS (MPa) | (σ1−σ3) MPa | (σ2−σ3) MPa | Quality |
|---|---|---|---|---|---|---|---|---|---|---|---|---|---|---|---|---|
| −3245.90 | 66 | 50–450 | 106/67 | 34/56 | 1 | N011-68 | N080-08 | N167-20 | 0.51 | 0.46 | 0.213 | 32 | 9 | 43 | 22 | B |
| | | | | 34/56 | 2 | N017-11 | N097-40 | N120-48 | 0.53 | 0.87 | 0.183 | 32 | 9 | 49 | 26 | B |
| −3292.33 | 79 | 30–100 | 153/84 | 61/64 | 1 | N135-34 | N150-55 | N50-07 | 0.6 | 1.7 | 0.146 | 40 | 12 | 80 | 48 | C |
| | | | | | | | | | | | | | 10 | 67 | 40 | |
| | | | | 52/70 | 2 | N95-37 | N04-01 | N93-53 | 0.48 | 0.87 | 0.145 | 34 | 12 | 80 | 40 | B |
| | | | | | | | | | | | | | 10 | 67 | 33 | |
| −3294.35 | 76 | 100–500 | 178/50 | 75/41 | 1 | N099-14 | N002-28 | N033-59 | 0.55 | 0.95 | 0.09 | 42 | 7 | 78 | 43 | A |
| | | | | | | | | | | | | | 8 | 89 | 49 | |
| | | | | 64/42 | 2 | N019-16 | N177-73 | N108-06 | 0.43 | 0.66 | 0.16 | 36 | 7 | 43 | 18 | B |
| | | | | | | | | | | | | | 8 | 50 | 22 | |
| −3323.52 | 51 | 100–500 | 118/32 | 44/27 | 1 | N001-70 | N91-00 | N001-20 | 0.25 | 0.25 | 0.2 | 38 | 7 | 35 | 19 | A |
| | | | | | | | | | | | | | 8 | 40 | 22 | |
| | | | | 44/24 | 2 | N016-11 | N040-77 | N107-05 | 0.39 | 0.93 | 0.09 | 38 | 7 | 67 | 26 | B |
| | | | | | | | | | | | | | 8 | 76 | 30 | |
| −3326.62 | 58 | 100–300 | 102/54 | 36/47 | 1 | N119-14 | N85-74 | N27-09 | 0.25 | 0.56 | 0.2 | 36 | 10 | 50 | 28 | A |
| | | | | 40/47 | 2 | N165-24 | N61-30 | N107-50 | 0.32 | 0.37 | 0.16 | 40 | 10 | 63 | 20 | B |
| −3454.69 | 76 | 100–450 | 170/82 | 51/70 | 1 | N176-04 | N082-46 | N089-43 | 0.53 | 0.90 | 0.16 | 32 | 8 | 50 | 26 | B |
| | | | | | | | | | | | | | 9 | 56 | 20 | |
| −3461.20 | 67 | 50–250 | 134/61 | 48/45 | 1 | N160-17 | N100-58 | N61-26 | 0.39 | 1.2 | 0.15 | 36 | 12 | 75 | 29 | B |
| | | | | | | | | | | | | | 7 | 44 | 17 | |
| | | | | 40/46 | 2 | N70-55 | N171-08 | N86-34 | 0.46 | 1.07 | 0.12 | 30 | 12 | 60 | 28 | B |
| | | | | | | | | | | | | | 7 | 35 | 16 | |
| −3461.76 | 76 | 50–350 | 138/90 | 38/74 | 1 | N149-34 | N081-28 | N020-43 | 0.54 | 1.2 | 0.21 | 28 | 12 | 57 | 31 | C |
| | | | | | | | | | | | | | 7 | 33 | 18 | |
| −3469.10 | 80 | 100–250 | 175/65 | 52/58 | 1 | N051-58 | N118-14 | N020-28 | 0.20 | 0.97 | 0.18 | 30 | 7 | 39 | 11 | B |
| | | | | | | | | | | | | | 10 | 56 | 8 | |
| −3469.75 | 81 | 50–200 | 189/54 | 64/42 | 1 | N012-48 | N042-38 | N120-15 | 0.70 | 0.66 | 0.16 | 34 | 12 | 76 | 53 | A |
| | | | | | | | | | | | | | 8 | 53 | 36 | |
| | | | | 71/38 | 2 | N177-11 | N088-02 | N008-79 | 0.55 | 0.94 | 0.14 | 38 | 12 | 88 | 48 | A |
| | | | | | | | | | | | | | 8 | 58 | 32 | |
| −3487.19 | 62 | 100–350 | 146/43 | 55/33 | 1 | N024-49 | N026-41 | N115-01 | 0.53 | 0.88 | 0.15 | 38 | 10 | 67 | 36 | B |
| | | | | | | | | | | | | | 6 | 40 | 21 | |
| | | | | 52/31 | 2 | N006-25 | N092-08 | N167-63 | 0.31 | 0.87 | 0.17 | 36 | 10 | 59 | 18 | A |
| | | | | | | | | | | | | | 6 | 35 | 11 | |
| −3491.05 | 72 | 100–300 | 172/44 | 51/36 | 1 | N71-05 | N159-17 | N178-72 | 0.52 | 0.39 | 0.19 | 30 | 10 | 54 | 28 | A |
| | | | | | | | | | | | | | 6 | 32 | 17 | |
| | | | | 61/31 | 2 | N137-75 | N003-11 | N091-11 | 0.65 | 0.90 | 0.15 | 36 | 10 | 68 | 44 | A |
| | | | | | | | | | | | | | 6 | 41 | 27 | |
| | | | | 65/37 | 3 | N169-22 | N077-06 | N151-67 | 0.33 | 0.73 | 0.12 | 38 | 10 | 83 | 27 | A |
| | | | | | | | | | | | | | 6 | 50 | 16 | |
| −3510.88 | 83 | 100–350 | 198/51 | 75/44 | 1 | N144-51 | N087-24 | N191-29 | 0.40 | 0.55 | 0.15 | 38 | 10 | 67 | 27 | A |
| | | | | | | | | | | | | | 6 | 40 | 16 | |
| | | | | 63/39 | 2 | N028-40 | N170-43 | N100-20 | 0.50 | 0.93 | 0.17 | 32 | 10 | 59 | 25 | B |
| | | | | | | | | | | | | | 6 | 35 | 17 | |
| | | | | 79/39 | 3 | N158-04 | N091-79 | N067-10 | 0.51 | 1.48 | 0.11 | 40 | 10 | 91 | 46 | C |
| | | | | | | | | | | | | | 6 | 55 | 28 | |

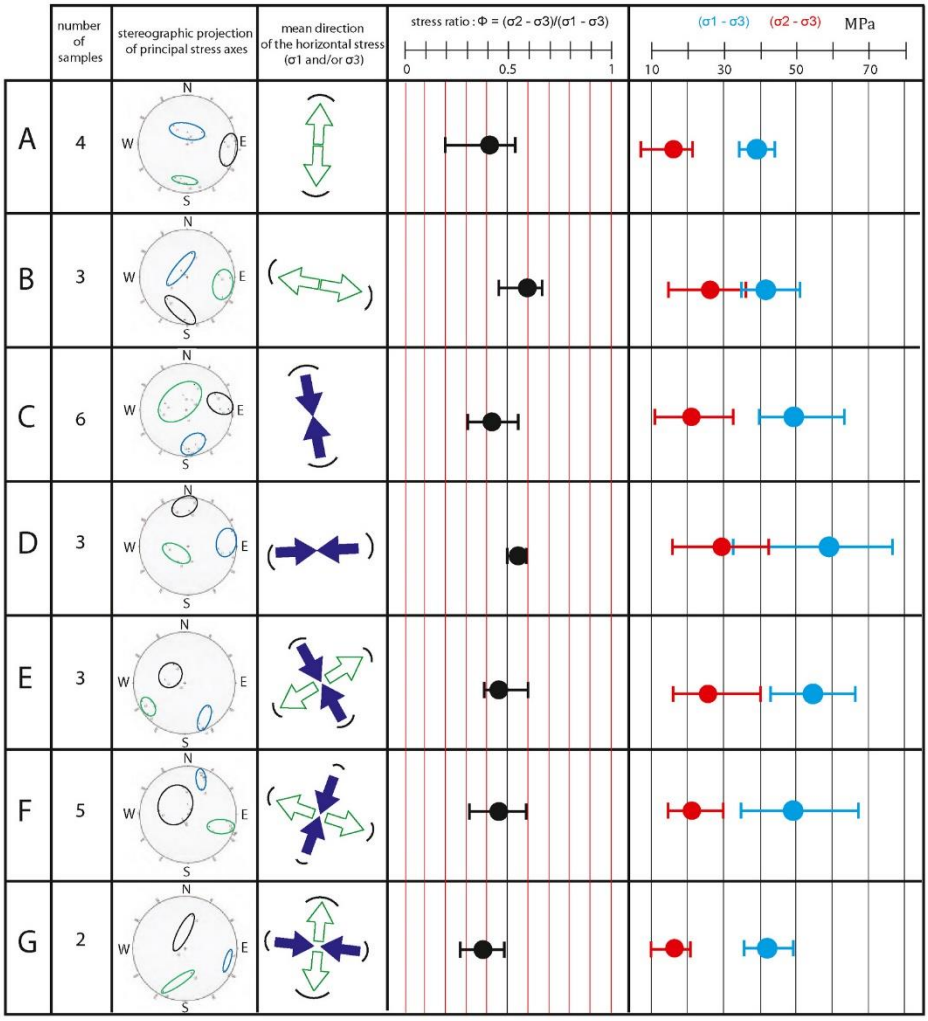


Fig. 12. Overview of stress tensor groups resulting from calcite twin inversion using CSIT-2. Each tensor group (from A to G) is characterized by a plot data in stereographic equal-area projection showing the mean orientation of the principal stress axes (blue for σ1, black for σ2, and green for σ3) and the representation of the average orientation of the horizontal stresses as arrows (with σ1 in blue and σ3 in green) in map view. Each tensor group is associated with several samples from which the related stress tensors were identified. The average values of the differential stress magnitudes for each group are shown in blue (σ1- σ3) and in red (σ2- σ3) and the average value of the stress ratio Φ in black.

related to the large halokinetic N160⁰ listric normal faults (Fig. 3), possibly having been even sampled within the damage zones of the normal fault network. In this hypothesis, these fractures were formed in a nearly E-W-oriented extensional regime associated with salt-related gravity tectonics in a roughly E-W direction. The extensional stress tensor group B recorded by calcite twins is therefore consistent with the formation of these mesoscale fractures and the kinematics of the listric normal fault, the vertical attitude of the σ1 axis being also consistent with the BPS development at that time. The stress tensor group A corresponds to the second purely extensional stress regime with σ3 oriented N–S in the present-day projected direction. Considering the complex pattern of interconnected normal faults as shown in Fig. 4 and the dome-like raft structure, it is likely that local extension may have temporarily switched or oscillated from E-W to N–S oriented extension during the paroxysm of the salt tectonics. This N–S extension is roughly consistent with the minor set (set 2) of mode II fractures as well as with the location of the well close to the northern boundary of the N'Kossa raft with a roughly NE-SW to E-W free edge. We therefore tentatively relate the N–S extension also to the gravity-related thin-skinned salt tectonics. The two extensional stress regimes therefore would be of local significance and restricted to the detached supra-salt cover, and associated with salt tectonics from 110 to 80 Ma, without reflecting any large-scale extensional crustal strain at that time.

6.2.2.2. Far-field stresses transferred to the Atlantic margin from distant plate boundaries. During the post-rift phase, several compressional or strike-slip states of stress (horizontal σ1) have been recorded onshore in central, western, and southern Africa (Fig. 16).

We interpret the strike-slip and compressional stress with σ1 oriented NW-SE for tensor group E, NNW-SSE for tensor group C, and NNE-SSW for tensor group F revealed by calcite twinning as reflecting intraplate compressional stresses transferred from the distant Africa-Eurasia plate boundary. The Santonian compressional phase (85-83 Ma) described by Guiraud and Bosworth (1997) was seemingly not

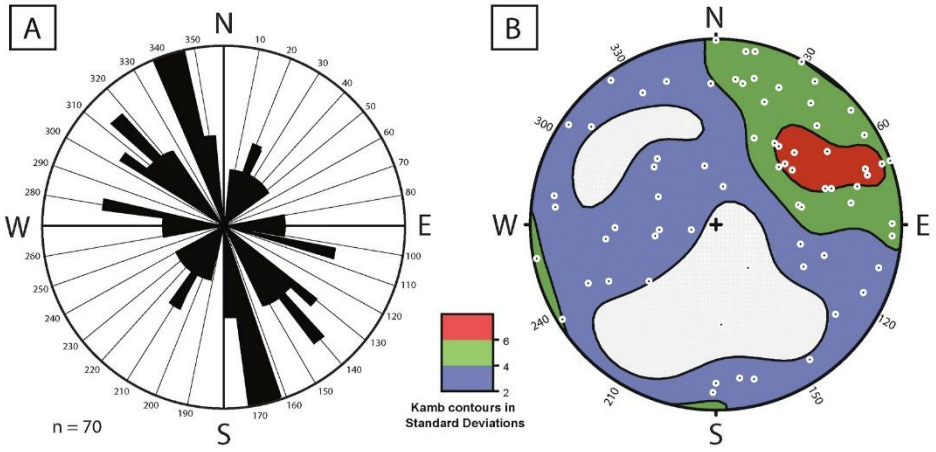


Fig. 13. A. Rose diagram of strikes for fractures described in the core sample. B. Kamb contours of fracture plane poles projected on the lower hemisphere of a Schmidt diagram.

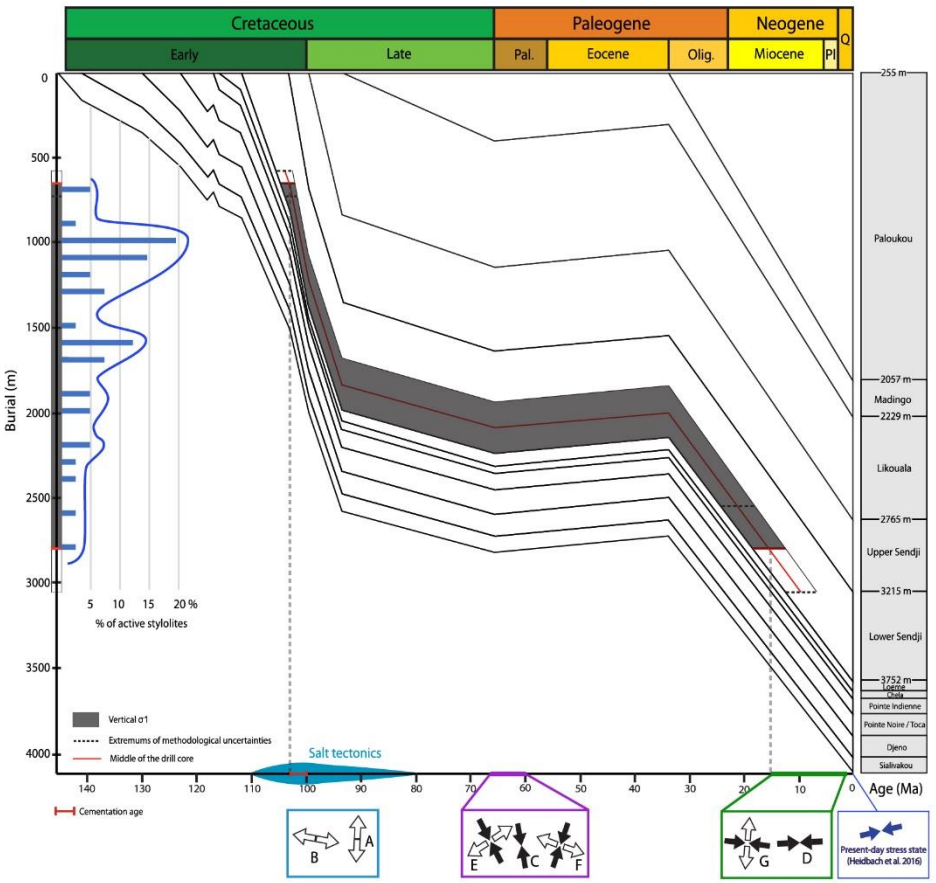


Fig. 14. Burial model of the syn-rift and post-rift formations of the Lower Congo Basin. The results of sedimentary stylolite roughness inversion in terms of depths of active pressure solution results are plotted as a depth histogram. Transitions from vertical to horizontal σ1 periods are illustrated by grey dashed lines (at 101 Ma, 75 Ma, 30 Ma, and 15 Ma) and these estimates are based on the middle of the drill core (indicated by the red line along the burial model). Dark grey areas show periods with vertical σ1 whereas black dashed lines indicate methodological uncertainty limits. The blue area represents the period of active salt tectonics. The average orientation of the horizontal stresses are shown as arrows (with σ1 in black and σ3 in white) in the map view for stress tensors likely coeval with salt tectonics (A and B, blue) possibly related to the intraplate NNW to NNE compressional event during the Maastrichtian-Paleocene times (C, E, and F, purple) and possibly related to the Atlantic ridge push (D and G, green). The present-day stress state is displayed by blue arrows (Heidbach et al., 2016).

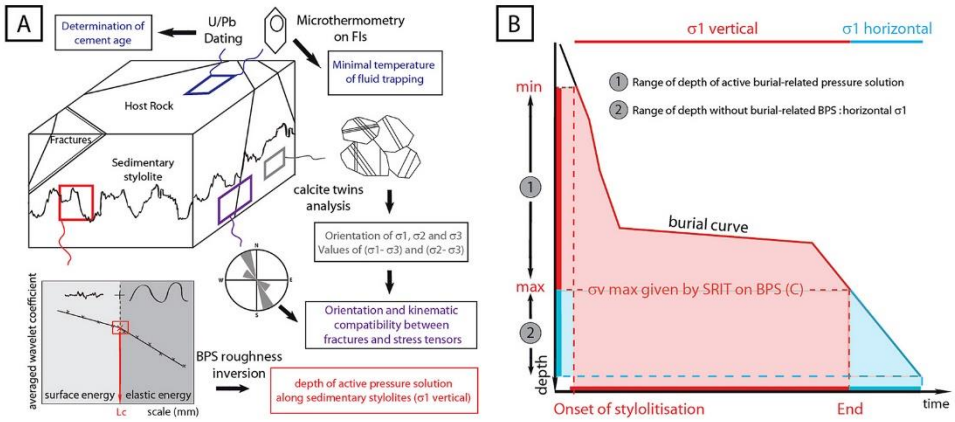


Fig. 15. A. Workflow of the multi-technique approach used in this study. B. Representation of the time conversion method for paleoburial obtained by stylolite roughness inversion using the burial model. Red periods are dominated by a vertical $\sigma_1$ as deduced from continuous stylolitization and blue periods are dominated by a σ1 that is likely no longer vertical, hence likely horizontal.

recorded in the N'Kossa field since this period corresponds to active pressure –solution along BPS under a vertical σ1 in the Sendji Fm (Fig. 16) and to the maximum of salt tectonic activity. The late Maastrichtian-early Paleocene N–S to NW-SE compressional episode described by Guiraud and Bosworth (1997) between 67 and 60 Ma could instead be consistent with our tensor groups C, E and F. A stress regime very close to our tensor group C was also recorded in two other locations in the pre-salt Toca Fm: (1) in a well located 2 km away from well 1 and (2) in a well located 46 km NE from well 1, closer to the continent (Bah et al., 2022). The record of this stress regime in a pre-salt formation precludes any possible halokinetic origin for this stress and therefore argues in favor of the far-field transfer of compressional crustal stresses. This supports the idea that the supra-salt formations which also recorded this state of stress were mechanically recoupled/welded to the underlying formations at that time, possibly because of the nearly complete salt removal.

The E-W compression tensor of group D is comparable to the current stress regime outlined by Heidbach et al. (2016). Additionally, Ziegler et al. (1995) and Guiraud et al. (2005) observed an E-W compressional stress regime in Africa, while Delvaux and Barth (2010) and Nkodia et al. (2020) noted a similar trend in the Congolese margin and continental Congo. These findings suggest a possible common origin for this compression. Ziegler et al. (1995) and Nkodia et al. (2020) further proposed that this intraplate E-W compression that prevailed from the Miocene onwards likely reflects a ridge push effect. The prevalence of this stress field with horizontal σ1 since ~15 Ma in the N'Kossa field would coincide with the definite end of compaction-related stylolitiza - tion there and may reflect the final switch of σ1 from vertical to horizontal due to gravitational ridge push forces overcoming overburden weight. Similarly, the strike-slip stress regime with σ1 oriented E-W (tensor group G) marks the onset of the ridge push effect during the Miocene, evolving towards pure compression in the present-day. This

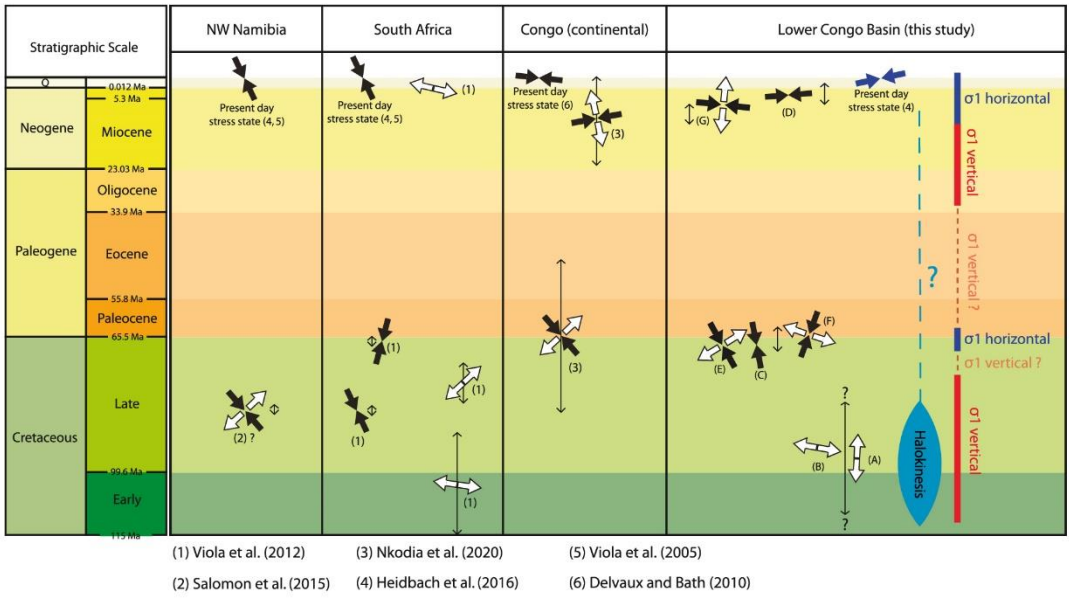


Fig. 16. Compilation of time distribution of tectonic events and related stress orientations (projected to the present-day position of Africa) since early Cretaceous time recorded in Congo, North West Namibia, and South Africa, together with the results of the present study.

interpretation is consistent with the suggestion by Wiens and Stein (1983, 1985) that the ridge push effect can efficiently control lithospheric stress long after the initiation of the spreading ridge.

The contribution of the ridge push effect to the Miocene to the present-day stress field can theoretically be questioned because of the large distance between the oceanic ridge and the passive margin (about 2400 km) since 15 Ma. However, the magnitude of the ridge-push force appears to be significantly less than the integrated strength of the oceanic part of the African (Nubian) plate, so the oceanic part of the plate is very little deformed and the stresses associated with the gravitational potential energy of the mid-Atlantic ridge may be transferred far into the interior of the oceanic and continental parts of the African plate (Mahatsente and Coblentz, 2015). Our interpretation is also in line with the work of Withjack et al. (1995) who reported that during the development of the passive margin of southeastern Canada, the Fundy rift basin on the western edge of the margin experienced shortening possibly associated with sea-floor spreading processes such as ridge push or continental resistance to plate motion. Recently, Nkodia et al. (2020) proposed that the present-day stress pattern in West-central Africa could be related to stress loading of the passive margin and interior Congo by the oceanic transform faults extending onland, triggering the reactivation of well oriented fault systems on the continental margin and onshore. In this scenario, the present-day stress pattern would not be controlled strictly speaking by the ridge push itself but would still be linked to a seafloor spreading process.

One can nevertheless wonder about possible alternate deep stress sources for the Miocene to present-day E-W compression. Medvedev (2016) suggest a mixed origin of the state of stress throughout the African plate, including density variations within the lithosphere, traction of the basal mantle, and flexural loading of the lithosphere in addition to the ridge push effect, in agreement with the findings of Pascal and Cloetingh (2009) in the south Norway shelf. The respective contributions of these various stress sources to the Miocene to present-day stress field at the west Africa passive margin remain to date poorly constrained.

To sum up, the inversion of calcite twins applied to the Sendji Fm suggests that the west African passive margin experienced a complex post-rift tectonic history including compressional events possibly related to far-field tectonic and gravitational stress transfer from active plate boundaries. Our interpretations are therefore consistent with earlier claims that the late Cretaceous–Cenozoic intraplate contractional deformation at the Norwegian continental shelf (northern Atlantic) was possibly related to far-field effects of active plate-margin processes and transfer of stresses across the plate as a consequence of the Alpine orogeny, with additional significant contribution of ridge push from the North Atlantic spreading particularly during the Neogene (Vågnes et al., 1998).

### 6.3. Stress magnitudesin the Sendji Fm and implications for fracture prediction in the reservoir

The combination of vertical stress estimates derived from the burial model with differential stress values provided by calcite twinning paleopiezometry enables us to estimate principal stress magnitudes at the time of deformation (Lacombe and Laurent, 1992; Lacombe, 2007). The comparison of the resulting values against the strength of the intact rock (i.e., its failure envelope) would serve not only as a test of the internal consistency of our result but may also help predict whether fracturing can be expected, hence predicted in the reservoir at the time of the successive stress regimes. To that aim, $\sigma_V$ magnitudes were calculated using equation (3) considering the weight of the overlying rock column either in dry conditions, $\sigma_V = \rho g h$ assuming nearly 0 fluid pressure, or assuming hydrostatic fluid pressure, $\sigma_V = (\rho - \rho_w) g h$, with $\rho$ the dry density of the rock column above the stylolite ($g.m^{-3}$), $\rho_w$ the density of water ($g.m^{-3}$), g the gravitational field acceleration ($m.s^{-2}$), and h the depth (m). Subsequently, we consider that the tangency of the ($\sigma1$-$\sigma3$) Mohr circle to the failure envelope is indicative of rock failure.

The late Maastrichtian-early Paleocene NNW to NNE compressional-strike-slip tectonic event was recorded by calcite twins (stress tensor groups E, C, and F) when the formation was buried at a nearly constant depth of 2100 m, which corresponds to a mean value of the vertical stress ($\sigma2$ or $\sigma3$) of ~49 MPa in dry conditions (Fig. 17A). The Mohr circles for stress tensor group E indicate rock failure whereas the Mohr circles for stress tensor groups C and F lie below the failure envelope (Fig. 17A) but can indicate failure if we consider the 30% of uncertainties on differential stress values. Hydrostatic conditions allow for rock failure for stress tensor group C but stress tensor groups E and F lie slightly above the Mohr envelope (Fig. 17B). This suggests that rock failure can be expected but low fluid pressure conditions in the reservoir at that time. No observed fracture could be assigned with certainty to the strike-slip stress regime (tensor groups E and F), but some may have been missed during coring or misinterpreted when related to halokinesis (see section 6.2.2.1). This result is consistent with the observations of mesoscale faulting related to this event in continental western Africa (Nkodia et al., 2020; Viola et al., 2012) although the investigated rocks were different there.

For the Neogene compressional phase with horizontal $\sigma_1$ trending E-W, the estimated vertical stress for tensor group D in dry conditions is 80 MPa at present-day, while the estimated vertical stress for tensor group G is 73 MPa at ~10 Ma in dry conditions (Fig. 17C). The Mohr circles for stress tensor groups D and G lie below the rupture envelope in dry conditions (Fig. 17C and D) and under hydrostatic conditions (Fig. 17D) but in the latter, considering uncertainties (~30%), failure would, however, be possible despite being unlikely. These observations indicate that despite relatively high differential stress magnitudes (especially for stress tensor group D), this phase would not cause significant faulting and that there was likely no fluid overpressure at that time.

For the E-W and N–S extensions that we propose to relate to halokinesis, we assume a $\sigma V$ of 49 MPa in dry conditions corresponding to the maximum burial depth of the Sendji Fm at the end of the main halokinetic deformation, at about 75 Ma. The resulting Mohr circles are tangent to the rock failure envelope thus predicting extensional faulting related to this event under a nearly null fluid pressure in the reservoir (Fig. 17E). This is consistent with the occurrence of mode II fractures in our dataset (Fig. 13) and with the extensional faulting associated with salt tectonics in the N'Kossa field.

Because the unique investigated core comes from an area where two large faults intersect and because the local salt flow might have altered the far-field stress transfer, one can wonder whether the local stress record is significant and representative of the scale of the oil field. In particular, the regional stress field might have been spatially deviated locally by the structures, with additional possible stress concentration in the fault damage zones leading to overestimated, hence anomalous, stress magnitudes. It must first be noticed that the extensional stress record (stress tensor groups A and B) is consistent with the kinematics of the normal faults bounding the area investigated, and that the associated differential stress magnitudes combined with the rock strength envelope derived from geomechanical tests consistently indicate normal faulting. After the salt tectonics phase ceased, these normal faults have had limited activity, with expectedly little or no reactivation in response to the post-rift late Cretaceous-Tertiary strike-slip and/or compressional stress fields (stress tensor groups E-C-F and G-D). As a result, one can safely assume little or no spatial local deviation of the remote stress fields. This is confirmed by the similarity of the post-rift stress orientations identified in the supra-salt Sendji Fm with (1) the stress orientations reconstructed in the infra-salt TOCA formation in a slightly distant well in the N'Kossa field (Bah et al., 2022) and (2) the results of previous stress studies (e.g., Viola et al., 2012). On the same line, the Mohr constructions provide no evidence of overestimation of the stress magnitudes for stress tensor groups E-C-F and G-D, with stress magnitudes never exceeding the rock strength in agreement with the absence of any related fractures in the core. Thus, we are confident that our stress results remain valid at the first order away from the well from which they

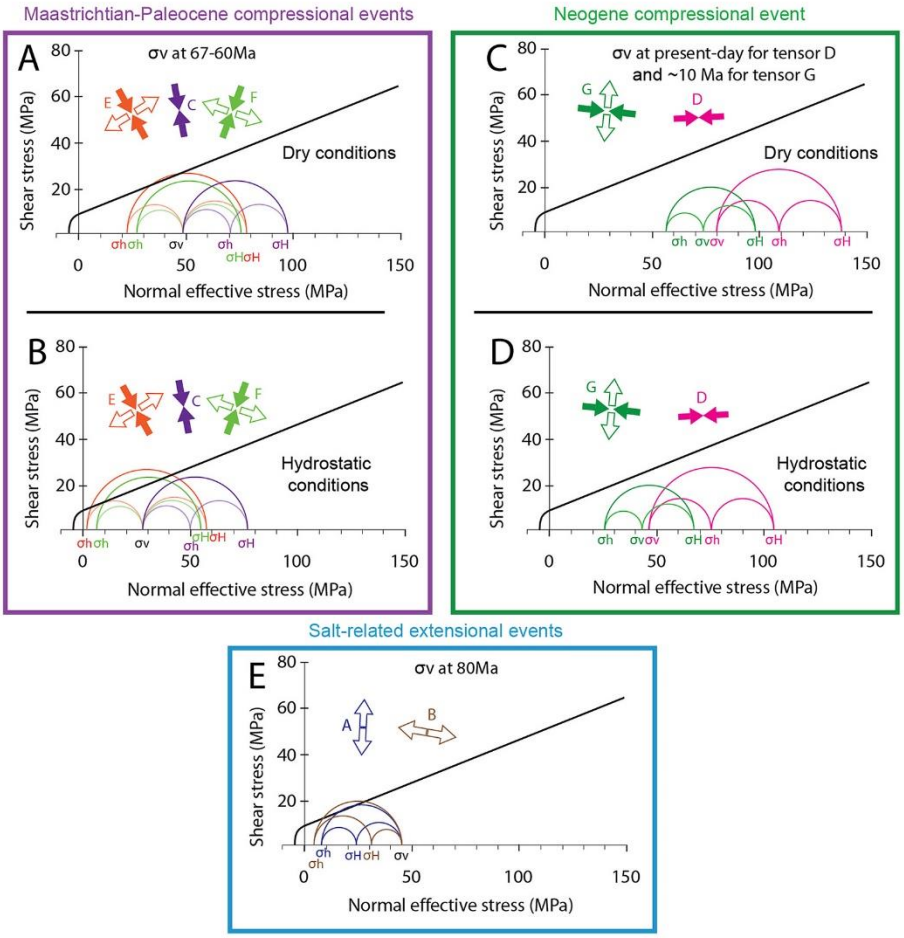


Fig. 17. Mohr diagrams showing the Mohr failure envelope of the Sendji Fm determined from rock mechanics tests and the Mohr circles related to differential stress magnitudes derived from the inversion of calcite twins from each tectonic event, in dry and hydrostatic conditions (see text for details). A, B: Mohr construction for tensor groups E, C, and F related to the far-field Maastrichtian-Paleocene compression between 67 and 60 Ma for dry conditions (A, σV = 49 MPa) and hydrostatic conditions (B, σV = 29 MPa). C, D: Mohr construction for tensor groups D and G related to Atlantic ridge push at present-day and at ~ 10 Ma respectively for dry conditions (C, σV = 80 MPa for tensors group D and 73 Ma for tensors group G) and hydrostatic conditions (D, σV = 47 MPa for tensors group D and 42 for tensors group G). E. Mohr construction for tensor groups A and B related to salt tectonics at 75 Ma in dry conditions (σV = 49 MPa) σV: vertical principal stress, σh: minimum horizontal principal stress and σH: maximum horizontal principal stress.

were established and are regionally representative.

### 6.4. Tentative reconstruction of the structural evolution of the N'Kossa structure

The main steps of the paleostress and paleoburial history of the Sendji Fm in the framework of the structural evolution of the N'Kossa structure are summarized through eight major stages illustrated in Fig. 18. The first stage (Fig. 18A, Early Albian) shows the deposition of the Lower Sendji on the Loeme salt, assumed to be still constant in thickness. The loading caused by the lower Sendji deposition initiated the movement of the underlying salt which began its migration toward the west of the margin. During the Upper Sendji deposition, salt turtle backs and rafts intensified deformation from the previous stage. In this context, the salt tectonics increased the flexure of the overlying sedimentary deposit and caused fractures to develop down to the salt layer. N–S faults provided pathways for hot and saline fluids to ascend at ~101 Ma, causing early cementation of the Sendji carbonates (Fig. 18B). During the deposition of the Likouala Fm, between 101 and 93.5 Ma, salt tectonics reached its peak activity with the development of a raft structure bounded by listric normal faults (Fig. 18C and D). At the basin scale, from 101 to 80 Ma, the maximum principal stress was vertical, associated with continuous sedimentation. In this context, the configuration of the faults that border the raft has temporarily influenced the stress field. Stress tensor groups A and B reflect the extension induced by salt tectonics at the oil field scale. From 80 to 75 Ma, N–S and E-W extension were no longer recorded (halokinetic activity decreased significantly from 80 Ma) but σ1 remained vertical, only burial stress being likely involved at this stage (Fig. 18D).

Fig. 18E illustrates the stress state prevailing by the Latest Cretaceous-early Paleocene (~67-60 Ma). Until now, salt was abundant enough to act as a detachment level decoupling the Sendji Fm from the infra-salt formations. The progressive decrease of the salt thickness in the proximal part of the margin and its accumulation in the distal part allowed the welding of the salt detachment and the progressive recoupling of the supra-salt series with the pre-salt series and basement. As a result, the Sendji Fm recorded the late Maastrichtian-earliest Paleocene compression (stress tensor groups C, E, and F) that we interpret as being transferred from the distant Africa-Eurasia plate boundary. This far-field stress record is consistent with a cessation of sedimentation (plateau in the burial-time model) and the onset of reservoir uplift, and with a transient halt of dissolution along BPS (Fig. 15). Between 30 and 15 Ma, σ1 became temporarily vertical again before switching definitely to horizontal from ~15 Ma onwards (Fig. 18F). The cessation of dissolution along BPS since ~15 Ma in the Sendji Fm implies that the maximum stress σ1 was no longer vertical. Fig. 18G illustrates the record of stress tensor group G with an E-W oriented σ1 during the Paloukou Fm deposition whereas Fig. 18H illustrates the current stress state with the complete post-rift series deposited. The Atlantic ridge push is likely to be the main distant source of this Neogene stress field.

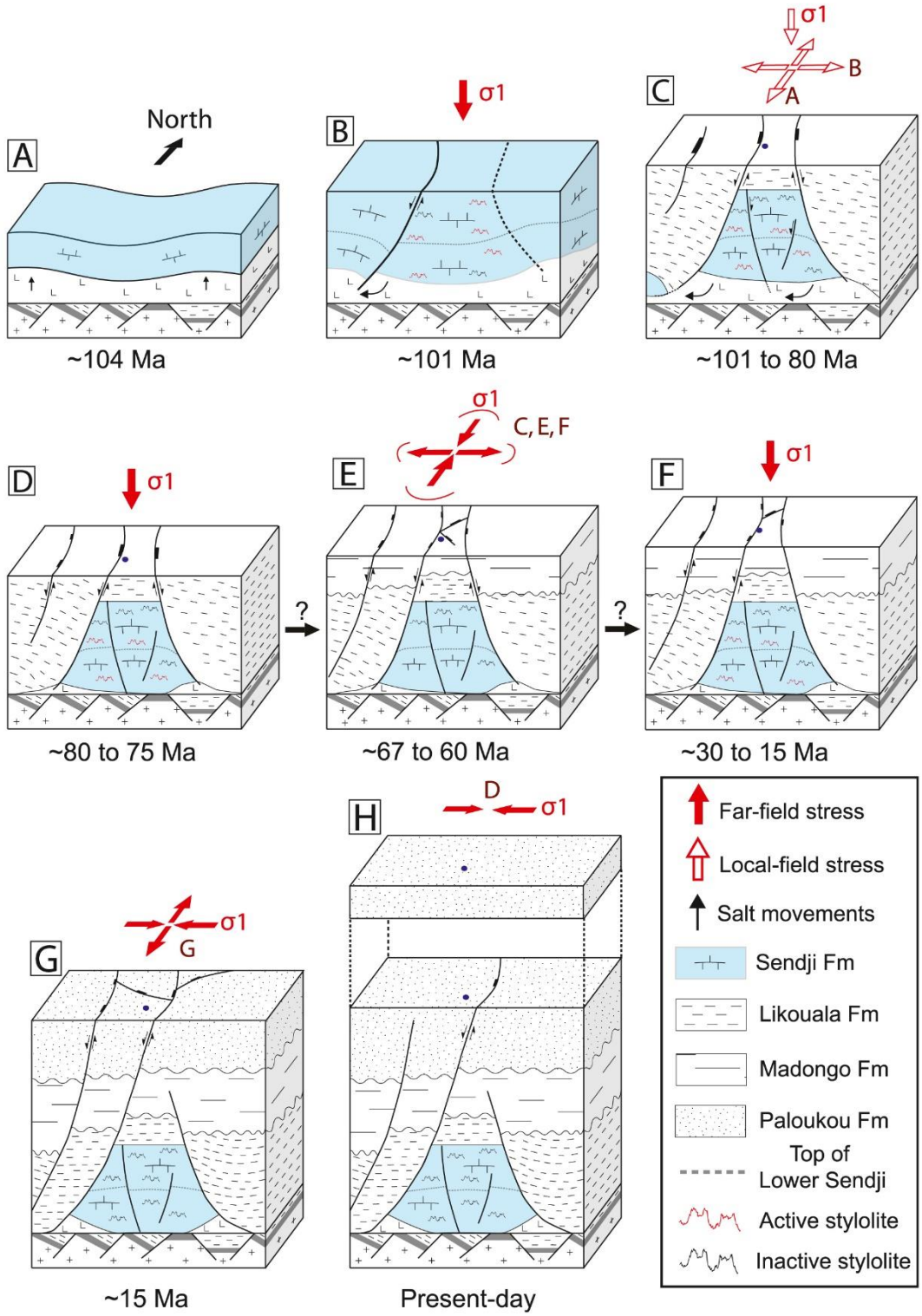


Fig. 18. Sketched structural evolution of the N'Kossa structure area and associated stress regimes at each burial stage of the Sendji Formation (blue layer), from 104 Ma to present-day.

## 7. Conclusions

This study focuses on the supra-salt carbonate Sendji Fm at the top of an offshore raft structure in the lower Congo basin (west Africa passive margin). The original combination of burial modeling, absolute U–Pb dating of diagenetic cement, fracture analysis, and stress inversion of calcite twins and sedimentary stylolite roughness in a 306 m drill core constitutes an original approach to obtaining unprecedented information on the burial and paleostress history of this reservoir. The analysis of calcite twins yielded successive stress regimes, the timing of which was constrained by the reconstruction of the maximum depth of active compaction-related pressure solution combined with burial modeling. During the burial, calcite twins recorded three main events: (1) extensional salt tectonics after 101 Ma and before 80 Ma, with E-W extension alternating with N–S extension; (2) NNW-SSE to NNE-SSW compression between 67 and 60 Ma likely related to the far-field transfer of orogenic stress from the Africa-Eurasia plate boundary; (3) E-W compression mainly related to the mid-Atlantic ridge push from 15 Ma onwards. We suggest that the sedimentary cover was decoupled from the crust during salt tectonics and then recoupled from the late Cretaceous onwards, leading to a complex stress history. Our results suggest that during its long-lasting, post-rift geological evolution, the west African passive margin underwent the combined influence of local gravitational stress related to salt tectonics and of far-field tectonic and gravitational lithospheric stress transmitted from distant plate boundaries. These findings may have obvious implications for other passive margins worldwide.

Beyond regional implications, our study reveals the unique potential of the combination of thermometric, geochronological, microstructural and paleopiezometric analyses on cores for the reconstruction of the burial history and paleostress evolution of poorly accessible, deep-buried reservoirs like those located in offshore passive margins. This new information is of prime importance for the understanding and prediction of fracture development, timing of diagenetic cementation, duration of chemical compaction (stylolitization), and fluid circulations, hence of carbonate reservoir properties.

## Declaration of competing interest

The authors declare that they have no known competing financial interests or personal relationships that could have appeared to influence the work reported in this paper.

## Data availability

Data will be made available on request.

## Acknowledgments

The authors are very grateful to TotalEnergies for the complete financial support of this research, for providing the cores, and for permission to publish. We would like to thank Philippe Marchina for his help in carrying out the geomechanical tests and for the discussions on the results, and Abel Guihou for his technical support in U–Pb analyses by LA-ICPMS. NEB is funded through the isite-E2S, supported by the ANR PIA and the Rėgion Nouvelle-Aquitaine. The laser UPb dating analyses were carried out as part of the CEREGE-Total Energies collaborative R&D project DATCARB (2018 –2021), co-funded by the "Excellence Initiative " program of Aix Marseille University A*MIDEX, TotalEnergies, and Sud region. The constructive comments by Laura Giambiagi, Enrique Gomez-Rivas, and an anonymous reviewer helped improve the quality of the manuscript.

## Appendix A. Supplementary data

Supplementary data to this article can be found online at https://doi.org/10.1016/j.marpetgeo.2023.106219 .

## References

Aharonov, E., Katsman, R., 2009. Interaction between pressure solution and clays in stylolite development: insights from modeling. Am. J. Sci. 309 (7), 607–632.

Ala, M.A., Selley, R.C., 1997. The west African coastal basins. In: Sedimentary Basins of the World, vol. 3. Elsevier, pp. 173–186.

Amrouch, K., Lacombe, O., Bellahsen, N., Daniel, J.-M., Callot, J.P., 2010. Stress and strain patterns, kinematics and deformation mechanisms in a basement-cored anticline: sheep Mountain anticline (Wyoming, USA). Tectonics 29, TC1005 .

Anka, Z., Seranne, M., Di Primio, R., 2010. Evidence of a large Upper-Cretaceous depocentre across the Continent-Ocean boundary of the Congo-Angola basin. Implications for palaeo-drainage and potential ultra-deep source rocks. Mar. Petrol. Geol. 27 (3), 601–611.

Artyushkov, E.V., 1973. Stresses in the lithosphere caused by crustal thickness inhomogeneities. J. Geophys. Res. 78 (32), 7675–7708.

Bah, B., Beaudoin, N.E., Lacombe, O., Girard, J.P., Gout, C., Godeau, N., Deschamps, P., 2023. Multi-proxy reconstruction of the burial history and porosity evolution of the TOCA carbonate formation in the lower Congo basin (south west Africa). Mar. Petrol. Geol., 106018

Bah, B., Lacombe, O., Beaudoin, N., Girard, J.-P., Gout, C., Godeau, N., 2022. Paleoburial and Paleostress History of a Carbonate Syn-Rift Reservoir : Constraints from Inversion of Calcite Twins and Stylolite Roughness in the Toca Formation (Lower Congo Basin, South Atlantic), vol. 2022. EGU General Assembly 2022, Vienna, Austria, pp. 23–27. https://doi.org/10.5194/egusphere-egu22-13406 . EGU22-13406.

Barabási, A.L., Stanley, H.E., 1995. Fractal conceptsin surface growth Cambridge university press.

Beaudoin, N., Lacombe, O., 2018. Recent and future trends in paleopiezometry in the diagenetic domain: insights into the tectonic paleostress and burial depth history of fold-and-thrust belts and sedimentary basins. J. Struct. Geol. 114, 357–365.

Baudouy, S., LeGorjus, C., 1991. Sendji field — People's Republic of Congo, Congo Basin. In: Beaumont, E.A., Foster, N.H. Ž (Eds.), Structural Traps V: AAPG Treatise of Petroleum Geology, Atlas of Oil and Gas Fields, pp. 121–149.

Beaudoin, N., Gasparrini, M., David, M.E., Lacombe, O., Koehn, D., 2019. Bedding-parallel stylolites as a tool to unravel maximum burial depth in sedimentary basins: application to Middle Jurassic carbonate reservoirs in the Paris basin, France. Geological Society of America. Bulletin 131 (7–8), 1239–1254.

Beaudoin, N.E., Lacombe, O., Hoareau, G., Callot, J.P., 2022. How the geochemistry of syn-kinematic calcite cement depicts past fluid flow and assists structural interpretations: a review of concepts and applications in orogenic forelands. Geol. Mag. 159 (11–12), 2157–2190.

Beaudoin, N., Lacombe, O., Koehn, D., David, M.E., Farrell, N., Healy, D., 2020a. Vertical stress history and paleoburial in foreland basins unravelled by stylolite roughness paleopiezometry: insights from bedding-parallel stylolites in the Bighorn Basin, Wyoming, USA. J. Struct. Geol. 136, 104061 .

Beaudoin, N.E., Labeur, A., Lacombe, O., Koehn, D., Billi, A., Hoareau, G., Boyce, A., John, C.M., Marchegiano, M., Roberts, N.M., Millar, I.L., Claverie, F., Pecheyran, C., Callot, J.P., 2020b. Regional-scale paleofluid system across the Tuscan Nappe–Umbria–Marche Apennine Ridge (northern Apennines) as revealed by mesostructural and isotopic analyses of stylolite–vein networks. Solid Earth 11 (4), 1617–1641.

Beglinger, S.E., Doust, H., Cloetingh, S., 2012. Relating petroleum system and play development to basin evolution: west African South Atlantic basins. Mar. Petrol. Geol. 30 (1), 1–25.

Bertotti, G., de Graaf, S., Bisdom, K., Oskam, B., Vonhof, H.B., Bezerra, F.H., et al., 2017. Fracturing and fluid-flow during post-rift subsidence in carbonates of the Jandaíra Formation, Potiguar Basin, NE Brazil. Basin Res. 29 (6), 836–853.

Bott, M.H.P., 1993. Modelling the plate-driving mechanism. J. Geol. Soc. 150 (5), 941–951.

Bracken, B. R., 1994, Syn-rift lacustrine beach and deltaic sandstone reservoirs- pre-salt (Lower Cretaceous) of Cabinda, Angola, west Africa, in A.J. Lomando, B. C. Schrieber, and P. M. Harris, eds., Lacustrine Reservoirs and Depositional Systems: SEPM Core Workshop No. 19, p. 173-200.

Brice, S.E., Cochran, M.D., Pardo, G., Edwards, A.D., 1982. Tectonics and sedimentation of the South Atlantic Rift Sequence. In Studies in Continental Margin Geology. AAPG Mem. No. 34, ed. J. S. Watkins, C. L. Drake, pp. 5-1 8. Tulsa, Okla: Am. Assoc. Pet. Geol.

Brognon, G.P., Verrier, G.R., 1966. Oil and geology in cuanza basin of Angola. AAPG (Am. Assoc. Pet. Geol.) Bull. 50 (1), 108–158.

Brownfield, M.E., Charpentier, R.R., 2006. Geology and Total Petroleum Systems of the West-Central Coastal Province (7203), West Africa (No. 2207-B). US Geological Survey.

Burkhard, M., 1993. Calcite twins, their geometry, appearance and significance as stress-strain markers and indicators of tectonic regime: a review. J. Struct. Geol. 15 (3–5), 351–368.

Cainelli, C., Mohriak, W.U., 1999. Some remarks on the evolution of sedimentary basins along the Eastern Brazilian continental margin. Episodes-Newsmagazine Int. Uni. Geol. Sci. 22 (3), 206–216.

Catuneanu, O., Wopfner, H., Eriksson, P.G., Cairncross, B., Rubidge, B.S., Smith, R.M.H., Hancox, P.J., 2005. The Karoo basins of south-central Africa. J. Afr. Earth Sci. 43 (1–3), 211–253.

Chaboureau, A.C., Guillocheau, F., Robin, C., Rohais, S., Moulin, M., Aslanian, D., 2013. Paleogeographic evolution of the central segment of the South Atlantic during Early Cretaceous times: paleotopographic and geodynamic implications. Tectonophysics 604, 191–223.

Craddock, J.P., Jackson, M., van der Pluijm, B.A., Versical, R.T., 1993. Regional shortening fabrics in eastern north America: far-field stress transmission from the appalachian-ouachita orogenic belt. Tectonics 12 (1), 257–264.
Covey-Crump, S.J., Schofield, P.F., Oliver, E.C., 2017. Using neutron diffraction to examine the onset of mechanical twinning in calcite rocks. J. Struct. Geol. 100, 77–97.
Delpomdor, F., Tack, L., Préat, A., 2008. Microstructures in the Neoproterozoic Tillites Around the Congo River Basin (CRB), Democratic Republic of Congo (DRC): Comparison with the Karoo Tillites from the Dekese Borehole in the CRB. In: In 22nd Colloquium of African Geology (CAG22) & 13th Conference of the Geological Society of Africa (GSAf13), p. 108.
Delvaux, D., Barth, A., 2010. African stress pattern from formal inversion of focal mechanism data. Tectonophysics 482 (1–4), 105–128.
Duval, B., Cramez, C., Jackson, M.P.A., 1992. Raft tectonics in the Kwanza basin, Angola. Mar. Petrol. Geol. 9 (4), 389–404.
Ebner, M., Koehn, D., Toussaint, R., Renard, F., Schmittbuhl, J., 2009. Stress sensitivity of stylolite morphology. Earth Planet Sci. Lett. 277 (3–4), 394–398.
Ebner, M., Piazolo, S., Renard, F., Koehn, D., 2010. Stylolite interfaces and surrounding matrix material: nature and role of heterogeneities in roughness and microstructural development. J. Struct. Geol. 32 (8), 1070–1084.
Ehrenberg, S.N., 2006. Porosity destruction in carbonate platforms. J. Petrol. Geol. 29 (1), 41–52.
Ferrill, D.A., Morris, A.P., Evans, M.A., Burkhard, M., Groshong Jr., R.H., Onasch, C.M., 2004. Calcite twin morphology: a low-temperature deformation geothermometer. J. Struct. Geol. 26 (8), 1521–1529.
Gaullier, V., Brun, J.P., Gue, G., Lecanu, H., 1993. Raft tectonics: the effects of residual topography below a salt de' collement. Tectonophysics 228 (3–4), 363–381.
Godeau, N., Deschamps, P., Guihou, A., Leonide, P., Tendil, A., Gerdes, A., et al., 2018. U-Pb dating of calcite cement and diagenetic history in microporous carbonate reservoirs: case of the Urgonian Limestone, France. Geology 46 (3), 247–250.
Goldstein, R.H., Reynolds, T.J., 1994. Systematics of Fluid Inclusions in Diagenetic Minerals.
Gomez-Rivas, E., Martín-Martín, J.D., Bons, P.D., Koehn, D., Griera, A., Travé, A., et al., 2022. Stylolites and stylolite networks as primary controls on the geometry and distribution of carbonate diagenetic alterations. Mar. Petrol. Geol. 136, 105444.
Guiraud, R., Bosworth, W., 1997. Senonian basin inversion and rejuvenation of rifting in Africa and Arabia: synthesis and implications to plate-scale tectonics. Tectonophysics 282 (1–4), 39–82.
Guiraud, R., Bosworth, W., Thierry, J., Delplanque, A., 2005. Phanerozoic geological evolution of northern and central Africa: an overview. J. Afr. Earth Sci. 43 (1–3), 83–143.
Harris, N.B., 2000. Evolution of the Congo rift basin, west Africa: an inorganic geochemical record in lacustrine shales. Basin Res. 12 (3-4), 425–445.
Heidbach, O., Rajabi, M., Reiter, K., Ziegler, M., 2016. World Stress Map 2016. GFZ Data Services.
Heine, C., Zoethout, J., Müller, R.D., 2013. Kinematics of the South Atlantic rift. Solid Earth 4 (2), 215–253.
Hintze, J.L., Nelson, R.D., 1998. Violin plots: a box plot-density trace synergism. Am. Statistician 52 (2), 181–184.
Jamison, W.R., Spang, J.H., 1976. Use of calcite twin lamellae to infer differential stress. Geol. Soc. Am. Bull. 87 (6), 868–872.
Johnston, S.T., 2000. The Cape Fold Belt and Syntaxis and the rotated Falkland Islands: dextral transpressional tectonics along the southwest margin of Gondwana. J. Afr. Earth Sci. 31 (1), 51–63.
Jolivet, L., Faccenna, C., Agard, P., Frizon de Lamotte, D., Menant, A., Sternai, P., Guillocheau, F., 2016. Neo-Tethys geodynamics and mantle convection: from extension to compression in Africa and a conceptual model for obduction. Can. J. Earth Sci. 53 (11), 1190–1204.
Kadima, E., Delvaux, D., Sebagenzi, S.N., Tack, L., Kabeya, S.M., 2011. Structure and geological history of the Congo Basin: an integrated interpretation of gravity, magnetic and reflection seismic data. Basin Res. 23 (5), 499–527.
Koehn, D., Ebner, M., Renard, F., Toussaint, R., Passchier, C.W., 2012. Modelling of stylolite geometries and stress scaling. Earth Planet Sci. Lett. 341, 104–113.
Koehn, D., Rood, M.P., Beaudoin, N., Chung, P., Bons, P.D., Gomez-Rivas, E., 2016. A new stylolite classification scheme to estimate compaction and local permeability variations. Sediment. Geol. 346, 60–71.
Koehn, D., Koehler, S., Toussaint, R., Ghani, I., Stollhofen, H., 2022. Scaling analysis, correlation length and compaction estimates of natural and simulated stylolites. J. Struct. Geol., 104670
Kounov, A., Viola, G., De Wit, M., Andreoli, M.A.G., 2009. Denudation along the Atlantic passive margin: new insights from apatite fission-track analysis on the western coast of South Africa. Geol. Soc. London Special Publ. 324 (1), 287–306.
Kulikowski, D., Amrouch, K., 2017. Combining geophysical data and calcite twin stress inversion to refine the tectonic history of subsurface and offshore provinces: a case study on the Cooper-Eromanga Basin, Australia. Tectonics 36, 515–541.
Labeur, A., Beaudoin, N.E., Lacombe, O., Emmanuel, L., Petracchini, L., Daëron, M., et al., 2021. Burial-deformation history of folded rocks unraveled by fracture analysis, stylolite paleopiezometry and vein cement geochemistry: a case study in the Cingoli Anticline (Umbria-Marche, Northern Apennines). Geosciences 11 (3), 135.
Lacombe, O., Angelier, J., Laurent, P., Bergerat, F., Tourneret, C., 1990. Joint analyses of calcite twins and fault slips as a key for deciphering polyphase tectonics: burgundy as a case study. Tectonophysics 182 (3–4), 279–300.
Lacombe, O., Laurent, P., 1992. Determination of principal stress magnitudes using calcite twins and rock mechanics data. Tectonophysics 202 (1), 83–93.
Lacombe, O., Laurent, P., 1996. Determination of deviatoric stress tensors based on inversion of calcite twin data from experimentally deformed monophase samples: preliminary results. Tectonophysics 255 (3–4), 189–202.
Lacombe, O., 2007. Comparison of paleostress magnitudes from calcite twins with contemporary stress magnitudes and frictional sliding criteria in the continental crust: mechanical implications. J. Struct. Geol. 29 (1), 86–99.
Lacombe, O., Amrouch, K., Mouthereau, F., Dissez, L., 2007. Calcite twinning constraints on late Neogene stress patterns and deformation mechanisms in the active Zagros collision belt. Geology 35 (3), 263–266.
Lacombe, O., 2010. Calcite twins, a tool for tectonic studies in thrust belts and stable orogenic forelands. Oil & Gas Sci. Tech. Revue d'IFP Energ. Nouvelles 65 (6), 809–838.
Lacombe, O., Parlangeau, C., Beaudoin, N.E., Amrouch, K., 2021a. Calcite twin formation, measurement and use as stress–strain indicators: a review of progress over the last decade. Geosciences 11 (11), 445.
Lacombe, O., Beaudoin, N., Hoareau, G., Labeur, A., Pecheyran, C., Callot, J.P., 2021b. Dating folding beyond folding, from layer-parallel shortening to fold tightening, using mesostructures : lessons from the Apennines, Pyrenees and Rocky Mountains. Solid Earth 12 (10), 2145–2157.
Laurent, P., Kern, H., Lacombe, O., 2000. Determination of deviatoric stress tensors based on inversion of calcite twin data from experimentally deformed monophase samples. Part II. Axial and triaxial stress experiments. Tectonophysics 327 (1–2), 131–148.
Lehner, P., De Ruiter, P.A.C., 1977. Structural history of atlantic margin of Africa. AAPG (Am. Assoc. Pet. Geol.) Bull. 61 (7), 961–981.
Lock, B.E., 1980. Flat-plate subduction and the Cape Fold Belt of South Africa. Geology 8 (1), 35–39.
Mahatsente, R., Coblentz, D., 2015. Ridge-push force and the state of stress in the Nubia-Somalia plate system. Lithosphere 7 (5), 503–510.
Martín-Martín, J.D., Gomez-Rivas, E., Gómez-Gras, D., Travé, A., Ameneiro, R., Koehn, D., Bons, P.D., 2018. Activation of stylolites as conduits for overpressured fluid flow in dolomitized platform carbonates. Geol. Soc. London Special Publ. 459 (1), 157–176.
Marton, L.G., Tari, G.C., Lehmann, C.T., 2000. Evolution of the Angolan passive margin, West Africa, with emphasis on post-salt structural styles. Geophy. Monograph Am. Geophysical Union 115, 129–150.
Medvedev, S., 2016. Understanding lithospheric stresses: systematic analysis of controlling mechanisms with applications to the African Plate. Geophys. J. Int. 207 (1), 393–413.
Mounguengui, M.M., Guiraud, M., 2009. Neocomian to early aptian syn-rift evolution of the normal to oblique-rifted north Gabon margin (interior and N'komi basins). Mar. Petrol. Geol. 26 (6), 1000–1017.
McGinnis, J.P., Driscoll, N.W., Karner, G.D., Brumbaugh, W.D., Cameron, N., 1993. Flexural response of passive margins to deep-sea erosion and slope retreat: implications for relative sea-level change. Geology 21 (10), 893–896.
Meyers, M.A., Vöhringer, O., Lubarda, V.A., 2001. The onset of twinning in metals: a constitutive description. Acta Mater. 49 (19), 4025–4039.
Moulin, M., 2003. Etude géologiqueet géophysiquedes margescontinentalespassives: exemple du Zaïre et de l'Angola(Doctoral dissertation, Universit é de Bretagne Occidentale).
Moulin, M., Aslanian, D., Unternehr, P., 2010. A new starting point for the South and equatorial Atlantic Ocean. Earth Sci. Rev. 98 (1–2), 1–37.
Newman, J., 1994. The influence of grain size and grain size distribution on methods for estimating paleostresses from twinning in carbonates. J. Struct. Geol. 16 (12), 1589–1601.
Nkodia, H.V., Miyouna, T., Delvaux, D., Boudzoumou, F., 2020. Flower structures in sandstones of the Paleozoic Inkisi Group (Brazzaville, Republic of Congo): evidence for two major strike-slip fault systems and geodynamic implications. S. Afr. J. Geol. 123 (4), 531–550.
Nürnberg, D., Müller, R.D., 1991. The tectonic evolution of the South atlantic from late jurassic to present. Tectonophysics 191 (1–2), 27–53.
Parlangeau, C., Lacombe, O., Schueller, S., Daniel, J.M., 2018. Inversion of calcite twin data for paleostress orientations and magnitudes: a new technique tested and calibrated on numerically-generated and natural data. Tectonophysics 722, 462–485.
Parlangeau, C., Dimanov, A., Lacombe, O., Hallais, S., Daniel, J.M., 2019. Uniaxial compression of calcite single crystals at room temperature: insights into twinning activation and development. Solid Earth 10 (1), 307–316.
Pascal, C., Cloetingh, S.A., 2009. Gravitational potential stresses and stress field of passive continental margins: insights from the south-Norway shelf. Earth Planet Sci. Lett. 277 (3–4), 464–473.
Penge, J., Munns, J.W., Taylor, B., Windle, T.M.F., 1999. Rift–raft Tectonics: Examples of Gravitational Tectonics from the Zechstein Basins of Northwest Europe. InGeological Society. In: Petroleum Geology Conference Series, vol. 5. Geological Society of London, London, pp. 201–213. No. 1.
Perrier, R., Quiblier, J., 1974. Thickness changes in sedimentary layers during compaction history; methods for quantitative evaluation. AAPG Bull. 58 (3), 507–520.
Rabinowitz, P.D., LaBrecque, J., 1979. The mesozoic South Atlantic ocean and evolution of its continental margins. J. Geophys. Res. Solid Earth 84 (B11), 5973–6002.
Raynaud, S., Carrio-Schaffhauser, E., 1992. Rock matrix structures in a zone influenced by a stylolite. J. Struct. Geol. 14 (8–9), 973–980.
Renard, F., Schmittbuhl, J., Gratier, J.P., Meakin, P., Merino, E., 2004. Three-dimensional roughness of stylolites in limestones. J. Geophys. Res. Solid Earth 109 (B3).
Roberts, N.M., Drost, K., Horstwood, M.S., Condon, D.J., Chew, D., Drake, H., et al., 2020. Laser ablation inductively coupled plasma mass spectrometry (LA-ICP-MS)

U–Pb carbonate geochronology: strategies, progress, and limitations. Geochronology 2 (1), 33–61.
Rocher, M., Lacombe, O., Angelier, J., Deffontaines, B., Verdier, F., 2000. Cenozoic folding and faulting in the south Aquitaine Basin (France): insights from combined structural and paleostress analyses. J. Struct. Geol. 22 (5), 627–645.
Rocher, M., Lacombe, O., Angelier, J., Chen, H.-W., 1996. Mechanical twin sets in calcite as markers of recent collisional events in a fold-and-thrust belt : evidence from the reefal limestones of southwestern Taiwan. Tectonics 15 (5), 984–996.
Rolland, A., Toussaint, R., Baud, P., Schmittbuhl, J., Conil, N., Koehn, D., et al., 2012. Modeling the growth of stylolites in sedimentary rocks. J. Geophys. Res. Solid Earth 117 (B6) .
Rolland, A., Toussaint, R., Baud, P., Conil, N., Landrein, P., 2014. Morphological analysis of stylolites for paleostress estimation in limestones. Int. J. Rock Mech. Min. Sci. 67, 212–225.
Rosenbaum, G., Lister, G.S., Duboz, C., 2002. Relative motions of Africa, iberia and europe during alpine orogeny. Tectonophysics 359 (1–2), 117–129.
Rowan, M.G., Tilton, J., Lebit, H., Fiduk, J.C., 2022. Thin-skinned extensional salt tectonics, counterregional faults, and the Albian Gap of Brazil. Marine and Petroleum Geology 137, 105478 .
Rowe, K.J., Rutter, E.H., 1990. Palaeostress estimation using calcite twinning: experimental calibration and application to nature. J. Struct. Geol. 12 (1), 1–17.
Rouby, D., Raillard, S., Guillocheau, F., Bouroullec, R., Nalpas, T., 2002. Kinematics of a growth fault/raft system on the West African margin using 3-D restoration. J. Struct. Geol. 24 (4), 783–796.
Salomon, E., Koehn, D., Passchier, C., Hackspacher, P.C., Glasmacher, U.A., 2015. Contrasting stress fields on correlating margins of the South Atlantic. Gondwana Res. 28 (3), 1152–1167.
Sapin, F., Ringenbach, J.C., Clerc, C., 2021. Rifted margins classification and forcing parameters. Sci. Rep. 11 (1), 1–17.
Schmittbuhl, J., Renard, F., Gratier, J.P., Toussaint, R., 2004. The roughness of stylolites: implications of 3D high-resolution topography measurements. Phys. Rev. Lett. 93 (23), 238501 .
Séranne, M., Anka, Z., 2005. South Atlantic continental margins of Africa: a comparison of the tectonic vs climate interplay on the evolution of equatorial west Africa and SW Africa margins. J. Afr. Earth Sci. 43 (1–3), 283–300.
Tack, L., Delvaux, D., Kadima, E., Delpomdor, F., Tahon, A., Dumont, P., et al., 2008. The 1.000 M Thick Redbeds Sequence of the Congo River Basin (CRB): a Generally Overlooked Testimony in Central Africa of Post-gondwana Amalgamation (550 Ma) and Pre-karoo Break-Up (320 Ma). In22nd Colloquium African Geology (CAG22), pp. 86–88.
Torsvik, T.H., Rousse, S., Labails, C., Smethurst, M.A., 2009. A new scheme for the opening of the South Atlantic Ocean and the dissection of an Aptian salt basin. Geophys. J. Int. 177 (3), 1315–1333.
Tourneret, C., Laurent, P., 1990. Paleo-stress orientations from calcite twins in the North Pyrenean foreland, determined by the Etchecopar inverse method. Tectonophysics 180 (2–4), 287–302.
Toussaint, R., Aharonov, E., Koehn, D., Gratier, J.P., Ebner, M., Baud, P., et al., 2018. Stylolites: a review. J. Struct. Geol. 114, 163–195.
Tullis, T.E., 1980. The use of mechanical twinning in minerals as a measure of shear stress magnitudes. J. Geophys. Res. Solid Earth 85 (B11), 6263–6268.
Turner, F.J., Griggs, D.T., Heard, H., 1954. Experimental deformation of calcite crystals. Geol. Soc. Am. Bull. 65 (9), 883–934.
Unternehr, P., G. Pèron-Pinvidic, G. Manatschal, and E. Sutra (2010), Hyper-extended crust in the South Atlantic: In search of a model, Pet. Geosci., 16, 207–215.
Vågnes, E., Gabrielsen, R.H., Haremo, P., 1998. Late Cretaceous–Cenozoic intraplate contractional deformation at the Norwegian continental shelf: timing, magnitude, and regional implications. Tectonophysics 300 (1–4), 29–46.
Viola, G., Kounov, A., Andreoli, M.A.G., Mattila, J., 2012. Brittle tectonic evolution along the western margin of South Africa: more than 500 Myr of continued reactivation. Tectonophysics 514, 93–114.
Wiens, D.A., Stein, S., 1983. Age dependence of oceanic intraplate seismicity and implications for lithospheric evolution. J. Geophys. Res. Solid Earth 88 (B8), 6455–6468.
Wiens, D.A., Stein, S., 1985. Implications of oceanic intraplate seismicity for plate stresses, driving forces and rheology. Tectonophysics 116 (1–2), 143–162 (r).
Withjack, M.O., Olsen, P.E., Schlische, R.W., 1995. Tectonic evolution of the Fundy rift basin, Canada: evidence of extension and shortening during passive margin development. Tectonics 14 (2), 390–405.
Wonham, J.P., Cyrot, M., Nguyen, T., Louhouamou, J., Ruau, O., 2010. Integrated approach to geomodelling and dynamic simulation in a complex mixed siliciclastic –carbonate reservoir, N'Kossa field, Offshore Congo. Geol. Soc. London Special Publ. 347 (1), 133–163.
Wright, K., Cygan, R.T., Slater, B., 2001. Structure of the (1014) surfaces of calcite, dolomite and magnesite under wet and dry conditions. Phys. Chem. Chem. Phys. 3, 839–844.
Zhou, S., Sandiford, M., 1992. On the stability of isostatically compensated mountain belts. J. Geophys. Res. Solid Earth 97 (B10), 14207–14221.
Ziegler, P.A., Cloetingh, S., van Wees, J.D., 1995. Dynamics of intra-plate compressional deformation: the Alpine foreland and other examples. Tectonophysics 252 (1–4), 7–59.
Zoback, M.L., 1992. First-and second-order patterns of stress in the lithosphere: the World Stress Map Project. J. Geophys. Res. Solid Earth 97 (B8), 11703–11728.

# Chapitre IV : Reconstitution des paléocontraintes dans un réservoir infra-salifère : le cas de la formation syn-rift TOCA

Ce chapitre est divisé en deux parties :

(1) un article à resoumettre au journal Tectonophysics après les révisions modérées demandées par l'éditeur.
(2) la présentation de données complémentaires sur l'inversion de la rugosité d'un stylolite tectonique et l'analyse de la susceptibilité magnétique sur des échantillons provenant de l'une des carottes de la formation TOCA (Well-1). Ces résultats n'ont pas été intégrés dans l'article car ils ne sont pas assez robustes (peu de données) pour une publication scientifique mais présentent néanmoins un intérêt certain quand ils sont combinés avec les autres approches pour la compréhension de l'évolution tectonique régionale.

En parallèle de ce qui a été réalisé sur la formation Sendji supra-salifère, il a été décidé de faire un travail symétrique sur les carbonates de la TOCA infra-salifère afin (1) de voir l'effet des contraintes sur le réservoir caractérisé précédemment dans le chapitre 2, et (2) pour discuter du rôle éventuel du sel dans le découplage des contraintes enregistrées au-dessus et au-dessous de lui pendant la phase halocinétique ayant affecté les formations supra-sel dans le bassin.

L'approche paléopiézométrique utilisée est la même que celle appliquée sur les carbonates supra-salifère (chapitre 3). Elle est appliquée sur deux carottes de forage offshore orientées ayant atteint les carbonates de la TOCA (Well-1 et Well-2). L'objectif était là-aussi de caractériser l'évolution des paléocontraintes des réservoirs carbonatés profondément enfouis sur la marge proximale offshore.

Les états de contraintes reconstruits par inversion des macles de la calcite dans la formation TOCA sont comparés avec ceux reconstruits dans la formation Sendji pour mieux contraindre le calendrier de la déformation enregistré par les macles de la calcite dans la formation TOCA infra-sel.

# Paleostress evolution of the Western Africa passive margin: new insights from calcite twinning paleopiezometry in the deeply buried syn-rift TOCA formation (Lower Congo basin).

Boubacar BAH[1], Olivier LACOMBE[1], Nicolas E. BEAUDOIN[2], Aniès ZEBOUDJ[1], Claude GOUT[2,3], Jean-Pierre GIRARD[2,3], Pierre-Alexandre TEBOUL[3]

[1] Sorbonne Université, Institut des Sciences de la Terre de Paris (ISTeP), CNRS-INSU, 75005 Paris, France.

[2] Universite de Pau et des Pays de l'Adour, Laboratoire des Fluides Complexes et Leurs Réservoirs (LFCR), E2S UPPA, CNRS, TotalEnergies, 64000 Pau, France.

[3] TotalEnergies, Centre Scientifique et Technique Jean Féger (CSTJF), 64000 Pau, France.

* Correspondence: boubacar.bah@sorbonne-universite.fr

## Abstract

Accurate characterization of reservoirs requires a good understanding of the paleostress history of the host sedimentary basin. This study aims at reconstructing the paleoburial and paleostress history of the syn-rift Barremian TOCA Fm. in the Lower Congo basin (West African margin). Two oriented borehole cores drilled offshore Congo were investigated using stress inversion techniques applied to calcite mechanical twins to constrain paleostress orientations and magnitudes. The inversion of calcite twins was performed on a widespread early diagenetic cement (~129 to ~113 Ma) and revealed that the TOCA Fm. has undergone a complex polyphase stress history, including (1) extensional stress regimes with σ1 vertical and σ3 trending NE-SW and WNW-ESE (N100) associated to the rifting episode preceding the opening of the South Atlantic (130 to 112 Ma), and with mean differential stresses of ~47 MPa for (σ1-σ3) and ~20 MPa for (σ2-σ3). The early N100 extension is associated with the development of normal faults striking N-S that likely reactivated inherited basement anisotropies. The direction of extension evolved during the Barremian into the main NE-SW extension marked by the dominant normal faults striking NW-SE. (2) Compressional and strike-slip stress regimes with horizontal σ1 oriented ~N-S possibly related to the far-field intraplate transmission of orogenic stresses generated at the distant Africa-Eurasia plate boundary at ~67-60 Ma, and with mean differential stresses of 40 MPa for (σ1-σ3) and 28 MPa for (σ2-σ3). (3) Compressional and strike-slip stress regimes with horizontal σ1 oriented ENE-WSW to ~E-W that we tentatively relate to the mid-Atlantic ridge push and prevailing since ~15 Ma onwards,

associated with mean differential stresses of ~45 MPa for (σ1-σ3) and ~18 MPa for (σ2-σ3). Our results reveal that the TOCA Fm. recorded mainly far-field stress effects that could be related to interactions between the African plate and surrounding plates, and that divergent passive margins may experience a complex tectonic history including both extensional and compressional events.

## 1. Introduction

Continental rifting and drifting result in the formation of divergent passive margins. During the rifting stage, extensional stress generally prevails. This extensional stress originates from boundary tectonic forces linked to plate motions, to frictional forces exerted by the convective mantle at the base of the lithosphere (e.g., Ziegler, 1995), and to a lesser extent to body forces developing in the lithosphere above mantle plumes (Bott, 1993; Burov and Gerya, 2014; Koptev et al., 2018). Structural and thermo-rheological inheritance may also play a role in modulating the local response of the rifted lithosphere (Cloetingh et al., 2013), causing high levels of structural complexity and possibly changing regional or local trends of extension during rifting (Morley et al., 2007).

The present-day stress pattern in the lithosphere is controlled at first order by plate boundary forces (Heidbach et al., 2007). At the regional scale however, additional local sources of stress are necessary to fully account for the orientation of the horizontal maximum principal stress SH and the tectonic regime. Within the oceanic part of plates, the oceanic ridge push often governs the intraplate stress field. This statement is supported by the observation that in many instances, the intraplate SH trends perpendicular to oceanic ridges in a strike-slip or thrust faulting regime (Zoback, 1992; Heidbach et al., 2008, 2016). At passive margins, the present-day stress field is often dominated by a SH oriented roughly perpendicular to both the trend of the margin and the oceanic ridge and in a strike-slip or thrust faulting regime, so the ridge push is thought to be a possible significant source of the present-day stress at passive margins (e.g., Pascal & Cloetingh, 2009). Other stress sources, such as gravitational stress arising from (1) lithosphere bending due to loading related to rapid sedimentation rates, (2) postglacial rebound, and (3) difference in elevation and associated gravitational potential energy between the continent and the margin, should not be neglected (Pascal, 2006; Pascal and Cloetingh, 2009). However, those are often considered as being of local and/or short term importance (Seeber and Armbruster, 1988; Stein et al., 1989; Zoback, 1992). During the long lasting post-rift evolution of passive margins between continental break-up to present day, it is also likely that both ridge push and

far-field compressional tectonic stresses transferred from distant convergent plate boundaries may have, at least transiently, played some role (Ziegler, 1995, Withjack et at al., 1995; Vagnes et al., 1998).

The South Atlantic passive margins result from the rifting between Africa and South America and subsequent oceanization (e.g., Chaboureau et al., 2013). However, their evolution is currently a matter of debate (Karl et al., 2013), with two contrasting theories on the tectonic and paleostress evolution on both sides of the South Atlantic (Salomon et al., 2015). Some authors argue that the Brazilian and SW African margins were influenced by flexure due to offshore sediment loading (e.g., Lima et al., 1997; Dauteuil et al., 2013; Reis et al, 2013). Cobbold et al., (2001) argue that the distant stresses of the Andean orogeny caused compression perpendicular to the Brazilian continental margin throughout the Cenozoic. On the African margin the upwelling of the African superplume, a large thermal anomaly in the lower mantle beneath southern Africa (e.g., Ritsema et al., 2011) is thought to be responsible for the high mean topography of southern and eastern Africa (e.g., Al-Hajri et al., 2009; Moucha and Forte, 2011; Flament et al., 2014).). The model of Japsen et al., (2012) favours the idea that both continental margins underwent the same multiple uplift events driven by the transfer of far-field stresses from one continent to the other. The different interpretations summarized above illustrate that the stress evolution at divergent passive margins like the West African margin is still poorly understood. Consequently, a better appraisal of the behaviour of divergent continental margins before and after continental break-up is essential to the understanding of plate tectonics and of the respective contribution of far-field gravitational or tectonic stresses. However, our knowledge of the paleostress history of passive margins suffers from the lack of direct paleostress information gained directly in the offshore domain.

Recent discoveries of deeply buried hydrocarbon reservoirs offshore Brazil have renewed the interest in understanding the sedimentary, burial and structural evolution of the presalt sedimentary series (Davison, 2007; Carminati et al., 2008; Saller et al., 2016; see synthesis in Teboul 2017). The term “presalt” refers to the lower Cretaceous deposits (mainly carbonates) underlying the widespread upper Aptian salt deposits (Guardado et al., 1989; McHargue, 1990; Dale et al., 1992). Structural and stratigraphic similarities of the plays encountered in both the Brazilian and the West African conjugate margins have been thoroughly documented (Brownfield & Charpentier, 2006; Chaboureau et al., 2013; Péron-Pinvidic et al., 2015; Thompson et al., 2015), inducing a similar exploration scheme for both areas. In subsurface exploration, structural information comes mainly from seismic data, while stratigraphic,

sedimentary and burial information comes from the study of drilling cores in exploration wells (Bjørlykke, 2014). In offshore sedimentary environments, especially in carbonate series, mesoscale fractures and stylolites as well as microscale deformation features such as calcite twins observed at core scale are the main markers of deformation and recorders of the stress evolution (Beaudoin and Lacombe, 2018). The analysis of calcite twins is a long established tool to unravel the paleostress history (see review in Lacombe, 2010 and Lacombe et al., 2021a), allowing for the reconstruction of both paleostress orientations and magnitudes in a variety of settings, including sedimentary basins (Lacombe et al., 1990, 1994; Rocher et al., 2000; Kulikowski and Amrouch, 2017), fold-and-thrust belts (Craddock et al., 1993; Rocher et al., 1996; Lacombe, 2001; Lacombe et al., 2007; Amrouch et al., 2010; 2011) and even oceanic environments (Craddock et al., 1994, 2004; Brandstätter et al., 2017).

This study aims at reconstructing the paleostress history of the deeply buried, Barremian (130-125 Ma) TOCA Fm. (TOCA stands for TOp CArbonates) in the offshore Lower Congo basin (West African passive margin) using the stress inversion of calcite mechanical twins from two oriented deep borehole cores. The timing of the reconstructed paleostresses is further constrained using earlier results on the inversion of the roughness of sedimentary stylolites (Bah et al., 2023; Zeboudj et al., 2023) and burial-time modeling (Bah et al., 2023; this study). The TOCA Fm. was selected because it was deposited during rifting (Harris, 2000; Beglinger et al., 2012) and is therefore likely to have recorded most of the tectonic evolution of the South Atlantic since the early Cretaceous. Our study complements earlier paleostress studies conducted onshore West Africa: in the Inkisi group (Paleozoic sandstone) in Republic of Congo (Nkodia et al., 2020), in the Etendeka volcanics and the Twyfelfontein Sandstone (Neocomian-Barremian) in Namibia (Salomon et al., 2015) and in the Proterozoic metamorphic rocks in Namaqualand, western South Africa (Viola et al., 2012). It must be noticed that because syn-rift formations are scarce or absent onshore, the dating of the paleostress events has only been indirect to date, i.e., based mainly on regional correlations of paleostress orientations. Beyond providing important information on the paleostress regimes at the reservoir scale, this study will also feed the debate about the extent to which far-field tectonic and gravitational lithospheric stress transferred from active plate boundaries may have played a role in the evolution of the West African passive margin. To that respect, the work reported here has implications for the interpretation of the dynamics of divergent passive margins worldwide.

# 2. Geological setting

## 2.5.Tectono-sedimentary framework of the West African margin

The south Atlantic continental margins are the result of Jurassic to Cretaceous rifting and subsequent continental breakup between the South American and African plates during the dislocation of the mega-continent Gondwana (Mohriak et al., 2008; Matton and Jébrak, 2009; Pletsch et al., 2001; Szatmari & Milani, 2016). Different rift segments were generated under an overall NE-SW-oriented extension during the opening of the South Atlantic (Rabinovich and LaBrecque, 1979; Moulin et al., 2010; Chaboureau et al., 2013): the equatorial segment, the central segment, the southern segment and the Falkland segment, the central segment being the focus of this study. These segments are characterized by distinct extensional and subsidence histories and are bounded by NE-SW-striking transform structures (Mbina Mounguengui and Guiraud, 2009).

The West African central segment is composed of three main sedimentary basins, namely: the Gabon, Lower Congo and Kwanza basins (Fig. 1a) (Standlee et al., 1992). These basins are characterized by the presence of a salt layer approximately 1 to 2 km thick (Brognon and Verrier, 1966; Masson, 1972; Brice et al., 1982; Giresse, 1982; Teisserenc and Villemin, 1990), overlying mainly continental sedimentary sequences (145-116 Ma). The salt is overlain by marine clastics and carbonates (112 Ma to present day) (Doyle et al., 1982; Mussard, 1996). Three tectono-sedimentary episodes have marked the history of the central segment : continental rifting, transition phase (or rift/drift - sag cycle) and post-rift (or post-salt/drift - marginal sag) episodes (Da Costa et al., 1999; Karner et al., 2003; Contrucci et al., 2004; Moulin et al., 2005; Aslanian et al., 2009; Beglinger et al., 2012; Chaboureau et al., 2013).

The rift phase: The first part of this period, from the Neocomian to the middle Barremian, is characterized by significant extensional tectonic activity that produced a series of horsts and grabens (Lehner and De Ruiter, 1977; Karner et al., 1997; Contrucci et al., 2004; Beglinger et al., 2012). These faulted blocks developing from the Atlantic hinge towards the mainland have allowed the sedimentation of two syn-rift sequences that correspond to lacustrine series with black clays lattery passing to sandstones and conglomerates on the rift margin (Karner et al., 1997; Marton et al., 2000; Séranne and Anka, 2005; Brownfield & Charpentier 2006). The sandstone-conglomerate series consists of the Basal Sandstone and includes formations with names that change according to the different segments of the margin: Vandji - Lucula - Basal Sandstone - N'dombo (Fig.1b). Tectonic activity decreased from the middle Barremian to the early Aptian, with draping of the tilted blocks and clay bevels on the high zones.

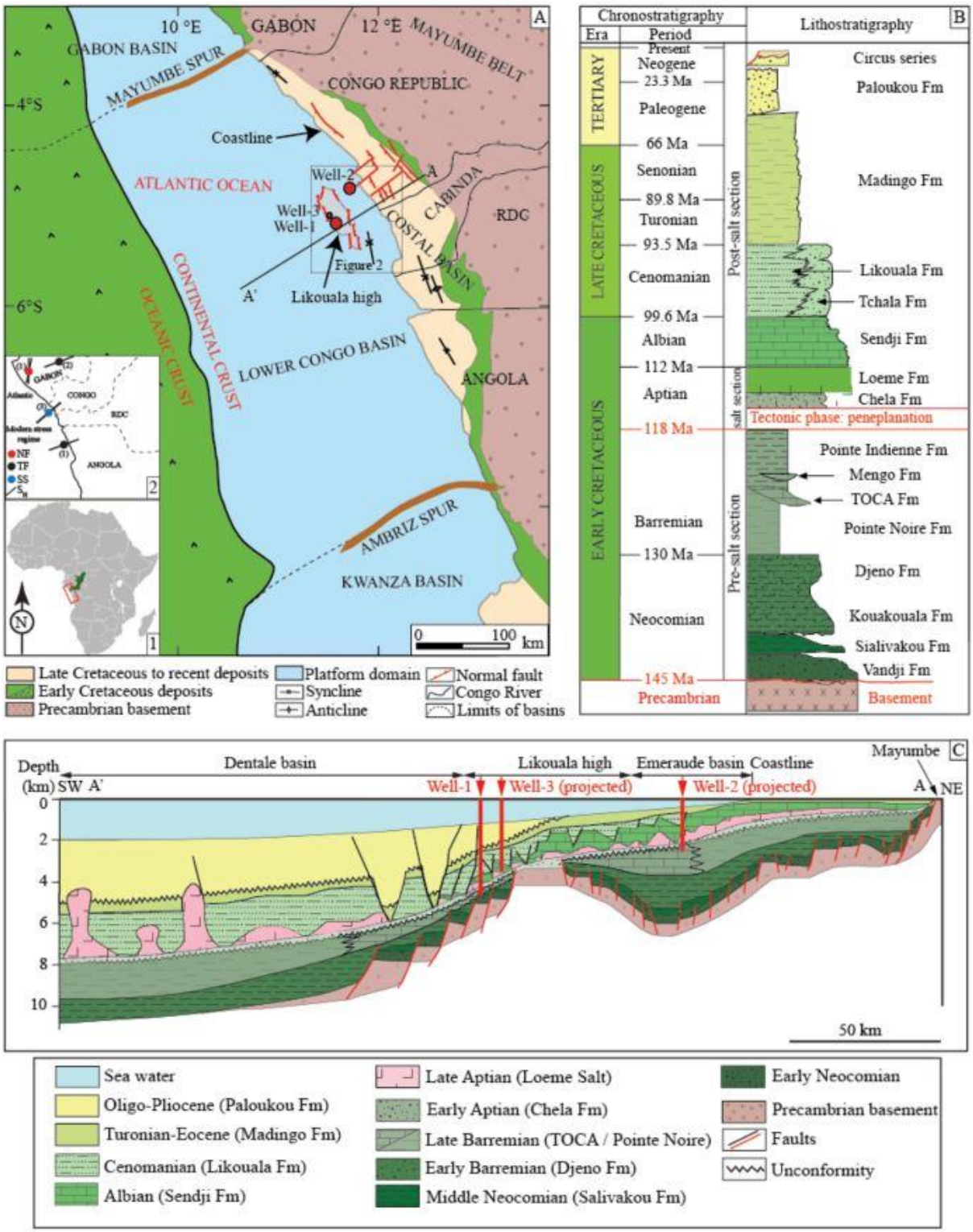


**Figure 1:** (A) Structural map of Africa along the South Atlantic from Gabon to Angola with basins location. In the marine domain, the Cretaceous oceanic crust is represented by the green color. The insert (1) shows the location of the study area. The insert (2) shows the present-day stress regime derived from earthquake focal mechanism (1) from Nkodia et al., (2022) and (2) from Heidbach et al., (2016), respectively, and from borehole breakouts (3) (unpublished

TotalEnergies report). (B) Stratigraphic chart of Lower Congo basin modified from unpublished TotalEnergies internal report. (C) Regional geological cross-section through the Congolese margin. Modified after Vernet et al., 1996 (see 1A for section location).

This decrease or even stop of tectonic activity either would announce the sag period (Beglinger et al., 2012), or corresponds to a third syn-rift phase characterized by a sealing series of shallow lacustrine sandstone-clays (Contrucci et al., 2004; Séranne and Anka, 2005).

The Aptian transition phase marks the transition between rifting and thermally-induced lithospheric subsidence affecting the South Atlantic basins. This phase corresponds to the end of crustal stretching, rifting and basement faulting activity (Uncini et al., 1998; Beglinger et al., 2012), and is marked by the 'break-up unconformity' (Beglinger et al., 2012) along with evaporite deposition (Lehner and De Ruiter, 1977; Teisserenc and Villemin, 1989; Aslanian et al., 2009). The phase started with deposition of a transgressive clastic sequence, fluvio-deltaic sandstone and lacustrine clays, which evolved upwards into evaporite alternations. Subsequently, these series were sealed by widespread salt deposition during the middle and late Aptian (Burwood, 1999; Séranne and Anka, 2005). The onset of salt deposition is probably linked to progressive marine transgressions in the proto-South Atlantic (Asmus & Ponte, 1973; Beglinger et al., 2012) and to more arid conditions (Bate, 1999; Karner & Gambôa, 2007).

The post-rift phase started in the Albian times and is marked by continental break-up and subsequent oceanization (Aslanian et al., 2009; Guiraud et al., 2010). The post-rift phase is characterized by thermal subsidence, regional marine transgression to the north and gravity-driven salt tectonics (Lehner and De Ruiter, 1977; Guiraud and Maurin, 1991; Dingle, 1999; Karner and Driscoll, 1999). The series deposited during this stage can be divided into 3 sedimentary episodes. The first episode (Albian to Eocene) is characterized by a long-term retrograding sedimentary system in which marine carbonate sediments were deposited on top of the previous evaporitic series on a ramp/platform in a shallow marine environment (Beglinger et al., 2012). From the late Turonian onwards, the depositional environments changed drastically, with progressive disappearance of carbonates and deposition of shallow to deep clastics (Beglinger et al., 2012). Consequently, a new ramp profile of the margin developed. The end of this episode, from the Senonian to the early Paleogene, is marked by a drastic decrease in the sedimentation rate (Séranne and Anka, 2005). From the lower Oligocene onwards, a major stratigraphic reorganization prevailed in the Southwest African margin. After a phase of submarine erosion linked to sea level fall, a prograding sedimentary system

developed from the Miocene to the present day probably linked to the onset of a deltaic system and to the proper thermal subsidence of the passive margin which continued after the transition phase (Contrucci et al., 2004). Finally, the prograding sedimentary system extended towards the deep basin generating the vast turbidite system of the deep Congo fan, while sedimentation continued on the platform with fine terrigenous or hemipelagic inputs reworked by deep-sea currents (Séranne and Anka, 2005).

### 2.6.Paleostress history and contemporary stress of the SW African margin

The South Atlantic margins underwent a complex tectonic and paleostress history owing to their geodynamic evolution. This section summarises published data on the past and present stress states of the West African margin in the South Atlantic. Stress orientations reported hereinafter refer to the current African plate position.

The Inkisi Group (early to middle Paleozoic: pre-late Carboniferous) is one of the red beds units that are cropping out around the Congo basin and are observed also in boreholes inside the Congo basin (Delvaux et al., 2021). Within the Congo basin, they are covered by the Late Carboniferous-Permian Lukuga series (belonging to the Karoo Supergroup) which are locally deformed as seen in the Dekese well and also in seismic profiles (Daly et al., 1992; Kadima et al, 2011; Delvaux et al., 2021). In the Congo basin, these rocks are overlain over a major and widespread unconformity by the late Jurassic-Cretaceous series. During the pre-rift phase, the Congo basin therefore recorded a major deformation phase sometimes between the Permian and the Jurassic that has been related to the Gondwanides orogeny on the southern margin of the Gondwana (Johnston, 2000).

During the rift phase (late Jurassic to early Cretaceous), the West African margin underwent a NE-SW extension linked to the opening of the Atlantic Ocean (Rabinovich and LaBrecque, 1979; Nurnberg and Muller, 1991). In Namibia, Salomon et al., (2015) highlighted two extensional trends: (1) an ENE-WSW extension perpendicular to the continental margin and related to continental rifting and (2) a NNE-SSW extension the importance of which remains unclear. Viola et al., (2012) also identified a ENE-WSW extension further south in South Africa.

During the post-rift phase, the western coast of South Africa underwent a major uplift from the Albian to the Turonian (115-90 Ma) (Kounov et al., 2009). This uplift triggered an erosion of up to 2-3 km and has been related to an E-W extensional event (Viola et al., 2012). Two distinct phases of N-S to NW-SE intraplate compression and a NE-SW extension were also identified and associated with the opening of the Atlantic Ocean (Viola et al., 2012). These

stress regimes were not dated but were tentatively correlated, mainly on the basis of consistent stress orientations, to the compressional (and extensional) tectonic events recognized in Central and North Africa by Guiraud and Bosworth (1997), namely (1) late Santonian N-S to NW-SE compression; (2) Campanian-Maastrichtian NE-SW extension; (3) late Maastrichtian N-S to NW-SE compression. These compressional events are related to a plate reorganisation during the Alpine cycle and to the shift in the opening directions of the Atlantic oceanic spreading centers and the subsequent counter clockwise rotational northward drift of Africa–Arabia into Eurasia. A strike-slip stress regime associated with a horizontal principal stress σ1 oriented NW-SE has also been documented in continental Congo (Nkodia et al., 2020) and in Namibia (Salomon et al., 2015). Although still not dated because of the lack of stratigraphic constraints, this stress regime was tentatively related to the late Santonian NW-SE compression of Guiraud and Bosworth, (1997) and/or to the NNW-SSE compressional phase of Viola et al., (2012).

At the present day, an ENE-WSW to E-W oriented compression has been identified on both margins of the South Atlantic ocean, in Central Africa (Ziegler, 1995; Delvaux and Barth, 2010; Heidbach et al., 2016) and in Brazil (Fernandes and Amaral, 2002; Salomon et al., 2015). In the segment of the margin investigated in this study, the few available stress data indicate a SH oriented nearly perpendicular to both the passive continental margin and the mid-Atlantic ridge, in Gabon (World Stress Map, SH oriented N70 - N70 stands for N070°E hereinafter -, compressional stress regime) and in offshore Republic of Congo (borehole breakout data from petroleum wells, unpublished TotalEnergies report, SH oriented N50, strike-slip stress regime) (Fig. 1a). The recent inversion of earthquake focal mechanisms (Nkodia et al., 2022) reveals a compressional stress regime with SH oriented N70 in offshore Angola in the Lower Congo basin that progressively switches to a strike-slip stress regime with SH oriented N80 to N100-120 (ENE-WSW to WNW- ESE) in the interior of the Congo basin. Along the West African margin in Gabon, these authors also document a contemporary extensional stress regime with SH oriented N-S to NNE-SSW while the stress regime is compressional with a SH oriented ~N80 in the interior Gabon.

On the basis of the analysis of mesoscale faults in the Inkisi Group in onshore Congo, Nkodia et al. (2020) identified a strike-slip stress regime with □1 oriented N70 which trend is close to the ENE-WSW SH trend of the current state of stress (insert 2 of Fig.1A). In the absence of any time constraint, the authors speculate that this stress regime would have started in the Miocene and would be related to some degree to the Atlantic ridge push. The changes in the late Tertiary/contemporary stress regime (SH ~ENE-WSW in either reverse or strike-slip fault regime) in space (along and across the strike of the western African margin) and in time suggest

the occurrence of local σ2 / σ3 stress permutations possibly related to structural complexities (e.g., Hu and Angelier, 2004).

### 2.7.The Lower Congo basin: stratigraphy and sedimentology

The Lower Congo basin is located between Gabon and Angola on the eastern margin of the central segment of the South Atlantic (Vernet et al., 1996; Harris, 2000; Aslanian et al., 2009). The basin stratigraphy is divided into three main sections from rifting to the present-day (Fig. 1b): (1) the pre-salt section (145-116 Ma), which is mainly continental, (2) the salt section (118-112 Ma), which marks the major incursion of the South Atlantic Ocean into the rift (transitional phase), and (3) the post-salt section (112 Ma to the present day), which mainly consists of marine sequences (McHargue, 1990). The Cretaceous-Cenozoic sedimentary series rests directly on the Precambrian "basement" (Fig. 1b & 1c) due to the absence of the Jurassic, Triassic and Palaeozoic series (Bidiet et al., 1998). The so-called “basement” includes both the crystalline part of the Congo craton and the overlying Precambrian pre-rift sediments (Delpomdor et al., 2008; Mbina Mounguengui and Guiraud, 2009; Préat et al., 2010). Pre-salt basins are mainly filled by fluvial and lacustrine deposits (Guiraud et al., 2010), and have been dated using ostracod biozones, pollens and spores (Grosdidier, 1967; Chaboureau et al., 2013). The pre-salt section is composed of the Neocomian sandstones and clays of the Vandji, Sialivakou, Kouakouala and Djeno formations, and are overlain by the lower Barremian clay of the Pointe Noire (PN) Fm. (Fig. 1b) and the studied TOCA Fm., deposited in a shallow, lacustrine environment (Harris, 2000) during the terminal phase of rifting on top and sides of the Likouala high. Laterally, the TOCA Fm. changes to deeper organic rich shale deposits of Pointe Noire in the Dental and Emeraude basins. The late Barremian clay deposits of the Pointe Indienne Fm. complete the pre-salt section (Harris, 2000).

In this study, we focus on the syn-rift TOCA lacustrine carbonates. On the basis of sedimentological and biological features, Harris (2000) identified three units for the TOCA Fm., from bottom to top: (i) TOCA 1 characterized by microbialites; (ii) TOCA 2 containing microbial encrustations of shells, microbial mats and thromboliths; and (iii) TOCA 3 composed of a substantial accumulation of granular and coquina facies, i.e., in which constitutive elements consist mainly of freshwater lamellibranch tests belonging to the Unionidae group (Grosdidier et al., 1996). The identification of the AS9 ostracod biozone (base AS9 ~130 Ma, top AS9 ~125 Ma) (Grosdidier et al., 1996; Bate, 1999; Gradstein et al, 2004) in the TOCA Fm indicates a Barremian age of deposition.

### 2.8.The Lower Congo basin: structure

The Lower Congo basin is bounded by two oceanic fracture zones referred to as "arches" (Asmus & Ponte, 1973; Beglinger et al., 2012): the Mayumbe Arch to the north and the Ambriz Arch to the south. The basin rests unconformably on the Mayumbe Precambrian basement to the east (Fig. 1a). The Lower Congo basin includes the onshore coastal basin and the offshore basin which makes most of the margin. In the central Lower Congo basin (Fig. 1a & 2a), the Emeraude and Dentale basins, located on either sides of the Likouala high, represent the depocenters of the syn-rift series (Figs. 1a & 1c).

The map of the top TOCA (top Barremian) (Fig. 2a) shows three main orientations of deep, basement rooted faults at the hectometric to pluri-kilometric scale, consistent with the regional structural pattern in this part of the West African margin (Tack et al., 2001). Two of these three orientation groups comprise normal faults oriented N-S and NW-SE (Fig. 2a) (unpublished TotalEnergies report). Both fault strikes can be recognized in the Likouala high and the adjacent basins, but the N-S strike seemingly prevails atop of the high where the TOCA Fm. either never deposited or has been completely eroded, while the NW-SE strike dominates in the areas of the basin where the TOCA Fm. is thicker. The third set, oriented NE–SW, corresponds to transverse faults (Fig. 2a) often referred to as “lineaments” where they are recognized at the larger scale but with poorly-defined vertical offsets on seismics. These transverse lineaments generally line up with onshore features such as paleo-valleys and mapped NE–SW faults and are seen further offshore on gravimetric-magnetic data (unpublished TotalEnergies report).These NE–SW lineaments are considered as a structural expression of margin segmentation during initial northward propagation of the Atlantic rifting.

The data used in this paper come from two offshore wells (Well-1 and Well-2), located ~47 km apart in two distinct domains of the basin on both parts of the Likouala high (Figs. 1 & 2a). The dataset was completed by some fracture orientation data from cores from lateral wells (unpublished TotalEnergies report) (Fig. 2a). The dataset and stress results from Well-3 cutting the post-rift section (Zeboudj et al., 2023) are used for the sake of comparison.

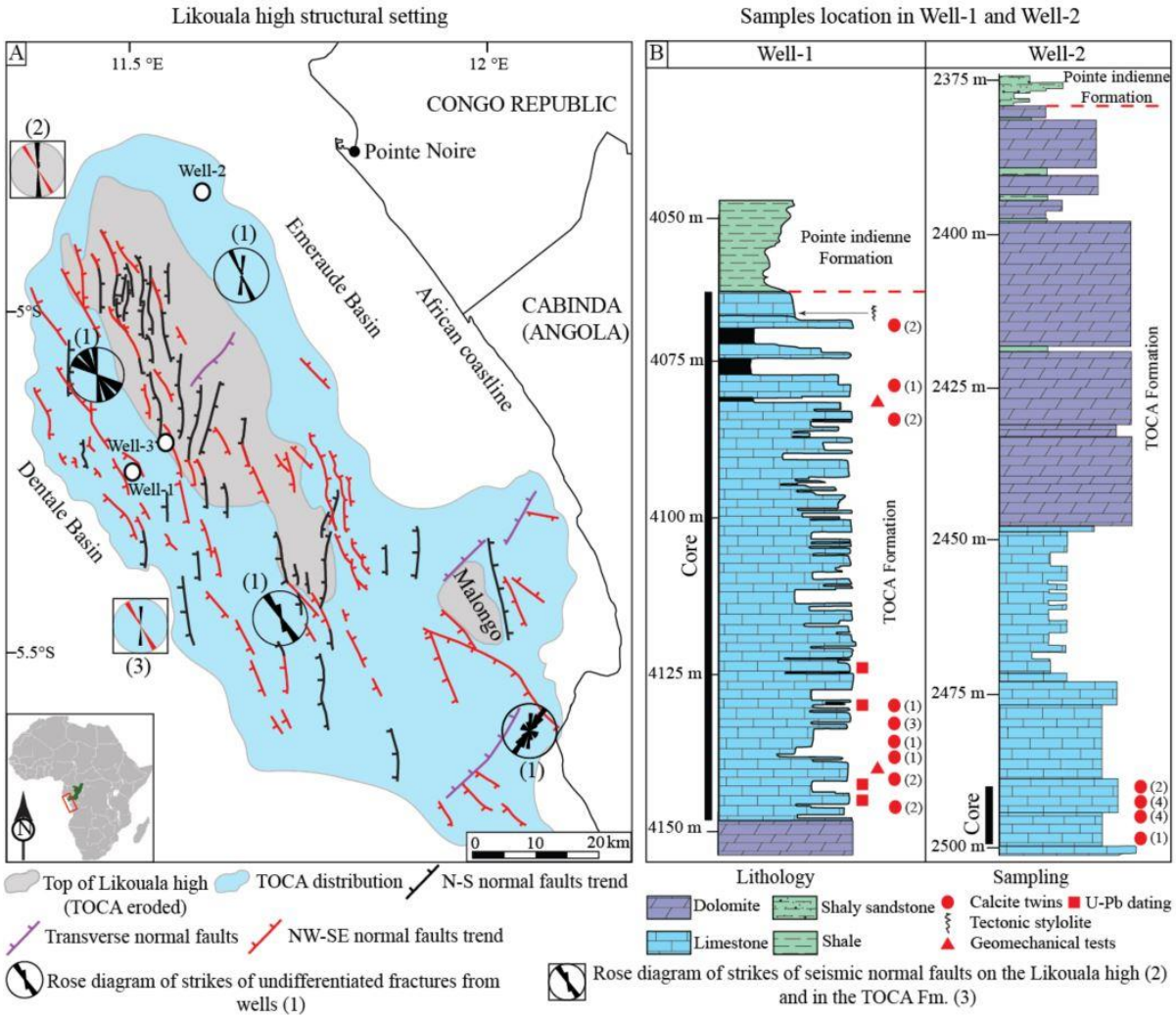


**Figure 2:** (A) Main normal faults affecting the TOCA 3 unit and Likouala high basement from unpublished TotalEnergies report. The two rose diagrams in the squares represent the statistical distribution of fault strike (N-S in black and NE-SW in red) on the Likouala high and in the TOCA Fm. Please note that the faults in the Emeraude basin near Well-2 have not been mapped. (B) Schematic stratigraphic chart of the two studied drill cores showing the samples location used in this study. The solid black line shows the cored section for each well

## 3. Materials and methods

### 3.1.Studied material

The cores of the TOCA Fm. available for this study amounts to 81 m in Well-1 (4069-4150 m) and 9 m in Well-2 (2490-2499 m) (Fig. 2b), and they exhibit the same sedimentary facies composed of oncolite limestone locally dolomitized. The studied intervals were selected on their representativity of the sedimentary facies encountered in both well cores.

This study focuses on the TOCA 3 unit which has already been investigated in Well-1 by Bah et al., (2023). In their study, the authors quantified the amount and timing of porosity destruction in the TOCA reservoir. The absolute age of the key paragenetic events controlling reservoir properties have been constrained: mechanical compaction (130-127 Ma based on TemisFlow™ modeling), early cementation (127.4 ± 2.2 to 119.4 ± 6.4 Ma based on U–Pb dating on calcite diagenetic cement), and chemical compaction (117-95 Ma based on sedimentary stylolite roughness inversion). The results reveal that the initial porosity of the TOCA Fm. was reduced down to its current value of 4-8% during the first 35 Ma of its burial history and has not significantly evolved since 95 Ma. Thanks to the early cementation the textures of the TOCA 3 unit display large areas of sparitic calcite grains suitable for calcite twin analysis (Well-1 and Well-2; Fig. 3).

## 3.2.Methods

### *3.2.1. Optical and cathodoluminescence microscopy*

In order to complement the petro-diagenetic description of the TOCA Fm. in Well-1 (Bah et al., 2023), we conducted a petrographic study of the TOCA Fm. in Well-2, based on the analysis of new 36 thin-sections using a Zeiss Axioplot polarizing microscope equipped with a Nikon Digital sight DS_U2/Ds_Fi1 camera. The petrographic phases were observed and identified under unanalyzed polarized light (LPNA) and analyzed polarized light (LPA). The diagenetic state of carbonates was further investigated under cathodoluminescence on a NewTec scientific Cathodyne model CATHOD-SP01 equipped with an IDS UI-3850CP-C-GL R camera (vacuum of 90 mTorr, 12-15 kV voltage and 200 µA intensity). All microscopic work was carried out at the laboratory facilities of the TotalEnergies technical and scientific center (CSTJF, Pau, France).

### *3.2.1. Strength and failure envelope of the TOCA limestones from mechanical tests*

In order to determine the mechanical properties of the TOCA limestones, multitriaxial tests were run on two plugs (38 mm diameter x 76 mm height) and brazilian tests on two other plugs (38 mm diameter x 18 mm height) cut along the vertical axis of the core within the two most frequent textures, namely wackestone and packstone. The principle of the multitriaxial test (also referred to as multi-stage test) is the same as the conventional single-stage triaxial test, except that only one test specimen is used for different confining pressures (see Bah et al., 2023 for detail). The results of the tests were used to constrain the elastic properties of the rock (Bah et al., 2023) and to build its intrinsic failure envelope (this study).

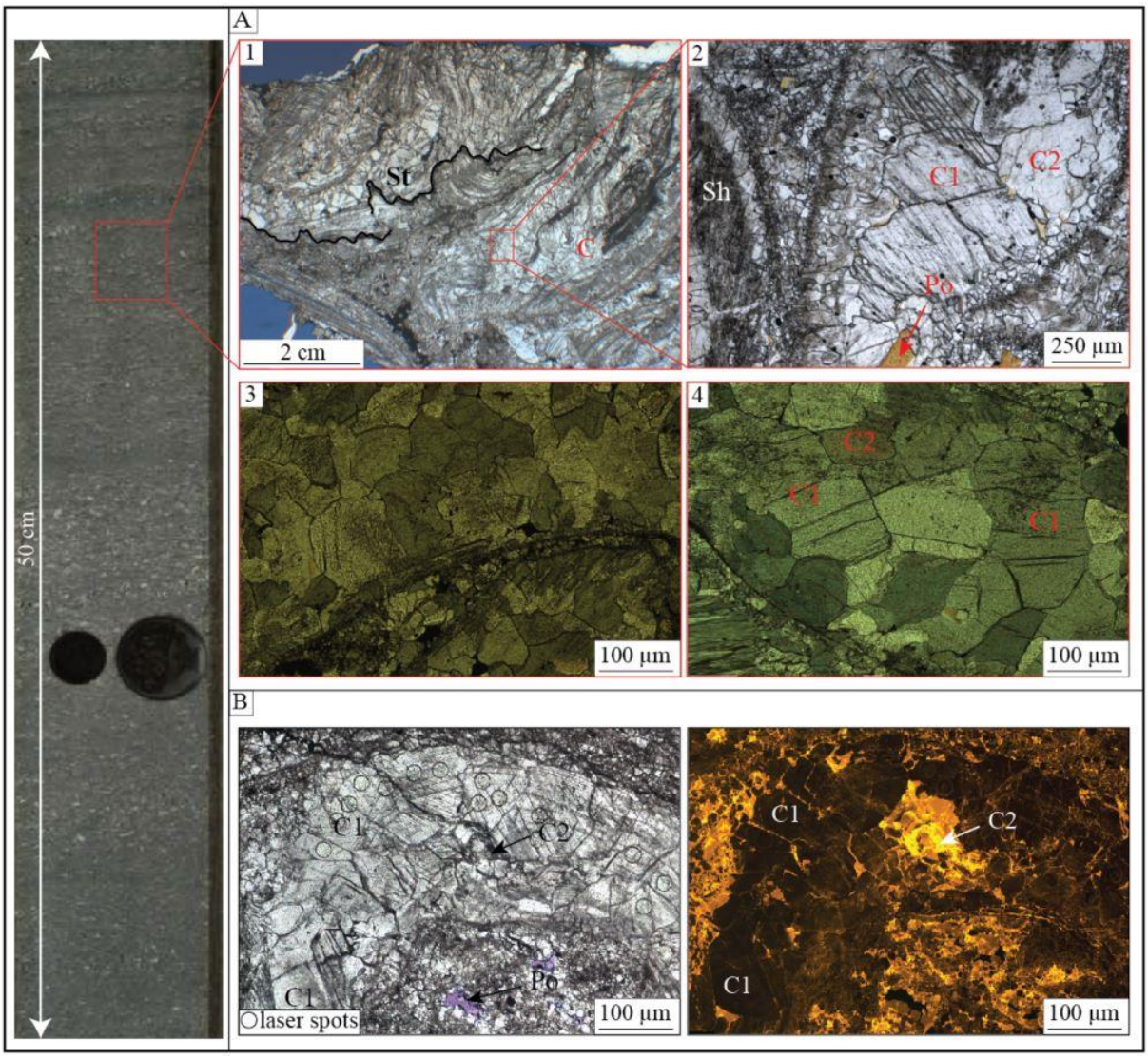


**Figure 3:** Photographs of the core showing the studied material. (A) wackestone to packstone texture in Well-1 (A1 & A2) and Well-2 (A3 & A4); (B) Microscopic image in polarized light and cathodoluminescence showing twinned calcite and the different calcite cements. Sh – shells; C1 and C2 – Blocky calcite cement; St – Stylolite.

### *3.2.2. Calcite twin inversion for stress applied on oriented cores*

Mechanical twinning is a common mechanism of plastic deformation in calcite crystals at low pressure and temperature (Burkhart, 1993; Ferrill et al., 2004; Lacombe et al., 2021a). Twinning occurs by an approximation to simple shear in a particular direction and sense along specific crystallographic e planes. The effect of strain rate, temperature, and confining pressure is negligible on twinning activation, the latter being mainly dependent on differential stress, grain size and strain (Turner, 1953; Turner et al., 1954; Rowe and Rutter, 1990; Laurent et al., 2000; Lacombe et al., 2021a).

Calcite twinning paleopiezometry (e.g., Jamison and Spang, 1976; Lacombe and Laurent, 1992; Lacombe, 2007) is a well-established technique to quantify paleostress orientations and magnitudes (e.g., Lacombe et al., 2007, 2009; Craddock et al., 1993; Rocher et al., 1996; Arboit et al., 2017. See Lacombe, 2010 and Lacombe et al., 2021a for reviews). Inversion of calcite twins for stress is especially appropriate to constrain the paleostress history from limited rock volumes such as cores from wells (e.g., Lacombe et al., 1994; Rocher et al., 2000; Kulikowski and Amrouch, 2017; Zeboudj et al., 2023). In addition to the presence of favorable petro-facies (i.e., sparitic calcite in rock matrix or veins), the technique requires the obvious availability of samples oriented in the geographical frame. For the purpose of paleostress reconstructions, the two investigated cores were oriented either directly in-situ or a posteriori by comparison with the FMS (Formation Micro-Scanner) images of the well.

#### 3.2.2.1.Calcite twin data acquisition

The samples used for calcite twin measurements (Fig. 3 & 4) were spatially oriented as follows: X axis parallel to the generator oriented with respect to north, Y axis parallel to the dip of the core and Z axis perpendicular to the XY plane. Mutually perpendicular thin-sections were cut for each sample from the XY, XZ plane and YZ planes. In each thin section (Fig. 4b), orientations of twin lamellae of optical axes were measured from ~30 crystals using an optical microscope equipped with a Universal Stage with the aid of the software of Tourneret and Laurent (1991). Once acquired, the measurements were restored into the geographical orientation and for each sample, they were plotted to check for the random distribution of the optical axes, hence the absence of any potential bias related to a preferred orientation related to crystal growth or deformation (Fig. 4d). We also ensured that calcite twins measurements were collected from grains of the same diagenetic phase based on cathodoluminescence images (Fig. 3b).

For a rough estimate of the strain accommodated by twinning, we summed the width of each twin lamella of a given twin set in a grain and divided this value by the width of the grain measured perpendicular to the twins. The 2-D grain size in each thin section was determined by adding the length of the long and short axes of the grain and dividing the sum by 2. The resulting grain size histogram allows us to eliminate the outliers, i.e., the under-represented smallest and/or largest size values (Fig. 4d).

### 3.2.2.2.Calcite twin data inversion for stress

A number of methods of calcite twin inversion for stress have been proposed (e.g., Laurent et al., 1981; Etchecopar, 1984; Laurent et al., 1990; Yamaji, 2015; Parlangeau et al., 2018; see review in Lacombe et al., 2021a). They are based on different principles but share the same conditions of application, i.e., low strain, which warrants coaxiality between stress and strain, and homogeneous stress field at the grain/aggregate scale. Twinning deformation is considered to be irreversible, and twinning occurs if the applied resolved shear stress $\tau s$ is equal to, or greater than, the Critical Resolved Shear Stress for twinning (CRSS) $\tau a$ (Jamison and Spang 1976; Tullis, 1980; Lacombe and Laurent, 1996; Ferrill, 1998; Laurent et al., 2000; see review and discussion on the meaning of the CRSS in Lacombe et al., 2021a). Thus, one assumes that for twinned planes: $\tau s \geq \tau a$ and for untwinned planes: $\tau s < \tau a$. Calcite twinning is easier (lower CRSS) in large grains and more difficult (higher CRSS) in small grains. In addition, because calcite hardens once twinned the CRSS increases as twinning strain increases, making further twinning more difficult (Parlangeau et al., 2019; Lacombe et al., 2021a).

In this study, we used the stress inversion technique (CSIT-2) developed by Parlangeau et al., (2018) to determine the successive paleostress tensors from the measured twin sets. The principle of the inversion is to find a stress tensor (or several stress tensors) which verifies the inequalities (1) for the largest number of twinned planes and the whole set of untwinned planes. The solution has the form of a reduced stress tensor with 4 parameters: the orientations of principal stress axes ($\sigma_1$, $\sigma_2$, $\sigma_3$) and the stress ratio ($\Phi$):

$$1 \geq \Phi = \frac{\sigma 2 - \sigma 3}{\sigma 1 - \sigma 3} \geq 0 \quad \text{with} \quad \sigma_1 \geq \sigma_2 \geq \sigma_3 \quad (1)$$

CSIT-2 method allows the presence of one or more tensors to be detected automatically. Considering the complete dataset (twinned and untwinned planes), the first step of the process consists of a systematic search in the 3-D space for the three Euler angles (defining the orientations of the axes of the stress tensors) with a regular interval of 10°, the stress ratio being fixed at 0.5, in order to select the reduced stress tensors accounting for at least 20% of twinned planes. For each tensor, the penalization function f defined as:

$$f = \sum_{j=1}^{j=n} (\tau_s^j - \tau_s^{min}) \quad (2)$$

with $\tau_s^j$ the resolved shear stress applied on the j untwinned planes such as $\tau_s^j \geq \tau_s^{min}$ and $\tau_s^{min}$ the smallest resolved shear stress applied on the twinned planes compatible with the tensor, is calculated.

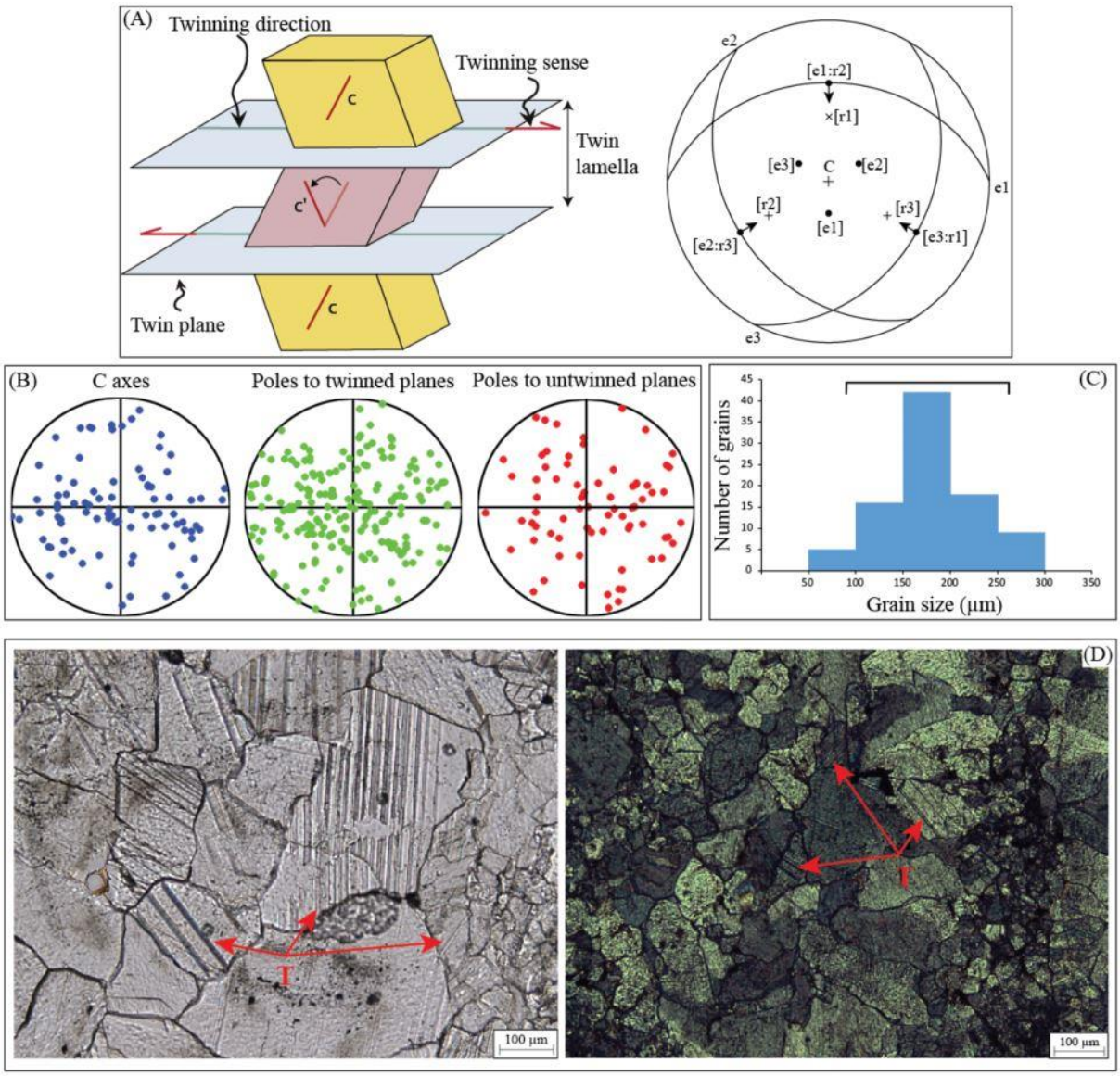


**Figure 4:** (A) Schematic and stereographic representation of calcite twinning with the C and C' optical axes of the host crystal and the twinned portion of the crystal (Lacombe et al. 2021a). (B) Example of spatial distribution of optical axes (blue) and poles to twinned (green) and untwinned (red) planes of sample 6 (2493.9 m depth) in Well-2. (C) Example of grain size distribution in the same sample than in B, with the range of grain sizes considered for the CSIT-2. (D) Photographs in natural light of the representative facies in the drill core showing twinned calcite in the matrix in wells 1 & 2 on the left- and right hand side, respectively. T- Twins.

From a theoretical point of view, the penalization function should be equal to 0 for a perfect data set and it increases if incompatible untwinned planes are incorporated in the solution. The stress tensors with a penalization function lower than 0.5 are retained after this first step and each of them is weighted by the number of its nearest neighbours based on a

similarity criterion. This allows the simultaneous and automatic detection of different clusters of tensors that share a high percentage of compatible twinned planes and are associated with low values of the penalization function (for more details, see Parlangeau et al., 2018). The reference reduced stress tensor of each cluster is then applied to the set of twinned and untwinned planes while the percentages of twinned planes to be explained is progressively increased. The optimal tensor is obtained when 1) the maximum number of twinned planes are taken into account; 2) the minimum number of untwinned planes are taken into account; 3) the value of the penalization function is minimal.

This inversion process yields for each tensor the orientation of the principal stress axes ($\sigma_1$, $\sigma_2$, $\sigma_3$), the stress ratio ($\Phi$) and a non-dimensional differential stress $\frac{(\sigma_1 - \sigma_3)}{\tau a}$ which is related to the final value of $\tau s^{min}$:

$$\frac{(\sigma_1 - \sigma_3)}{\tau a} = \frac{1}{\tau s^{min}} \quad (3)$$

The choice of the right $\tau a$ value to be used in equation 3 is of prime importance for the reliable calculation of differential stress magnitudes. In order to estimate the appropriate CRSS value, we rely on the empirical curves proposed by Parlangeau et al (2019) which reflect the decrease of the CRSS value with increasing grain size (Hall-Petch's rule) and the increase of the CRSS value with strain. Moreover, despite the poor dependence of the CRSS value on temperature, we also paid attention to the range of temperatures of deformation in our samples, considering both the twinning regime (e.g., thin twins denoting twinning at low temperature < 170-200°C: Ferrill et al., 2004; Lacombe et al., 2021a) and the maximum temperature reached during burial in order to evaluate the possible variations of the CRSS with temperature (De Bresser et al., 1997; Lacombe et al. 2021a). The $\tau a$ value ultimately retained for calculation is therefore estimated on the basis of the mean grain size and the internal twinning strain of the samples, and to - a lesser extent - of the estimated temperature of deformation at each stage of the burial history.

Using the $\tau s^{min}$ value derived from the inversion process we then determined the values of the differential stresses ($\sigma_1$-$\sigma_3$) and ($\sigma_2$-$\sigma_3$) using equation (3), hence the 5 parameters of the deviatoric stress tensor.

The ability of CSIT-2 to detect, separate and determine stress tensors from monophase and polyphase twin datasets, including measurements errors or various grain sizes, has been demonstrated by multiple tests on numerically generated twin datasets as well as naturally

deformed polyphase samples (Parlangeau et al., 2018). The associated methodological uncertainty is ± 10° for the orientations of the principal stresses, ± 0.1 for the stress ratio and ±30% for the values of the differential stresses.

### *3.2.3. Burial-time model*

In order to reconstruct the burial evolution of the TOCA Fm. over time, we have built a 1-D burial-time model of the TOCA Fm. using TemisFlow$^{TM}$ basin modelling software. In this study we present the burial model for Well-2, which complements the burial model for Well-1 available in Bah et al., (2023). The workflow is summarized below (see Bah et al., 2023 for detail).

The geometry simulation is based on the top-base depths of the formations as measured in Well-2. The properties of each lithology (porosity, permeability) were defined from Well-2 and available seismic interpretations (TotalEnergies internal maps) were used to define the erosional phases to be taken into account, namely the early Aptian erosion (~75 m) related to the peneplanation of the Likouala high during the transition period uplift and the early Tertiary erosion (~100 m) related to the global uplift of the margin. The chronostratigraphic column (Table 1 in Supplementary Material) shows the parameters of the 14 periods modelled for Well-2. Paleo-bathymetry is specified for each period. Additional physical properties such as thermal conductivity, heat capacity and radiogenic production, as well as the compaction constitutive law were defined with respect to the ratio of the different sedimentary textures (limestone, shale, sandstone) described in the layer.

The backstripping process allows for the inversion of the evolution of the basin geometry through time using a 1-D backward modelling. The restoration was performed from the present day to the deposition of the first layer at 145.5 Ma, which corresponds to the age of the basement top. For each period, after removing the overlying layer, the remaining sedimentary formations were decompacted, or compacted (in the case of erosion), by using porosity vs depth curves calibrated empirically for each lithology. The results of the backstripping is the evolution of thickness with time for each layer.

# 4. Results

## 4.1.Macroscopic and microscopic petrographic observation

The TOCA Fm. in Well-2 shows the same sedimentary facies and textures than in Well-1 (Bah et al., 2023). Observations on cores and thin-sections reveal two main types of facies: a bioclastic facies (F1) and a mudstone facies (F2). The bioclastic limestone facies is the most common and is composed of broken or preserved unio shells, gastropods and rare oncoids in a microsparitic matrix, occurring as wackestones to floatstones (F1b) and as packstones to rudstones (F1c) (Fig. 3). The less abundant mudstone facies is mainly abiotic but with sometimes gastropods and ostracods shells. These two microfacies represent about 90 % of the cored sections in Well-1 and Well-2, the remaining 10% of the core being composed of grainstones and black shales.

Two predominant diagenetic calcite cements were identified in both Well-1 (Bah et al., 2023) and Well-2 on the basis of cathodoluminescence (Fig. 3b). The early blocky calcite cement C1, dated 127.4 ± 2.2 to 119.4 ± 6.4 Ma in Well-1 (Bah et al., 2023), is essentially non-luminescent (dark colour) and develops as an intrabioclast and interstitial cement. The later (unfortunately non dated) calcite cement C2 exhibits a rather bright orange cathodoluminescence and often occurs as overgrowth around C1 crystals or in residual porosity after C1 cementation (Fig. 3b).

## 4.2.Strength and failure envelope of the TOCA limestones from mechanical tests

The elastic parameters for the two carbonate textures studied, namely wackestone (F1b) and packstone (F1c), have been reported in Bah et al., (2023). The values of the maximum principal stress σ1 at 10, 30 and 50 MPa determined from the triaxial tests were used to build the Mohr circles for each loading (Fig. 5). The value of the rock tensile strength was determined from the results of the Brazilian test (Table 2 in Supplementary Material and Fig. 5). The Mohr circles associated to each loading and the rock tensile strength enabled us to build the failure envelope for each texture. According to the Mohr-Coulomb criterion, the failure envelope was approximated by a straight line in the positive normal stress domain according to equation (4):

$$\tau = S_0 + \mu \sigma_n \quad (4)$$

with $\tau$ the shear stress component, $S0$ the cohesion of the material, μ the coefficient of internal friction and $\sigma n$ the normal stress component.

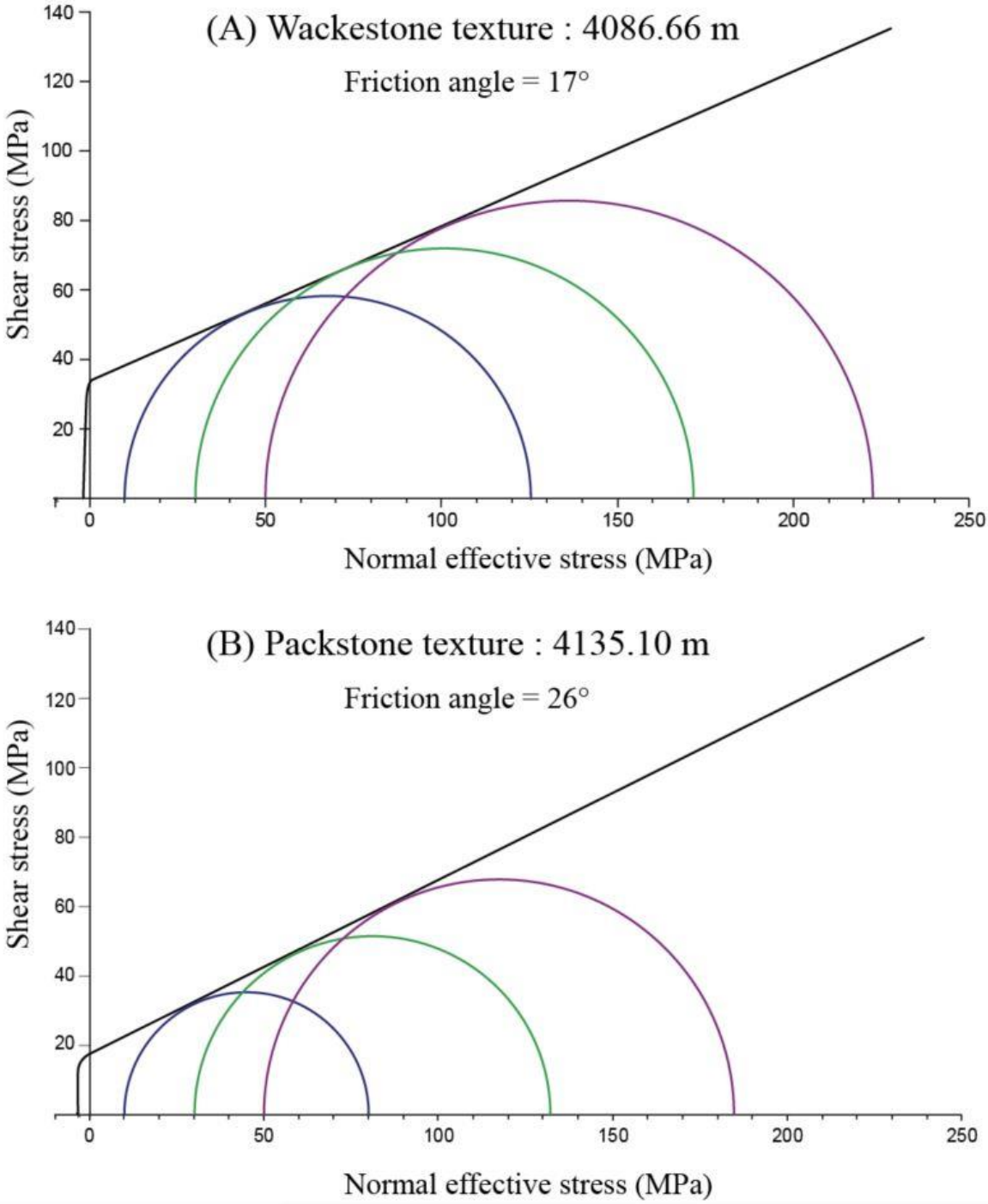


**Figure 5:** Mohr diagrams showing the Mohr failure envelope of the TOCA Fm. determined from rock mechanics tests in the wackestone (A) and packstone (B) textures.

Brazilian test results which indicate that the rock tensile strength is ~1.69 MPa and ~3.13 MPa for wackestone (F1b) and packstone (F1c), respectively, were used in the domain of negative normal stress. It should be noted that the two studied cores did not intersect any visible fractures in the cored section. Although extensional fractures and faults were reported in nearby wells (Fig. 2a), this unfortunate lack of mesoscale brittle structures may be explained

by the limited length of cores investigated together with the expected steep dip of the extensional fractures, i.e., oriented nearly parallel to the well axis.

### 4.3.Results of the inversion of calcite twins for stress

A total of 26 samples were collected in Well-1 and Well-2 in the pre-salt TOCA carbonates at different depths. 15 samples were taken in Well-1 between 4070.25 m and 4148.30 m and 11 samples in Well-2 between 2490.14 m and 2499.25 m. The depth distribution of the samples is shown in Figure 2 and in the supplementary material. Twins were measured in the C1 cement which displays large blocky calcite crystals. Only a few measurements could be made in the C2 cement due to the small grain size; the resulting twin dataset was unfortunately too limited to carry out a meaningful inversion for stress.

All the twins observed in the samples are very thin (< 1 µm) and straight (Fig. 4), and belong to Type I twins (Burkhard, 1993) which indicates that twinning strain remained small (Ferrill et al., 2004; Lacombe et al., 2021a) and occurred at low temperature (T < ~170-200°), in agreement with the maximum temperature (Well-1 present-day bottom hole temperature) of 164° reached by the TOCA Fm. during its continuous burial (Bah et al., 2023).

The samples further show a random distribution of optical axes of grains (Fig. 4e), which is a prerequisite for the reliable inversion of calcite twin data for stress. Grain-size histograms for most studied samples show a distribution of calcite grain sizes between 100 and 350 µm, with a modal value around 200 µm. Only one sample displays smaller grain sizes, with a modal value of around 100 µm. Twinning strain was roughly estimated to be less than 2%. This very small value ensures that twinning strain can be approximated by coaxial conditions so the orientation of twinning strain can be reliably correlated with paleostress orientation (Burkhard, 1993; Amrouch et al., 2010; Wakamori and Yamaji, 2020). The mean grain size and the maximum strain value allowed us to define the appropriate CRSS values to be used for the calculation of the differential stress on the basis of the empirical curves published by Parlangeau et al. (2019) and Lacombe et al. (2021a). These CRSS values were plotted against temperature of deformation to check for consistency. The final CRSS values, between 6 and 7 MPa (except for one sample from Well-2), are reported in Table 3 (Supplementary Material).

Only 6 out of the 26 samples yielded a single stress tensor. All other samples (i.e., ~77%) yielded two, three or four superimposed stress tensors. For the sake of simplicity, the stress tensors obtained from each well were gathered into different groups on the basis of consistent principal stresses orientations and stress regime (extensional, vertical $\sigma_1$; compressional, vertical $\sigma_3$; strike-slip, vertical $\sigma_2$) (Fig. 6 and Figs. 1, 2 in Supplementary Material).

Starting from the 56 stress tensors determined from the 26 samples (Table 3, Supplementary Material), a total of 7 main groups of stress tensors could be defined (Fig. 6): three extensional stress tensor groups (A, B and C), two compressional stress tensor groups (D and E), and two strike-slip stress tensor groups (F and G).

For the extensional stress regimes, group A was identified in 10 samples (8 and 2 for Well-1 and Well-2, respectively) and is characterized by a $\sigma_3$ oriented ~NE-SW and by mean differential stress magnitudes of 50 MPa for ($\sigma_1$ - $\sigma_3$) and 20 MPa for ($\sigma_2$ - $\sigma_3$). Group B was recognized from 17 samples (12 and 5 for Well-1 and Well-2, respectively), with a $\sigma_3$ oriented ~N100 and mean differential stress magnitudes of 40 Ma for ($\sigma_1$- $\sigma_3$) and 20 MPa for ($\sigma_2$- $\sigma_3$). Group C was recognized from 4 samples only (2 and 2 for Well-1 and Well-2, respectively), with a $\sigma_3$ oriented ~N-S and mean differential stress magnitudes of 50 Ma for ($\sigma_1$- $\sigma_3$) and 20 MPa for ($\sigma_2$- $\sigma_3$).

Regarding the compressional stress regimes, group D was recognized from 15 samples (10 and 5 for Well-1 and Well-2, respectively), with a σ1 oriented ~N70 and mean differential stress magnitudes of 42 Ma for ($\sigma_1$- $\sigma_3$) and 15 MPa for ($\sigma_2$- $\sigma_3$). Group E was recognized from 6 samples (2 and 4 for Well-1 and Well-2, respectively), with a $\sigma_1$ oriented ~N-S and mean differential stress magnitudes of 35 Ma for ($\sigma_1$- $\sigma_3$) and 22 MPa for ($\sigma_2$- $\sigma_3$).

Regarding the strike-slip stress regimes, groups F and G were identified only in Well 2 from 2 and 3 samples, respectively; they are characterized by a horizontal $\sigma_1$ oriented ~N-S (F), and ~E-W (G) and by mean differential stress magnitudes of 45 MPa for ($\sigma_1$- $\sigma_3$) and 28 Ma for ($\sigma_2$- $\sigma_3$) for F, and 48 MPa for ($\sigma_1$- $\sigma_3$) and 22 MPa for ($\sigma_2$- $\sigma_3$) for G.

### 4.1.Burial-time model

The burial-time model developed for Well-2 (Fig. 9) is very similar to that published for Well-1 (Bah et al., 2023). It shows five phases of burial evolution over time: (1) 130 Ma to 118 Ma, a first phase of moderate burial (~25 m/Ma) during the early Cretaceous rifting episode followed by a 75 m erosion. This erosional event observed at 118-117 Ma represents a margin uplift with a peneplanation event (see Fig. 1b). The second phase corresponds to a rapid deposition of sandstones and evaporites with an average burial rate of 197 m/Ma during the transition phase. The post-rift phase starts with (3) a moderate burial rate (~22 m/Ma) from 112 Ma to 63 Ma, followed by (4) a moderate uplift (63 Ma to 35 Ma), leading to a moderate erosion in the lower Tertiary, and ends by (5) a third phase of gentle burial (~3.5 m/Ma) from 35 Ma to present day.

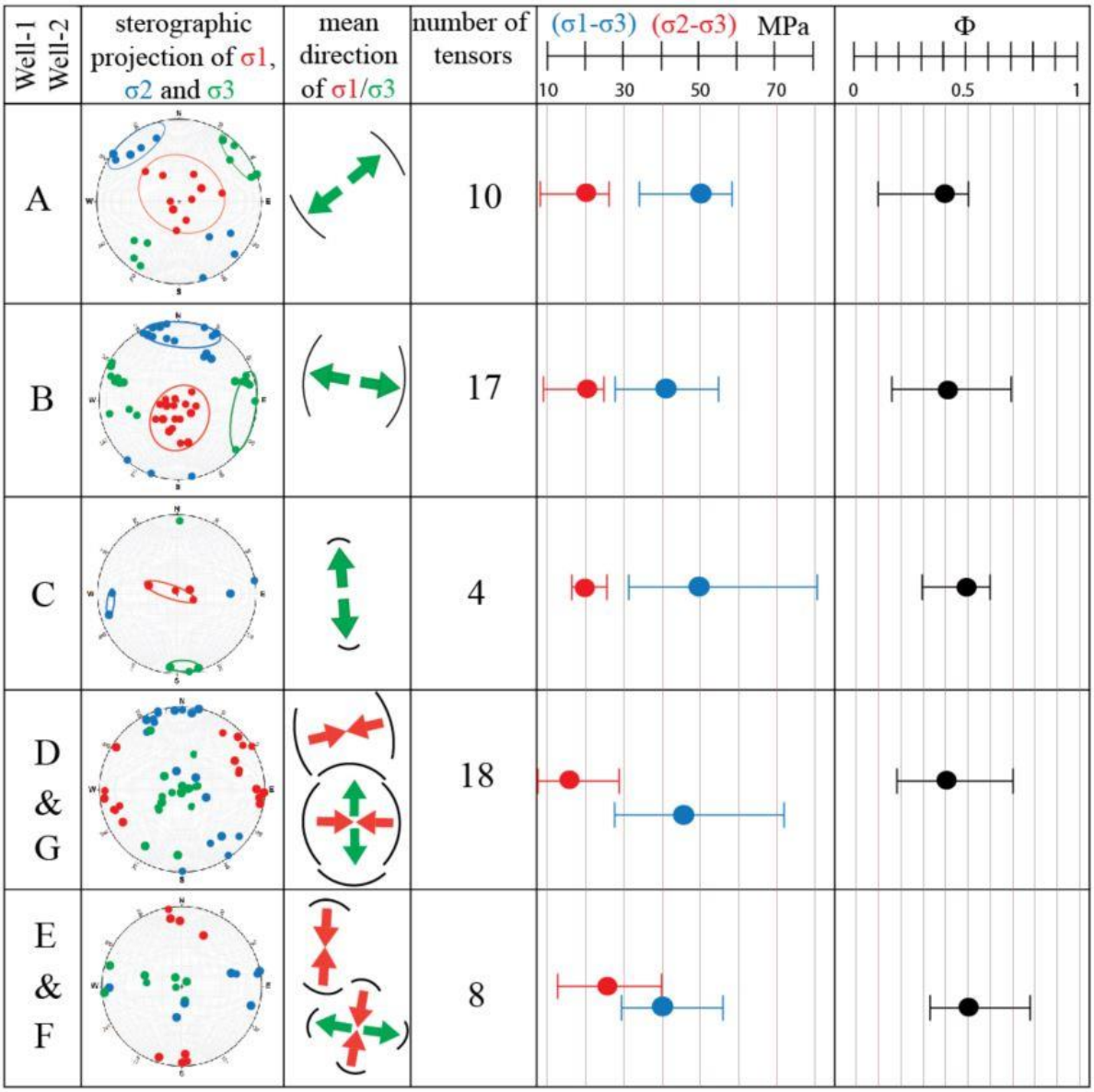


**Figure 6:** Summary of stress tensor groups derived from calcite twin inversion using CSIT-2 for Well-1 and Well-2. Each tensor group (from A to G) is characterized by a plot data in stereographic equal-area projection showing the mean orientation of the principal stress axes (red for σ1, blue for σ2 and green for σ3) and the representation of the average orientation of the horizontal stresses as arrows (red for σ1, green for σ3, map view). Each tensor group is associated with the number of samples from which the related stress tensors were identified. The average values of the differential stress magnitudes for each group are shown in blue (σ1 - σ3) and in red (σ2 - σ3) and the average value of stress ratio Φ in black.

The comparison between the Well-2 and Well-1 models (Fig. 7) shows that the burial rates of the first phase during the early Cretaceous rifting are in the same order of magnitude. Although the thickness of the Loeme salt is very different in the two wells due to the pre-salt paleotopography and to the salt migration during salt tectonics, the strong post-rift subsidence is also of the same order of magnitude, while slightly delayed in time for Well-1 on the Likouala high. The Late Cretaceous quiescence is the same but the Oligo-Miocene burial is much higher on the slope of the margin (Well-1).

## 5. Interpretation of results

The results of the inversion of calcite twins document a complex, polyphase paleostress history. The depositional age of the TOCA Fm. derived from biostratigraphy (Grosdidier et al., 1996) and the absolute U-Pb dating of the C1 calcite cement (127.4 ± 2.2 to 119.4 ± 6.4 Ma, Bah et al., 2023) provide time constraints on the beginning of the evolution (Fig. 7).

The distribution of depth ranges of sedimentary stylolite activity projected onto burial-time curves provides the time periods of compaction-related active pressure-solution along sedimentary stylolites, hence the periods dominated by a stress regime with a vertical $\sigma_1$ (Bah et al., 2023) (Fig. 7). Because sedimentary stylolites develop under a vertical $\sigma_1$, the maximum depth of active pressure solution can be interpreted as the depth (and so the time once projected onto the burial model) at which $\sigma_1$ switched from vertical to horizontal as a result of the horizontal tectonic stress becoming large enough to overcome the vertical stress. This idea has been illustrated and validated in foreland fold-and-thrust belts (Beaudoin et al., 2020; Labeur et al., 2021; Lacombe et al., 2021b). At passive margins, it is sound to consider that the halt in sedimentary stylolite development can alternatively be due to reservoir scale fluid overpressure, possibly related to hydrocarbon migration (Schoellkopf and Patterson, 2000; Brownfield and Charpentier, 2006; Beglinger et al., 2012; Bah et al., 2023). Whatever the reason of the end of stylolite development, this places significant constraints on the time periods when the σ1 was vertical, i.e., until 95 Ma at least (Fig. 7). As a result, the time periods for which there is no positive evidence of vertical $\sigma_1$ as ascertained by active stylolitization are potentially those periods when horizontal $\sigma_1$ was prevailing, which constrain the possible timing of strike-slip and compressional stress regimes recorded by calcite twinning.

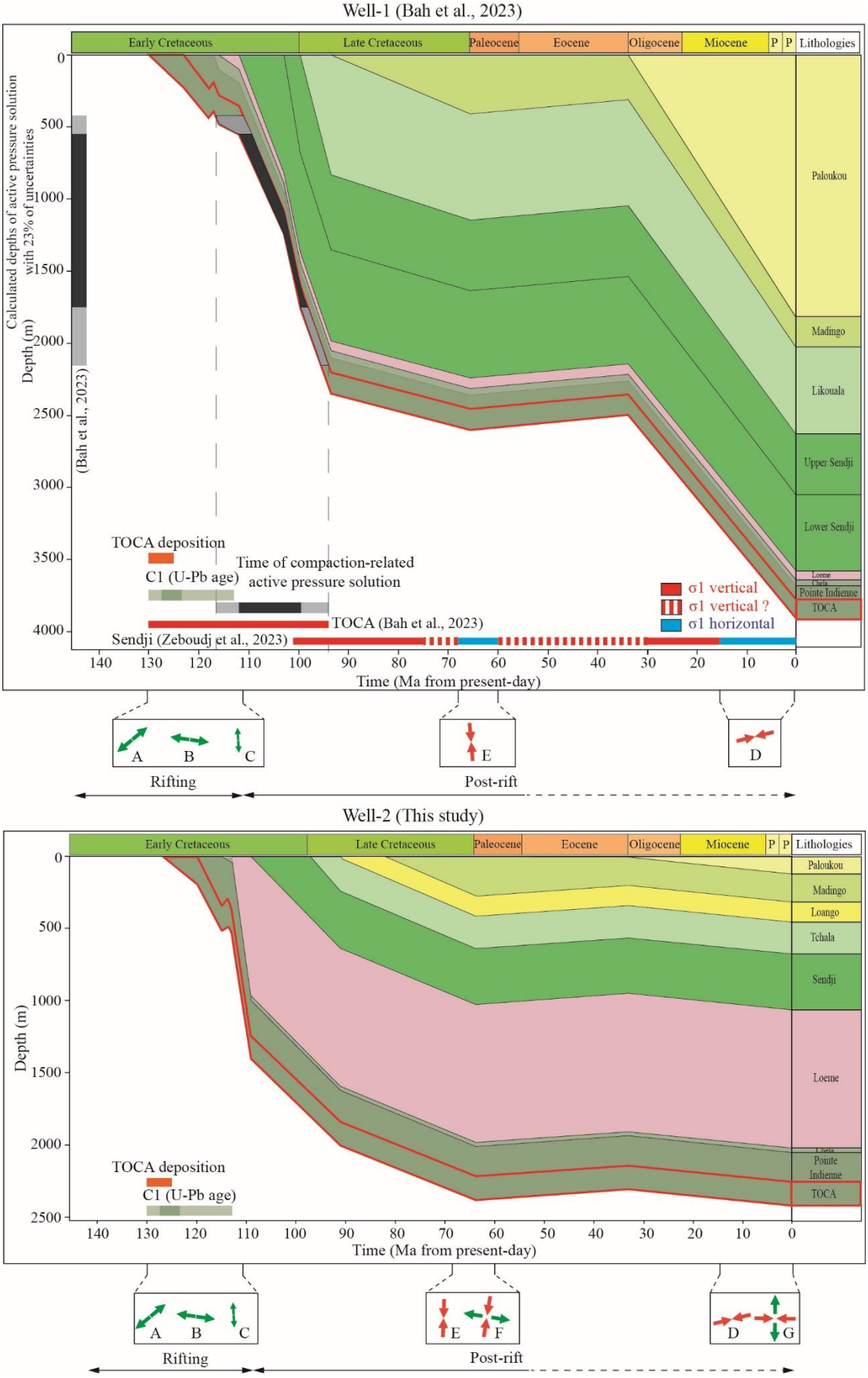
Well-1 (Bah et al., 2023)
Early Cretaceous
Late Cretaceous
Paleocene
Eocene
Oligocene
Miocene
P
P
Lithologies
Calculated depths of active pressure solution with 23% of uncertainties (Bah et al., 2023)
Depth (m)
Paloukou
Madingo
Likouala
Upper Sendji
Lower Sendji
Loeme
Chela
Pointe Indienne
TOCA
TOCA deposition
C1 (U-Pb age)
Time of compaction-related active pressure solution
TOCA (Bah et al., 2023)
Sendji (Zeboudj et al., 2023)
σ1 vertical
σ1 vertical ?
σ1 horizontal
Time (Ma from present-day)
A
B
C
D
E
Rifting
Post-rift
Well-2 (This study)
Loango
Tchala
Sendji
F
G

**Figure 7:** Burial model constructed from Well-1 (Bah et al., 2023) and Well-2 data corrected for mechanical compaction. The depth on the model is counted from the sea-bed. The calculated depth range of active pressure-solution from bedding-parallel stylolite inversion is reported for the TOCA Fm. as grey levels on the y-axis. The stress regimes recorded by the calcite twins inversion were also reported (map view).

For the part of the story which is not directly constrained by our dataset, we used the results from Zeboudj et al., (2023) on the post-rift carbonates of the Sendji Fm. (Well-3 on Fig. 1) which recorded a longer history of compaction-related pressure solution than the TOCA Fm. These results, combined with earlier paleostress reconstructions along the passive margins of western and southern Africa, enabled us to propose a consistent (paleo)stress evolution over time since the deposition of the syn-rift TOCA Fm.

### 5.1.Rift-related extensional paleostresses

On the basis of the results of the inversion of the roughness of the sedimentary stylolites in the TOCA Fm. of Well-1 (Bah et al., 2023) and the known age of the onset of rifting (Beglinger et al., 2012; Salomon et al., 2015), one can state that the stress regime has been dominated by a vertical $\sigma_1$ from ~130 Ma (age of basal TOCA Fm.) until at least 95 Ma. From 95 Ma to the present day, there is no direct evidence of compaction-related pressure solution in the TOCA Fm. We, therefore, propose that the extensional paleostresses recorded by calcite twinning (stress tensor groups A, B and C) be dated between ~130 (earlier absolute age of C1 cement considering uncertainties) and 95 Ma, and more probably between 130 and ~112 Ma (end of rifting). From ~112 Ma to 95 Ma, burial stress and related vertical compaction dominated.

The tensor group A (Fig. 6 and Figs. 1, 2 in Supplementary Material) associated with a NE-SW direction of extension is consistent with that recorded on the southern and western coasts of Africa (Viola et al., 2012; Salomon et al., 2015; Nkodia et al., 2020). This direction of extension is related to the opening of the South Atlantic Ocean. The stress tensor group B (Fig. 6 and Figs. 1, 2 in Supplementary Material) is probably associated with a transient state of stress that predated the main NE-SW extension (see section 6.5). The N-S trend (stress tensor group C) has been recognized from 4 samples only and may be of local significance.

### 5.2.Timing and sequence of post-rift paleostress events

The absence of any constraint on the attitude of $\sigma_1$ after 95 Ma leaves room for the interpretation on the timing of the stress tensor groups D, E, F and G (Fig. 6 and Figs. 1, 2 in Supplementary Material) associated with horizontal $\sigma_1$ as obtained by inversion of calcite twins and that we interpret as post-rift paleostresses. After 95 Ma, either $\sigma_1$ has switched to horizontal, meaning that tectonic stresses overcame the vertical stress related to burial so vertical compaction ended, or for some reason (e.g., massive cementation/clogging of porosity, fluid overpressure) chemical compaction in the TOCA Fm. ceased (Bah et al., 2023) while $\sigma_1$ was still vertical.

Our results therefore suggest a post-95 Ma age for the stress regimes with horizontal $\sigma_1$ oriented either ~N-S (stress tensor groups E and F) or ENE-WSW to E-W (stress tensor groups D and G). Noticeably, during the period of time starting at ~95 Ma and running until 33 Ma, the burial rate strongly slowed down and the reservoir even uplifted (between 66 and 33 Ma, Fig. 7). Because the N-S compression has a trend and a possible timing consistent with the latest Cretaceous-Paleocene compression described by Guiraud and Bosworth (1997), we tentatively propose to assign a latest Cretaceous-early Paleocene age (~67-60 Ma) to the stress tensor groups (E and F). This late Cretaceous-Paleocene compression therefore would be concomitant with the onset of the Paleogene margin uplift (Fig. 7), eventhough a causal link between these two events remains difficult to ascertain.

The compressional and strike-slip stress tensor groups (D and G, respectively) are both associated with horizontal $\sigma_1$ oriented ENE-WSW and E-W, respectively, hence are consistent with the present-day stress (Figs. 1 and 8; Heidbach et al., 2016; Nkodia et al., 2022). We, therefore, propose to relate these stress tensor groups, as well as the development of the sole tectonic stylolite documented in the core which exhibits horizontal peaks oriented ~N100 (Fig. 2), to the same state of stress than the present-day one. However, our results alone do not enable us to precisely date since when these strike-slip and/or compressional states of stress prevailed.

Calcite twin analyses from the TOCA Fm. (this study) and from the supra-salt Sendji Fm. (Zeboudj et al., 2023) yield similar results on most of the post-rift paleostress record (Figs. 7 and 8). The major difference between the stress records in the two formations is (1) that the syn-rift TOCA Fm. recorded the extensional stresses related to rifting, and (2) that the supra-salt Sendji Fm. recorded the post-rift halokinesis and related paleostresses that were not recorded in the pre-salt TOCA Fm. While being aware of these differences, one can combine

the results of the two studies to better constrain the timing of the compressional and strike-slip stress tensor groups. The inversion of the roughness of sedimentary stylolites in the post-salt Sendji Fm. (Zeboudj et al., 2023) indicates that most compaction-related stylolitization has been active between 102 and 15 Ma. After ~15 Ma, no sedimentary stylolite seems to have developed, which suggests that a stress regime with $\sigma_1$ horizontal (either strike-slip or compressional in type) prevailed since then. We therefore assign a post ~15 Ma (post 15-10 Ma to be conservative taking into account uncertainties, Zeboudj et al., 2023) to the stress tensor groups D and G. Because the present-day stress regime is rather compressional (Figs. 1A and 11), we propose that the period dominated by a σ1 horizontal oriented ENE-WSW to E-W started under a strike-slip stress regime (stress tensor group G) and evolved through time into a compressional stress regime (stress tensor group D), keeping in mind the probable occurrence of $\sigma_2$ / $\sigma_3$ stress permutations in space (along and across the strike of the margin) and time (since 15 Ma).

# 6. Discussion

In this section, the reconstructed successive paleostress orientations are discussed in the Africa-fixed reference through time.

## 6.1. Rifting-related faulting and extensional paleostresses in the Lower Congo basin

The absence of mesoscale fractures in the investigated cores from the two wells makes it difficult to bridge the gap between the scales of investigation, hence to link the geometry and kinematics of the regional fault patterns to the paleostresses reconstructed from calcite twins and to establish a sequence between the extensional trends. In particular, it is difficult to ascertain whether the three directions of extension (Figs. 7 and 8) identified over a limited depth (~50 m) range in the two cores (Fig. 2b) are regionally significant and consistent with the orientation of the regional normal faults.

The map of the top TOCA (Fig. 2a) shows that the N-S normal faults are observed mainly atop of the Likouala high where the TOCA was non deposited or totally eroded, but also affect the TOCA Fm. where present. The NW-SE normal faults are found mainly where the TOCA Fm. is present and to a minor extend on the eroded top of the Likouala high; they represent the dominant set of faults bounding the NW-SE oriented Likouala high. This distribution suggests that N-S normal faults were active before and during the deposition of the TOCA Fm. while NW-SE normal faults have been mainly active during the TOCA Fm.

deposition. This would imply that both normal fault sets were active during the TOCA Fm. deposition, but that the activity of N-S faults predated that of the NW-SE faults.

At the mesoscale, the fracture sets described in the TOCA section of other wells in the vicinity of the Likouala high and reaching the base of the TOCA Fm (rose diagrams Fig. 2a, unpublished TotalEnergies reports) show a strike distribution of high angle (extensional) faults from N-S to NW-SE with a dominance of the NW-SE strike, in agreement with the regional fault patterns (Mbina Mounguengui and Guiraud, 2009).

The consistency of the stress tensor groups A (NE-SW extension) and B (N100 to WNW-ESE extension) recorded by calcite twins with the geometry and kinematics of the NW-SE and the ~N-S fault sets, respectively, supports that these groups of tensors reflect the extensional phase associated with continental rifting leading to the opening of the South Atlantic, between 130 and 112 Ma. The dominant NW-SE striking normal faults are perpendicular to the NE-SW (to ENE-WSW) extension which corresponds to the main regional extensional direction (Rabinovich and LaBrecque, 1979; Nurnberg and Muller, 1991) (Fig. 8). A possible explanation for the change in normal fault strike and associated extensional trends during rifting consists in the influence of structural inheritance, especially the geometry of the Neoproterozoic basement structures, on the development of later extensional structures. The Mayumbe belt underlying the Lower Congo basin is dominated by NNW-SSE trending foliation (Pedrosa-Soares et al., 1992; Affaton et al., 2016), while the Kaoko belt in Namibia is dominated by approximately N-S trending foliation (e.g., Passchier et al., 2002; Goscombe and Gray, 2008). These inherited basement weaknesses were favorably oriented for extensional reactivation under an N100 to NE-SW extension. We, therefore, propose that N100 extension (stress tensor group B) (Fig. 8) dominated in the Lower Congo basin during the early continental rupture in relation to the development of the N-S striking normal faults owing to the reactivation of preexisting basement weaknesses. This extensional trend subsequently evolved during the Barremian into the regional NE-SW extension (stress tensor group A) associated with the development of the dominant pattern of NW-SE striking normal faults. The third group of extensional stress tensors (C) was identified only in very few samples (Figs. 7 and 8), which would suggest that the N-S extensional trend is of limited regional importance. We propose that the N-S extension, which is consistent with the few E-W (to ENE-WSW) striking normal faults that possibly acted as transfer faults (Fig. 2a), may reflect a local state of stress at the basin scale.

Alternatively, one could propose that whereas the NE-SW extension (Fig. 8) reflects the divergent motion between the African and South American plates (i.e., the boundary conditions), additional lithospheric doming related to mantle upwelling during rifting may have caused second-order radial pattern of gravitational extensional trends. Salomon et al., (2015) reported two extensional directions for the South Atlantic rifting episode derived from the analysis of mesoscale striated faults in Namibia (Fig. 8), and proposed that the diversity of extensional directions during rifting may have resulted from the combined effects of flexural bending due to sediment loading offshore and continuous upwelling of the African superplume that remained located below the African continent after the break-up of Gondwana (Braun et al., 2014). Although this scenario of a plume-related lithospheric doming should not be overlooked, we favor the role of crustal structural inheritance and of possibly slightly changing boundary conditions (e.g., divergence between Africa and South America) as the more likely explanation of the changing extensional trends in the Lower Congo basin during rifting.

### 6.2. Post-rift compressional and strike-slip paleostresses on the Lower Congo basin

During the post-rift evolution of the South Atlantic Ocean, several states of stress, either strike-slip or compressional in type, have been recorded onshore along the central and southern West Africa margin (Fig 8). This result is in line with the findings by Withjack et al., (1995) that passive margins may not have a simple two-stage evolution of rifting and drifting, but instead may have experienced a complex tectonic history including extension and shortening during passive margin development.

Our interpretation that the post-95 Ma ~N-S compressional trend corresponds to the latest Cretaceous-Paleocene (~67-60 Ma) compression described by Guiraud and Bosworth (1997) suggests that compressional stresses generated at the distant Africa-Eurasia plate boundary were transferred far across the African plate (Figs. 7 and 8). This far-field stress transmission would likely require a deep stress guide, such as a high strength (rigid) continental lithosphere. This hypothesis is in line with the observation of similar compressional trends in the pre-rift section of Well-1 and Well-2 located on both sides of the Likouala high, as well as in the post-rift Sendji Fm. of Well-3 after welding of the supra-salt formations due to salt removal (Zeboudj et al., 2023).

The reconstructed strike-slip and compressional stress regimes with horizontal $\sigma_1$ trending ENE-WSW to E-W are consistent with the present-day stress regime (Fig. 8) (Delvaux and Barth, 2010; Heidbach et al., 2016; Nkodia et al., 2022). Zeboudj et al., (2023) have tentatively associated this stress regime with an intraplate ~E-W compression prevailing from the Miocene (~15 Ma) onwards and possibly related to the Atlantic ridge push effect (Fig. 8). We also propose that the compressional / strike-slip stress regimes with $\sigma_1$ oriented ENE-WSW to E-W be related to a far-field effect of the mid-Atlantic ridge push, prevailing from ~15 Ma onwards. This interpretation is consistent with the idea that the ridge push could have efficiently controlled the lithospheric stress long after the initiation of the spreading ridge (e.g., Wiens and Stein, 1983, 1985). If this interpretation is correct, our results would support a transmission of the ridge push-related compressional stress over a large distance (~2500 km between the oceanic ridge and the study area since ~15 Ma. This interpretation is in line with the numerical models of Mahatsente and Coblentz (2015) that show that the magnitude of the Atlantic ridge-push force is significantly less than the integrated strength of the oceanic part of the African (Nubian) plate, so this part of the plate is very little deformed and the stresses related to the ridge push can be transferred far into the interior of the oceanic and continental parts of the African plate. Our results also agree with the findings of Withjack et al., (1995) that during the development of the southeastern Canadian passive margin, the Fundy rift basin on the western edge of the margin experienced shortening possibly associated with sea-floor spreading processes such as ridge push or continental resistance to plate motion. Recently, Nkodia et al., (2022) proposed that the present-day stress pattern in the Lower Congo basin (offshore Angola) could be related to stress loading of the passive margin and interior Congo by the oceanic transform faults extending onland, which would trigger the reactivation of well oriented faults systems. In this scenario, the present-day stress pattern would not be strictly controlled by the ridge push but would still be related to a sea-floor spreading process. However, alternate stress sources also may have contributed to the late Tertiary-present stress field in the western African margin. Some modelling studies (e.g., Medvedev et al., 2016) suggest that in addition to the ridge push effect other stress sources (e.g., density variations within the lithosphere, flexural loading of the lithosphere) are involved throughout the African plate. This mixed origin of the recent/contemporary stress pattern would be in agreement with the results of Pascal and Cloetingh (2009).

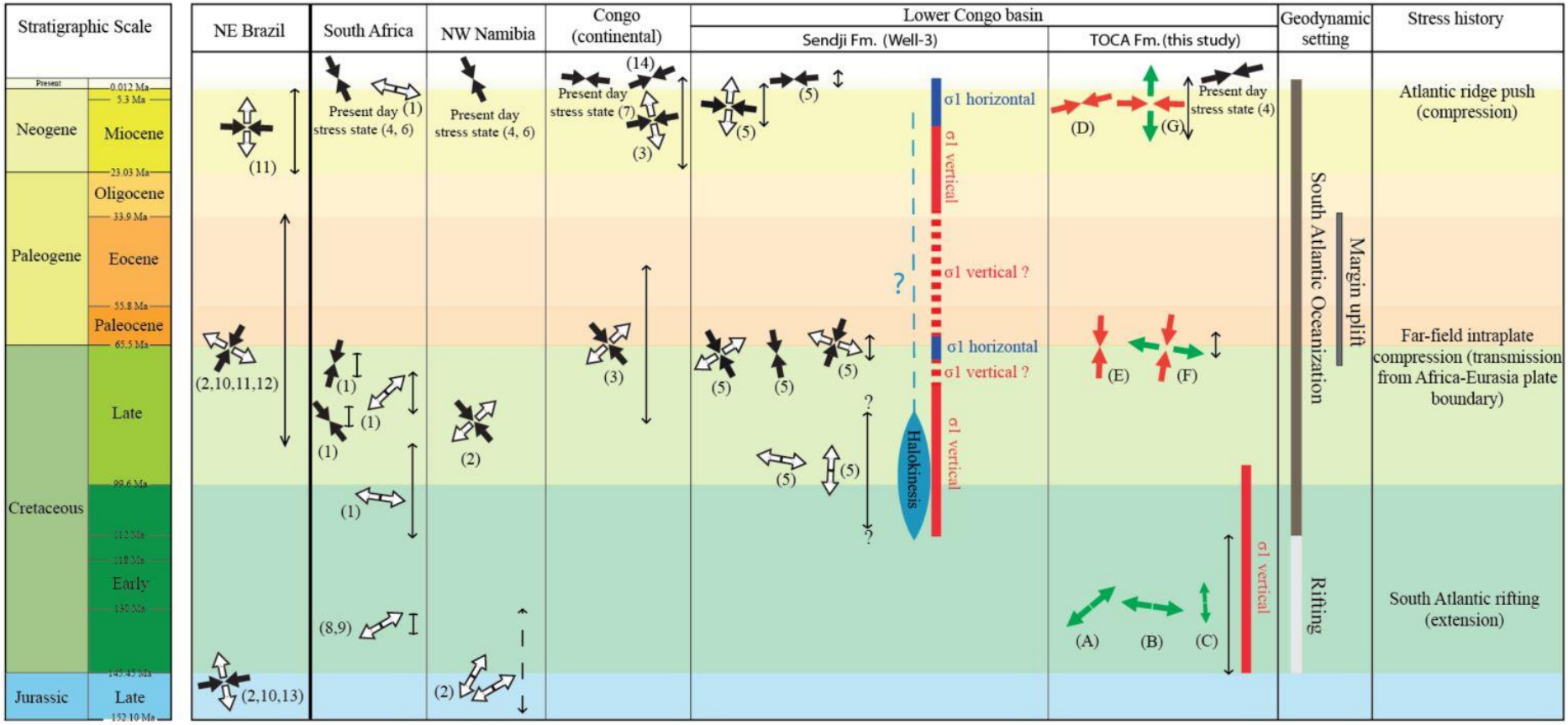


**Figure 8:** Summary of the time distribution of tectonic events and associated stress orientations (projected onto the present position of Africa in map view) since early Cretaceous to present recorded in the southern West Africa (Congo, Namibia, Angola and South Africa) and Brazil.

Our stress results do not allow the formal recognition of the post-rift Campanian-Maastrichtian NE-SW extension that Guiraud and Bosworth (1997) consider as an Africa-wide extensional event. Possible explanations include (1) the weak transmission of far-field extensional stresses into the investigated offshore part of the margin, or (2) the unability of our calcite-twin dataset to discriminate among the superimposed effects of this extensional stress and of the rifting-related extensional stresses. The reason why the late Santonian (~83-85 Ma) N-S to NW-SE compression described by Guiraud and Bosworth (1997) has not been recorded by calcite twinning in our samples from the Lower Congo basin (Zeboudj et al., 2023; this study) while it was seemingly identified in Namibia and South Africa (Viola et al., 2012; Salomon et al., 2015) remains unclear at this time.

To sum up, the inversion of calcite twins for stress applied to the TOCA Fm. suggests that during its post-rift tectonic history, the west Africa margin underwent compressional and/or strike-slip stress regimes, being either tectonic (compressional stress transfer from the distant collisional Africa-Eurasia plate boundary) or gravitational (ridge push transmitted from the mid-Atlantic ridge) origins. Our interpretations are consistent with earlier claims that the late Cretaceous–Cenozoic intraplate contractional deformation at the Norwegian continental shelf was possibly related to far-field effects of active plate-margin processes and transfer of stresses across the plate as a consequence of the sub Hercynian and Paleocene ‘Laramide’ event of the Alpine orogeny, with additional significant contribution of ridge push from the North Atlantic spreading particularly during the Neogene (Vagnes et al., 1998).

### 6.3.Significance of the reconstructed paleostress fields in the kinematic history of Africa and the south Atlantic

Several kinematic reconstructions have been proposed for the opening of the South Atlantic based on paleomagnetic data (Bullard et al., 1965; Vink et al., 1982; Torsvik et al., 2009; Aslanian et al., 2009; Heine et al., 2013; Pérez-Diaz and Eagles, 2014). All reconstructions involve a relative motion of South America with respect to fixed Africa combining both a clockwise rotation of ~40-45° and a translation. The different reconstructions are quite similar since the onset of oceanic spreading (112 Ma), but may show significant differences for the rifting phase (see discussions in Aslanian and Moulin, 2010; Moulin et al., 2010; Chaboureau et al., 2013; Pérez-Diaz and Eagles, 2014), mainly due to the difficulty of having reliable markers to constrain the exact position of Africa and South America at the onset of rifting.

The main stages of the paleostress evolution recorded by the TOCA Fm. are reported on a series of paleogeographic maps (considering Africa fixed) spanning from the Barremian to the present (Fig.9). These maps are based on the kinematic reconstructions of Heine et al. (2013) for the rifting episode and the onset of oceanization (Barremian to Albian) and of Moulin et al., (2010) for the Paleocene until the present because the reconstructions of Heine et al. are not available after 100 Ma.

In the early Barremian (130 Ma, Fig. 9a), the extension between Africa and South America that was initiated in the Neocomian continued while the carbonates of the TOCA Fm. started to be deposited in a continental lacustrine environment. In the late Barremian (127 Ma, Fig. 9b), an ~N100 extension prevailed in the Lower Congo basin, associated with the reactivation of pre-existing basement structures and the formation of N-S striking normal faults (Fig. 9). The minor stress tensor group C (~N-S $\sigma_3$) which could be related either to reactivation of the transverse faults within the basin or to a $\sigma_2/\sigma_3$ stress permutation during N100 extension has not been plotted. The reconstructions by Heine et al., (2013) involve an E-W divergent motion between Africa and South America at 132 Ma changing to a NE-SW divergent motion at 126 Ma. Considering the deposition age of the TOCA Fm. and the age of the C1 cement from which calcite twin measurements were taken, a (progressive?) change from E-W to NE-SW extension occurring at ~126 Ma would be consistent with both our paleostress results and the observed normal fault pattern in the Lower Congo basin.

In the Aptian (120 Ma, Fig. 9c), continental rifting continued and propagated northwards. A NE-SW extension prevails in the Lower Congo basin (Fig. 9), associated with the activity of the NW-SE normal faults.

In the Albian (110 Ma, Fig. 9d), sea-floor spreading started to be active and the Sendji Fm. deposited while the extension continued in the Equatorial Atlantic (Loparev et al., 2021).

In the early Paleocene (60 Ma, Fig. 9e), while the spreading of the South Atlantic was active, the stress regime of the West African passive margin became transiently compressional or strike-slip in type with $\sigma_1$ oriented ~N-S. This state of stress possibly reflects a far-field compressional stress transfer from the distant active Africa-Eurasia convergent plate boundary.

From the middle Miocene (Fig. 9f) to present (Fig. 9g), the prevailing stress regime in western Africa is mainly compressional or strike-slip with $\sigma_1$ oriented ENE-WSW to E-W and is thought to originate mainly from the mid-Atlantic ridge push (Fig. 9).

### 6.4.Paleostress magnitude and implications for fracture prediction in the TOCA Fm.

The consideration on the attitude of $\sigma_1$ derived from sedimentary stylolite roughness paleopiezometry combined with burial-time evolution of the syn-rift TOCA Fm (Bah et al., 2023) and the post-rift Sendji Fm (Zeboudj et al., 2023) helps unlock the full determination of principal stress magnitudes which requires the knowledge of the burial depth of the rocks at the time of deformation (Beaudoin and Lacombe, 2018). Hereinafter, the differential stress values provided by calcite twin paleopiezometry are combined with the vertical stress estimates derived from the burial model to estimate principal stress magnitude at the time of deformation (Lacombe and Laurent, 1992; Lacombe, 2007). The resulting principal stress magnitudes are further compared with the strength of the intact whole rock derived from geomechanical tests (i.e., failure envelope) to evaluate the consistency of the stress results and to help predict whether fracturing can be expected in the reservoir under the reconstructed paleostresses. We also compare stress magnitudes related to syn-rift extension and post-rift compressions recorded by the TOCA Fm. in the two wells (Well-1 and Well-2) in which the final burial depths of the TOCA Fm. are different, as well as stress magnitudes related to post-rift compressions in the TOCA Fm. in Well-1 and in the Sendji Fm. in Well-3 (Zeboudj et al., 2023) (Fig. 10) because the two formations reached nearly similar final burial depths. For this purpose, the value of $\sigma_v$ was calculated at the time the paleostress of interest prevailed, assuming either dry conditions $\sigma_V = \rho gh$ or hydrostatic fluid pressure: $\sigma_V = (\rho - \rho_w)gh$, with $\rho$ the dry density of the rock column above (2600 kg.m$^{-3}$), $\rho_w$ the density of water (1000 kg.m$^{-3}$), g the gravitational field acceleration (9.81 m.s$^{-2}$), and h the depth (m). Hereafter, we consider that the tangency of the ($\sigma_1$- $\sigma_3$) Mohr circle to the failure envelope is indicative of rock failure.

The lower Cretaceous extensional tectonic event was recorded by calcite twins (stress tensor groups A, B and C) when the TOCA Fm. was buried at maximum ~500 m and ~1000 m depth in Well-1 and Well-2, respectively (Fig. 7). These burial depths correspond to mean values of 18 MPa and 28 MPa for the vertical stress $\sigma_1$ in dry conditions for Well-1 and Well-2, respectively. The values of the principal stresses $\sigma_2$ and $\sigma_3$ are then deduced from the differential stress values ($\sigma_1$-$\sigma_3$) and ($\sigma_2$-$\sigma_3$) (Fig. 6 and Figs. 1, 2 in Supplementary Material). For dry conditions, the value of $\sigma_3$ is negative (i.e., in the tensile domain on the Mohr diagram; Fig. 10) for both stress regimes and in both wells, and its absolute value is even larger than the rock tensile strength as indicated by geomechanical tests, so the corresponding Mohr circle exceeds the strength envelope of the intact rock.

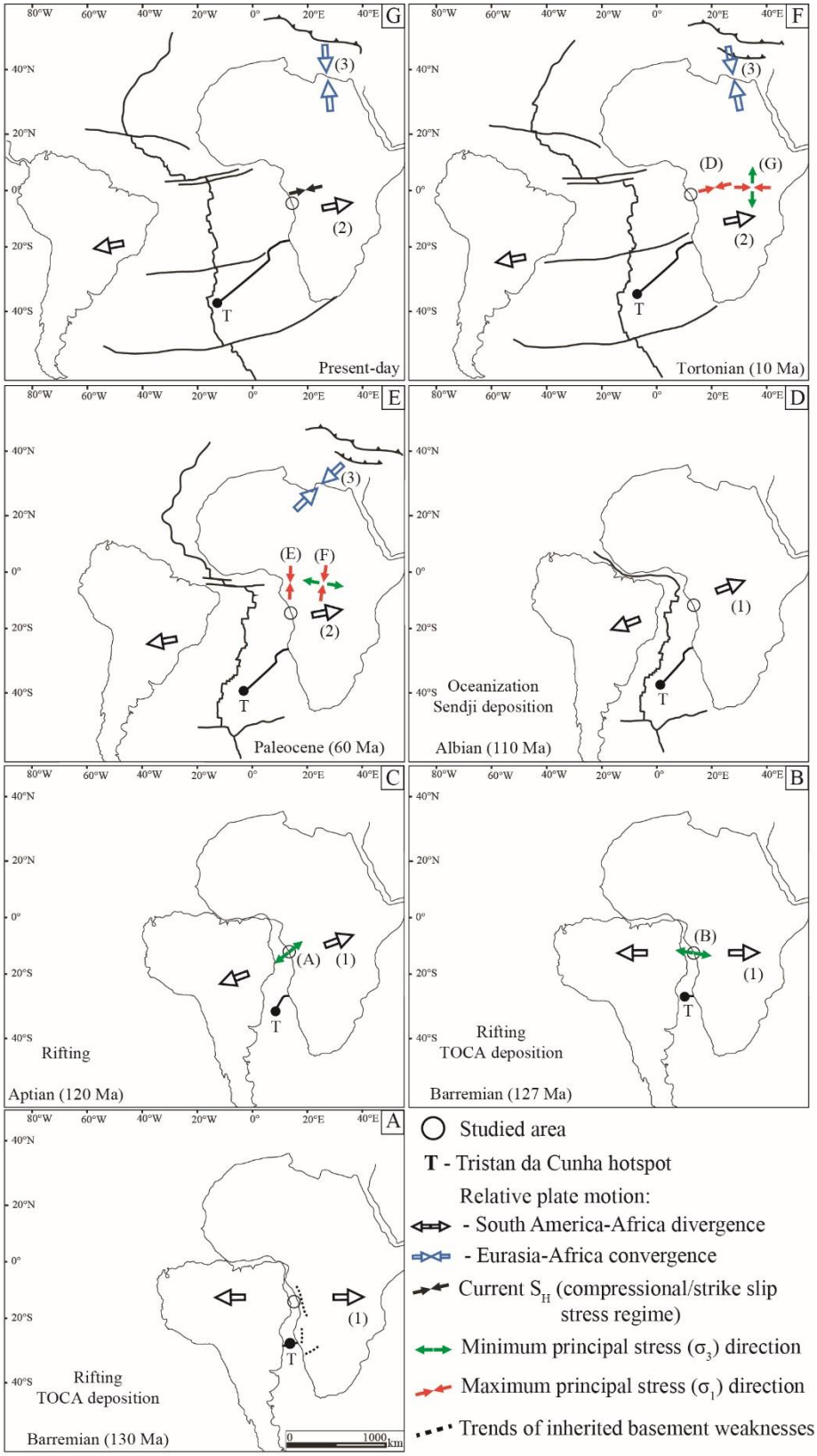


**Figure 9:** Paleogeographic reconstruction maps on which the directions of the paleostresses resulting from the inversion of the calcite twins are plotted in map view (see text for more details).

The assumption of a hydrostatic fluid pressure would lead to even more negative effective stress values of $\sigma_3$, which is impossible. This means that the differential stresses related to the extensional stress regimes are possibly overestimated, even when considering the possible uncertainties on their values (±30%, Fig. 10) (see section 3.2.4.2). In contrast, differential stress magnitudes for compressional and strike-slip stress regimes are in line with expected shallow crustal stresses (Lacombe, 2001, 2007; Beaudoin and Lacombe, 2018). Lacombe et al., (1990, 1994) already reported abnormally high differential stress magnitudes related to Eocene-Oligocene extension in the Paris basin, that Lacombe and Laurent (1992) tentatively related to the superimposition of extensional paleostress tensors that the method could hardly discriminate. One possible explanation would be that the calcite twin population which recorded the extensional stress regimes actually formed not only during rifting, but also during continuing post-rift burial as long as the vertical principal stress $\sigma_1$ was vertical. In other words, a longer duration of the application of a causative differential stress would have allowed for the cumulative development of twins within randomly oriented grains less favorably oriented to twin (Lacombe et al., 2021a). This means that the unexpectedly high differential stress values returned by calcite twin analysis for extensional stress groups might possibly result from the superimposed effects of differential stress related to syn-rift extension and of the differential stress related to later post-rift burial under a vertical principal stress $\sigma_1$ that prevailed at least until 95 Ma (Bah et al., 2023).

To test this hypothesis and to estimate the theoretical possible contribution of post-rift burial on the differential stress values for the extensional stress regimes, we assumed that the effect of burial can be approximated by a state of stress with $\sigma_1 > \sigma_h = \sigma_H$ ($=\sigma_2=\sigma_3$). This is more likely the case during the burial of the TOCA Fm. between 112 and 95 Ma, i.e., after the rifting. In contrast, during the rifting period, this assumption is theoretically incorrect since calcite twinning paleopiezometry indicates that ($\sigma_2$-$\sigma_3$) values are about 15-20 MPa (Fig. 6 and Figs. 1, 2 in Supplementary Material).

The burial-time model (Fig. 7) performed on Well-1 and Well-2 indicates that the TOCA Fm. was buried from ~500 m depth at 112 Ma (end of rifting) to ~2100 m at 95 Ma in Well-1 and from ~1000 m depth at 112 Ma to ~1860 m at 95 Ma in Well-2. The depth difference, ~1600 m and ~860 m in Well-1 and Well-2, respectively, was used to calculate the corresponding range of values for $\sigma_v=\sigma_1$. The resulting vertical stress is ~41 MPa and ~22 Ma for Well-1 and Well-2, respectively. Considering these values and the mean Poisson ratio of the TOCA limestones determined from geomechanical tests (see section 4.2), and assuming uniaxial strain, we use equation (5):

$$\sigma_H = \sigma_h = \left(\frac{\nu}{1-\nu}\right)\sigma_v \quad (5)$$

to derive a burial-related maximum differential stress magnitude ($\sigma_v$-$\sigma_h$) of ~30 MPa and ~15 MPa for Well-1 and Well-2, respectively between 112 and 95 Ma. The maximum differential stress value obtained in Well-1 is comparable to the average differential stress value (considering uncertainties) derived from calcite twins for the extensional rifting event (~45 MPa) in contrast to that obtained in Well-2 which shows a lower value. With a mean CRSS for twinning in our samples of 6-7 MPa (except for one sample from Well-2; Table 3 in Supplementary Material), this indicates that the lithostatic differential stress was likely high enough to practically cause twinning to occur under a vertical $\sigma_1$, especially in Well-1. Even though it is impossible to establish to what degree twinning caused by differential stress related to post-rift continuing burial may have cumulated with twinning caused by extension-related differential stress to return the high differential stress magnitudes reconstructed for the extensional stress groups, this rough estimate suggests that the burial effect might provide a reasonable explanation for the likely overestimate of extensional differential stress magnitudes ($\sigma_1$-$\sigma_3$) using calcite twinning paleopiezometry. This still unsolved question will require further methodological and experimental developments which are out of the scope of this paper.

The absence of fit of the Mohr circles related to extensional stresses with the failure envelope (Fig. 10) precludes any definite conclusion on the occurrence of extensional mesostructures such as mode I fractures and normal faults in the studied wells. However, there is no doubt that the differential stress values related to extension were such that mode I fractures and normal faults did develop in the TOCA Fm. at regional scale (Fig. 2a).

For the stress regimes with horizontal $\sigma_1$ oriented ~N-S (stress tensor groups E) that we tentatively dated at ~67-60 Ma, the vertical stress estimated at 60 MPa is rather close for Well-1 and Well-2 (i.e., 64 MPa and 61 MPa, respectively, assuming dry conditions) (Fig. 10). The corresponding Mohr circles (Fig. 10) lie much below the rupture envelope, under both dry and hydrostatic fluid pressure conditions, and so despite uncertainties (Fig. 10). These observations indicate that the far-transferred ~N-S compressional stress was unlikely to induce fractures of either types without fluid overpressure (i.e., supra-hydrostatic fluid pressure). This is in line with the findings by Zeboudj et al., (2023) for the same compressional phase in the Sendji Fm. and with the observation that no mesostructures possibly related to ~N-S compression have been so far identified and reported from nearby wells (Fig. 10a).

For the compressional event with horizontal $\sigma_1$ oriented ~ENE-WSW (stress tensor groups D) that we tentatively dated from the middle Miocene (~15 Ma) onwards, the current vertical stress is estimated at 105 MPa and 64 MPa for Well-1 and Well-2 respectively, assuming dry conditions (Fig. 10). The corresponding Mohr circles (Fig. 10) lie much below the rupture envelope and it is the same if hydrostatic conditions are assumed. Like for the Maastrichtian-Paleocene compressional event, the differential stresses recorded for this event were unlikely to cause fractures in the TOCA Fm. Zeboudj et al., (2023) reported similar observations for the same compressional stress in the post-salt Sendji Fm (Fig. 10a).

For both compressional events, a fluid overpressure of at least 50 MPa would be needed to possibly cause fracture development. Although we cannot definitely exclude the occurrence of fluid overpressure in the TOCA reservoirs during its post-rift burial history because of the hydrocarbon migration in the Lower Congo basin from the Cenomanian to the Paleocene (Bah et al., 2023) and the occurrence of the overlying salt level that would likely act as a fluid barrier preventing upward fluid escape, the absence of any fractures consistent with the post-rift compressional events suggest that fluid overpressure -if any- never exceeded such a value.

Noticeably, the overall consistency between differential stress magnitudes recorded independently in the different wells (1 and 2) emphasizes that calcite twinning paleopiezometry is a robust and reliable method to reconstruct stress magnitude even at great depth and in complex tectonic settings.

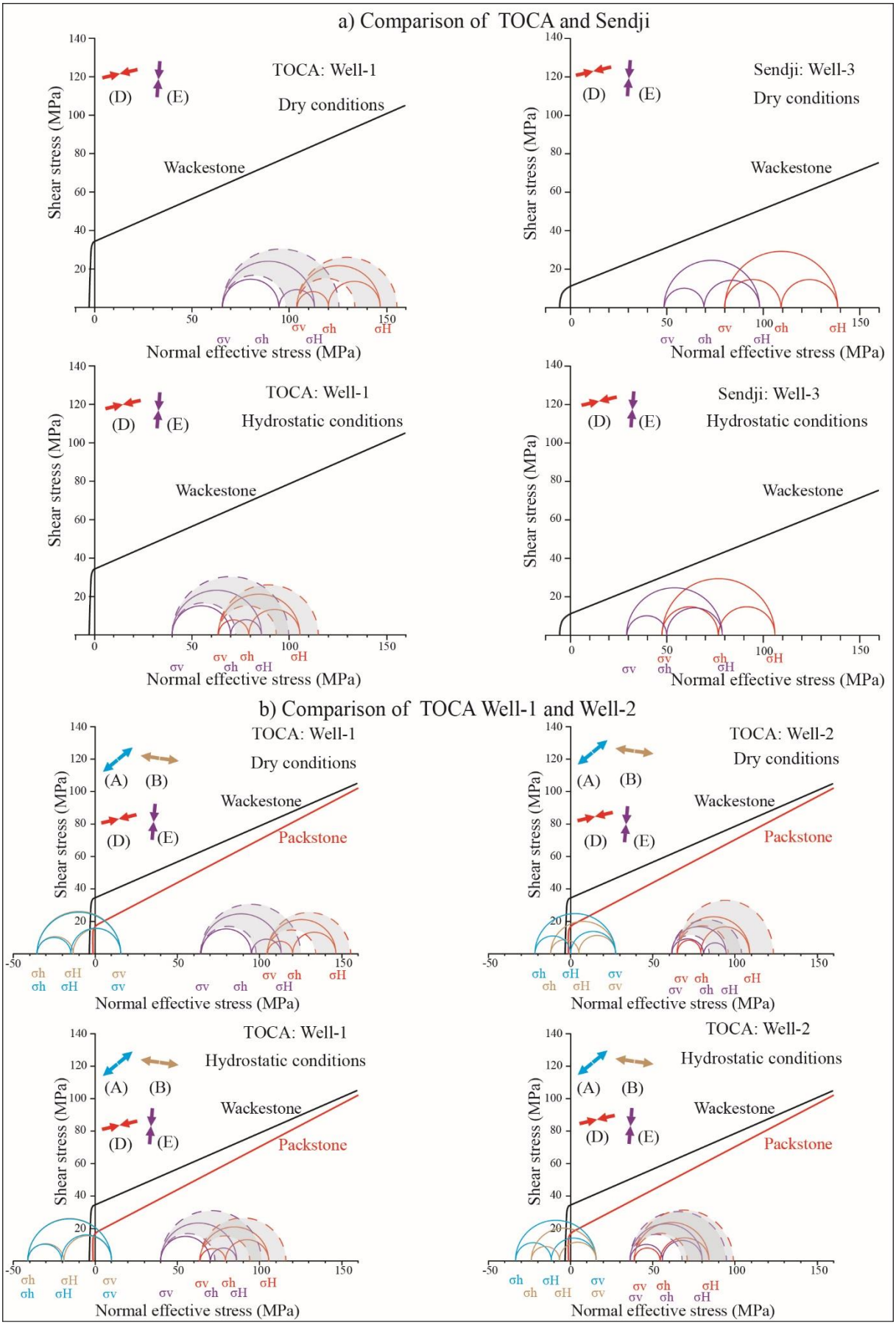
a) Comparison of TOCA and Sendji
TOCA: Well-1
Dry conditions
Wackestone
Sendji: Well-3
Dry conditions
Wackestone
TOCA: Well-1
Hydrostatic conditions
Wackestone
Sendji: Well-3
Hydrostatic conditions
Wackestone
Shear stress (MPa)
Normal effective stress (MPa)
(D)
(E)
b) Comparison of TOCA Well-1 and Well-2
TOCA: Well-1
Dry conditions
Wackestone
Packstone
TOCA: Well-2
Dry conditions
Wackestone
Packstone
TOCA: Well-1
Hydrostatic conditions
Wackestone
Packstone
TOCA: Well-2
Hydrostatic conditions
Wackestone
Packstone
(A)
(B)
(D)
(E)
Shear stress (MPa)
Normal effective stress (MPa)

**Figure 10:** Mohr diagrams displaying the failure envelope of the TOCA Fm. determined from rock mechanics tests and the Mohr circles related to the differential stress magnitudes resulting from the inversion of the calcite twins of each tectonic event, under dry and hydrostatic conditions (see text for more details). Comparison of stress magnitudes related to post-rift compressions in the TOCA and Sendji formations (a) and stress magnitudes related to syn-rift extension and post-rift compressions recorded by the TOCA Fm. in the two wells (b). The dashed circles and the greyed area in between represent the ±30 % uncertainty on (σ1-σ3) values.

## 7. Conclusions

This study focuses on the pre-salt carbonate TOCA Fm. investigated in two offshore wells in the Lower Congo basin. The novel combination of burial modelling and inversion of calcite twins for stress provides an original approach to obtain unprecedented information on the burial and paleostress history of this deeply buried reservoir. The inversion of the calcite twins allowed the determination of distinct stress regimes, the timing of which was constrained by the reconstruction of the maximum depth of compaction-related active pressure solution combined with burial modelling.

The TOCA Fm. recorded three main tectonic events during its burial history : (1) extension between 130 and 112 Ma, with $\sigma_3$ evolving from a N-S to a NE-SW trend associated to the rifting preceding the opening of the South Atlantic; (2) intraplate ~N-S compression, possibly dated between 67 and 60 Ma and reflecting an intraplate far-field transfer of orogenic stress from the distant Africa-Eurasia active plate boundary; (3) ENE-WSW to E-W compression that we propose to mostly relate to the mid-Atlantic ridge push from ~15 Ma onwards. For each state of stress, calcite twinning paleopiezometry combined with burial modelling and rock mechanics tests enabled us to discuss the stress magnitudes which prevailed within the reservoir.

Our results demonstrate that the TOCA Fm. reservoir in the Lower Congo basin, and more generally the West African margin of the South Atlantic have recorded a complex tectonic history, including extension and compression. Beyond the reservoir scale, this study provides a new support to how tectonic and gravitational lithospheric stresses can be transferred far away from active plate boundaries and how their succession has controlled the tectonic evolution of passive margins.

## Acknowledgments

The authors are very grateful to TotalEnergies for granting financial support to this research, for providing the cores and prior data, and for permission to publish. We would like to thank Philippe Marchina for his help in carrying out the geomechanical tests and for the discussions on the results. NEB is funded through the isite-E2S, supported by the ANR PIA and the Région Nouvelle-Aquitaine. The authors would also like to thank the journal editor Samuel Angiboust as well as Damien Delvaux and an anonymous reviewer for their useful comments and suggestions that improved the quality of the paper.

## Supplementary material

**Table 1 Suppl. Mat:** Chronostratigraphic chart used for the burial model of Well-2. The simulation begins at –145.5 Ma and ends at the present day. The basin model input parameters such as age; present-day thickness and initial porosity of each formation are indicated.

| Event | | | Age (Ma) | | Thickness (m) | Initial porosity (%) | Solide density (kg/m$^3$) |
|---|---|---|---|---|---|---|---|
| Formation | Lithology | Number | From | To | | | |
| Paloukou | Shales | 14 | 33.9 | 0.0 | 118 | 59.6 | 2.65 |
| Erosion | | 13 | 65.5 | 33.9 | -100 | | |
| Madingo | Shales | 12 | 93.5 | 65.5 | 195 | 62.7 | 2.65 |
| Loango | Limestones/Sandstones | 11 | 99.6 | 93.5 | 139 | 53.0 | 2.83 |
| Tchala (Likouala) | Limestones/Sandstones | 10 | 103 | 99.6 | 223 | 45.7 | 2.70 |
| Sendji | Limestones | 9 | 112 | 103 | 384 | 50.2 | 2.69 |
| Loeme | Salt & Anhydrite | 8 | 116 | 112 | 957 | 10.0 | 2.20 |
| Chela | Limestones/Sandstones | 7 | 117 | 116 | 29 | 45.2 | 2.69 |
| Erosion | | 6 | 118 | 117 | -75 | | |
| Pointe Indienne | Shales | 5 | 123 | 118 | 205 | 62.3 | 2.65 |
| TOCA | Limestones | 4 | 127 | 123 | 163 | 51.5 | 2.69 |
| Pointe Noire | Shales | 3 | 130 | 127 | 60 | 57.0 | 2.68 |
| Djeno | Sandstones | 2 | 141 | 130 | 110 | 51.5 | 2.68 |
| Basal sandstones | Sandstones | 1 | 146 | 141 | 90 | 44.5 | 2.68 |

**Table 2 Suppl. Mat:** Results of the multitriax and Brazilian tests for four samples (2 samples for each test) representative of the studied carbonate facies (wackestone and packstone), sampled at 4086 m and 4135 m depth respectively in Well-1 drill core. The multitriax samples were tested at 10, 30 and 50 MPa confining pressure (Pconf).

| Sample depth (m) | Multitriax test | | | | | | Brazilian test |
|---|---|---|---|---|---|---|---|
| | Pconf (MPa) | Yield (MPa) | Rupture (MPa) | Estimated rupture (MPa) | Friction angle (°) | Cohesion (MPa) | Tensile strength (MPa) |
| 4086 (Wackestone) | 10 | 55 | - | 113.2 | 17.4 | 33.9 | 1.69 |
| | 30 | 70 | - | 144.5 | | | |
| | 50 | 100 | 205 | - | | | |
| 4135 Packstone) | 10 | 41 | - | 81.8 | 26.2 | 17.2 | 3.13 |
| | 30 | 65 | - | 131.7 | | | |
| | 50 | 90 | 185 | - | | | |

**Table 3 Suppl. Mat:** Paleostress tensors determined from calcite twin inversion (CSIT-2). The quality of each tensor is estimated on the basis of several criteria such as the stability of principal stress orientations, the value of the penalization function and the number of incompatible untwinned planes. TP - Twinned planes; UP - Untwinned planes.

| Depth (m) | $\sigma_1$ trend (°) | $\sigma_1$ plunge (°) | $\sigma_2$ trend (°) | $\sigma_2$ plunge (°) | $\sigma_3$ trend (°) | $\sigma_3$ plunge (°) | Penalization function | $\Phi$ | $_{TS}^{min}$ | (CRSS) MPa | $(\sigma_1-\sigma_3)$ MPa | $(\sigma_2-\sigma_3)$ MPa | Total number of TP/UP | Number of compatible TP/UP | Quality |
|---|---|---|---|---|---|---|---|---|---|---|---|---|---|---|---|
| Well-1 | | | | | | | | | | | | | | | |
| 4070.25 | 206 | 81 | 306 | 1 | 36 | 8 | 0.1 | 0.6 | 0.196 | 7 | 36 | 21 | 81/51 | 26/46 | A |
| 4070.8 | 351 | 1 | 81 | 5 | 249 | 85 | 0.3 | 0.7 | 0.120 | 7 | 58 | 40 | 80/52 | 24/49 | A |
| | 183 | 61 | 314 | 20 | 51 | 20 | 0.6 | 0.4 | 0.207 | | 34 | 15 | | 27/43 | B |
| 4070.8 | 114 | 72 | 270 | 17 | 2 | 7 | 1.0 | 0.6 | 0.149 | 6 | 40 | 25 | 85/38 | 31/29 | C |
| 4075.53 | 328 | 60 | 122 | 28 | 218 | 11 | 1.8 | 0.2 | 0.123 | 7 | 57 | 9 | 119/34 | 49/22 | C |
| 4080.8 | 59 | 1 | 329 | 20 | 152 | 70 | 0.4 | 0.3 | 0.127 | 6 | 47 | 14 | 135/45 | 43/40 | A |
| 4086.61 | 175 | 8 | 79 | 34 | 276 | 54 | 0.6 | 0.7 | 0.228 | 7 | 31 | 21 | 135/42 | 43/34 | B |
| 4126.92 | 272 | 82 | 162 | 3 | 71 | 8 | 1.4 | 0.4 | 0.128 | 7 | 55 | 20 | 98/52 | 57/40 | C |
| 4130.09 | 73 | 28 | 338 | 10 | 230 | 60 | 1.0 | 0.5 | 0.185 | 7 | 38 | 19 | 135/36 | 38/21 | C |
| | 183 | 61 | 1 | 29 | 91 | 1 | 1.1 | 0.4 | 0.204 | | 34 | 14 | | 41/20 | C |
| | 162 | 70 | 341 | 20 | 71 | 0 | 1.1 | 0.6 | 0.203 | | 34 | 20 | | 38/24 | C |
| 4132.05 | 208 | 84 | 29 | 6 | 299 | 0 | 0.8 | 0.3 | 0.137 | 7 | 51 | 13 | 153/39 | 52/30 | B |
| | 255 | 23 | 152 | 27 | 19 | 53 | 0.8 | 0.5 | 0.202 | | 35 | 17 | | 43/23 | B |
| 4132.83 | 111 | 80 | 21 | 0 | 290 | 10 | 1.3 | 0.3 | 0.126 | 6 | 47 | 14 | 119/34 | 49/23 | C |
| 4139.87 | 311 | 45 | 140 | 44 | 45 | 4 | 1.8 | 0.4 | 0.110 | 6 | 55 | 23 | 135/48 | 54/21 | C |
| | 54 | 10 | 145 | 3 | 252 | 80 | 0.5 | 0.6 | 0.193 | | 31 | 17 | | 38/32 | A |
| 4141.9 | 78 | 45 | 325 | 22 | 217 | 37 | 0.9 | 0.3 | 0.103 | 6 | 58 | 17 | 116/37 | 40/29 | B |
| | 270 | 7 | 179 | 2 | 70 | 83 | 0.7 | 0.4 | 0.159 | | 38 | 15 | | 40/28 | B |
| 4143.84 | 91 | 0 | 1 | 1 | 190 | 89 | 1.1 | 0.5 | 0.134 | 7 | 52 | 27 | 136/38 | 49/25 | C |
| | 107 | 69 | 199 | 1 | 290 | 20 | 0.8 | 0.3 | 0.168 | | 42 | 14 | | 41/26 | B |
| | 78 | 76 | 303 | 10 | 211 | 10 | 1.0 | 0.4 | 0.131 | | 53 | 23 | | 43/25 | C |
| 4145.92 | 336 | 87 | 83 | 1 | 173 | 3 | 0.4 | 0.3 | 0.073 | 6 | 82 | 25 | 136/53 | 54/51 | A |
| | 30 | 59 | 134 | 8 | 229 | 29 | 0.5 | 0.5 | 0.103 | | 58 | 30 | | 63/47 | A |
| | 116 | 8 | 26 | 4 | 270 | 81 | 1.0 | 0.2 | 0.140 | | 43 | 9 | | 43/47 | C |
| 4147.56 | 315 | 88 | 220 | 0 | 130 | 2 | 0.8 | 0.5 | 0.149 | 7 | 47 | 23 | 174/45 | 59/35 | B |
| | 36 | 17 | 129 | 11 | 250 | 69 | 0.7 | 0.4 | 0.199 | | 35 | 16 | | 48/36 | B |
| 4148.3 | 65 | 71 | 167 | 4 | 258 | 19 | 1.0 | 0.4 | 0.148 | 7 | 47 | 19 | 135/42 | 40/29 | C |
| | 253 | 16 | 343 | 1 | 76 | 74 | 1.3 | 0.3 | 0.110 | | 64 | 21 | | 54/29 | C |
| Well-2 | | | | | | | | | | | | | | | |
| 2490.14 | 178 | 15 | 76 | 36 | 287 | 50 | 0.4 | 0.7 | 0.239 | 7 | 29 | 19 | 182/88 | 54/81 | A |
| | 198 | 57 | 31 | 32 | 297 | 6 | 1.4 | 0.2 | 0.185 | | 38 | 9 | | 69/74 | C |
| 2490.95 | 242 | 79 | 127 | 5 | 36 | 10 | 0.2 | 0.4 | 0.168 | 7 | 42 | 18 | 181/59 | 61/52 | A |
| | 316 | 4 | 146 | 86 | 46 | 1 | 0.8 | 0.6 | 0.189 | | 37 | 20 | | 61/49 | B |
| 2492.7 | 236 | 7 | 336 | 53 | 141 | 36 | 0.2 | 0.4 | 0.137 | 10 | 73 | 28 | 216/54 | 82/48 | A |
| 2492.9 | 97 | 2 | 6 | 10 | 199 | 79 | 0.2 | 0.4 | 0.191 | 7 | 37 | 15 | 112/38 | 40/31 | A |
| | 68 | 79 | 253 | 11 | 163 | 1 | 0.2 | 0.6 | 0.218 | | 32 | 20 | | 31/31 | A |
| | 0 | 12 | 153 | 77 | 269 | 6 | 0.6 | 0.7 | 0.121 | | 58 | 40 | | 35/30 | B |
| 2493.15 | 49 | 7 | 141 | 20 | 300 | 69 | 0.5 | 0.4 | 0.206 | 6 | 29 | 11 | 200/70 | 60/63 | A |
| | 64 | 26 | 332 | 5 | 233 | 63 | 0.5 | 0.4 | 0.198 | | 30 | 13 | | 64/63 | A |
| 2493.9 | 238 | 20 | 108 | 60 | 336 | 21 | 1.0 | 0.6 | 0.165 | 7 | 42 | 26 | 197/73 | 55/57 | C |
| | 179 | 5 | 269 | 5 | 49 | 83 | 0.8 | 0.5 | 0.211 | | 33 | 17 | | 47/58 | B |
| | 244 | 60 | 58 | 30 | 149 | 3 | 0.9 | 0.5 | 0.187 | | 37 | 20 | | 55/60 | B |
| 2494.45 | 101 | 0 | 11 | 3 | 196 | 87 | 0.2 | 0.2 | 0.229 | 7 | 31 | 6 | 181/38 | 40/34 | A |
| | 77 | 53 | 319 | 19 | 217 | 30 | 1.0 | 0.5 | 0.131 | | 54 | 26 | | 54/30 | C |
| | 137 | 73 | 30 | 5 | 298 | 16 | 0.6 | 0.6 | 0.168 | | 42 | 23 | | 46/31 | B |
| 2494.9 | 261 | 4 | 352 | 6 | 137 | 83 | 0.9 | 0.3 | 0.127 | 7 | 55 | 16 | 205/65 | 73/50 | A |
| | 171 | 45 | 35 | 36 | 287 | 24 | 1.0 | 0.6 | 0.163 | | 43 | 25 | | 69/52 | C |
| | 348 | 15 | 79 | 3 | 180 | 74 | 0.8 | 0.5 | 0.167 | | 42 | 21 | | 61/54 | B |
| 2495.15 | 249 | 75 | 345 | 1 | 75 | 15 | 1.4 | 0.5 | 0.149 | 6 | 40 | 18 | 217/53 | 86/41 | C |
| | 304 | 9 | 58 | 68 | 210 | 19 | 0.9 | 0.5 | 0.168 | | 36 | 19 | | 60/39 | B |
| 2495.67 | 24 | 25 | 185 | 63 | 290 | 7 | 0.6 | 0.4 | 0.201 | 6 | 30 | 12 | 203/67 | 56/55 | B |
| | 287 | 56 | 90 | 33 | 185 | 8 | 1.1 | 0.5 | 0.154 | | 39 | 20 | | 56/56 | C |
| | 90 | 1 | 357 | 72 | 180 | 18 | 0.8 | 0.7 | 0.153 | | 39 | 26 | | 52/54 | B |
| | 224 | 61 | 335 | 11 | 71 | 26 | 0.7 | 0.5 | 0.207 | | 29 | 13 | | 56/56 | B |
| 2499.25 | 198 | 7 | 106 | 10 | 321 | 77 | 0.8 | 0.6 | 0.194 | 7 | 36 | 21 | 181/89 | 50/75 | B |
| | 25 | 0 | 115 | 0 | 207 | 90 | 0.9 | 0.5 | 0.199 | | 35 | 18 | | 50/72 | B |

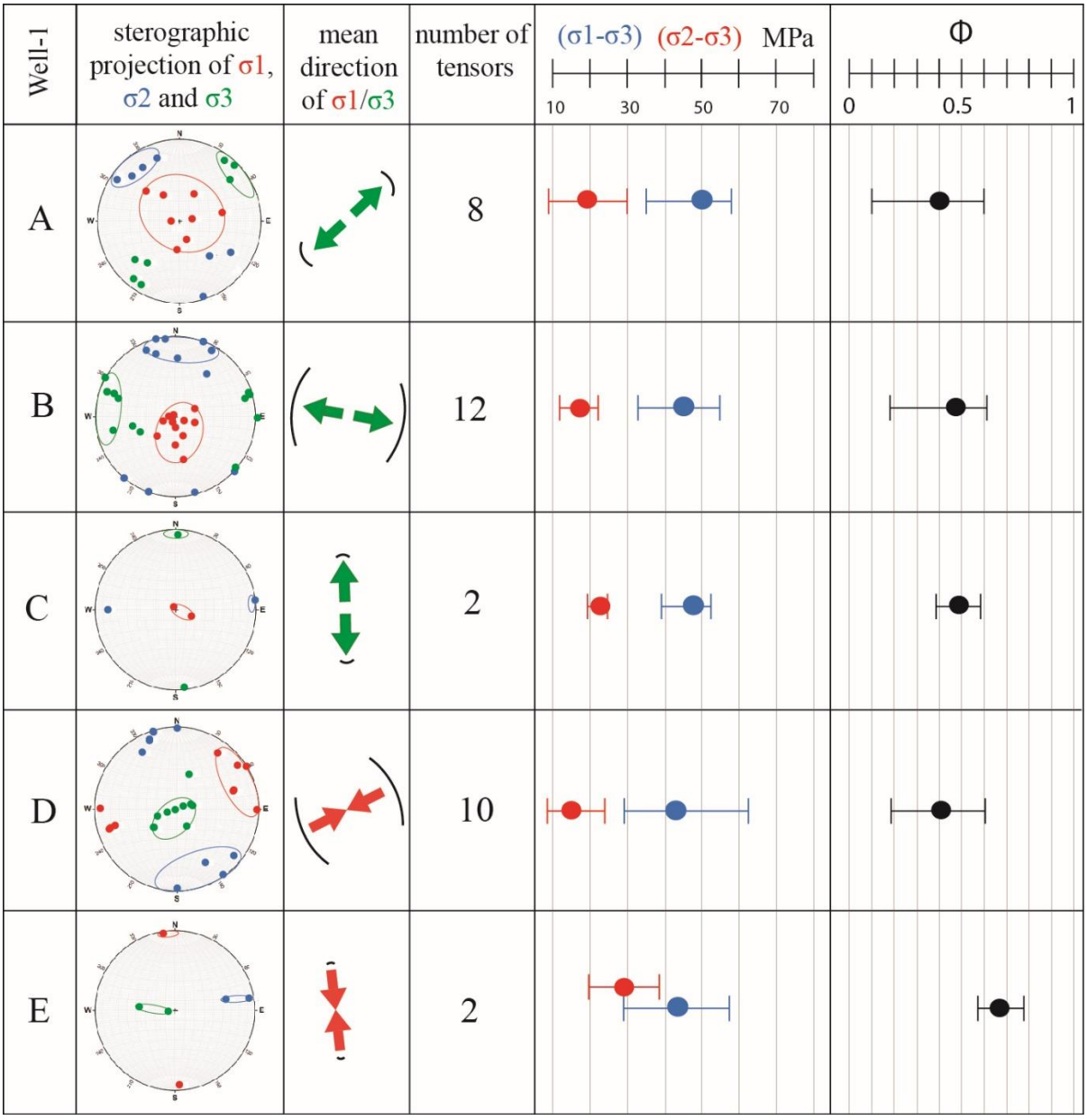


**Figure 1 Sup.Mat:** Summary of stress tensor groups derived from calcite twin inversion using CSIT-2 for Well-1 and Well-2. Each tensor group (from A to E) is characterized by a plot data in stereographic equal-area projection showing the mean orientation of the principal stress axes (red for $\sigma_1$, blue for $\sigma_2$ and green for $\sigma_3$) and the representation of the average orientation of the horizontal stresses as arrows (red for $\sigma_1$, green for $\sigma_3$, map view). Each tensor group is associated with the number of samples from which the related stress tensors were identified. The average values of the differential stress magnitudes for each group are shown in blue ($\sigma_1$-$\sigma_3$) and in red ($\sigma_2$-$\sigma_3$) and the average value of stress ratio $\Phi$ in black.

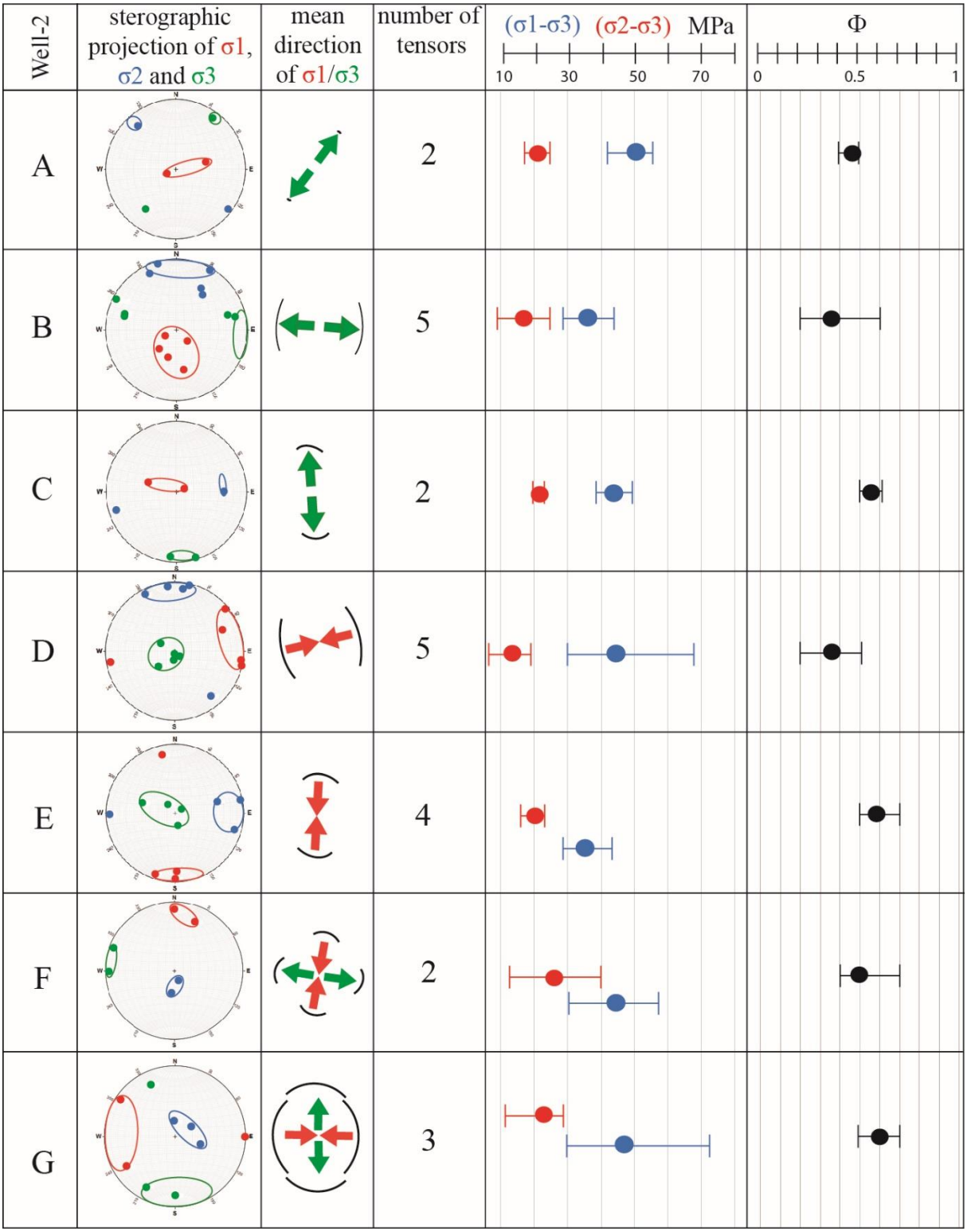


**Figure 2 Sup.Mat:** Summary of stress tensor groups derived from calcite twin inversion using CSIT-2 for Well-2: see caption to figure 1.

# References

Affaton, P., Kalsbeek, F., Boudzoumou, F., Trompette, R., Thrane, K., Frei, R. 2016. The Pan-African West Congo belt in the Republic of Congo (Congo Brazzaville): stratigraphy of the Mayombe and West Congo Supergroups studied by detrital zircon geochronology. Precambrian Research, 272, 185-202.

Amrouch K., Lacombe O., Bellahsen N., Daniel J.-M., Callot J.P., 2010, Stress and strain patterns, kinematics and deformation mechanisms in a basement-cored anticline: Sheep Mountain anticline (Wyoming, USA). Tectonics, 29, TC1005

Amrouch, K., Beaudoin, N., Lacombe, O., Bellahsen, N., Daniel, J. M. 2011. Paleostress magnitudes in folded sedimentary rocks. Geophysical Research Letters, 38, L17301.

Al-Hajri, Y., White, N., Fishwick, S., 2009. Scales of transient convective support beneath Africa. Geology 37, 883–886.

Arboit, F., Amrouch, K., Collins, A. S., King, R., Morley, C. 2015. Determination of the tectonic evolution from fractures, faults, and calcite twins on the southwestern margin of the Indochina Block, Tectonics, 34, 1576–1599.

Arboit, F., Amrouch, K., Morley, C., Collins, A. S., King, R. 2017. Palaeostress magnitudes in the Khao Khwang fold-thrust belt, new insights into the tectonic evolution of the Indosinian orogeny in central Thailand. Tectonophysics, 710, 266-276.

Aslanian, D., Moulin, M., Olivet, J. L., Unternehr, P., Matias, L., Bache, F., Rabineau, M., Klingelheofer, F., Contrucci, I., Labails, C. 2009. Brazilian and African passive margins of the Central Segment of the South Atlantic Ocean: Kinematic constraints. Tectonophysics, 468(1-4), 98-112.

Aslanian, D., Moulin, M. 2010. Comment on ‘A new scheme for the opening of the South Atlantic Ocean and the dissection of an Aptian salt basin’by Trond H. Torsvik, Sonia Rousse, Cinthia Labails and Mark A. Smethurst. Geophysical Journal International, 183(1), 20-28.

Asmus, H. E., Ponte, F. C. 1973. The Brazilian marginal basins. In The South Atlantic (87-133). Springer, Boston, MA.

Bah, B., Beaudoin, N.E., Lacombe, O., Girard, J.-P., Gout, C., Godeau, N., Deschamps, P. 2023. Multi-proxy reconstruction of the burial history and porosity evolution of the TOCA

carbonate formation in the Lower Congo basin (South West Africa), Marine and Petroleum Geology, 148, 106018.

Basile, C., Mascle, J., Guiraud, R., 2005. Phanerozoic geological evolution of the Equatorial Atlantic domain. Journal of African Earth Sciences 43, 275-282.

Bate, R. H. 1999. Non-marine ostracod assemblages of the Pre-Salt rift basins of West Africa and their role in sequence stratigraphy. Geological Society, London, Special Publications, 153(1), 283-292.

Beaudoin, N., Lacombe, O., 2018. Recent and future trends in paleopiezometry in the diagenetic domain: insights into the tectonic paleostress and burial depth history of fold-and-thrust belts and sedimentary basins. Journal of Structural Geology 114, 357–365.

Beaudoin, N., Lacombe, O., Koehn, D., David, M. E., Farrell, N., Healy, D. 2020. Vertical stress history and paleoburial in foreland basins unravelled by stylolite roughness paleopiezometry: Insights from bedding-parallel stylolites in the Bighorn Basin, Wyoming, USA. Journal of Structural Geology, 136, 104061.

Beglinger, S. E., Doust, H., Cloetingh, S. 2012. Relating petroleum system and play development to basin evolution: West African South Atlantic basins. Marine and Petroleum Geology, 30(1), 1-25.

Bidiet, J., Kinga, A., Loemba, C., Assoua-Wande, C., Hossie, G., Mahoukou-Sounga, A. 1998. Aperçu géologique et pétrolier des bassins du congo. Rapport de l'association des producteurs de pétrole africains, Hydro-Congo, Elf-Congo, AGIP Congo, Ministère des Mines et de l'Energie. RF11904.

Bjørlykke, K. 2014. Relationships between depositional environments, burial history and rock properties. Some principal aspects of diagenetic process in sedimentary basins. Sedimentary Geology, 301, 1-14.

Bott, M. H. P. 1993. Modelling the plate-driving mechanism. Journal of the Geological Society, 150(5), 941-951.

Brandstätter, J., Kurz, W., Rogowitz, A. 2017. Microstructural analysis and calcite piezometry on hydrothermal veins: Insights into the deformation history of the Cocos Plate at Site U1414 (IODP Expedition 344). Tectonics, 36(8), 1562-1579.

Braun, J., Guillocheau, F., Robin, C., Baby, G., Jelsma, H. 2014. Eroding a large continental area by tilting it over a source of mantle upwelling to explain the late Cretaceous South African erosional event. Geophysical Research Abstracts 16 (EGU2014-4219).

Brice, S. E., Cochran, M. D., Pardo, G., Edwards, A. D. 1982. Tectonics and sedimentation of the South Atlantic Rift Sequence: Cabinda, Angola: rifted margins: field investigations of margin structure and stratigraphy. In Studies in Continental Margin Geology, AAPG Special Volumes, 5-18.

Brognon, G. P., Verrier, G. R. 1966. Oil and geology in Cuanza Basin of Angola. AAPG Bulletin, 50(1), 108-158.

Brownfield, M.E., Charpentier, R.R. 2006. Geology and total petroleum systems of the West-Central Coastal Province (7203), West Africa. United States Geological Survey Bulletin, 2207-B, 52.

Bullard, E.C., 1965. Fit of the continents around the Atlantic, Science, 148**,** 664

Burkhard, M. 1993. Calcite twins, their geometry, appearance and significance as stress-strain markers and indicators of tectonic regime: a review. Journal of structural geology, 15(3-5), 351-368.

Burov, E., Gerya, T. 2014. Asymmetric three-dimensional topography over mantle plumes. Nature, 513(7516), 85-89.

Burwood, R. 1999. Angola: source rock control for Lower Congo Coastal and Kwanza Basin petroleum systems. Geological Society, London, Special Publications, 153(1), 181-194.

Carminatti, M., Wolff, B., Gamboa, L., 2008. New Exploratory Frontiers in Brazil: Proceedings of the 19th World Petroleum Congress. Spain, Madrid. June 29-July 3, 2008, 11.

Chaboureau, A. C., Guillocheau, F., Robin, C., Rohais, S., Moulin, M., Aslanian, D. 2013. Paleogeographic evolution of the central segment of the South Atlantic during Early Cretaceous times: Paleotopographic and geodynamic implications. Tectonophysics, 604, 191-223.

Cloetingh, S., Burov, E., Matenco, L., Beekman, F., Roure, F., Ziegler, P. A. 2013. The Moho in extensional tectonic settings: Insights from thermo-mechanical models. Tectonophysics, 609, 558-604.

Cobbold, P.R., Meisling, K.E., Mount, V.S., 2001. Reactivation of an obliquely rifted margin, Campos and Santos basins, southeastern Brazil. AAPG Bulletin 85, 1925–1944.

Contrucci, I., Matias, L., Moulin, M., Géli, L., Klingelhofer, F., Nouzé, H., Aslanian, D., Olivet, J. L., Réhault, J. P., Sibuet, J. C. 2004. Deep structure of the West African continental margin (Congo, Zaïre, Angola), between 5°S and 8°S, from reflection/refraction seismics and gravity data. Geophysical Journal International, 158(2), 529-553.

Craddock, J. P., Jackson, M., van der Pluijm, B. A., Versical, R. T. 1993. Regional shortening fabrics in eastern North America: Far-field stress transmission from the Appalachian-Ouachita Orogenic Belt. Tectonics, *12*(1), 257-264.

Craddock, J. P., Farris, D. W., Roberson, A. 2004. Calcite-twinning constraints on stress-strain fields along the Mid-Atlantic Ridge, Iceland. Geology, 32(1), 49-52.

Da Costa, J. L., Schirmer, T. W., Laws, B. R. 1999. Lower Congo basin, deepwater exploration province, offshore West Afri~ AAPG Bulletin, 83(12).

Dale, C.T., Lopes, J.R., Abilio, S., 1992. Takula oil field and the Greater Takula area, Cabinda, Angola. In: Halbouty, M.T. (Ed.), Giant Oil and Gas Fields of the Decade 1978–1988, 54. AAPG memoir, pp. 197–215

Daly, M. C., Lawrence, S. R., Diemu-Tshiband, K., Matouana, B., 1992. Tectonic evolution of the cuvette centrale, Zaire. Journal of the Geological Society, 149(4), 539-546.

Dauteuil, O., Deschamps, F., Bourgeois, O., Mocquet, A., Guillocheau, F. 2013. Post-breakup evolution and palaeotopography of the North Namibian Margin during the Meso-Cenozoic. Tectonophysics 589, 103–115

Davison, I. 2007. Geology and tectonics of the South Atlantic Brazilian salt basins. Geological Society, London, Special Publications, 272(1), 345-359.

De Bresser, J.H.P., Spiers, C.J., 1997. Strength characteristics of the r, f, and c slip systems in calcite. Tectonophysics, 272, 1–23.

Delpomdor, F., Tack, L., Préat, A. 2008. Microstructures in the Neoproterozoic tillites around the Congo River Basin (CRB), Democratic Republic of Congo (DRC): Comparison with the Karoo tillites from the Dekese borehole in the CRB. In 22nd Colloquium of African Geology (CAG22) & 13th Conference of the Geological Society of Africa (GSAf13) (p. 108).

Delvaux, D., Maddaloni, F., Tesauro, M. & Braitenberg, C., 2021. The Congo Basin: Stratigraphy and subsurface structure defined by regional seismic reflection, refraction and well data. Global and Planetary Change 198(2), 103407.

Delvaux, D., & Barth, A. 2010. African stress pattern from formal inversion of focal mechanism data. Tectonophysics, 482(1-4), 105-128.

Dingle, R. V. 1999. Walvis Ridge barrier: its influence on palaeoenvironments and source rock generation deduced from ostracod distributions in the early South Atlantic Ocean. Geological Society, London, Special Publications, 153(1), 293-302.

Doyle, J. A., Jardiné, S., Doerenkamp, A. 1982. Afropolis, un nouveau genre de pollen d'Angiosperme précoce, avec de données sur la palynostratigraphie et les paléoenvironnements du Crétacé du Nord-Gondwana. Bulletin des Centres de Recherche et d'Exploration-Production Elf-Aquitaine, 6, 39-117.

Etchecopar, A., 1984. Etudes des états de contrainte en tectonique cassante et simulations de déformations plastiques (approche mathématiques). Unpublished thesis. Université des Sciences et Techniques du Languedoc.

Ferrari, A.L., 2001. Evolução Tectônica do Graben da Guanabara (PhD thesis) Instituto de Geociências da Universidade de São Paulo, p. 412.

Ferrill, D.A., 1998. Critical re-evaluation of differential stress estimates from calcite twins in coarse-grained limestone. Tectonophysics 285, 77–86.

Ferrill, D. A., Morris, A. P., Evans, M. A., Burkhard, M., Groshong Jr, R. H., Onasch, C. M. 2004. Calcite twin morphology: a low-temperature deformation geothermometer. Journal of structural Geology, 26(8), 1521-1529.

Fernandes, A.J., Amaral, G., 2002. Cenozoic tectonic events at the border of the Paraná Basin, São Paulo, Brazil. Journal of South American Earth Sciences 14, 911–931.

Flament, N., Gurnis, M., Williams, S., Seton, M., Skogseid, J., Heine, C., Müller, R.D. 2014. Topographic asymmetry of the South Atlantic from global models of mantle flow and lithospheric stretching. Earth and Planetary Science Letters 387, 107–119.

Giresse, P. 1982. La succession des sédiments dans les bassins marins et continentaux du Congo depuis le début du Mésozoïque. Sciences Géologiques, bulletins et mémoires, 35(4), 183-206.

Goscombe, B.D., Gray, D.R., 2008. Structure and strain variation at mid-crustal levels in a transpressional orogen: a review of Kaoko Belt structure and the character of West Gondwana amalgamation and dispersal. Gondwana Research 13, 45–85.

Gradstein, F. M., Ogg, J. G., Smith, A. G., Bleeker, W.,Lourens, L. J. 2004. A new geologic time scale, with special reference to Precambrian and Neogene. Episodes, 27(2), 83-100.

Grosdidier, E. 1967. Quelques ostracodes nouveaux de la Série anté–salifère ("Wealdienne") des bassins côtiers du Gabon et du Congo. Revue de Micropaléontologie, 10(2), 107-118.

Grosdidier, E., Braccini, E., Dupont, G., Moron, J.M., 1996. Biozonation du Crétacé Inférieur non marin des bassins du Gabon et du Congo. Bulletin des Centres de recherches exploration-production Elf-Aquitaine. Memoir (16), 67–82.

Guardado, L. R., Gamboa, L. A. P., Lucchesi, C. F. 1989. Petroleum geology of the Campos Basin, Brazil, a model for a producing atlantic type basin: Part 1.

Guiraud, R., Maurin, J. C. 1991. Le Rifting en Afrique au Cretace inferieur; synthese structurale, mise en evidence de deux etapes dans la genese des bassins, relations avec les ouvertures oceaniques peri-africaines. Bulletin de la Société géologique de France, 162(5), 811-823.

Guiraud, R., Bosworth, W. 1997. Senonian basin inversion and rejuvenation of rifting in Africa and Arabia: synthesis and implications to plate-scale tectonics. Tectonophysics, 282(1-4), 39-82.

Guiraud, R., Bosworth, W., Thierry, J., Delplanque, A. 2005. Phanerozoic geological evolution of Northern and Central Africa: an overview. Journal of African Earth Sciences, 43(1-3), 83-143.

Guiraud, M., Buta-Neto, A., Quesne, D. 2010. Segmentation and differential post-rift uplift at the Angola margin as recorded by the transform-rifted Benguela and oblique-to-orthogonal-rifted Kwanza basins. Marine and Petroleum Geology, 27(5), 1040-1068.

Harris, N. B., 2000. TOCA Carbonate, Congo Basin: response to an evolving rift lake, in M. R. Mello and B. J. Katz, eds., Petroleum systems of South Atlantic margins: American Association of Petroleum Geologists Memoir 73, 341–360.

Heidbach, O., Reinecker, J., Tingay, M., Müller, B., Sperner, B., Fuchs, K., Wenzel, F. 2007, Plate boundary forces are not enough: Second- and third-order stress patterns highlighted in the World Stress Map database, Tectonics, 26, TC6014

Heidbach, O., Tingay, M., Barth, A., Reinecker, J., Kurfess, D., Müller, B., 2008. The 2008 release of the World Stress Map (available online at www.world-stress-map.org).

Heidbach, O., Rajabi, M., Reiter, K., Ziegler, M., 2016. World Stress Map 2016. GFZ Data Services

Heine, C., Zoethout, J., Müller R.D. 2013, Kinematics of the South Atlantic rift. Solid Earth, 5(1), 41–116

Hu, J. C., Angelier, J., 2004. Stress permutations: Three-dimensional distinct element analysis accounts for a common phenomenon in brittle tectonics. Journal of Geophysical Research: Solid Earth, 109(B9).

Jamison, W. R., Spang, J. H., 1976. Use of calcite twin lamellae to infer differential stress. Geological Society of America Bulletin, 87(6), 868-872.

Japsen, P., Chalmers, J.A., Green, P.F., Bonow, J.M., 2012. Elevated, passive continental margins: not rift shoulders, but expressions of episodic, post-rift burial and exhumation. Global and Planetary Change 90–91, 73–86.

Johnston, S. T. 2000. The Cape Fold Belt and Syntaxis and the rotated Falkland Islands: dextral transpressional tectonics along the southwest margin of Gondwana. Journal of African Earth Sciences, 31(1), 51-63.

Jolivet, L., Baudin, T., Calassou, S., Chevrot, S., Ford, M., Issautier, B., Lasseur, E., Masini, E., Manatschal, G., Mouthereau, F., Thinon, I., Vidal, O. 2021. Geodynamic evolution of a wide plate boundary in the Western Mediterranean, near-field versus far-field interactions. *BSGF*-Earth Sciences Bulletin, 192(1), 48.

Kadima, E., Delvaux, D., Sebagenzi, S. N., Tack, L., Kabeya, S. M. 2011. Structure and geological history of the Congo Basin: an integrated interpretation of gravity, magnetic and reflection seismic data. Basin Research, 23(5), 499-527.

Karl, M., Glasmacher, U.A., Kollenz, S., Franco-Magalhaes, A.O.B., Stockli, D.F., Hackspacher, P.C., 2013. Evolution of the South Atlantic passive continental margin in

southern Brazil derived from zircon and apatite (U–Th–Sm)/He and fission-track data. Tectonophysics 604, 224–244.

Karner, G. D., Driscoll, N. W., McGinnis, J. P., Brumbaugh, W. D., Cameron, N. R. 1997. Tectonic significance of syn-rift sediment packages across the gabon-cabinda continental margin. Marine and Petroleum Geology, 14(7): 973 1000.

Karner, G. D., Driscoll, N. W. 1999. Tectonic and stratigraphic development of the West African and eastern Brazilian Margins: insights from quantitative basin modelling. Geological Society, London, Special Publications, 153(1), 11-40.

Karner, G. D., Driscoll, N. W., Barker, D. H. N. 2003. Syn-rift regional subsidence across the West African continental margin: the role of lower plate ductile extension. Geological Society, London, Special Publications, 207(1), 105-129.

Karner, G. D., Gambôa, L. A. P. 2007. Timing and origin of the South Atlantic pre-salt sag basins and their capping evaporites. Geological Society, London, Special Publications, 285(1), 15-35.

Koptev, A., Burov, E., Gerya, T., Le Pourhiet, L., Leroy, S., Calais, E., Jolivet, L. 2018. Plume-induced continental rifting and break-up in ultra-slow extension context: Insights from 3D numerical modeling. Tectonophysics, 746, 121-137.

Kounov, A., Viola, G., De Wit, M., Andreoli, M. A. G. 2009. Denudation along the Atlantic passive margin: new insights from apatite fission-track analysis on the western coast of South Africa. Geological Society, London, Special Publications, 324(1), 287-306.

Kulikowski, D., Amrouch, K. 2017. Combining geophysical data and calcite twin stress inversion to refine the tectonic history of subsurface and offshore provinces: A case study on the Cooper-Eromanga Basin, Australia. Tectonics, 36(3), 515-541.

Labeur, A., Beaudoin, N. E., Lacombe, O., Emmanuel, L., Petracchini, L., Daëron, M., Klimowicz, S., Callot, J. P. 2021. Burial-deformation history of folded rocks unraveled by fracture analysis, stylolite paleopiezometry and vein cement geochemistry: a case study in the Cingoli Anticline (Umbria-Marche, Northern Apennines). Geosciences, 11(3), 135.

Lacombe, O., Angelier, J., Laurent, P., Bergerat, F., Tourneret, C. 1990. Joint analyses of calcite twins and fault slips as a key for deciphering polyphase tectonics: Burgundy as a case study. Tectonophysics, 182(3-4), 279-300.

Lacombe O., Laurent P., 1992. Determination of principal stress magnitudes using calcite twins and rock mechanics data. Tectonophy., 202, 83-93

Lacombe O., Laurent P., Angelier J., 1994. Calcite twins as a key to paleostresses in sedimentary basins: preliminary results from drill cores of the Paris basin. In "Peri-Tethyan Platforms", F. Roure Ed., Technip, 197-210

Lacombe, O., Laurent, P. 1996. Determination of deviatoric stress tensors based on inversion of calcite twin data from experimentally deformed monophase samples: preliminary results. Tectonophysics, 255(3-4), 189-202.

Lacombe O., 2001. Paleostress magnitudes associated with development of mountain belts: insights from tectonic analyses of calcite twins in the Taiwan Foothills. Tectonics, 20, 6, 834-849

Lacombe, O. 2007. Comparison of paleostress magnitudes from calcite twins with contemporary stress magnitudes and frictional sliding criteria in the continental crust: Mechanical implications. Journal of Structural Geology, 29(1), 86-99.

Lacombe, O., Amrouch, K., Mouthereau, F., Dissez, L. 2007. Calcite twinning constraints on late Neogene stress patterns and deformation mechanisms in the active Zagros collision belt. Geology, 35(3), 263-266.

Lacombe, O., Malandain, J., Vilasi, N., Amrouch, K., Roure, F. 2009. From paleostresses to paleoburial in fold-thrust belts: preliminary results from calcite twin analysis in the outer Albanides. Tectonophysics, In “the Geology of Vertical Movements of the Lithosphere”, 475, 128-141

Lacombe, O. 2010. Calcite twins, a tool for tectonic studies in thrust belts and stable orogenic forelands. Oil & Gas Science and Technology–Revue d’IFP Energies nouvelles, 65(6), 809-838.

Lacombe, O., Parlangeau, C., Beaudoin, N. E., Amrouch, K. 2021a. Calcite Twin Formation, Measurement and Use as Stress–Strain Indicators: A Review of Progress over the Last Decade. Geosciences, 11(11), 445.

Lacombe O., Beaudoin N., Hoareau G., Labeur A., Pecheyran C., Callot J.P. 2021b. Dating folding beyond folding, from layer-parallel shortening to fold tightening, using mesostructures : Lessons from the Apennines, Pyrenees and Rocky Mountains. Solid Earth, 12, 10, 2145-2157

Laurent, P., Bernard, P., Vasseur, G., Etchecopar, A. 1981. Stress tensor determination from the study of e twins in calcite: a linear programming method. Tectonophysics, 78(1-4), 651-660.

Laurent, P., Kern, H., Lacombe, O. 2000. Determination of deviatoric stress tensors based on inversion of calcite twin data from experimentally deformed monophase samples. Part II. Axial and triaxial stress experiments. Tectonophysics, 327(1-2), 131-148.

Lehner, P., De Ruiter P.A.C, 1977, Structural History of the Atlantic Margin of Africa, AAPG Bulletin, 61, 7, 961-981.

Lima, C., Nascimento, E., Assumpção, M., 1997. Stress orientations in Brazilian sedimentary basins from breakout analysis: implications for force models in the South American plate. Geophysical Journal International 130, 112–124.

Loparev, A., Rouby, D., Chardon, D., Dall'Asta, M., Sapin, F., Bajolet, F., Ye, J., Paquet, F. 2021. Superimposed rifting at the junction of the Central and Equatorial Atlantic: formation of the passive margin of the Guiana Shield. Tectonics, 40(7), e2020TC006159.

Machado, R., Roldan, L.F., Jacques, P.D., Fassbinder, E., Nummer, A.R., 2012. Tectônica transcorrente Mesozoica-Cenozoica no Domo de Lages-Santa Catarina. Revista Brasileira de Geociencias 42, 799–811.

Mahatsente, R.,Coblentz, D. 2015. Ridge-push force and the state of stress in the Nubia-Somalia plate system. Lithosphere, 7(5), 503-510.

Marton, L. G., Tari, G. C., Lehmann, C. T., Mohriak, W. 2000. Evolution of the Angolan passive margin, West Africa, with emphasis on post-salt structural styles. Geophysical Monograph-American Geophysical Union, 115, 129-150.

Masson, M. P. 1972. L'exploration pétrolière en Angola: Revue de l'Association Française des Techniciens du Pétrole, v. 212.

Matton, G., Jébrak, M. 2009. The Cretaceous Peri-Atlantic Alkaline Pulse (PAAP): Deep mantle plume origin or shallow lithospheric break-up? Tectonophysics, 469(1-4), 1-12.

Mbina Mounguengui, M., Guiraud, M. 2009. Neocomian to early Aptian syn-rift evolution of the normal to oblique-rifted North Gabon margin (interior and N'Komi basins). Marine and Petroleum Geology, 26(6):1000-1017.

McHargue, T. R. 1990. Stratigraphic Development of Proto-South Atlantic Rifting in Cabinda, Angola--A Petroliferous Lake Basin: Chapter 19.

Medvedev, S., 2016. Understanding lithospheric stresses: systematic analysis of controlling mechanisms with applications to the African Plate. Geophysical Journal International, 207(1), 393-413.

Mohriak, W., Nemčok, M., Enciso, G. 2008. South Atlantic divergent margin evolution: rift-border uplift and salt tectonics in the basins of SE Brazil. Geological Society, London, Special Publications, 294(1), 365-398.

Morley, C. K., Gabdi, S., Seusutthiya, K., 2007. Fault superimposition and linkage resulting from stress changes during rifting: Examples from 3D seismic data, Phitsanulok Basin, Thailand. Journal of structural geology, 29(4), 646-663.

Moucha, R., Forte, A.M., 2011. Changes in African topography driven by mantle convection. Nature Geoscience 4, 707–712.

Moulin, M., Aslanian, D., Olivet, J. L., Contrucci, I., Matias, L., Géli, L., Klingelhoefer, F., Nouzé, H., Unternehr, P. 2005. Geological constraints on the evolution of the Angolan margin based on reflection and refraction seismic data (ZaïAngo project). Geophysical Journal International, 162(3), 793-810.

Moulin, M., Aslanian, D., Unternehr, P. 2010. A new starting point for the South and Equatorial Atlantic Ocean. Earth-Science Reviews, 98(1-2), 1-37.

Muller, R. D., Seton, M., Zahirovic, S., Williams, S. E., Matthews, K. J., Wright, N. M., Shephard, G.E., Maloney, K.T., Barnett-Moore, N., Hosseinpour, M., Bower, D.J., Cannon, J. 2016. Ocean basin evolution and global-scale plate reorganization events since Pangea breakup. Annual Review of Earth and Planetary Sciences, 44(1), 107-138.

Mussard, J. M. 1996. Les palynomorphes, indicateurs des variations du niveau marin relatif: analyses quantitatives dans l'Albien supérieur de la République du Congo. S. Jardiné, I. de Klasz, J.-P. Debenay (Eds.), Géologie de l'Afrique et de l'Atlantique Sud, Compte Rendus des Colloques de géologie d'Angers, 16–24 juillet 1994, Mémoires du Bulletin des Centres de Recherche et d'Exploration-Production d'Elf, vol. 16 (1996), 57-66.

Nkodia, H. V., Miyouna, T., Delvaux, D., Boudzoumou, F. 2020. Flower structures in sandstones of the Paleozoic Inkisi Group (Brazzaville, Republic of Congo): evidence for two

major strike-slip fault systems and geodynamic implications. South African Journal of Geology, 123(4), 531-550.

Nkodia, H. M. D.-V., Miyouna, T., Kolawole, F., Boudzoumou, F., Loemba, A. P. R., Bazebizonza Tchiguina, N. C., Delvaux, D. 2022. Seismogenic fault reactivation in western Central Africa: Insights from regional stress analysis. Geochemistry, Geophysics, Geosystems, 23, e2022GC010377.

Nurnberg, D., Müller, R. D. 1991. The tectonic evolution of the South Atlantic from Late Jurassic to present. Tectonophysics, 191(1-2), 27-53.

Parlangeau, C., Lacombe, O., Schueller, S., Daniel, J. M. 2018. Inversion of calcite twin data for paleostress orientations and magnitudes: A new technique tested and calibrated on numerically-generated and natural data. Tectonophysics, 722, 462-485.

Parlangeau, C., Dimanov, A., Lacombe, O., Hallais, S., Daniel, J. M. 2019. Uniaxial compression of calcite single crystals at room temperature: insights into twinning activation and development. Solid Earth, 10(1), 307-316.

Pascal, C., Cloetingh, S. A. 2009. Gravitational potential stresses and stress field of passive continental margins: Insights from the south-Norway shelf. Earth and Planetary Science Letters, 277(3-4), 464-473.

Pascal, C., 2006. On the role of heat flow, lithosphere thickness and lithosphere density on gravitational potential stresses. Tectonophysics 425, 83–99.

Passchier, C.W., Trouw, R.A.J., Ribeiro, A., Paciullo, F.V.P., 2002. Tectonic evolution of the southern Kaoko belt, Namibia. Journal of African Earth Sciences 35, 61–75.

Pedrosa-Soares, A. C., Noce, C. M., Vidal, P., Monteiro, R. L. B. P., Leonardos, O. H. 1992. Toward a new tectonic model for the late proterozoic Araçuaí (SE Brazil)-West Congolian (SW Africa) belt. Journal of South American Earth Sciences, 6(1-2), 33-47.

Pérez-Díaz, L., Eagles, G. 2014, Constraining South Atlantic growth with seafloor spreading data, Tectonics, 33, 1848–1873

Péron-Pinvidic, G., Manatschal, G., Masini, E., Sutra, E., Flament, J.M., Haupert, I., Unternehr, P., 2015. Unravelling the along-strike variability of the Angola-Gabon rifted margin: a mapping approach. In: Sabato Ceraldi, T., Hodkinson, R.A., Backe, G. (Eds.). Pet. Geosc. of West Africa Margin. Geol Soc., London, Special Publ, 438.

Préat, A., Kolo, K., Prian, J. P., Delpomdor, F. 2010. A peritidal evaporite environment in the Neoproterozoic of south Gabon (Schisto-Calcaire Subgroup, Nyanga Basin). Precambrian research, 177(3-4), 253-265.

Rabinowitz, P. D., LaBrecque, J. 1979. The Mesozoic South Atlantic Ocean and evolution of its continental margins. Journal of Geophysical Research: Solid Earth, 84(B11), 5973-6002.

Reis, Á.F.C., Bezerra, F.H.R., Ferreira, J.M., do Nascimento, A.F., Lima, C.C., 2013. Stress magnitude and orientation in the Potiguar Basin, Brazil: implications on faulting style and reactivation. Journal of Geophysical Research — Solid Earth 118.

Riccomini, C., 1995. Padrão de fraturamentos do Maciço Alcalino de Cananéia, Estado de São Paulo: relações com a tectônica mesozóico-cenozóica do sudeste do Brasil. Revista Brasileira de Geociencias 25, 79–84.

Ritsema, J., Deuss, A., van Heijst, H.J., Woodhouse, J.H., 2011. S40RTS: a degree-40 shear velocity model for the mantle from new Rayleigh wave dispersion, teleseismic traveltime and normal-mode splitting function measurements. Geophysical Journal International 184, 1223–1236.

Rocher M., Lacombe O., Angelier J., Chen H.-W, 1996. Mechanical twin sets in calcite as markers of recent collisional events in a fold-and-thrust belt : evidence from the reefal limestones of southwestern Taiwan. Tectonics, 15,5, 984-996.

Rocher M., Lacombe O., Angelier J., Deffontaines B., Verdier F., 2000. Cenozoic folding and faulting in the North Pyrenean Foreland (Aquitaine Basin, France): insights from combined structural and paleostress analyses. J. Struct. Geol., 22, 5, 627-645

Rocher, M., Cushing, M., Lemeille, F., Lozac'h, Y., Angelier, J., 2004. Intraplate paleostresses reconstructed with calcite twinning and faulting: improved method and application to the eastern Paris Basin (Lorraine, France). Tectonophysics 387, 1–21.

Rowe, K.J., Rutter, E.H., 1990. Palaeostress estimation using calcite twinning: experimental calibration and application to nature. Journal of Structural Geology. 12, 1–17.

Saller, A., Rushton, S., Buambua, L., Inman, K., McNeil, R., Dickson, J.A.D., 2016. Presalt stratigraphy and depositional systems in the Kwanza Basin, offshore Angola. AAPG Bulletin 100 (7), 1135–1164.

Salomon, E., Koehn, D., Passchier, C., Hackspacher, P. C., Glasmacher, U. A. 2015. Contrasting stress fields on correlating margins of the South Atlantic. Gondwana research, 28(3), 1152-1167.

Seeber, L. Armbruster, 1988, Seismicity along the Atlantic Seaboard of the US; Intraplate neotectonics and earthquake hazards. The Atlantic continental margin, US: Boulder, Colorado, Geological Society of America,: Geology of North America, I-2, 565-582.

Séranne, M., Anka, Z. 2005. South Atlantic continental margins of Africa: a comparison of the tectonic vs climate interplay on the evolution of equatorial west Africa and SW Africa margins. Journal of African Earth Sciences, 43(1-3), 283-300.

Standlee, L., Brumbaugh, W., Cameron, N. 1992. Controlling factors in the initiation of the south atlantic rift system. Compte rendus des colloques de géologie de libreville, Elf Aquitaine. Mémoire Elf Aquitaine 13.

Stein, C. A., S. Cloetingh, R. 1989. Wortel, Seasat-derived gravity constraints on stress and deformation in the northeastern Indian Ocean, *Geophys. Res. Lett.*, **16**, 823–826.

Szatmari, P., Milani, E. J. 2016. Tectonic control of the oil-rich large igneous-carbonate-salt province of the South Atlantic rift. Marine and Petroleum Geology, 77, 567-596.

Tack, L., Wingate, M.T.D., Liegeois, J.-P., Fernandez-Alonso, M., Deblond, A. 2001. Early Neoproterozoic magmatism (1000-910Ma) of the Zadinian and Mayumbian Groups (Bas-Congo): onset of Rodinia rifting at the western edge of the Congo craton. Prec. Res., 110, 277-306.

Tack, L., Delvaux, D., Kadima, E., Delpomdor, F., Tahon, A., Fernandez-Alonso, M., Baudet, D., Dewaele, S., Cibambula, E., Kanda-Nkula, V., Mpiana, C. 2009. The 1.000 m thick Redbeds sequence of the Congo River Basin (CRB): a generally overlooked testimony in

Teboul, P-A. 2017. Diagenesis of Lower Cretaceous Presalt Continental Carbonates from the West African Margin Simulations and Analogues. Unpublished thesis. Aix- Marseille Université.

Teisserenc, P., Villemin, J. 1989. Sedimentary basin of Gabon--geology and oil systems. In J.D. Edwards, P.A. Santogrossi (Eds.), Divergent/passive margins basins, AAPG, vol. 48 (1990), 117-199.

Thompson, D. L., Stilwell, J. D., Hall, M. 2015. Lacustrine carbonate reservoirs from Early Cretaceous rift lakes of Western Gondwana: Pre-salt coquinas of Brazil and West Africa. Gondwana Research, 28(1), 26-51.

Torsvik, T.H., Rousse, S., Labails, C., Smethurst, M.A., 2009. A new scheme for the opening of the South Atlantic Ocean and the dissection of an Aptian salt basin. Geophysical Journal International 177, 1315–1333.

Tourneret, C., Laurent, P. 1990. Paleo-stress orientations from calcite twins in the North Pyrenean foreland, determined by the Etchecopar inverse method. Tectonophysics, 180(2-4), 287-302.

Torsvik, T. H., Rousse, S., Labails, C., Smethurst, M. A. 2009. A new scheme for the opening of the South Atlantic Ocean and the dissection of an Aptian salt basin. Geophysical Journal International, 177(3), 1315-1333

Tullis, T. E. 1980. The use of mechanical twinning in minerals as a measure of shear stress magnitudes. Journal of Geophysical Research: Solid Earth, 85(B11), 6263-6268.

Turner, F.J. 1953. Nature and dynamic interpretation of deformation lamellae in calcite of three marbles. American Journal of Science. 251, 276–298.

Turner, F. J., Griggs, D. T., & Heard, H. 1954. Experimental deformation of calcite crystals. Geological Society of America Bulletin, 65(9), 883-934.

Uncini, G., Brandao, M., Giovannelli, A. 1998. Neocomian-Upper Aptian Pre-Salt sequence of southern Kwanza Basin: a regional view. In ABGP/AAPG International Conference and Exhibition November 8-11, 1998, Rio de Janeiro, Brazil.

Vagnes, E., Gabrielsen, R. H., Haremo, P. 1998. Late Cretaceous–Cenozoic intraplate contractional deformation at the Norwegian continental shelf: timing, magnitude and regional implications. *Tectonophysics*, *300*(1-4), 29-46.

Vernet, R., Assoua-Wande, C., Massamba, L., Sorriaux, P. 1996. Paléogéographie du Crétacé (Albien-Maastrichtien) du bassin côtier congolais. Bulletin des Centres de recherches exploration-production Elf-Aquitaine. Mémoire, (16), 39-55.

Vink, G.R., 1982. Continental rifting and the implication for plate tectonics reconstructions, Journal of geophysical Research, 87, 10677–10688.

Viola, G., Andreoli, M., Ben-Avraham, Z., Stengel, I., Reshef, M., 2005. Offshore mud volcanoes and onland faulting in southwestern Africa: neotectonic implications and constraints on the regional stress field. Earth and Planetary Science Letters 231, 147–160.

Viola, G., Kounov, A., Andreoli, M. A. G., Mattila, J. 2012. Brittle tectonic evolution along the western margin of South Africa: more than 500 Myr of continued reactivation. Tectonophysics, 514, 93-114.

Wakamori, K.; Yamaji, A., 2020. The integrated stress-strain analysis of calcite twins: Consistent stress and strain determined from natural data. In EGU General Assembly Conference Abstracts; European Geosciences Union, Vienna; p. 12819.

Wiens, D. A., Stein, S. 1983. Age dependence of oceanic intraplate seismicity and implications for lithospheric evolution. Journal of Geophysical Research: Solid Earth, 88(B8), 6455-6468.

Wiens, D. A., Stein, S. 1985. Implications of oceanic intraplate seismicity for plate stresses, driving forces and rheology. Tectonophysics, 116(1-2), 143-162.

Withjack, M. O., Olsen, P. E., Schlische, R. W. (1995). Tectonic evolution of the Fundy rift basin, Canada: evidence of extension and shortening during passive margin development. Tectonics, 14(2), 390-405.

Yamaji, A. 2015. Generalized Hough transform for the stress inversion of calcite twin data. Journal of Structural Geology, 80, 2–15.

Zeboudj, A., Bah, B., Lacombe, O., Beaudoin, N.E., Gout, C., Godeau, N., Girard, J.-P., Deschamps, P. 2023. Depicting past stress history at passive margins: A combination of calcite twinning and stylolite roughness paleopiezometry in supra-salt Sendji deep carbonates, Lower Congo Basin, west Africa. Marine and Petroleum Geology, 152, 106219.

Ziegler, P. A., Cloetingh, S., van Wees, J. D. 1995. Dynamics of intra-plate compressional deformation: the Alpine foreland and other examples. Tectonophysics, 252(1-4), 7-59.

Zoback, M. L. 1992. First-and second-order patterns of stress in the lithosphere: The World Stress Map Project. Journal of Geophysical Research: Solid Earth, 97(B8), 11703-11728.

# Données complémentaires

## 1. Inversion de la rugosité des stylolites tectoniques

Un seul stylolite tectonique vertical (Fig. 8) a été observé dans le Well-1. Comme pour les fractures, la rareté des stylolites tectoniques verticaux peut être en partie liée à leur attitude verticale, c'est-à-dire parallèle à l'axe de la carotte. Les pics du stylolite sont horizontaux et ont une direction N100 qui correspond à l'orientation de la contrainte principale maximale horizontale ($\sigma_H=\sigma_1$) à partir de laquelle le stylolite s'est formé (Koehn et al., 2007).

L'application de la méthode détaillée dans le chapitre 1 section 2.1.1 a donné les résultats suivants :

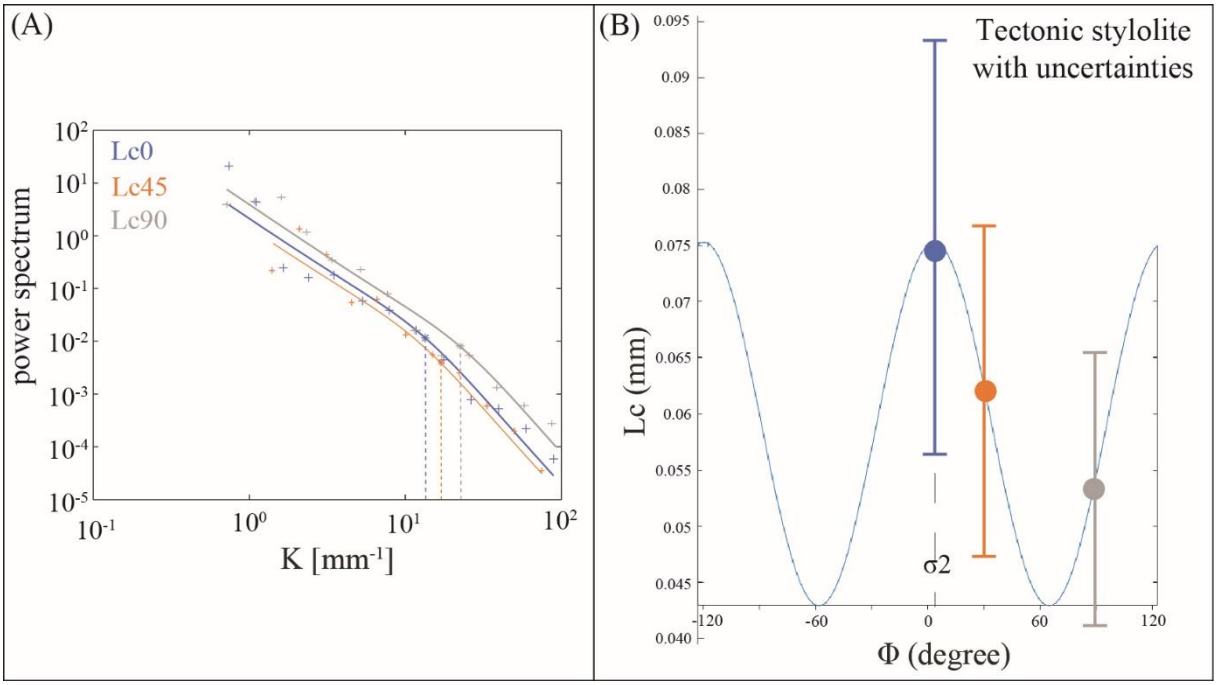


**Figure 8:** Exemple d'inversion de la rugosité de stylolite tectonique. (A) L'échantillon a été coupé le long de trois plans parallèles aux pics à un angle par rapport au plan vertical contenant le stylolite (qui est de 0°, les mesures d'angle sont dans le sens inverse des aiguilles d'une montre). (B) La fonction sinusoïdale modélisant l'anisotropie de la longueur de coupure (Lc) par rapport à la section verticale (0°) avec les incertitudes sur l'estimation de la $L_C$.

Pour rappel, la courbe sinusoïdale sur laquelle est reporté la Lc des trois coupes permet d'obtenir l'orientation de $\sigma_2$ et $\sigma_3$. Le plan passant par le Lc minimum de la courbe contient la direction de $\sigma_3$ et le plan passant par le Lc maximum contient la direction de $\sigma_2$. D'après la sinusoïde reconstruite (équation 17; Fig. 8B), le stylolite est compatible avec un régime de

contrainte décrochant avec une contrainte verticale $\sigma_v = \sigma_2$. Néanmoins les incertitudes montrent qu'il est possible qu'il y ait eu des permutations entre $\sigma_2$ et $\sigma_3$.

Le stylolite tectonique avec des pics horizontaux orientés N100 pourrait être lié à la période post-15 Ma de $\sigma_1$ horizontal orienté ~E-W. Étant donné que (1) l'inversion de la rugosité du stylolite tectonique indique que le stylolite s'est développé sous un régime de contrainte décrochant (Fig. 8B) et (2) que le régime de contrainte actuel est plutôt compressif, nous proposons que le début de la période avec $\sigma_1$ horizontal orienté ~E-W a commencé par un régime de contrainte décrochant qui a évolué au fil du temps vers le régime de contrainte compressif actuel. Sur la base de l'âge de 15 Ma ci-dessus, nous déduisons la profondeur minimale à laquelle le stylolite s'est formé, c'est-à-dire ~3300m de profondeur. La valeur correspondante de la contrainte verticale $\sigma_v = \sigma_2$ est de ~84 MPa. En reportant cette valeur de $\sigma_v$ dans l'équation (15), on peut déterminer les grandeurs des contraintes principales horizontales $\sigma_H = \sigma_1$ (orientée N100°) et $\sigma_h$, respectivement 101 MPa et 64 MPa.

Nos résultats soulignent que les grandeurs des différentiels de contraintes ($\sigma_1$-$\sigma_3$) données par les deux méthodes sont proches, de 33 à 50 MPa pour l'inversion des macles de la calcite et 37 MPa pour l'inversion du stylolite tectonique. Ces valeurs comparables montrentt que l'inversion de la rugosité des stylolites tectoniques est un paléopiézomètre avec un potentiel significatif pour l'estimation des grandeurs des paléocontraintes comme les macles de la calcite.

### 7.1.2. Anisotropie de la susceptibilité magnétique (ASM)

L'anisotropie de la susceptibilité magnétique (ASM) est un outil standard utilisé pour étudier l'enregistrement des déformations de la matrice afin de caractériser la distribution texturale des grains, la forme des grains, la porosité et la microfracturation (Averbuch et al., 1992; Borradaile and Henry, 1997; Hrouda, 1982). Elle est particulièrement pertinente pour les roches faiblement déformées (Aubourg et al., 1999; Rochette et al., 1999, Rochette et al., 1992). L'ASM permet de détecter rapidement et simplement des anomalies magnétiques en surface, associées à de très faibles déformations, d'estimer la concentration en minéraux magnétiques en fonction de la température. Les principaux avantages de l'ASM sont la rapidité d'acquisition des mesures, la fiabilité, et la simplicité de la mise en œuvre. Néanmoins la méthode ne permet pas de dissocier deux groupes de grains ayant une orientation préférentielle différente.

Cette technique a été utilisée dans de nombreuses études dans les grès, les schistes, les argiles, en contexte de chaînes plissées et de bassins d'avant-pays (par exemple, Bakhtari et al., 1998; Averbuch et al., 1992; Parés et al., 1999; Parés and van der Pluijm, 2002; Saint-Bezar et

al., 2002; Aubourg et al., 2004; Weil et Yonkee, 2009; Weil et Yonkee, 2012). L'ASM est très peu utilisé dans les roches carbonatés (Parés and van der Pluijm, 2002; Amrouch et al., 2010b.) à cause du caractère peu magnétique des minéraux constitutifs de ces roches.

Des études ont souligné la difficulté d'établir la relation entre l'ASM et la déformation, à cause de la complexité de la nature du support minéralogique des signaux de susceptibilité magnétique dans la roche (Robion et al., 1999; Aubourg and Robion, 2002; Weil et al., 2016).

La fabrique magnétique d'une roche quant à elle, est définie à partir de l'orientation soit de la foliation magnétique, c'est-à-dire du plan contenant les axes $K_1$ et $K_2$ lorsque $K_1 \approx K_2 \gg K_3$, soit de la linéation magnétique, c'est-à-dire de la direction de l'axe $K_1$ (Fig. 9). Deux principaux paramètres d'anisotropie caractérisent la fabrique magnétique : le degré d'anisotropie (P), et la forme de l'ellipsoïde ASM (T) (allant de -1 pour les ellipsoïdes de forme prolate à 1 pour les ellipsoïdes de forme oblate) (Jelinek, 1981). D'après Rochette et al., (1992) P est fortement contrôlée par la minéralogie magnétique. Les paramètres d'anisotropie déterminent si les échantillons sont affectés ou non par des processus tectoniques et dans quelle mesure la matrice est déformée (Lartigau et al., 2023).

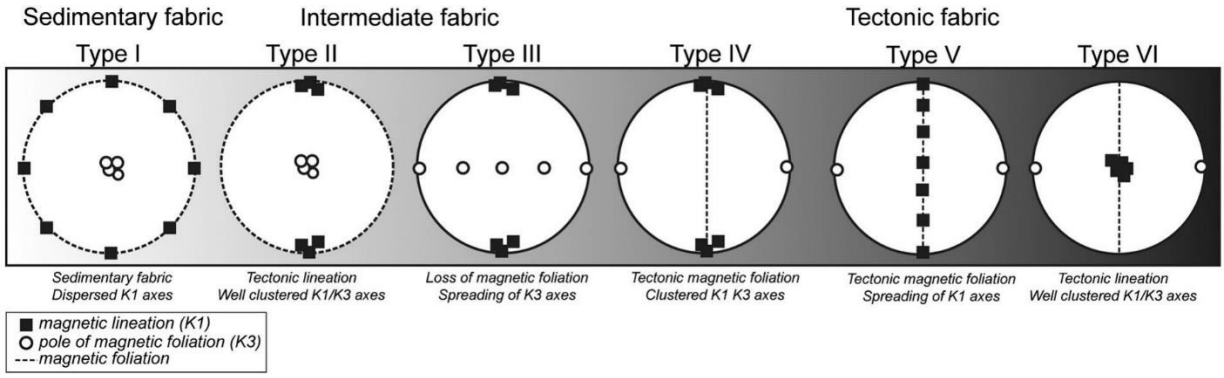


**Figure 9:** Les principaux types de foliation magnétique dans les roches faiblement déformées, montrant les quatre stades de développement de la géométrie de la linéation magnétique (K1) et du pôle de la foliation magnétique (K3). (D'après Lartigau et al., 2023).

L'intérêt même d'étudier l'ASM dans les carbonates est considéré comme limité. Des études précédentes d'ASM à champ faible sur les mudstones ont suggéré que le degré d'anisotropie est directement lié à la quantité d'argile paramagnétique (Charpentier et al., 2003; Potter et al., 2008), et il semble probable qu'il en soit de même pour les carbonates.

**Application à la formation TOCA**

Afin de confirmer les interprétations des macles de la calcite, j'ai réalisé une étude ASM sur 22 échantillons sélectionnées entre 4060 et 4150 m de profondeur à l'actuel. Cette analyse a été réalisé en collaboration avec le Pr. Charles Aubourg à l'Université de Pau et des Pays de l'Adour en décembre 2020. Pour réaliser ce travail, 22 plugs orientés (25 mm de diamètre, 20 mm de longueur) ont été prélevés dans les faciès mudstones des carbonates syn-rift de la TOCA enfouis entre 4060 et 4150 m de profondeur à l'actuel. Sur les 22 échantillons (Fig. 9) 5 échantillons, soit 23% des échantillons montrent un signal exploitable pour lequel le plan magnétique est proche de la stratification et avec des angles bien définis.

L'ASM a été mesurée à l'aide d'un susceptomètre Kappabridge MFK1-fa et les tenseurs de susceptibilité ont été calculés à l'aide du logiciel SAFIR-7. Pour la mesure, nous avons utilisé une intensité de champ magnétique standard (200 A/m) et une fréquence (976 Hz).

Pour les échantillons dont la densité des axes magnétiques principaux montre un $K_3$ dans le plan du litage (Fig. 10), on observe trois points alignés indiquant une direction d'anisotropie $K_{max}$ moyen NE-SW (~N30°). Cette direction d'anisotropie NE-SW est grossièrement compatible avec la direction d'extension NE-SW reconstitué à partir de l'inversion des macles de la calcite fossilisée sur la marge congolaise actuel.

Certes ces données restent limitées d'un point de vue statistique. Il y a lieu de préciser que la discussion de la pertinence de l'utilisation de l'ASM sur une roche carbonatée ne fait pas partie de mon travail de thèse, mais force est de constater que les résultats obtenus, même si statistiquement discutables, font preuve d'une cohérence avec les autres proxies, ce qui tend à soutenir le fait que les carbonates peuvent être utilisés avec succès par l'ASM.

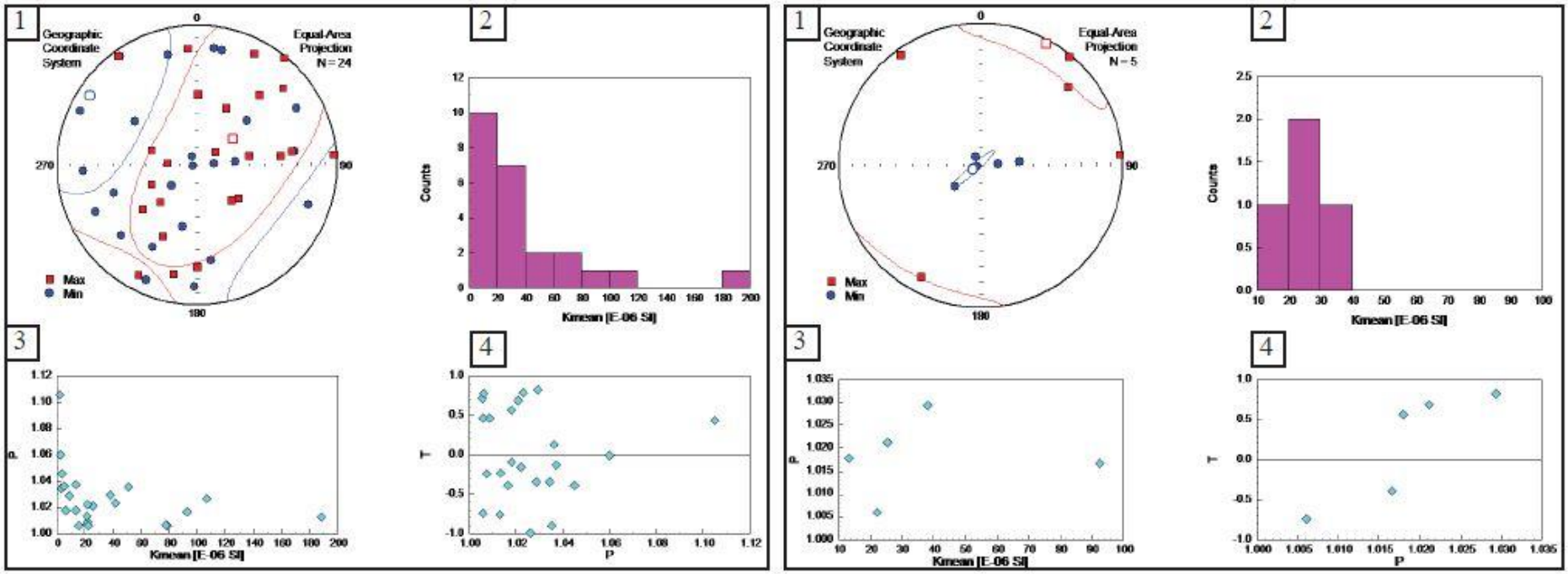


**Figure 10:** Résultats de l'analyse de l'anisotropie de la susceptibilité magnétique pour tous les échantillons (a) et les échantillons qui montrent un signal cohérent (b). (1) Exemples de fabriques magnétiques dans le repère géographique observés dans cette étude. (2) Histogramme des valeurs de susceptibilités magnétiques. (3) Susceptibilité magnétique en fonction du degré d'anisotropie (P). (4) Degré d'anisotropie (P) en fonction du paramètre de forme (T).

# Chapitre V: Reconstitution de l'histoire des paléocontraintes dans le bassin de Kwanza

Ce chapitre est une discussion du caractère reproductible des résultats obtenus dans le bassin du Bas Congo et de la validité de leur interprétation à l'échelle régionale. Pour ce faire, une étude similaire a été conduite dans le bassin de Kwanza adjacent au bassin du Bas Congo. Ce bassin a été choisi pour être un cas d'étude pour la validation de la méthode paléopiézométrique utilisée dans ce travail de thèse car il fait partie du même segment de l'Atlantique Sud, et son histoire sédimentaire est similaire à celle du bassin du Bas Congo.

# A. Reconstitution de l'histoire d'enfouissement et des paléocontraintes dans le bassin de Kwanza

## A1. Matériel

Les carottes de la série carbonatée pre-sel (section Barrémo-Aptienne équivalent-TOCA) (Fig. 11) disponibles pour cette étude ont une longueur de 13,3 m (4625-4638,3 m) dans le Well-4, de 13 m (4697-4700 m et 4755-4765 m) dans le Well-5 et de 20,3 m (4912-4921,2 m et 4924-4935,3 m) dans le Well-6, et présentent le même faciès sédimentaire composé de calcaires microbialites dolomitisés.

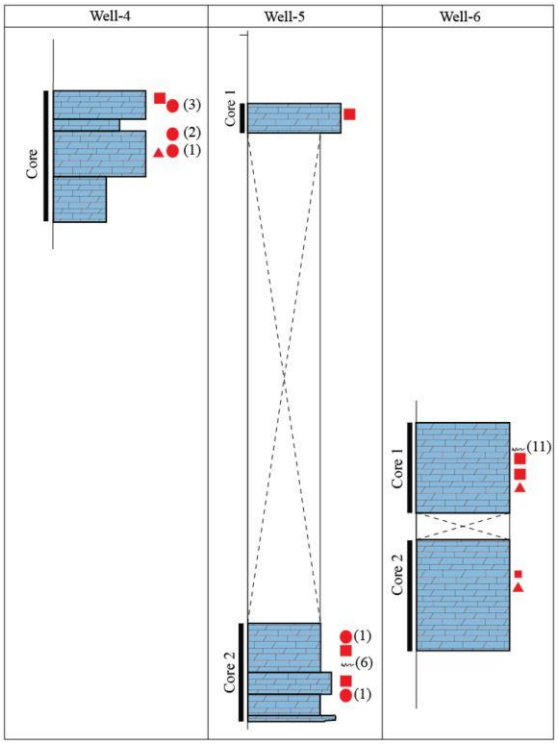


**Figure 11:** Localisation des échantillons sur les logs synthétiques des trois carottes. Les profondeurs n'ont pas été reportées pour des raisons de confidentialité. Les symboles pour les échantillons sont : carrés pour la datation U-Pb ; les sphères pour les macles de la calcite et les triangles pour les essais géomécaniques.

Les intervalles étudiés ont été sélectionnés sur la base de la représentativité des faciès sédimentaires rencontrés dans les différentes carottes. La description pétrographique est basée sur l'analyse pétrographique de 30 lames minces sous un microscope polarisant Zeiss Axioplot équipé d'une caméra Nikon Digital DS_U2/Ds_Fi1. Les phases pétrographiques ont été observées et identifiées sous lumière polarisée non analysée (LPNA) et sous lumière polarisée analysée (LPA). Toutes les observations macroscopiques et microscopiques ont été réalisés au Centre Scientifique et Technique Jean Féger de TotalEnergies (CSTJF, Pau, France).

### 1.1.Description pétrographique des carottes de la TOCA:

A partir des observations réalisées sur les carotte et sur les lames minces, un seul faciès sédimentaire bioclastique a été identifié. Il est caractérisé par son contenu minéralogique et paléontologique et ses caractéristiques sédimentologiques (texture, granulométrie, etc.). Ce faciès est formé principalement de microbialite packstone à boundstone en lits individuels dont l'épaisseur varie de quelques cm à 20 cm avec des limites de lits microbiens floues et généralement graduelles. A l’échelle de la carotte, les lits microbiens montrent des intervalles macroscopiques limités d'altération diagénétique (de silice, de dolomite et de calcite). Cependant, à l'échelle des lames minces, la séquence diagénétique semble être la même dans tout l'intervalle carotté.

De nombreuses fractures (Fig. 11) naturelles sont aussi présentes dans les carottes des Well-4 & 6. La majorité des fractures sont ouvertes ou partiellement ouvertes. Les fractures naturelles semblent être plus rares sur le Well-5. Lorsqu'elles sont présentes, elles semblent être confinées dans le lit microbien et partiellement ou entièrement cimentées.

### 1.2.Description diagénétique des carbonates de la TOCA:

Une analyse des lames minces par microscopie optique (LPNA) a permis d'identifier plusieurs événements (Fig. 13). Ces événements qui sont sédimentaires et diagénétiques comprennent, dans l'ordre chronologique, le dépôt, la calcite primaire matricielle sous forme de sphérules ou de (micro-)sparite, la dolomitisation, la silicification, la stylolitisation, et la précipitation de la calcite C « blocky ». Le détail des différentes phases diagénétiques ne fait pas l’objet de cette étude, nous présentons juste les principales phases de carbonates observées dans les carottes.


**Figure 12:** (A) Photographie d'une carotte montrant le matériel étudié. (B) Fractures ouvertes et cimentés sur la carotte. (C) Photos en LPNA des cristaux de calcite maclés dans la matrice. T- Macles. (D) Photos de stylolites sédimentaire et tectonique observés sur la carotte.

La dolomite apparait principalement en remplacement de la calcite primaire matricielle (M) et localement en ciment intergranulaire, la calcite C est observée sous forme de ciment de remplissage de pores. La silice est présente sous forme de micro-quartz de remplissage de pores (ciment) et de silice/calcédoine de remplacement de la calcite primaire. La silice est surtout fréquente le long des fractures où la matrice environnante est fortement cimentée (Fig. 11). Les observations sur les lames minces montrent que la calcite C « blocky » est postérieure à la dolomite et à la silice. La séquence diagénétique observée en lames minces, semble indiquer une relation étroite entre la porosité et la dissolution (Fig. 13).

La question de savoir s'il existe une relation entre les faciès microbialites et la cimentation préférentielle de la dolomite et de la silice n'est pas traitée dans ce travail. Les phénomènes de pression-solution affectent la calcite primaire (M), le ciment calcitique C, la silice et la dolomite. La pression-solution semble donc avoir été active pendant une grande partie de l'histoire diagénétique (Fig. 12E).

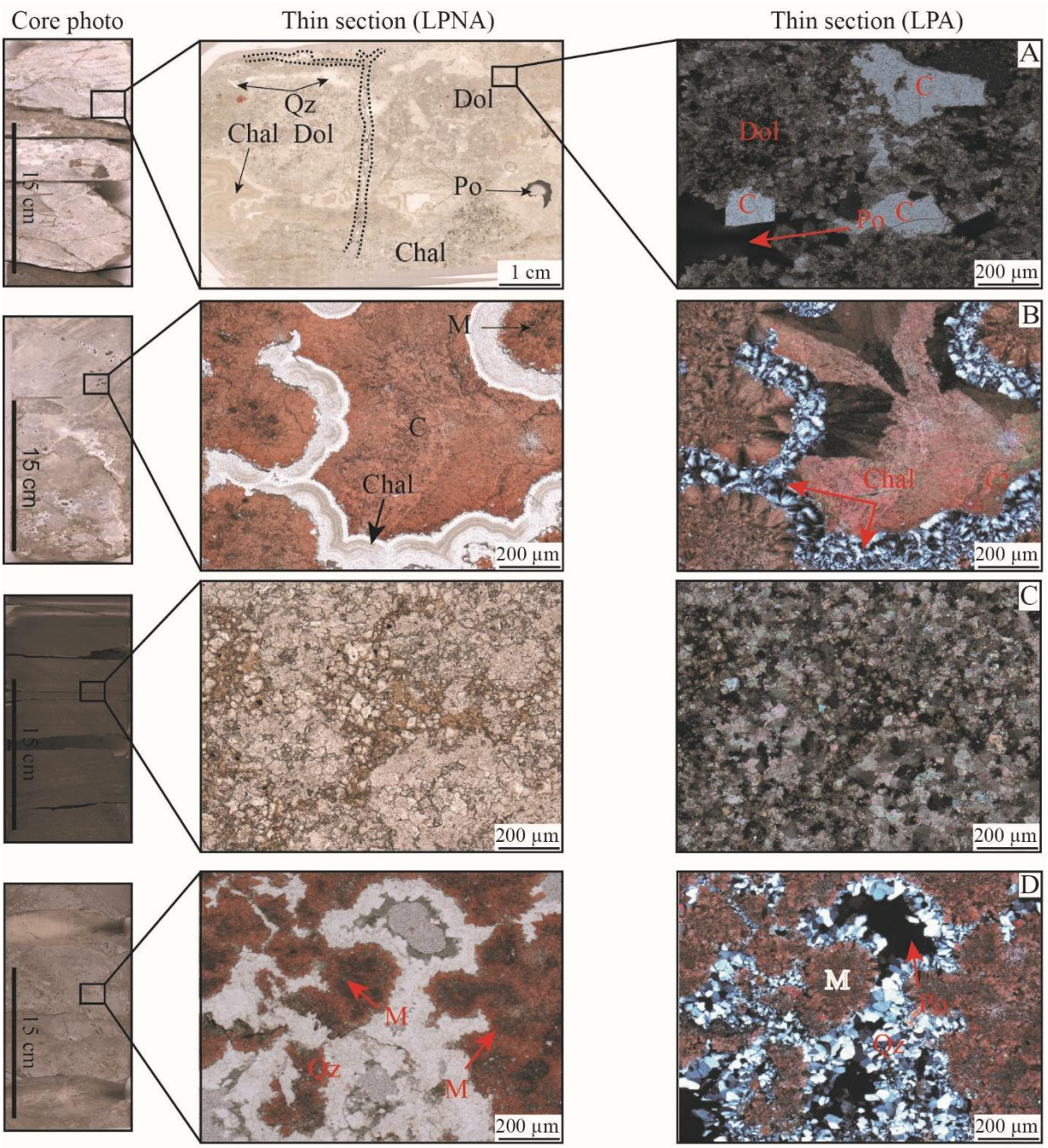


Simplified diagenetic sequence (major events) observed in the cores

| E Diagenetic event | Paragenetic sequence: Oldest → Youngest |
|---|---|
| Deposition | |
| Primary calcite (M) | |
| Early dolomitization (replacive) | |
| Early silicification (replacive and pore filling) | |
| Stylolitization | |
| Blocky calcite C (vug and vein filling) | |

**Figure 13:** Exemple de processus diagénétiques observé dans les lames minces en lumière polarisée non (LPNA) et en lumière polarisée analysée (LPA). Les lames minces ont été colorées avec de l'alizarine rouge S. La calcite apparaît en rouge, et la porosité en bleu. (A) Calcite (C) « blocky » postérieure à la dolomite (Dol). (B) La calcédoine en remplacement de la calcite primaire. (C & D) Pétro-faciès fortement silicifié et dolomitisé. La silice et la dolomite remplace la calcite primaire de dépôt. (E) Processus diagénétiques décrites à partir des lames minces.

## A2. Résultats des datation géochronologique U-Pb sur la dolomite

Seul la phase dolomitique a donné des âges U-Pb fiables. Le ciment calcitique n'a pas pu être daté. 8 échantillons ont été datés dont 1 échantillon sur le Well-4, 4 échantillons sur le Well-5 et 3 échantillons sur le Well-6 (Fig. 11). L'âge obtenu sur la dolomite de la carotte du Well-4 est de 119,8 ± 3,4 Ma. Les échantillons de la carotte du Well-5 ont donné des âges de 118,7 ± 3.0 Ma, 117,1 ± 1,7 Ma, 116,3 ± 3.4 Ma et 107,6 ± 2,5 Ma ; et ceux de la carotte du Well-6, 114,4 ± 2,3 Ma, 111,3 ± 1,3 Ma et 110,4 ± 1,9 Ma. A titre d'exemple, la figure 14 montre un diagramme de Tera-Wasserburg illustrant la bonne qualité des données U-Pb (excellent alignement des points individuels sur une large plage du rapport 238U/206Pb), donnant un âge isochrone très précis. Les résultats complets sont présentés en annexe n°1[1].

Les données biostratigraphiques disponibles dans la région d'étude (Grosdidier et al., 1996; Bate, 1999; Gradstein et al., 2004) ont permis d'identifier le sommet de la phase syn rift (sommet AS10/C6 « sommet BA4 »). Les études biostratigraphiques récentes destinées à mettre à jour les données disponibles (Rapport interne de TotalEnergies) ont montré que la TOCA eq. a un âge Aptien inférieur (121-115 Ma) sur le Well-4, Barrémien-Aptien inférieur (130-121 Ma) sur le Well-5 et Aptien (121-115 Ma) sur le Well-6. Au vu des âges biostratigraphiques, les âges U-Pb indiquent que la dolomite a précipité très tôt dans l'histoire diagénétique des carbonates pré-sel. La dolomite étant quasi syn-sédimentaire ou de diagénèse précoce dans tous les puits étudiés.

[1] Les données de datation U-Pb ont été acquises dans le cadre d'un projet R&D parallèle entre le CEREGE et TotalEnergies, nommé DATCARB (2018-2021) et cofinancé par le programme A*MIDEX, la région PACA, la métropole Aix-Marseille…. Les analyses ont été réalisées par les personnels du laboratoire de datation U-Pb laser du CEREGE (N. Godeau et A. Guihou) sous la supervision de P. Deschamps (IRD-CEREGE) et J-P. Girard (TotalEnergies). Nous remercions les équipes de TotalEnergies qui ont bien voulu accepter que ces données soient intégrées dans ma thèse.

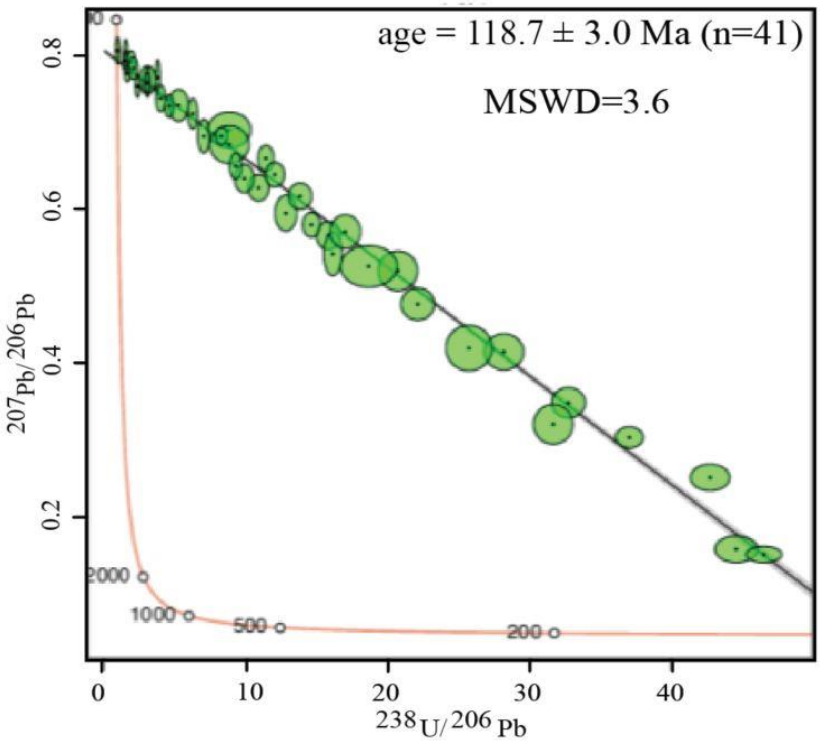


**Figure 14:** Diagramme Tera-Wasserburg obtenu pour la dolomite d'un échantillon de carbonate pre-sel du Well-5 et permettant de calculer un âge U-Pb de 118,7 ± 3,0. n - nombre de points de mesures effectués.

## A3. Résultats des tests géomécaniques

Les essais mécaniques ont été réalisés sur le faciès boundstone qui est le faciès majoritaire sur les carottes. Les tests effectués sur le Well-6 montrent que le module d'Young E varie entre 8.95 et 20.47 GPa. Le coefficient de Poisson ν quant à lui varie entre 0,23 et 0,37 (Rapport interne TotalEnergies). Les valeurs moyennes des paramètres élastiques déterminées à partir des données des tests géomécaniques sur l'ensemble des carottes (Mastina and Zerbinati, 2021) sont E = 25 GPa et ν = 0,27. L'incertitude sur la détermination de E et ν est de ±10% et ±20%, respectivement.

Les valeurs de la contrainte principale maximale $\sigma_1$ à 5, 15 et 30 MPa de confinement déterminées à partir des essais triaxiaux ont été utilisées pour construire les cercles de Mohr pour chaque chargement (Fig. 15).

Les diagrammes de Mohr sont assez similaires aux deux profondeur échantillonnées sur la carotte.

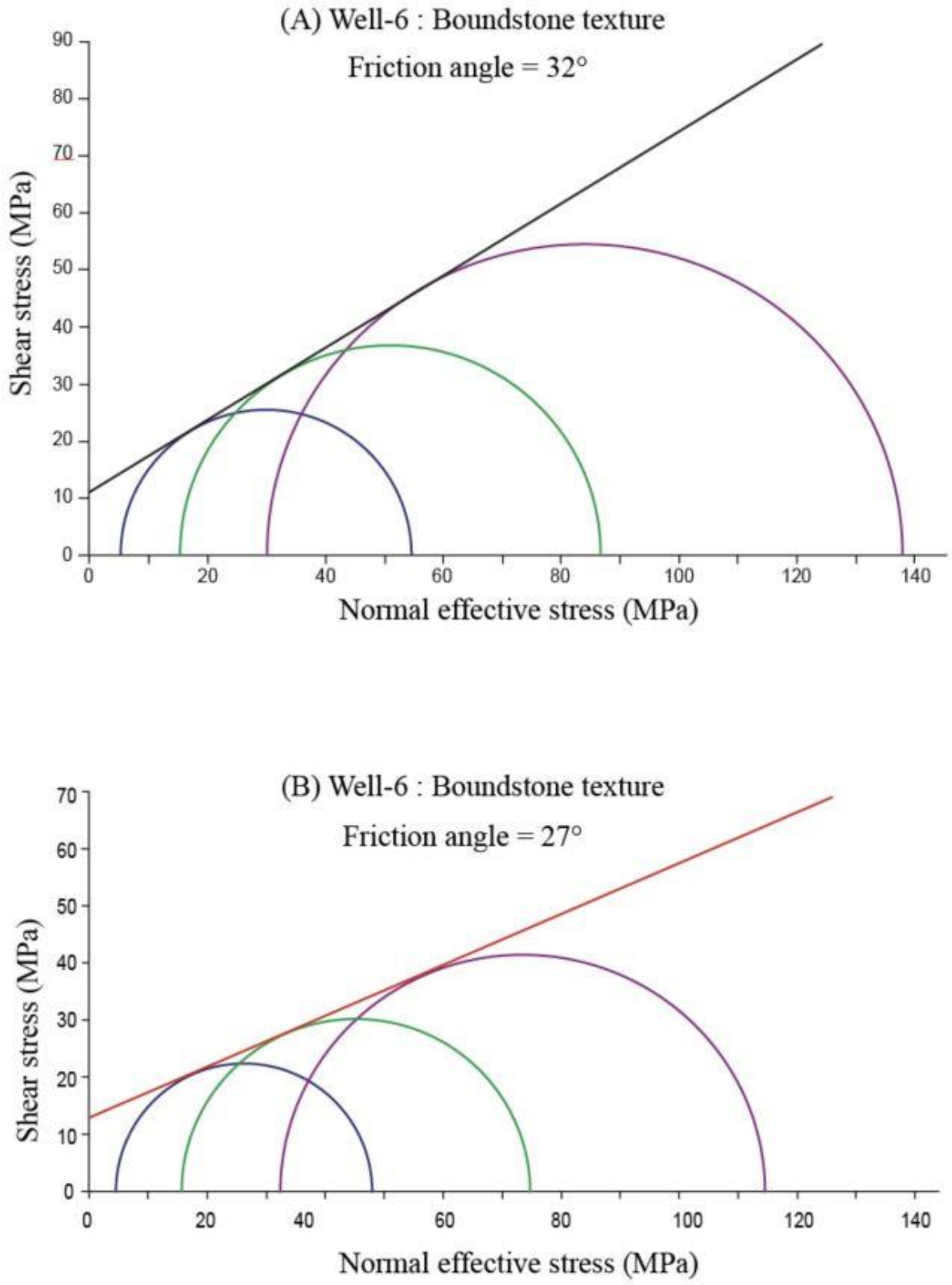


**Figure 15:** Exemples de diagrammes de Mohr montrant l'enveloppe de rupture de Mohr de la TOCA déterminée à partir d'essais géomécaniques dans le faciès boundstone à différentes profondeurs sur le Well-6.

## A4. Résultats de l'inversion des macles de la calcite

L'inversion des macles de la calcite a été réalisée à partir de 8 échantillons prélevés entre 4626,47 m et 4762,30 m de profondeur (Tableau 1; Fig. 16). L'observation en cathodoluminescence a révélé que les échantillons ne présentaient qu'une seule calcite sparitique maclée, de sorte que tous les cristaux ont pu être traités ensemble. Les cristaux de calcite montrent tous des macles fines et rectilignes (Fig. 12), ce qui indique une déformation à basse température inférieure à 170°C (Ferrill et al., 2004; Lacombe et al., 2021a). Nos échantillons montrent une distribution aléatoire des axes optiques des grains, ce qui est une condition préalable à la fiabilité de l'inversion des données des macles de la calcite. Les histogrammes de la taille de grains pour les échantillons étudiés montrent une distribution de la taille des grains comprise entre 50 et 250 µm, avec une valeur modale autour de 200 µm. La quantité de déformation a été estimée grossièrement à moins de 2 % et cette valeur a été prise en compte avec la plus grande taille de grains (car plus la taille de grain est grande, plus le seuil de maclage est faible) pour définir la valeur du seuil de maclage utilisée pour le calcul du différentiel de contrainte (Parlangeau et al., 2019; Lacombe et al., 2021a) comme indiqué dans le tableau 1.

Seuls 2 des 8 échantillons analysés pour les macles de la calcite ont donné un seul tenseur de contrainte (Tableau 3. Tous les autres échantillons (~75%) ont donné deux, ou trois tenseurs de contrainte superposés. Afin de simplifier au maximum la description des résultats, les tenseurs de contrainte obtenus ont été rassemblés en différents groupes sur la base de l'orientations des contraintes principales et du régime de contrainte (extension, vertical $\sigma_1$; compression, vertical $\sigma_3$; décrochement, vertical $\sigma_2$). A partir des 17 tenseurs déterminés à partir des 8 échantillons (Tableau 1), un total de 9 groupes principaux de tenseurs a pu être défini (Fig. 16): quatre groupes de tenseurs extensifs (A, B, C et D), trois groupes de tenseurs compressifs (E, F et G), et deux groupes de tenseurs décrochant (H et I).

Pour les régimes de contrainte extensifs, le groupe A a été identifié dans 1 échantillon et est caractérisé par une orientation $\sigma_3$ N40 et par une magnitude de différentiels de contraintes moyenne de 47 MPa pour ($\sigma_1$-$\sigma_3$) et 23 MPa pour ($\sigma_2$-$\sigma_3$). Le groupe B a été identifié dans 1 échantillon, avec un $\sigma_3$ ~N110 et des magnitudes de différentiels de contraintes moyenne de 40 MPa pour ($\sigma_1$-$\sigma_3$) et 24 MPa pour ($\sigma_2$-$\sigma_3$). Le groupe C a été identifié dans 3 échantillons et est caractérisé par une orientation $\sigma_3$ ~E-W et par une magnitude de différentiels de contraintes moyenne de 30 MPa pour ($\sigma_1$-$\sigma_3$) et 13 MPa pour ($\sigma_2$-$\sigma_3$).

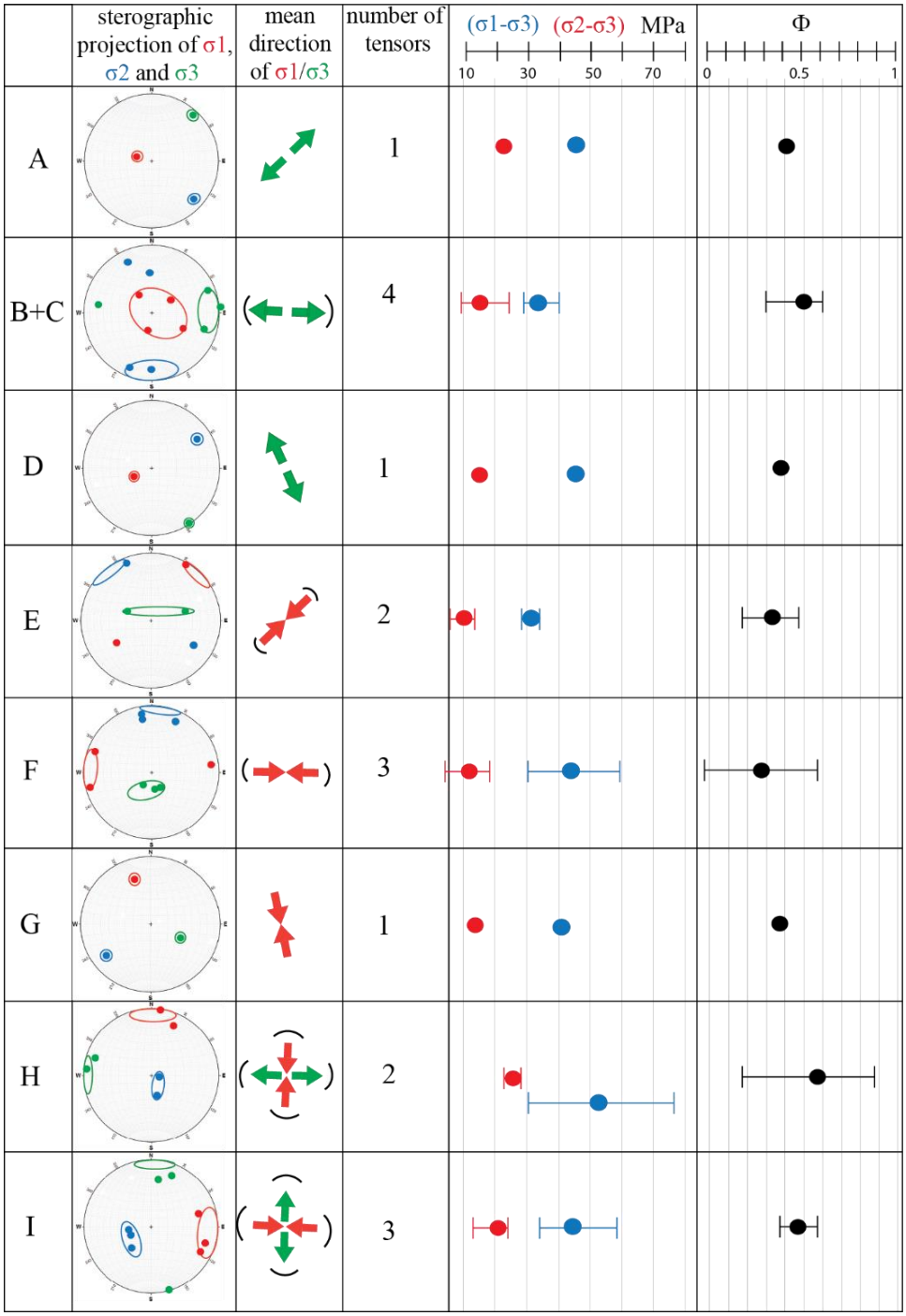


**Figure 16:** Groupes de tenseurs de contrainte obtenus par l'inversion des macles de la calcite. Chaque groupe de tenseurs (A à I) est caractérisé par une projection stéréographique montrant l'orientation des axes des contraintes principales (rouge pour $\sigma_1$, bleu pour $\sigma_2$ et vert pour $\sigma_3$) et la représentation de la direction moyenne des contraintes principales horizontales sous forme de flèches (rouge pour $\sigma_1$, vert pour $\sigma_3$, en vue cartographique). Le nombre d'échantillons pour chaque groupe de tenseurs est indiqué ainsi que les valeurs moyennes des magnitudes des différentiels de contrainte pour chaque groupe : en bleu ($\sigma_1$-$\sigma_3$) ; en rouge ($\sigma_2$-$\sigma_3$) et en noir la valeur moyenne du rapport Φ.

Le groupe D a été identifié dans 1 échantillon, avec un $\sigma_3$ orientée ~N-S et des magnitudes de différentiels de contrainte moyenne de 48 MPa pour ($\sigma_1$-$\sigma_3$) et 19 MPa pour ($\sigma_2$-$\sigma_3$). Comme les groupes de tenseurs B et C sont relativement proches en termes d'orientation des contraintes principales et de magnitudes de différentiels de contrainte moyenne, compte tenu des incertitudes, nous avons décidé de les combiner en un seul super groupe de tenseurs B+C, qui est probablement plus représentatif que chacun des sous-groupes.

Pour ce qui est des régimes de contrainte compressifs, le groupe E a été identifié dans 2 échantillons avec un $\sigma_1$ orienté ~N45 et des magnitudes de différentiels de contrainte moyenne de 31 MPa pour ($\sigma_1$-$\sigma_3$) et 10 MPa pour ($\sigma_2$-$\sigma_3$). Le groupe F a été identifié dans 3 échantillons avec un $\sigma_1$ orienté ~E-W et des magnitudes de différentiels de contrainte moyenne de 43 MPa pour ($\sigma_1$-$\sigma_3$) et 12 MPa pour ($\sigma_2$-$\sigma_3$). Le groupe G a été identifié dans 1 échantillon avec un $\sigma_1$ orienté ~N-S et des magnitudes de différentiels de contrainte moyenne de 40 MPa pour ($\sigma_1$-$\sigma_3$) et 13 MPa pour ($\sigma_2$-$\sigma_3$).

En ce qui concerne les régimes de contrainte décrochants, le groupe H a été identifié dans 2 échantillons avec un $\sigma_1$ orienté ~E-W et des magnitudes de différentiels de contrainte moyenne de 52 MPa pour ($\sigma_1$-$\sigma_3$) et 27 MPa pour ($\sigma_2$-$\sigma_3$). Le groupe I a été identifié dans 3 échantillons avec un $\sigma_1$ orienté ~N-S et des magnitudes de différentiels de contrainte moyenne de 43 MPa pour ($\sigma_1$-$\sigma_3$) et 21 MPa pour ($\sigma_2$-$\sigma_3$).

## A5. Résultats de l’inversion de la rugosité des stylolites sédimentaires

Six échantillons ont été coupés et étudiés, dans lesquels 17 traces 2-D des stylolites sédimentaires ont été analysés par la méthode du Spectre de Puissance de Fourier (FPS ; Fig. 17). 12 stylolites ont présenté deux régimes auto-affines avec les coefficients de Hurst attendus, ce qui donne un taux de réussite de 71% (Tableau 2).

La figure 16 montre quatre exemples de traitement. Trois sont acceptables car l'inversion fournit une tendance montrant deux pentes bien marquées avec des coefficients de Hurst cohérents avec ceux prédits par le modèle de croissance (Fig. 17A, 17B & 17C). En revanche, la figure 17D montre un cas non acceptable car l'inversion fournit une tendance monotone sans changement de pente.

**Tableau 1:** Tenseurs de contraintes déterminés à partir de l'inversion des macles de la calcite. La qualité de chaque tenseur est estimée sur la base de plusieurs critères tels que la stabilité des orientations des contraintes principales, la valeur de la fonction de pénalisation et le nombre de plans non maclés incompatibles. TP - Plans maclés; UP - Plans non maclés.

| Depth (m) | σ1 trend (°) | σ1 plunge (°) | σ2 trend (°) | σ2 plunge (°) | σ3 trend (°) | σ3 plunge (°) | Penalization function | Φ | τs | (CRSS) MPa | (σ1-σ3) MPa | (σ2-σ3) MPa | Total number of TP/UP | Number of compatible TP/UP | Quality |
|---|---|---|---|---|---|---|---|---|---|---|---|---|---|---|---|
| Cameia | | | | | | | | | | | | | | | |
| 4626.47 | 320 | 62 | 204 | 13 | 108 | 24 | 0.1 | 0.6 | 0.175 | 7 | 40 | 24 | 72/21 | 20/17 | B |
| | 118 | 21 | 251 | 61 | 20 | 20 | 0.1 | 0.6 | 0.167 | | 42 | 25 | | 30/19 | A |
| | 6 | 1 | 107 | 83 | 276 | 7 | 0.2 | 0.3 | 0.090 | | 78 | 26 | | 21/18 | C |
| 4626.68 | 338 | 29 | 236 | 20 | 117 | 54 | 0.4 | 0.4 | 0.165 | 7 | 42 | 17 | 124/53 | 42/44 | C |
| | 108 | 19 | 225 | 53 | 6 | 30 | 0.8 | 0.4 | 0.116 | | 60 | 24 | | 52/45 | C |
| 4627.60 | 290 | 9 | 23 | 19 | 176 | 69 | 0.2 | 0.6 | 0.187 | 6 | 32 | 20 | 112/38 | 35/31 | B |
| | 177 | 50 | 354 | 40 | 85 | 2 | 0.2 | 0.5 | 0.202 | | 30 | 14 | | 33/34 | A |
| 4629.86 | 82 | 15 | 348 | 13 | 220 | 70 | 0.4 | 0.0 | 0.099 | 6 | 61 | 0 | 89/37 | 37/31 | B |
| 4630.25 | 247 | 64 | 56 | 25 | 148 | 4 | 0.3 | 0.4 | 0.145 | 7 | 48 | 19 | 94/35 | 37/29 | A |
| | 284 | 68 | 134 | 19 | 40 | 10 | 0.4 | 0.5 | 0.149 | | 47 | 23 | | 28/31 | B |
| | 239 | 38 | 335 | 7 | 74 | 51 | 0.2 | 0.2 | 0.201 | | 35 | 7 | | 30/28 | C |
| 4632.90 | 257 | 4 | 348 | 20 | 156 | 70 | 0.2 | 0.4 | 0.136 | 6 | 44 | 18 | 176/55 | 59/49 | B |
| 4757.00 | 22 | 21 | 170 | 66 | 287 | 11 | 0.7 | 0.9 | 0.220 | 7 | 32 | 29 | 141/54 | 45/46 | B |
| | 199 | 68 | 333 | 16 | 67 | 15 | 0.5 | 0.5 | 0.213 | | 33 | 16 | | 42/46 | B |
| 4762.30 | 52 | 64 | 183 | 18 | 279 | 18 | 0.2 | 0.3 | 0.245 | 7 | 29 | 9 | 141/72 | 42/64 | A |
| | 29 | 6 | 122 | 33 | 290 | 57 | 0.4 | 0.5 | 0.233 | | 30 | 15 | | 39/68 | A |
| | 74 | 30 | 261 | 60 | 166 | 3 | 0.9 | 0.4 | 0.192 | | 36 | 16 | | 54/29 | C |

Pour l'inversion de la rugosité des stylolites, nous avons utilisé les valeurs moyennes des paramètres élastiques déterminés à partir des essais géomécaniques: E = 25 GPa et ν = 0,27. L'incertitude sur la longueur de coupure (Lc) est de ±23% (Rolland et al., 2014).

Après avoir calculé la valeur de la contrainte verticale pendant la période d'activité de la pression-solution le long des stylolites à partir de cette équation ($\sigma_v^2 = \frac{\gamma E}{\alpha L_C}$) avec $\alpha = \frac{(1-2\nu)(1+\nu)^2}{30\pi(1-\nu)^2}$ (Ebner et al., 2009b), il est possible de convertir la valeur de $\sigma_v$ (en Pa) en profondeur d'enfouissement (en m) en utilisant l'équation ($\sigma_v = \rho gh$) avec $\rho$ la densité de la roche hôte (2600 kg.m$^{-3}$) et g l'accélération du champ gravitationnel (9,81 m.s$^{-2}$).

La valeur de la contrainte verticale ($\sigma_1$) résultante est comprise entre 18 et 62 MPa correspondant à une gamme de profondeur de 750 à 2500 m (Fig. 18).

**Tableau 2:** Résultats de l'inversion de la rugosité des stylolites appliquée aux stylolites sédimentaires dans la formation TOCA. $\sigma_v$ est calculée avec les valeurs de E = 25 GPa et ν = 0,27 déterminées à partir d'essais de mécanique des roches. Les incertitudes sont de 23% sur la valeur de la Lc, de 12% sur la valeur de la contrainte verticale (Rolland et al. 2014).

| Samples | cross-over length(mm) | σv (MPa) | Depth (m) |
|---|---|---|---|
| CAM2_4758.06_00 | 0.245 | 48 | 1950 |
| CAM2_4758.06_00 | 0.599 | 30 | 1250 |
| CAM2_4758.80_00 | 0.446 | 35 | 1450 |
| CAM2_4758.80_00 | 0.230 | 49 | 2000 |
| CAM2_4761.44_00 | 0.188 | 54 | 2200 |
| CAM2_4761.44_00 | 0.489 | 34 | 1400 |
| CAM3_4916.31 | 1.670 | 18 | 750 |
| CAM3_4916.61_00 | 0.385 | 38 | 1550 |
| CAM3_4916.61_00 | 0.146 | 62 | 2500 |
| CAM3_4916.61_00 | 0.281 | 44 | 1800 |
| CAM3_4916.61_00 | 0.400 | 37 | 1500 |
| CAM3_4916.61_00 | 0.231 | 49 | 2000 |
| CAM3_4916.61_00 | 0.251 | 47 | 1900 |
| CAM3_4916.61_00 | 0.524 | 33 | 1300 |
| CAM3_4916.61_00 | 0.146 | 62 | 1500 |
| CAM3_4917.26_00 | 0.922 | 25 | 1000 |
| CAM3_4917.26_00 | 1.295 | 21 | 850 |

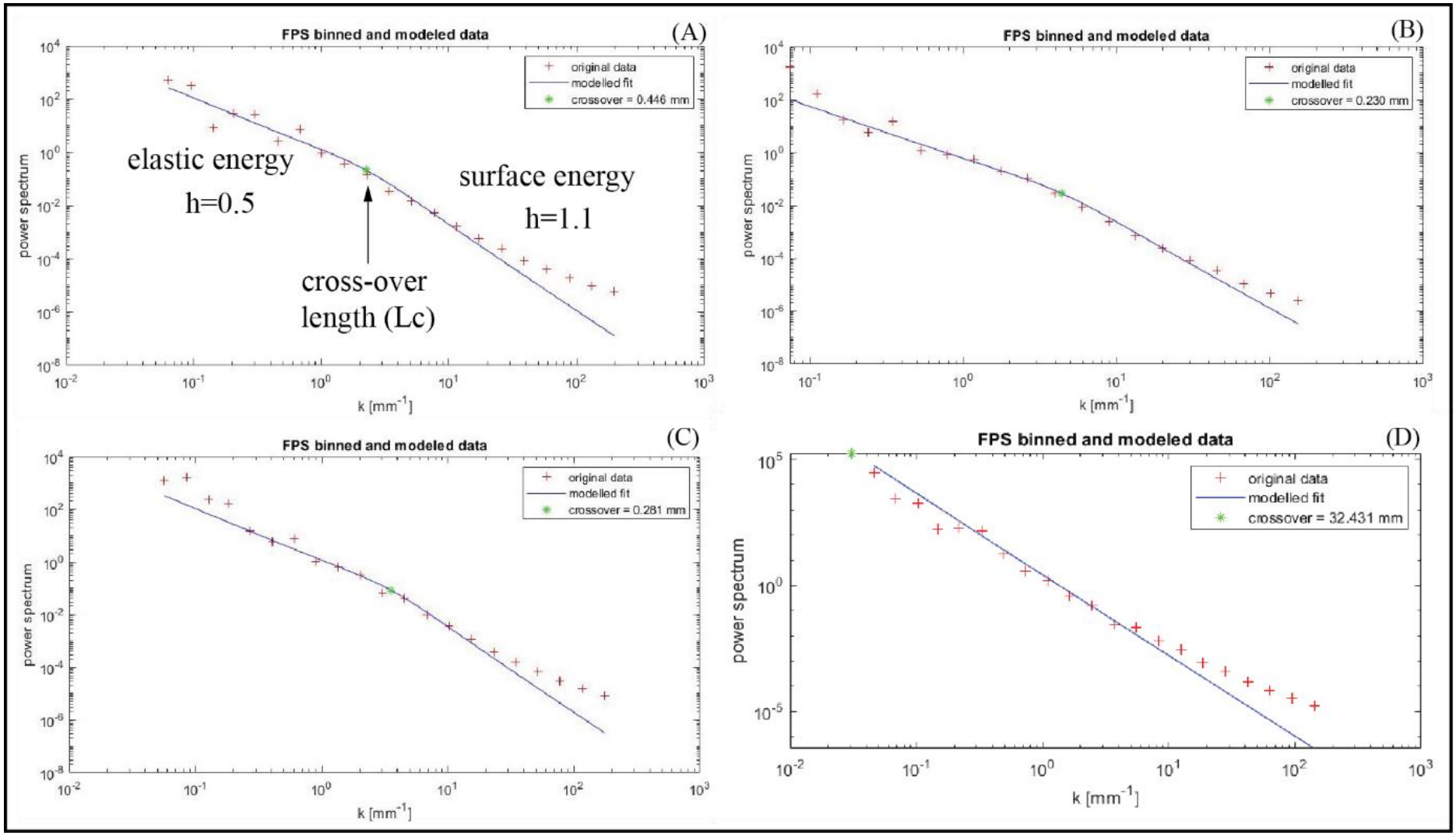


**Figure 17:** Définition de l'exposant de Hurst et de la longueur de coupure sur un tracé log-log de la méthode du spectre de puissance de Fourier (A) et exemples d'inversion de la rugosité des stylolites sédimentaires pour certains échantillons, soit réussis (B et C), soit échoués (D).

## A6. Distribution des fractures mesurées sur carotte

29 fractures ont été mesurées sur les carottes (Well-4, & 6). Le Well-4 présente une densité de fractures/mètre plus faible que sur le Well-6. L'intervalle de profondeur entre 4912 m et 4935 m dolomitique et bréchifié est celui qui présente le plus de fractures (partiellement cimentées et/ou totalement cimentées) de longueur variable. Toutes les fractures mesurées présentées sur la figure 19 proviennent de la carotte du puits Well-6.

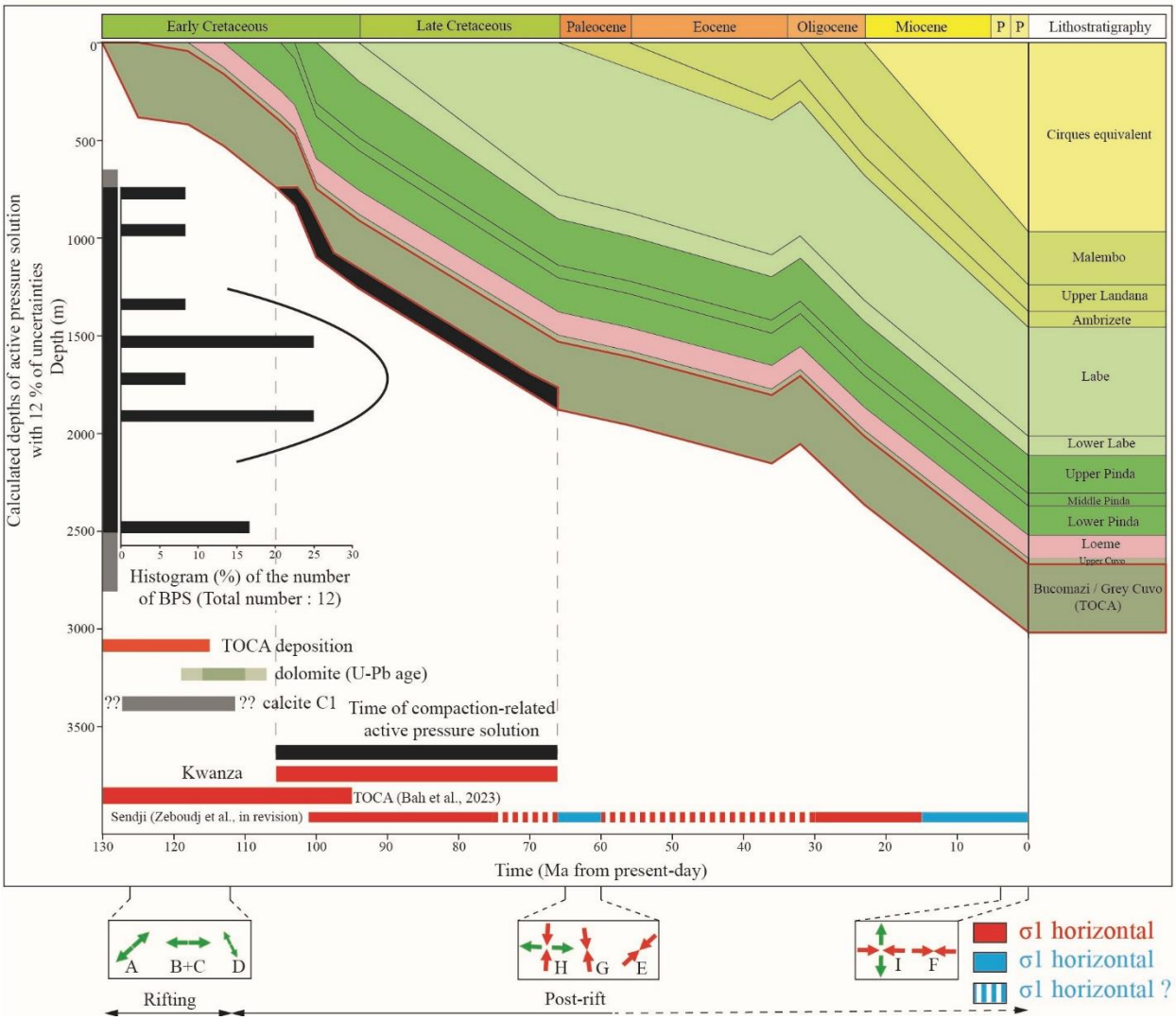


**Figure 18:** Modèle d'enfouissement construit à partir des données du Well-4 corrigées de la compaction mécanique. La profondeur sur le modèle est comptée à partir du fond de la mer. La gamme de profondeurs calculées de la pression-solution active à partir de l'inversion des stylolites sédimentaires est reportée pour les carbonates pré-sel étudié sous forme de niveaux de gris sur l'axe des ordonnées. Les régimes de contrainte enregistrés par l'inversion des macles de la calcite sont également rapportés (vue cartographique).

Les fractures présentent des pendages variant entre 35° et 90° et le mode d'ouverture est plutôt mixte mode 1-mode 2. Malgré la dispersion, la distribution des directions de fractures indique une prédominance de trois ensembles principaux: un ensemble comprenant des fractures (8) orientées NNW-SSE (N145° à N165°) et plongeant ~35-60°E (ensemble 1 en orange), un ensemble comprenant des fractures (9) orientées NE-SW (N15° à N45°) et plongeant ~50-60°E (ensemble 2 en vert) et un ensemble comprenant des fractures (9) orientées (~N85° à N125°) et avec des plongements variables vers le Sud (ensemble 9 en bleu) (Fig. 19).

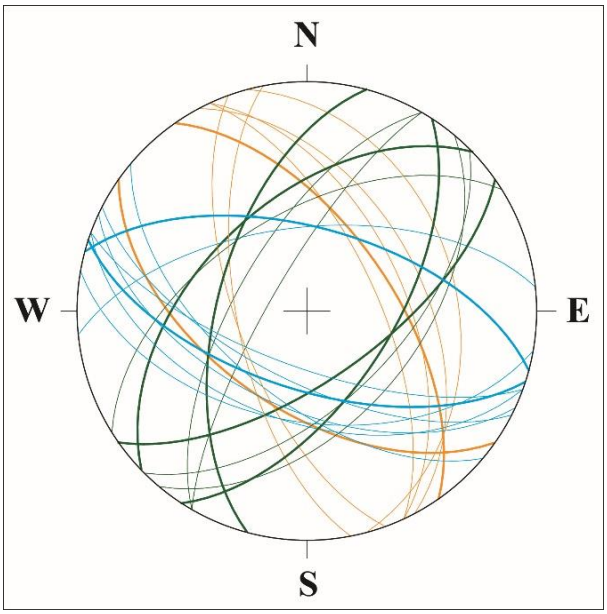


**Figure 19:** Réprésentation stéréographique en hémisphère inférieure de la direction des fractures décrites dans les échantillons de la carotte du Well-6. Les failles probablement conjuguées sont représentées avec les lignes épaisses.

L'ensemble 1 des fractures orientées N145° à N165° (orange; Fig. 19) est la première famille de fracture à se former d'après la séquence observée sur la carotte. Cet ensemble 1 est recoupée par l'ensemble 2 (Fig. 12B).

L'ensemble 2 d'orientation N15° à N45° (vert; Fig. 19) est présente sur toute la carotte. Cet ensemble est postérieur à l'ensemble 1 et est antérieur à l'ensemble 3.

L'ensemble 3 orienté N85° à N125° (bleu; Fig. 19) vient buter sur l'ensemble 2 mais ne le recoupe pas sur l'ensemble de la carotte.

Dans tous les ensembles de probable failles conjuguées sont observées dans le lot de données.

Un dernier ensemble de trois fractures orientées N-S a aussi été observé. Cette famille est considérée comme mineure (faible nombre de mesures) et n'a pas été affectée à l'un ou l'autre des ensembles majeurs. De ce fait, elle ne sera pas interprétée par la suite.

## A7. Modèle d'enfouissement

Le modèle d'enfouissement développé pour le Well- 4 et présenté à la figure 18 montre cinq phases d'évolution de l'enfouissement dans le temps : (1) 130 Ma à 118 Ma, une première phase d'enfouissement modéré (~25 m/Ma) pendant l'épisode de rifting du Crétacé inférieur. La deuxième phase correspond à un dépôt rapide de grès et d'évaporites avec un taux d'enfouissement moyen de 55 m/Ma pendant la phase de transition. (3) La phase post-rift commence par un taux d'enfouissement modéré (~25 m/Ma) de 112 Ma à 65 Ma, suivi par (4) un enfouissement faible (65 Ma à 35 Ma), conduisant à une érosion modérée au Tertiaire inférieur, et se termine par (5) une troisième phase d'enfouissement modéré (~3,5 m/Ma) de 30 Ma à nos jours. La figure 18 montre également l'histogramme des profondeurs maximales de l'activité de la pression-solution le long des stylolites sédimentaires, obtenues à partir de l'inversion de la rugosité des stylolites.

## B. Interprétations des résultats obtenus sur le bassin de Kwanza et comparaison avec le bassin du Bas Congo

Les résultats de l'inversion des macles de la calcite révèlent une histoire des paléocontraintes polyphasée. L'âge de dépôt de la TOCA dérivé de la biostratigraphie (Grosdidier et al., 1996) et la datation U-Pb absolue de la dolomite postérieure à la calcite primaire matricielle fournissent des contraintes temporelles sur le début de l'évolution (Fig. 18). La distribution des gammes de profondeur de l'activité des stylolites sédimentaires projetée sur les courbes d'enfouissement au cours du temps fournit les périodes d'activité de la pression-solution liée à la compaction le long des stylolites sédimentaires, donc les périodes dominées par un régime de contrainte avec un $\sigma_1$ vertical entre 109 et ~67 Ma (750- 2000 m) (Fig. 18). Néanmoins si on considère les deux stylolites les plus profonds (~2500 m de profondeur maximale) la période d'activité est comprise alors entre 109 et ~17 Ma. La calcite dans laquelle les mesures de macles de la calcite ont été réalisées n'a pas été datée, mais la datation U-Pb de la dolomite (120-108 Ma) qui est postérieure (et remplace) la calcite primaire permet de contraindre l'âge de cette calcite probablement au moment du dépôt des carbonates pré-sel étudié entre 130 et 110 Ma

(cette fourchette d'âge est en accord avec les résultats d'une étude interne de biostratigraphie de TotalEnergies effectuée sur le même puits et non publiée.

## B1. Rifting et paléocontraintes extensives associées à l'ouverture du segment central de l'Atlantique Sud.

Sur la base des résultats de l'inversion de la rugosité des stylolites sédimentaires et de l'âge connu du début du rifting (Lehner and De Ruiter, 1977; Karner et al., 1997; Contrucci et al., 2004; Beglinger et al., 2012; Salomon et al., 2015), on peut affirmer que le régime de contraintes des séries pré-sel (TOCA Fm et équivalent) a été dominé par un $\sigma_1$ vertical de ~145 Ma (âge du début du rifting) jusqu'à au moins ~67 Ma si l'on considère 2000 m de profondeur ou jusqu'à ~17 Ma à 2500 m.

Nous proposons donc que les paléocontraintes d'extension enregistrées par le maclage de la calcite et correspondant aux groupes de tenseurs de contraintes A, B+C et D soient datées entre ~130 et ~67 Ma, et plus probablement entre 130 et ~112 Ma (fin du rifting). La période de ~112 Ma à ~67 Ma, a été dominée par l'enfouissement et la compaction verticale.

Le groupe de tenseurs A (Fig. 16 & 18) associé à une direction d'extension NE-SW est cohérent avec celui enregistré sur les côtes sud-ouest de l'Afrique (Viola et al., 2012 ; Salomon et al., 2015; Nkodia et al., 2020). Cette direction d'extension est liée à l'ouverture de l'océan Atlantique Sud. Le groupe de tenseurs B+C (Fig. 16 & 18) est probablement associé à un état transitoire de contrainte qui a précédé l'extension principale NE-SW. La tendance N-S (groupe de tenseurs D) pourrait avoir une signification locale.

La carte du toit de la TOCA dans le bassin de Kwanza (âge Barrémien-Aptien inférieur) (Fig. 20B) montre deux ensembles principaux de failles normales NW-SE et N-S en rouge et noir respectivement, en accord avec la distribution des fractures méso-échelle rapportées dans les puits dans le bassin du Kwanza (Erdi and Jackson, 2021). Ce système de failles normales est aussi documenté dans le bassin du Bas Congo (Fig. 20A). Les failles normales dominantes de direction NW-SE sont perpendiculaires à la principale direction d'extension régionale NE-SW (à ENE-WSW).

Dans le bassin de Kwanza, nous avons eu accès à peu des données de puits ayant atteint les carbonates pré-sel (équivalent TOCA) pour réaliser une comparaison robuste et fiable entre les failles sismiques et les fractures dans d'autres puits que ceux étudiés à l'échelle du bassin. Malgré le peu de données de fracturation mesurées sur carotte (Fig. 19 & 20B), certaines

familles comportent des failles qui montrent des directions qui sont compatibles avec l'orientation des grandes de failles régionales d'une part et des orientations des tenseurs de contraintes reconstitués à parti des macles de la calcite d'autre part. Le groupe de tenseur A est compatible avec l'ensemble 1 de fractures (Fig. 19), qui sont majoritairement bien orientées par rapport à la direction d'extension ~NE-SW. Par contre les quelques failles dont la direction est proche de l'axe N-S sortent du lot et ne serait probablement pas associé à cette phase d'exension et pourrait être potentiellement liées à une direction d'extension orienntée ~E-W comme le groupe de tenseur B+C. L'ensemble 2 de fractures (NE-SW) n'est compatible avec aucun des tenseurs reconstitué dans les carbonates pré-sel et montre une direction oblique par rapport aux grandes failles régionales orientées N-S et E-W. L'ensemble 3 quant à elle est compatible avec une direction d'extension de N-S à NNE-SSW, donc il pourrait être associé au tenseur de contrainte D. Cependant, cette interprétation est incompatible avec la chronologie établie sur la base des orientations des failles et de leur chronologie relative dans le bassin du Bas Congo (Fig. 20A) où nous avons proposé avec l'aide des données de la littérature que la direction d'extension passe de E-W à NE-SW formant les failles N-S puis NW-SE ce qui semble être contradictoire avec notre set de données. Néanmoins le peu de données rend cette interprépation statistiquement moins fiable que celle établie dans le bassin du Bas Congo à partir de pluseirus données différentes. Par conséquent il est possible que la chronologie de la fracturation à méso-échelle dans une seule carotte ne reflète pas l'état de la fracturation régionale. Car l'état de contrainte régionale pourrait être perturbé par des effets locauxau vu del'emplacement des puits par rapport aux grandes failles dans le bassin (Fig. 20B).

## B2. Etat de contraintes post-rift à l'échelle du segment central de l'Atlantique Sud

Comme nous l'avons défini dans la section B1 ci-dessus, nous allons discuter du calendrier des paléocontraintes post-rift en fonction de la profondeur maximale d'arrêt de la dissolution le long des stylolites. Au vu des résultats de l'inversion de la rugosité des stylolites et de la quantité de données disponibles pour cette étude dans le bassin de Kwanza, on peut proposer deux interprétations possible en fonction de la profondeur d'arrêt de la stylolitisation:

Dans l'hypothèse d'une profondeur maximale de 2000 m, l'inversion des stylolites sédimentaires dans le bassin de Kwanza permet de contraindre une période de temps à $\sigma_1$ verticale 109-67 Ma. Après ~67 Ma, soit $\sigma_1$ serait devenu horizontal, ce qui signifie que les contraintes tectoniques auraient dépassé la contrainte verticale liée à l'enfouissement et que la

compaction verticale a pris fin, pour une raison interne (e.g. cimentation massive/clogging de la porosité, développement de surpression des fluides), soit la compaction chimique dans la formation TOCA aurait cessé alors que $\sigma_1$ était encore vertical.

Nos résultats suggèrent un âge postérieur à 67 Ma pour les régimes de contraintes avec des $\sigma_1$ horizontaux orientés soit N-S à NE-SW (groupes de tenseurs E, G, H) ou E-W (groupes de tenseurs F et I). Notamment, au cours de la période commençant à ~67 Ma et s'étendant jusqu'à ~35 Ma, le taux d'enfouissement a fortement ralenti et le réservoir a même été soulevé (entre ~35 et ~30 Ma, Fig. 18).

Etant donné que la compression N-S à NE-SW a une orientation et une chronologie compatible avec la compression Crétacé supérieur-Paléocène décrite par Guiraud et Bosworth (1997), nous proposons à titre temporaire d'attribuer un âge Crétacé supérieur-Paléocène inférieur (~67-60 Ma) aux groupes de tenseurs (E, G, H). Cette compression de la fin du Crétacé et du Paléocène serait donc contemporaine du début du soulèvement de la marge paléogène (Fig. 18), quoique le lien de cause à effet entre ces deux événements reste difficile à établir.

Les groupes de tenseurs de contraintes compressifs et décrochants (F et I, respectivement) sont tous deux associés à des $\sigma_1$ horizontaux orientés E-W, donc cohérents avec les orientations des contraintes actuelles (Heidbach et al., 2016 ; Nkodia et al., 2020, 2022). Cependant, nos résultats seuls ne nous permettent pas de dater précisément depuis quand ces états de contraintes décrochants et/ou compressifs ont prévalu. Dans cet hypothèse ces résultats seuls ne permettent de contraindre le calendrier de cette phase compressive mais nous pouvons nous aider des résultats dans le bassin du Bas Congo pour compléter le calendrier de l'histoire complète du bassin de Kwanza.

Dans l'hypothèse d'une profondeur maximale de 2500 m, l'inversion de la rugosité des stylolites sédimentaires dans le bassin de Kwanza permet de contraindre une période de temps à $\sigma_1$ vertical autour de 109-17 Ma. Dans ce cas-ci, on pourrait penser que $\sigma_1$ est toujours resté vertical jusqu'à ~17 Ma. Cette valeur est d'ailleurs très proche de ce qui a été obtenue dans Zeboudj et al., (2023) sur la formation Sendji post-rift dans le bassin du Bas Congo pour la compression actuelle (depuis ~15 Ma). Par contre ces résultats ne permettent pas de contraindre le calendrier de l'état de contrainte au Crétacé supérieur-Paléocène. Une hypothèse alternative est que le reservoir a enregistré des surpressions de fluides dûe au chargment ou à la migration des hydrocarbures permettant ainsi un développement des stylolites pendant toute la durée de l'enfouissment de la formation au cours du temps.

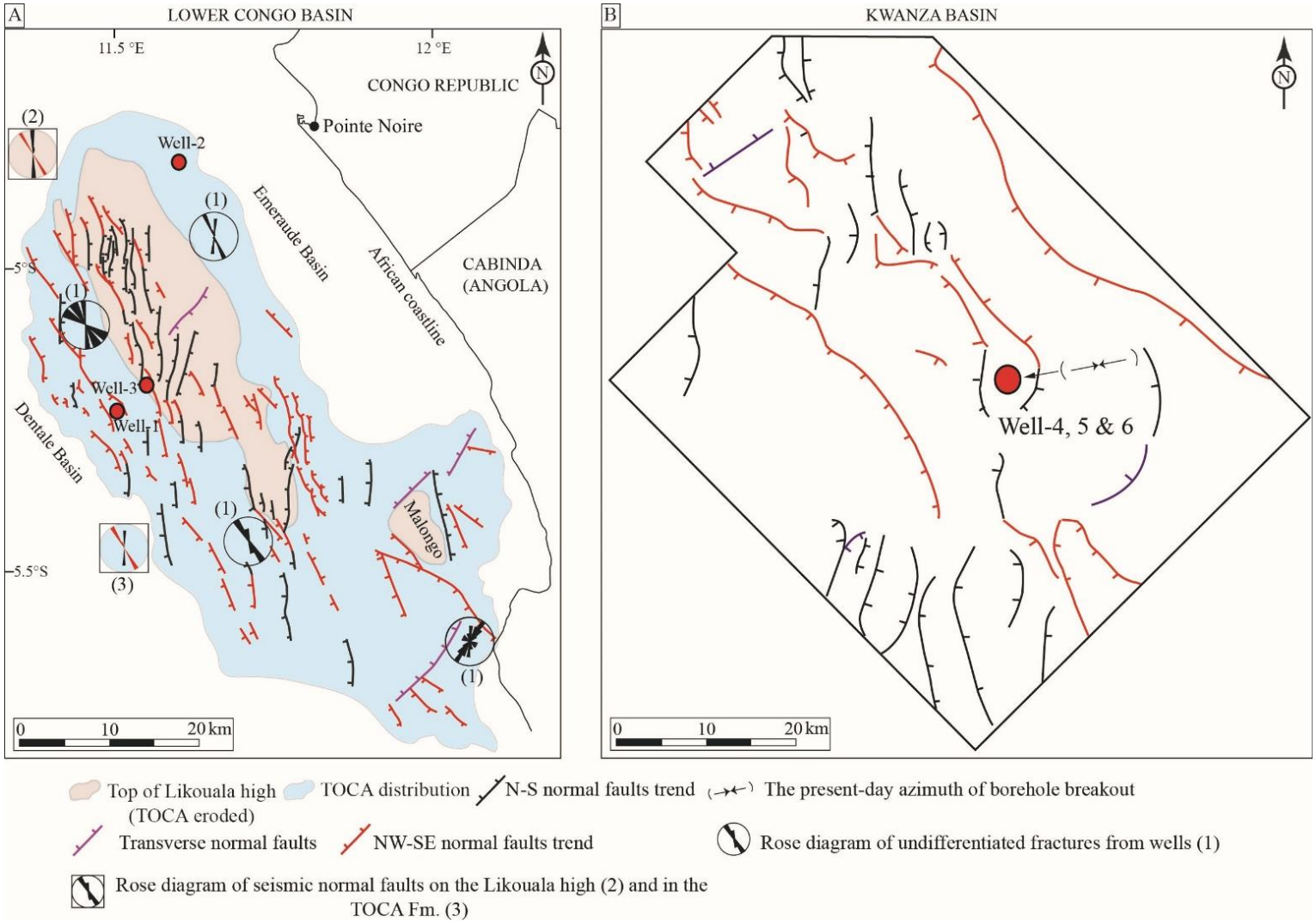


**Figure 20:** Les principales failles normales affectant : (A) le toit de la TOCA et du toit du horst de Likouala modifié d'après un rapport non publié de TotalEnergies dans le bassin du Bas Congo; et (B) le toit de la TOCA dans le bassin de Kwanza modifié d'après Erdi and Jackson, (2021).

Pour vérifier cette hypothèse il faudrait appliquée la méthode d'inversion de la rugosité des stylolites sédimentaires sur des réservoirs exploités ou en exploitation dont le calendrier de la migration des hydrocarbures est bien contraint pour voire si l'arrêt de la stylolitisation est bien coroborer avec l'arrivée des surpressions de fluides dans le réservoir.

## B.3 Transmission des contraintes sur une marge passive

La reconstitution de l'histoire des paléocontraintes sur la marge ouest africaine à partir de l'inversion des macles de la calcite a permis de révéler une histoire des paléocontraintes complexe, polyphasée. Les états de contraintes enregistrés sur la marge ont des origines diverses soit lié à des champs de contraintes locaux, soit lié à des champs de contraintes lointains.

Comme nous l'avons montré, l'état de contrainte enregistré par la formation TOCA (ou équivalent) dans le bassin du Bas Congo et dans le bassin de Kwanza réflète l'effet des états de contraintes associés à des champs de contraintes lointains. La tectonique salifère post-rift a été proposé par Zeboudj et al., (2023) comme ayant un effet local dans la région étudiée c'est-à-dire qui ne soit pas lié aux interactions aux limites de plaques tectoniques. Cet état de contrainte n'a été enregistré que dans les carbonates post-rift de la formation Sendji dans le bassin du Bas Congo et probablement son équivalent (Pinda) dans le bassin de Kwanza. La figure 21 illustre schématiquement la transmission des contraintes sur les deux marges de l'océan Atlantique Sud au cours du temps. Les directions des contraintes enregistrées sur la marge ouest africaine (à partir de l'inversion les macles de la calcite) et la marge Brésilienne (à partir de l'inversion des failles striées) ont été reportées.

Pendant le rifting (Barrémien-Aptien), plusieurs directions sont enregistrées pour l'extension associée à l'ouverture de l'océan Atlantique Sud (Fig. 21). Ces directions sont aussi documentées sur la partie continentale de l'Afrique au Namibie (Salomon et al., 2015). Une explication possible du changement de l'orientation des failles normales et des directions d'extension associées pendant le rifting provient de l'influence de l'héritage structural, en particulier de la géométrie des structures du socle néoprotérozoïque, sur le développement des structures d'extension ultérieures. La chaîne de Mayumbe sous-jacente au bassin du Bas-Congo est dominée par une foliation orientée NNW-SSE (Pedrosa-Soares et al., 1992; Affaton et al., 2016), tandis que la chaîne de Kaoko en Namibie est dominée par une foliation orientée approximativement N-S (par exemple, Passchier et al., 2002; Goscombe et Gray, 2008). Ces zones de faiblesse héritées dans le socle étaient favorablement orientées pour une réactivation

en extension sous une direction d'extension E-W à NE-SW. Nous proposons donc que l'extension E-W (groupe de tenseurs B+C) ait dominé dans le segment central de l'Atlantique Sud pendant les premiers stades de la rupture continentale, en relation avec le développement des failles normales orientées N-S, en raison de la réactivation de zones de faiblesses préexistantes dans le socle. Cette direction d'extension a ensuite évolué au cours du Barrémien pour devenir la direction d'extension régionale NE-SW (groupe de tenseurs A) associée au développement du réseau de failles normales d'orientation NW-SE. Nous proposons que l'extension N-S, qui est cohérente avec les quelques failles normales orientées E-W (à ENE-WSW) qui ont éventuellement joué en tant que failles de transfert (Fig. 20), puisse refléter un état local des contraintes à l'échelle du bassin.

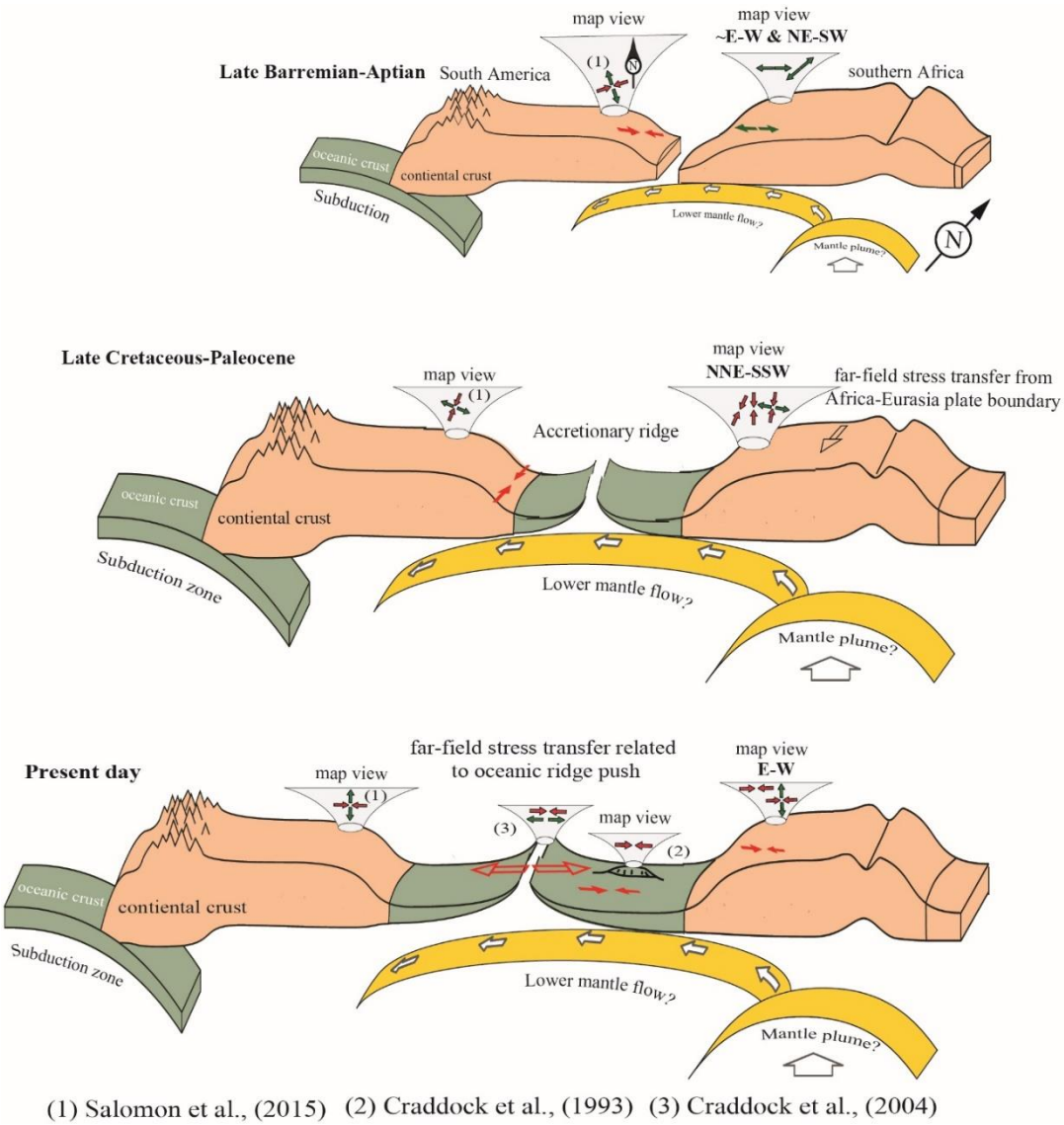


**Figure 21:** Coupes schématique à travers l'Afrique, l'Atlantique Sud et l'Amérique du Sud illustrant les sources des contraintes et les principaux régimes de contraintes obtenues à partir

de l'inversion des macles de la calcite sur la marge ouest africaine. A préciser que l'état de contrainte intraplaque océanique reporté sur la figure à l'actuel, a été obtenu dans l'océan Pacifique (Craddock et al., 1993). Il a été fait mention pour montrer que ce n'est pas une spécificité de la marge Atlantique.

A l'Albien supérieur après le dépôt de la Sendji inférieur, commence une phase de tectonique gravitaire en lien avec le fluage du sel. Le dépôt de la formation Sendji entraîne une expulsion du sel vers l'Est entraînant un épaississement des dépôts salifères dans cette partie distale. La tectonique salifère a atteint son paroxysme pendant le dépôt de la formation Likouala entre 101 et 93.5 Ma, avec le développement de structures en radeaux délimitées par des failles normales listriques. De 80 à 75 Ma, les extensions N-S et E-W enregistrées dans la formation Sendji dans le bassin du Bas Congo n'ont probablement plus été enregistrées (l'activité halocinétique a diminué de manière significative à partir de 80 Ma) mais la contrainte $\sigma_1$ est restée verticale, seul l'enfouissement a pu jouer un rôle à ce stade (Fig. 22). La diminution progressive de l'épaisseur du sel dans la partie proximale de la marge a permis la cohésion du niveau de décollement salifère et un recouplage mécanique progressif des séries supra-salifères avec les séries infra-salifères et le socle. L'état de contrainte local enregistré par la Sendji que nous avons attribué sur la base des orientations des fractures et des tenseurs associés à la tectonique salifère revelé par l'inversion des macles de la calcite et n'ayant pas été enregistré par la formation TOCA infra-salifère, suggère que la transmission des contraintes de la couverture vers la croûte à travers le sel n'a pas été éfficace pendant cette période.

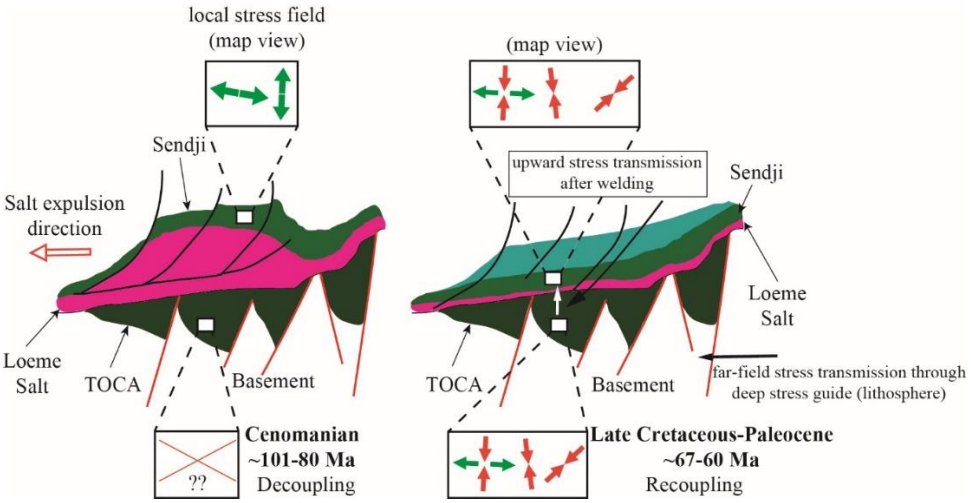


**Figure 22:** Illustration de la transmission des contraintes à travers le sel. A gauche le fluage du sel dû au poids des terrains susjascents induit une tectonique salifère localisée seulement au dessus du sel et l'effet n'a pas été enregistré par la TOCA syn-rift. A droite, recouplage entre les formations infra et supra sel.

Au Crétacé supérieur-Paléocène, l'Afrique est soumise à une compression N-S à NE-SW décrite par Guiraud and Bosworth, (1997) et cette compression a été identifiée par l'inversion des macles de la calcite sur la marge à la fois dans les formations supra et infra salifères.

A l'actuel, l'état de contrainte enregistré sur la marge est compressif probablement lié à la poussée à la ride médio-océanique. Des résultats similaires ont été obtenues par d'autres études à la fois en contexte intraplaque océanique dans le Pacifique (Craddock et al., 1993) et en Islande en contexte de ride médio-océanique (Craddock et al., 2004). Les résultats de l'inversion des macles de la calcite pour la déformation appliquée sur une carotte DSDP forée sur un mont sous-marin dans la plaque Pacifique (Craddock et al., 1993) ont mis en évidence une compression horizontale. Craddock et al., (2004) ont montré à partir de l'inversion des macles de la calcite que l'Islande est soumise à une compression et un raccourcissement perpendiculaire à l'axe de la dorsale médio-Atlantique comme le montrent nos résultats plus au sud sur la marge ouest africaine de l'Atlantique Sud. L'enregistrement d'une compression actuelle liée à l'effet de la poussée à la ride médio-Atlantique à différents endroits (Islande, Congo-Angola) conforte l'hypothèse que l'effet de la poussée à la ride pouvait être transmise dans la croûte terrestre loin de la source.Ces résultats sont confortés aussi par de nombreux « borehole breakouts » de puits pétroliers le long de la marge ouest africaine, de la République du Congo à l'Angola, qui indiquent une contrainte horizontale maximale ($SH_{max}$) orientée entre N50° et N90° sub-perpendiculaire à l'axe de la dorsale.

# Chapitre VI : Discussion méthodologique et développements

Ce chapitre consiste en une discussion méthodologique axée sur les incertitudes et les limites des méthodes paléopiézométriques, ainsi que sur les futurs développements suscités par les interprétations plus poussées des résultats de ce travail de thèse. Ainsi par exemple, on peut s'interroger sur la validité des grandeurs des différentiels de contraintes extensifs enregistrées par les macles de la calcite ainsi que sur le potentiel de l'inversion de la rugosité des stylolites sédimentaires anisotropes.

# 1. Fiabilité de la méthode d'inversion de la rugosité des stylolites (SRIT) et incertitudes associées

## 1.1. Développement des stylolites et impact du faciès sédimentaire sur le résultat de la SRIT

Du point de vue du développement des stylolites, ce travail a permis de montrer que dans les carbonates, les faciès mudstones sont les plus enclins à développer un réseau dense de stylolites que les packstones et les wackestones. Néanmoins, la plus grande densité de stylolites est documentée dans les wackestones boueux et riches en grains, une observation en accord avec celles de Xu et al., (2022).

Les résultats de l'inversion de la rugosité des stylolites mettent en évidence un effet de la texture sédimentaire sur les valeurs de la Lc reconstruites. En effet, les valeurs de la Lc des stylolites de classe 3 sont significativement différentes entre les textures « mud-supported » (mudstones et wackestones) pour lesquelles la valeur de la Lc est plus faible, et les textures « grain supported » (packstones) pour lesquelles la valeur de la Lc est significativement plus élevée. Nous pensons que cela est dû au rôle de la taille des grains dans le développement des stylolites. Koehn et al., (2016) ont démontré que la quantité de dissolution était inversement proportionnelle à la taille des grains du matériau soumis à la dissolution: plus les grains sont petits, plus la compaction chimique est importante, car les petits grains offrent une plus grande surface de réaction dans la roche. Ainsi, dans les carbonates boueux où la taille moyenne des grains est plus petite que dans les carbonates à gros grains, la dissolution pourrait durer plus longtemps, et le SRIT pourrait indiquer de plus grandes profondeurs d'activité de la pression-solution.

Comme le montre les résultats de cette étude, dans le bassin du Bas Congo la stylolitisation s'est arrêté plus tôt dans les carbonates pré-sel par rapport à celles de la Sendji post-sel. Cet'arrêt précoce dans la TOCA s'explique soit par un changement d'orientation de la

contrainte verticale ($\sigma_1$) qui passe à l'horizontal soit par l'arrivée des surpressions de fluide dans le réservoir. Cete dernière hypothèse nous semble plus plausible puisque la formation Sendji revèle que $\sigma_1$ est resté verticale pendant plus longtemps que ce que revèle les stylolites dans la TOCA. A noter que l'arrêt de la stylolitisation dans la TOCA à 95 Ma coincide avec la migration d'hydrocarbures dans le bassin du Bas Congo (Brownfield and Charpentier, 2006). Nous pouvons ainsi supposer que malgré que le réservoir de la TOCA sur le puit étudié soit « tight » les traces de bitumes dans la carotte indique que le réservoir a connu une période de chargement en hydrocarbures et qui aurait pu créer des surpressions de fluides causant ainsi l'arrêt des stylolites dans la TOCA. Si cette hypothèse est correcte, l'inversion des stylolites sédimentaires pourrait-être un marqueur de surpression de fluide. Le peu de données dans le bassin de Kwanza ne nous permet pas d'avoir une compraison fiable avec le bassin adjascent du Bas Congo.

### 1.2.Stylolites sédimentaires « anisotropes et développements futurs

L'analyse des stylolites sédimentaires (BPS) requiert l'hypothèse d'uniaxialité des contraintes dans le plan horizontal ($\sigma_v > \sigma_H = \sigma_h$) et qui est vérifiée par l'analyse de coupes perpendiculaires au plan du stylolite et obliques entre elles.

Nos résultats de SRIT sur la carotte du Well-1 (Fig. 23) montrent que dans le contexte faiblement déformé étudié, où l'enfouissement est la contrainte la plus importante, certains stylolites sédimentaires peuvent montrer une anisotropie mineure des contraintes dans le plan du stylolite (étoile verte sur la fig. 23A). La sinusoïde sur laquelle est reportée la Lc des trois coupes nous permet d'obtenir l'orientation de $\sigma_2$ et $\sigma_3$. Le plan passant par le Lc minimum de la courbe contient la direction de $\sigma_3$ et le plan passant par le Lc maximum contient la direction de $\sigma_2$. Ceci nous permet de définir le régime de contrainte (compressif - $\sigma_v = \sigma_3$, $\sigma_h = \sigma_2$ ou décrochant - $\sigma_v = \sigma_2$, $\sigma_h = \sigma_3$) sous lequel le stylolite tectonique s'est formé pour les stylolites tectoniques (plus de détail dans le chapitre introduction).

Nous avons pu identifier une direction de $\sigma_3$ dans le plan du stylolites orienté ~N30° (étoile verte sur la fig. 23C). Cette direction est compatible avec les résultats de l'étude de l'anisotropie de la susceptibilité magnétique qui indiquent un $K_3$ orienté ~N30° et le groupe de tenseur A (~N45°) obtenu par l'inversion des macles de la calcite qui est celle communément admise dans la littérature comme étant la direction d'extension ayant conduit à l'ouverture de l'océan Atlantique Sud.

Ainsi, pour la première fois, nous avons caractérisé un possible degré d'anisotropie de la contrainte dans les plans des stylolites dits « sédimentaires ». Bien qu'un seul stylolite a montrer une réelle anisotropie des contraintes dans la plan horizontal, l'inversion donne une orientation de contrainte significative au niveau régional. Bien que la capacité de certains stylolites sédimentaires à enregistrer les contraintes extensives doit être confirmée, nos résultats suggèrent que la croissance de certains stylolites sédimentaires a pu être influencée par les contraintes tectoniques régionales, ce qui ouvre la voie à l'élargissement de la boîte à outils disponible pour les reconstructions des paléocontraintes dans les bassins sédimentaires.

## 2. Grandeurs des paléocontraintes à partir des macles de la calcite et implication pour la prédiction des fractures et l'estimation des pressions de fluide

### 2.1.Méthode de quantification des contraintes principales et pressions de fluides

Les valeurs des différentiels de contrainte fournies par les macles de la calcite pour tous les échantillons provenant des deux bassins (sans les incertitudes de ± 30 %) varient entre 30 MPa et 82 MPa pour ($\sigma_1$-$\sigma_3$) et entre 8 MPa et 40 MPa pour ($\sigma_2$-$\sigma_3$) (Fig. 16). Ces valeurs sont combinées aux estimations des contraintes verticales dérivées du modèle d'enfouissement pour estimer la valeur des contraintes principales au moment de la déformation (Lacombe and Laurent, 1992; Lacombe, 2007). Pour cela la valeur de $\sigma_v$ a été calculée au moment où les régimes de contrainte considérés ont prévalu, en supposant soit en condition de pression lithostatique $\sigma_V$=ρgh, soit en condition de pression de fluide hydrostatique: $\sigma_V = (\rho - \rho_w)gh$, avec ρ la densité à sec de la colonne de roche au-dessus (2600 kg.m$^{-3}$), $\rho_w$ la densité de l'eau (1000 kg.m$^{-3}$), g l'accélération du champ gravitationnel (9,81 m.s$^{-2}$), et h la profondeur (m).

Les magnitudes calculées sont ainsi comparées à la résistance intrinsèque de la roche déterminée à partir des tests géomécaniques (c'est-à-dire son enveloppe de rupture) afin d'évaluer la cohérence des résultats des contraintes et d'aider à prédire si des fractures peuvent être attendues dans le réservoir dans les régimes de contraintes reconstruits et potentiellement des surpressions de fluides dans le système, avec la condition de tangence du cercle de Mohr ($\sigma_1$-$\sigma_3$) à l'enveloppe de rupture comme indicative de la néorupture de la roche (Fig. 24).

Cette combinaison de méthodes a été utilisée pour déterminer les contraintes effectives dans le bassin de Paris, France (Lacombe and Laurent, 1992); et dans plusieurs basins d'avant-pays: à Taiwan (Lacombe, 2001); dans le bassin de Bighorn, au Wyoming USA (Amrouch et al.,

2011; Beaudoin et al., 2012); en Italie (Beaudoin et al., 2016) ; en Australie (Kulikowski and Amrouch, 2018).

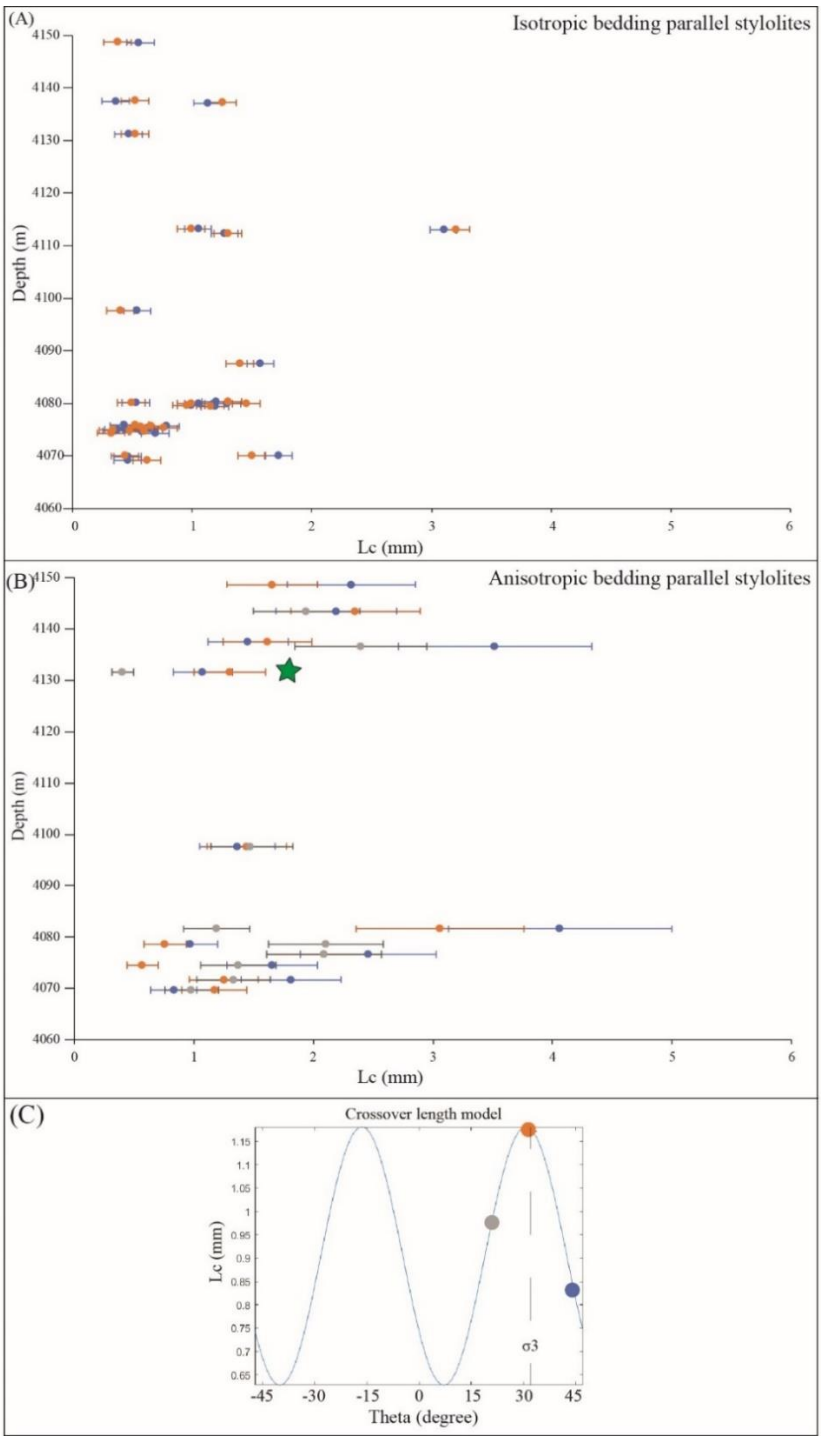


**Figure 23:** (A & B) Représentation de la Lc des 3 coupes réalisées en fonction de la profondeur pour des stylolites sédimetaires (BPS). L'étoile verte montre le stylolite qui montre une anisotropie des contraintes. (C) Représentation de la fonction sinusoïdale calculée de la longueur de coupure en fonction de l'angle de coupe d'observation du stylolite. Les incertitudes de ± 23% sur la Lc ont été aussi reportées.

Il est possible de déduire la pression de fluide si la profondeur d'enfouissement au moment du maclage est connue (Lacombe and Laurent, 1992; Lacombe, 2007; Amrouch et al., 2011; Beaudoin et al., 2014). Cela a permis de contraindre le calendrier de la déformation (c'est-à-dire la chronologie des tenseurs de contraintes enregistrée par les macles) et de déduire les profondeurs d'enfouissement maximale. Pour chacun des tenseurs de contraintes enregistré, la contrainte lithostatique verticale et la contrainte effective verticale avec une pression de fluide hydrostatique ont été calculées et ont été utilisé sur la figure 24.

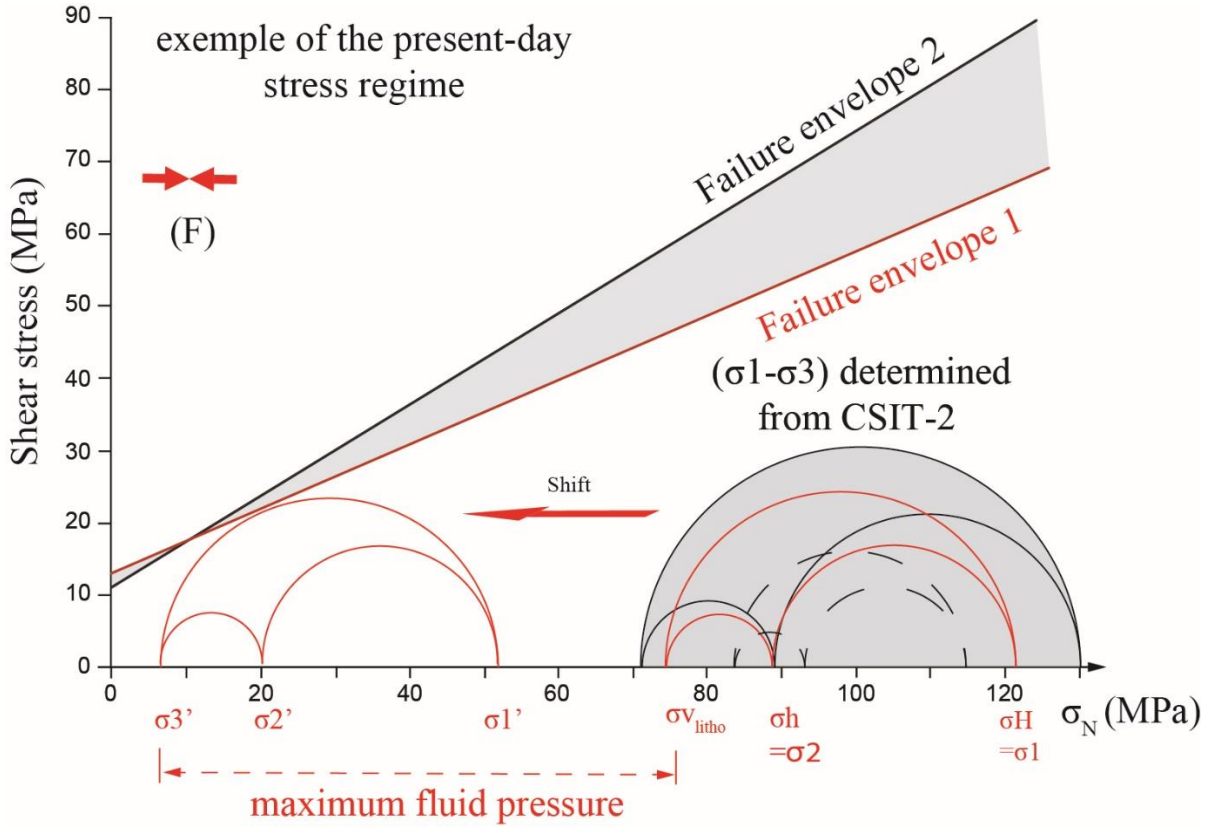


**Figure 24:** Illustration théorique de l'approche couplée du diagramme de Mohr pour obtenir le tenseur de contrainte effectif complet. Le différentiel des contraintes obtenues par l'inversion des macles est representé pour le groupe de tenseurs F (en rouge) avec les incertitudes (±30%) inférieur (en pointillé noir) et supérieur (en noir grisé).

Après que la contrainte lithostatique ait été calculée et le différentiel de contraintes obtenu par l'inversion des macles de la calcite soit reporté sur le diagramme, la valeur maximale de la pression de fluide qui aurait permit de fracturer est obtenue en translatant le cercle Mohr vers la gauche. Dans cet exemple on voit que la pression de fluide maximale permettant d'atteindre la fracturation est très proche de la contrainte lithostatique.

## 2.2. Application au réservoir de la TOCA (Bas Congo et Kwanza) et comparaison avec la formation Sendji

L'état de contrainte extensif du Crétacé inférieur a été enregistré par les macles de la calcite (groupes de tenseurs A, B+C et D) lorsque la TOCA était enfouie à une profondeur maximale de 500-600 mètres dans le bassin de Kwanza et entre 500-1000 mètres dans le bassin du Bas Congo.

Les magnitudes des différentiels de contraintes associées aux tenseurs extensifs obtenues par l'inversion des macles donnent des valeurs élevées (avec une moyenne arithmétique autour de 40 ± 10 MPa pour ($\sigma_1$-$\sigma_3$)) conduisant ainsi à une contrainte effective $\sigma_3$ négative, bien au-delà des valeurs que pourrait supporter les roches en tension. En extension, l'inversion des macles de la calcite renvoient systématiquement des valeurs de différentiels de contraintes dans la même gamme que celle observées sur la marge passive ouest africaine. Cette observation pourrait suggérer une surestimation des différentiels de contraintes par la méthode en contexte extensifs. Lacombe et al., (1990, 1994) ont déjà rapporté des grandeurs de différentiels de contraintes anormalement élevées associées à l'extension Éocène-Oligocène dans le bassin de Paris, que Lacombe et Laurent (1992) ont provisoirement reliées à la superposition de tenseurs de paléocontraintes extensif que la méthode pouvait difficilement discriminer.

Une explication possible est que ces valeurs élevées pourraient résulter de l'effet de la superposition de différentiels de contraintes lié à l'extension syn-rift et du différentiel de contraintes lié à l'enfouissement post-rift ultérieur sous un $\sigma_1$ vertical. Pour tester cette hypothèse et estimer la contribution théorique probable de l'enfouissement post-rift sur les valeurs des différentiels de contraintes obtenus par l'inversion des macles de la calcite pour les groupes de tenseurs extensifs, nous avons supposé que l'effet de l'enfouissement peut être approximé par un état de contrainte avec $\sigma_1 > \sigma_h = \sigma_H (=\sigma_2=\sigma_3)$. Cette hypothèse se vérifie plus probablement pendant l'enfouissement de la formation TOCA juste après le rifting avant que $\sigma_1$ ne change d'une position verticale à une position horizontale. Par contre, pendant le rifting, cette hypothèse est en théorie incorrecte puisque la paléopiézométrie basée sur l'inversion des des macles de la calcite indique que les différentiels de contraintes ($\sigma_2$-$\sigma_3$) ne sont pas égaux et donnent des moyenne arithmétiques d'environ 20 ± 10 MPa.

Bien qu'il soit impossible d'établir dans quelle mesure le maclage causé par le différentiel des contraintes liée à l'enfouissement post-rift a pu se cumuler avec le maclage causé

par le différentiel des contraintes liée à l'extension pour restituer les fortes valeurs de différentiel des contraintes reconstituées pour les groupes de tenseurs extensifs A et B+C, cette estimation approximative suggère que l'effet de l'enfouissement pourrait fournir une explication raisonnable de la surestimation probable des valeurs des différentiels de contraintes liée à l'extension ($\sigma_1$-$\sigma_3$) à l'aide de la paléopiézométrie du maclage de la calcite.

A ce jour cela reste un problème non résolu qui nécessiterait un développement méthodologique approfondi. Il est possible que les différentiels des contraintes reflètent ceux accompagnant le rifting auxquels se superposent ceux liés à la compaction / enfouissement post-rift, qui sont coaxiaux. Une possible solution pour résoudre ce problème est de réaliser une étude expérimentale de déformation mécanique sous presse d'échantillons naturels dans le but de simuler expérimentalement l'effet (1) du rifting et (2) de l'enfouissement post-rift sur les mêmes échantillons et réaliser une étude paléopiézométrique macles de la calcite sur les échantillons déformés afin: (1) de préciser si les différentiels de contraintes obtenus sur les échantillons correspondent ou non à la somme des différentiels de contraintes des scénarios (1 & 2) à la profondeur finale atteinte par les échantillons, et (2) de prédire la contribution relative des deux effets sur le résultat final.

Par contre, les magnitudes des différentiels de contraintes déduites de la paléopiézométrie des macles de la calcite pour les régimes de contraintes compressifs et décrochants sont cohérentes avec les estimations indépendantes d'autres indicateurs de contraintes tels que l'inversion des failles striées et en accord avec les contraintes obtenues dans la croûte superficielle (Lacombe, 2001, 2007; Beaudoin and Lacombe, 2018) en contexte d'avant-pays orogéniques.

La figure 24 montre un exemple d'estimation des pressions de fluide à l'aide des grandeurs des différentiels de contrainte et de la courbe de rupture de la TOCA en partant de la contrainte lithostatique. Sur cet exemple, pour que le groupe de tenseur F puisse avoir créé des failles, la pression de fluide maximale devrait être presque égale à la pression de fluide lithostatique même en considérant l'incertitude la plus élévée sur la valeur des différentiels de contraintes. La méthode a ensuite été appliquée sur toutes les carotes de la TOCA dans le bassin du Bas Congo et sur les carottes de la formation équivalente de la TOCA dans le bassin de Kwanza pour estimer les potentielles surpressions de fluides et les contraintes effectives associées à chaque phase de déformation au cours du temps.

La même approche a ensuite été testée sur la formation Sendji post-rift sur la même phase de déformation entregistré par les macles de la calcite dans la TOCA et dans la Sendji c'est -à- dire la compression récente à actuelle. La courbe de résistance de la Sendji est moins raide que celle obtenue pour la TOCA ce qui veut dire qu'elle est moins résistante que la TOCA. En considérant la profondeur déduite du modèle d'enfouissement réalisé sur les différents puits dans les deux formations et les différentiels des contraintes obtenues par l'inversion des macles de la calcite, la contrainte verticale (lithostatique et hydrostatique) a été calculée pour chacune cette phase de compression. En réportant cette valeur sur le diagramme de Mohr ainsi que les diffenrentiels de contraintes, la valeur maximale de la surpression de fluide est deduite du diagramme (Fig. 25A & 25C pour la TOCA et la Sendji respectivement dans le bassin du Bas Congo et pour les carbonates pré-sel (équivalent TOCA) dans le bassin de Kwanza (Fig. 25B).

Le fait que nous ayons eu des valeurs qui ne réflètent pas la réalité dans la TOCA pourrait s'expliquer par le fait que la résistance de la TOCA soit très élévée et que l'enfouissement soit la plus importante.

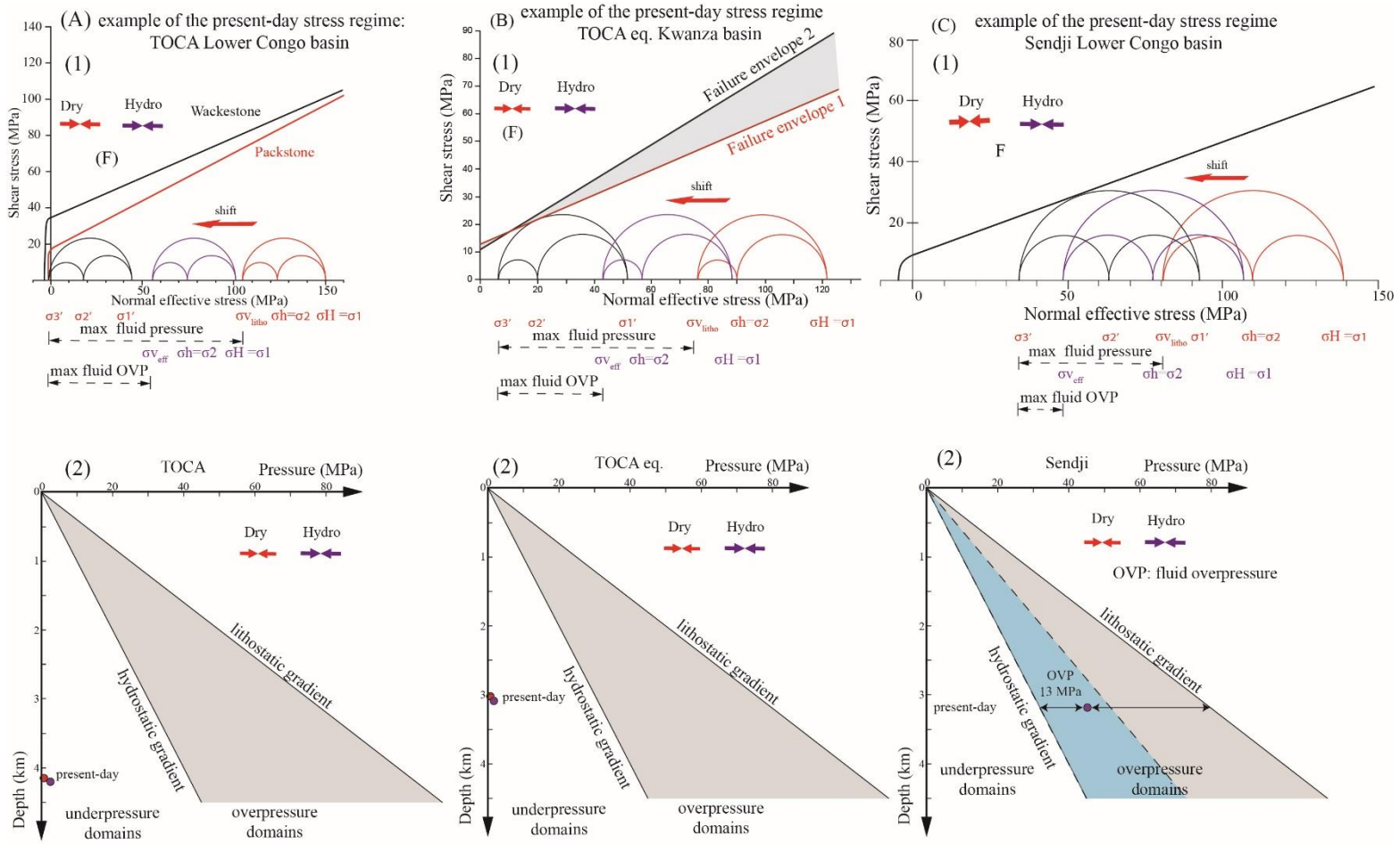


**Figure 25:** Répresentation de l'approche combinée diagramme de Mohr pour l'estimation des pressions de fluide maximale pouvant permettre la fracturation dans les réservoirs de la TOCA syn-rift (A1), de la Senfji post-rift (B1) et des carbonates pré-sel dans le bassin de Kwanza (C1). Les figures (A2, B2 et C2) présente schématiquement le résultat de  l'estimation des pressions de fluides maximales dans ces reservoirs.

# Chapitre VI : Conclusions

Cette étude menée sur les bassins du Bas Congo et de Kwanza constitue un exemple unique d'étude intégrée proposant une approche paléopiézométrique fondée sur l'inversion des macles de la calcite pour les paléocontraintes et l'inversion de la rugosité des stylolites pour les paléo-enfouissement, combinée avec l'analyse des données de la fracturation et un modèle d'enfouissement. Cette étude est une première aussi par le contexte de marge passive étudié avec cette approche et par le matériel utilisé pour cette étude, accessible seulement grâce aux forages pétroliers profonds effectués sur la marge. Les principaux résultats de ce travail sont décrits et discutés dans les chapitres précédents 2 3 et 4, de ce fait ne seront pas repris dans cette partie.

Pour rappel les objectifs de la thèse s'articulaient en trois principaux volets, chacun des volets est présenté sous forme de chapitre dont les résultats sont décrits sous forme d'articles publiés ou en cours de révision.

## 1. L'inversion des macles de la calcite

Cette étude renforce les études précédentes sur l'utilisation de l'inversion des macles de la calcite en tant que paléopiézomètre pour déchiffrer l'histoire des paléocontraintes (orientation des principales contraintes et magnitude des différentiels des contraintes) enregistrées par une formation carbonatée au cours du temps. Ce travail est une première, en effet c'est la première fois que l'analyse paléopiézométrique basée sur l'inversion des macles de la calcite pour reconstruire l'histoire des paléocontraintes est appliquée en contexte de marge passive.

Les macles de la calcite ont enregistré une histoire des paléocontraintes polyphasée. La comparaison de nos résultats avec ceux de la littérature sur le domaine continental à partir de l'inversion des failles striées, a permit d'affecter les tenseurs obtenus dans cette étude aux différentes phases de déformation tectonique ayant affectée le continent africain et sa marge ouest au cours du temps depuis l'ouverture de l'Atlantique Sud.

Ce travail a montré la robustesse de la méthode et sa capacité à fournir des résultats fiables et cohérents pour préciser l'histoire tectonique de la région. Avoir un outil qui permet de reconstruire l'histoire des paléocontraintes en orientation et en grandeur sur de petits volumes de roche comme les carottes est un atout majeur dans la compréhension globale de l'histoire tectonique de la marge où les seules données disponibles reposent en majeure partie sur les méthodes sismiques. La cohérence entre les résultats des macles de la calcite et les données de paléocontraintes régionales renforcent la fiabilité des résultats issus de l'inversion des macles

de la calcite. En plus de l'apport sur la compréhension de l'histoire tectonique régionale, l'inversion des macles de la calcite sur des formations infra et supra salifères a permis de monter qu'au cours du temps sur une marge passive où des dépôts salifères sont présents, les phénomènes de couplage ou de découplage entre les formations infra et supra salifère peuvent être enregistrés par les macles de la calcite. Cela a permis d'appréhender la façon dont les contraintes sont transmises à travers le sel.

Les états de contraintes enregistrés dans la formation Sendji et qui n'est pas enregistré par les carbonates pré-sel, a été interprété comme étant associé à la tectonique salifère sur la base de la compatibilité entre les groupes de tenseurs et l'orientation des fractures sur la carotte de la Sendji et les failles normales listrics.

## 2. L'inversion de la rugosité des stylolites

L'inversion de la rugosité des stylolites sédimentaires a permis d'obtenir la contrainte verticale. Cette contrainte verticale est par la suite convertie en profondeur pour obtenir les profondeurs maximales de dissolution le long de la trace de chaque stylolite traité. La combinaison de cette méthode avec un modèle d'enfouissement sur lequel les profondeurs maximales de dissolution ont été reportées a permis de définir les périodes de temps pendant lesquelles la dissolution liée à la compaction/l'enfouissement a été active et par conséquent les périodes où la contrainte principale $\sigma_1$ était verticale. Cette information apporte une contrainte sur la chronologie des tenseurs de contraintes obtenues à partir de l'inversion des macles de la calcite. Ce travail de thèse a montré aussi pour la première fois que certains stylolites supposés être des stylolites sédimentaires (contraintes horizontales isotrope) se développant en contexte tectonique extensif pourraient enregistrer pro parte la contrainte tectonique et présenter ainsi une légère anisotropie de contraintes horizontales dans le plan du stylolite. Cette partie mérite un développement méthodologique pour comprendre comment ce type de stylolites (sédimentaire 'anisotrope') pourrait être utilisé en terme d'inversion avec de nouvelles équations plus adaptées à ces stylolites sédimentaires 'anisotropes' Nous avons montré aussi que des stylolites faiblement anisotropes peuvent potentiellement être sensibles à une permutation entre $\sigma_2$ et $\sigma_3$, par conséquent un changement de régime de contrainte passant de décrochant à compressif vice versa.

## 3. La combinaison de l'inversion des macles de la calcite et de la rugosité des stylolites, de la fracturation et des essais géomécaniques

La combinaison de l'inversion des macles de la calcite qui permet d'obtenir l'orientation des contraintes et les grandeurs des différentiels de contraintes avec l'inversion de la rugosité des stylolites sédimentaires qui permet d'obtenir les périodes de temps où le $\sigma_1$ est verticale et les résultats de l'analyse des données de la fracturation (failles et/ou veines) sur les carottes ou à partir de l'imagerie de puits ainsi que les résultats des essais géomécaniques (courbe de rupture intrinsèque de la roche intacte) permet de contraindre l'histoire complète des paléocontraintes, d'attribuer un âge aux épisodes de déformations enregistrées par les macles de la calcite. Elle a aussi permis de proposer un schéma prédictif de la fracturation et surtout d'estimer les potentielles (sur)pressions de fluide au cours de la déformation si la profondeur d'enfouissement au moment de la déformation est connue.

## 4. Caractérisation du calendrier de la destruction de la porosité d'un réservoir carbonaté très enfouis.

Notre étude s'est concentrée sur les carbonates du Barrémien syn-rift (130-125 Ma) de la formation TOCA (ou équivalent) qui présentent des porosités actuelles extrêmement variables à l'échelle régionale, avec des valeurs allant de 1% à 30% selon les textures de dépôt, la localisation dans le bassin et l'intensité des processus diagénétiques. De ce fait il était particulièrement important de comprendre et de quantifier les processus diagénétiques, qui ont été les plus préjudiciables à la qualité des réservoirs, conduisant à des porosités inférieures à 10% (le seuil généralement admis pour une production économique). Dans ce travail, nous présentons une approche multi-proxy novatrice sans précédent qui combine des estimations semi-quantitatives de la proportion et le calendrier de la destruction de la porosité liée à (1) la compaction mécanique en utilisant un modèle de bassin, (2) la précipitation diagénétique du ciment dans les pores, au moyen de l'analyse d'images en lame mince, la datation géochronologique U-Pb et de la microthermométrie des inclusions fluides, et (3) la pression-solution basée sur la quantification de la compaction chimique le long des stylolites couplée à un modèle d'enfouissement. Cette étude a permis de déterminer l'âge absolu des principaux processus diagénétiques contrôlant les propriétés réservoirs : la compaction mécanique (~130 - 127 Ma à partir du modèle du bassin), la cimentation précoce (~125 ± 5 Ma à partir de la datation U-Pb du ciment de calcite diagénétique) et la compaction chimique (~117-95 Ma à partir de l'inversion de la rugosité des stylolites sédimentaires). Ceci fournit de nouvelles

contraintes sur la séquence diagénétique de la TOCA et une meilleure compréhension des processus diagénétiques et de leur chronologie absolue, ce qui est une information clé pour une meilleure prédiction des propriétés du réservoir dans l'exploration. Cette étude a montré aussi que tous les processus diagénétiques se sont produits tôt dans l'histoire de l'enfouissement de la formation TOCA, de telle sorte que la TOCA a acquis ses propriétés réservoir au cours des 35 premiers Ma suivant son dépôt. Cette étude a aussi montré que la migration des hydrocarbures dans le réservoir de la TOCA s'est produite après que la porosité initiale ait été largement détruite, ce qui explique le caractère 'tight' du réservoir de la TOCA dans le Well-1. Cette migration d'hydrocarbures est également contemporaine de la fin du développement des stylolites sédimentaires à ~95 Ma, de sorte que le rôle de l'augmentation de la pression de fluide locale (c'est-à-dire à l'échelle de l'interface de dissolution) par l'arrivée des hydrocarbures dans le réservoir sur l'arrêt du développement des stylolites peut être questionné.

## 5. Conclusions régionales

Ce travail de thèse apporte de nouvelles contraintes dans la compréhension de l'histoire tectonique et de l'Atlantique Sud en générale et de la marge ouest africaine du segment central en particulier. L'approche couplée de la paléopiézométrie des macles de la calcite et des stylolites combinée avec la fracturation, l'anisotropie de la susceptibilité magnétique et le modèle d'enfouissement a permis de déchiffrer l'histoire des paléocontraintes dans les bassins sédimentaires offshores du Bas Congo et de Kwanza cohérent avec les paléocontraintes enregistrés sur la partie continentale. Les macles de la calcite dans la matrice ont enregistré quatre phases de déformations tectoniques distinctes.

Une première phase extensive (130-95 Ma) qui a été attribuée sur la base des orientations (~E-W puis NE-SW) à l'épisode de rifting ayant conduit à l'ouverture de l'Atlantique Sud. Une seconde phase compressive/décrochante (~67-60 Ma) attribuée à la compression (N-S à NE-SW) générée par les interactions aux frontières de plaques tectoniques Afrique-Arabie et transmise à travers la plaque africaine jusqu'à la marge. Une troisième phase compressive/décrochant (depuis ~15 Ma) compatible avec le régime compressif/décrochant actuel (~E-W) probablement lié à l'effet de la poussée à la ride médio-Atlantique. Ces trois phases reflètent des contraintes d'origine lointaines en lien avec les interactions aux limites de plaques tectoniques. Une quatrième phase tectonique extension (101-80 Ma) $\sigma_3$ horizontale orienté ~N-S et E-W locale est enregistrée par la formations supra-salifère Sendji et attribuée à la tectonique gravitaire liée au fluage du sel.

# Références bibliographiques

Aubourg, C., Rochette, P., Stéphan, J. F., Popoff, M., & Chabert-Pelline, C. (1999). The magnetic fabric of weakly deformed Late Jurassic shales from the southern subalpines chains (French Alps): evidence for SW-directed tectonic transport direction. Tectonophysics, 307(1-2), 15-31.

Aubourg C. et Robion P., 2002. Composite ferromagnetic fabrics (magnetite, greigite) measured by AMS and partial AARM in weakly strained sandstones from western Makran: Geophysical Journal International, 151, 729-737.

Aubourg C., Smith B., Bakhtari H., Guya N., Eshraghi S. A., Lallemant S., Molinaro M., Braud X. et Delaunay S., 2004. Post Miocene Shortening Pictured by Magnetic Fabric Across The Zagros-Makran Syntaxis (Iran), Orogenic curvatures ; integrating paleomagnetic and structural analyses), Special paper - Geological Society of America, 1740.

Allen, P. A., & Allen, J. R. (2013). Basin analysis: Principles and application to petroleum play assessment. John Wiley & Sons.

Amrouch K., Lacombe O., Bellahsen N., Daniel J.-M. & Callot J.P., 2010, Stress/strain patterns, kinematics and deformation mechanisms in a basement-cored anticline: Sheep Mountain anticline (Wyoming, USA). Tectonics, 29, TC1005

Amrouch K., Robion P., Callot J.-P., Lacombe O., Daniel J.-M. et Bellahsen N., 2010b. Constraints on deformation mechanisms during folding based on rock physical properties: Example of Sheep Mountain anticline (Wyoming, USA). Journal Geophysical International, 182,1105-1123.

Amrouch, K., Beaudoin, N., Lacombe, O., Bellahsen, N., & Daniel, J. M. 2011. Paleostress magnitudes in folded sedimentary rocks. Geophysical Research Letters, 38(17).

Anka, Z., Seranne, M., & Di Primio, R. (2010). Evidence of a large upper-Cretaceous depocentre across the Continent-Ocean boundary of the Congo-Angola basin. Implications for palaeo-drainage and potential ultra-deep source rocks. Marine and Petroleum Geology, 27(3), 601-611.

Aslanian, D., Moulin, M., Olivet, J. L., Unternehr, P., Matias, L., Bache, F., Rabineau, M., Klingelheofer, F., Contrucci, I., & Labails, C. 2009. Brazilian and African passive margins

of the Central Segment of the South Atlantic Ocean: Kinematic constraints. Tectonophysics, 468(1-4), 98-112.

Asmus, H. E., & Ponte, F. C. 1973. The Brazilian marginal basins. In The South Atlantic (87-133). Springer, Boston, MA.

Averbuch O. Frizon de Lamotte D. et Kissel C., 1992. Magnetic fabric as a structural indicator of the deformation path within a fold-thrust structure: a test case from the Corbières (NE Pyrenees, France) Journal of Structural Geology, 14 (4), 461-474

Bah, B., Beaudoin, N.E., Lacombe, O., Girard, J.-P., Gout, C., Godeau, N., Deschamps, P. 2023. Multi-proxy reconstruction of the burial history and porosity evolution of the TOCA carbonate formation in the Lower Congo basin (South West Africa), Marine and Petroleum Geology, 148, 106018.

Bakhtari H., Frizon de Lamotte D., Aubourg C. et Hassanzadeh J., 1998. Magnetic fabric of Tertiary sandstones from the Arc of Fars (Eastern Zagros, Iran): Tectonophysics, 284, 299316.

Balen, R.V. and Cloetingh, S., 1995. Neural network analyses of stress induced overpressures in the Pannonian basin. Geophys. J. Int., 121: 532-544.

Bate, R. H. 1999. Non-marine ostracod assemblages of the Pre-Salt rift basins of West Africa and their role in sequence stratigraphy. Geological Society, London, Special Publications, 153(1), 283-292.

Baudouy, S., & Legorjus, C. (1991). Sendji field--People's Republic of Congo, Congo Basin

Beaudoin, N., Leprêtre, R., Bellahsen, N., Lacombe, O., Amrouch, K., Callot, J. P., ... & Daniel, J. M. 2012. Structural and microstructural evolution of the Rattlesnake Mountain Anticline (Wyoming, USA): new insights into the Sevier and Laramide orogenic stress build-up in the Bighorn Basin. Tectonophysics, 576, 20-45.

Beaudoin, N., Lacombe, O., Bellahsen, N., Amrouch, K., & Daniel, J. M. 2014. Evolution of pore-fluid pressure during folding and basin contraction in overpressured reservoirs: Insights from the Madison–Phosphoria carbonate formations in the Bighorn Basin (Wyoming, USA). Marine and Petroleum Geology, 55, 214-229.

Beaudoin, N., Koehn, D., Lacombe, O., Lecouty, A., Billi, A., Aharonov, E., & Parlangeau, C. (2016). Fingerprinting stress: Stylolite and calcite twinning paleopiezometry revealing the complexity of progressive stress patterns during folding—The case of the Monte Nero anticline in the Apennines, Italy. Tectonics, 35(7), 1687-1712.

Beaudoin, N., Lacombe, O., 2018. Recent and future trends in paleopiezometry in the diagenetic domain: insights into the tectonic paleostress and burial depth history of fold-and-thrust belts and sedimentary basins. Journal of Structural Geology 114, 357–365.

Beglinger, S. E., Doust, H., & Cloetingh, S. 2012. Relating petroleum system and play development to basin evolution: West African South Atlantic basins. Marine and Petroleum Geology, 30(1), 1-25.

Borradaile G.J. et Henry B., 1997. Tectonic applications of magnetic susceptibility and its anisotropy. Earth Sci. Rev. 42, 49–93.

Bian, D., Zhao, L., Chen, Y., Yu, L., & Fan, Z. (2011). Fracture characteristics and genetic mechanism of overpressure carbonate reservoirs: Taking the Kenkiyak Oilfield in Kazakhstan as an example. Petroleum Exploration and Development, 38(4), 394-399.

Bredehoeft, J.D., Wesley, J.B., Fouch, T.D., 1994. Simulations of the origin of fluid pressure, fracture generation, and movement of fluids in the Uinta basin, Utah. AAPG Bull. 78, 1729-1747.

Brice, S. E., Cochran, M. D., Pardo, G., & Edwards, A. D. 1982. Tectonics and sedimentation of the South Atlantic Rift Sequence: Cabinda, Angola: rifted margins: field investigations of margin structure and stratigraphy. In Studies in Continental Margin Geology, AAPG Special Volumes, 5-18.

Brownfield, M.E., Charpentier, R.R. 2006. Geology and total petroleum systems of the West-Central Coastal Province (7203), West Africa. United States Geological Survey Bulletin, 2207-B, 52.

Burwood, R. 1999. Angola: source rock control for Lower Congo Coastal and Kwanza Basin petroleum systems. Geological Society, London, Special Publications, 153(1), 181-194.

Burgin, H. B., Amrouch, K., Rajabi, M., Kulikowski, D., & Holford, S. P. (2018). Determining paleo-structural environments through natural fracture and calcite twin analyses: a case study in the Otway Basin, Australia. The APPEA Journal, 58(1), 238-254.

Cainelli, C., & Mohriak, W. U. (1999). Some remarks on the evolution of sedimentary basins along the Eastern Brazilian continental margin. Episodes Journal of International Geoscience, 22(3), 206-216.

Charpentier, J. F., Fadli, N., & Jennane, J. (2003). Study of ironless permanent magnet devices being both a coupling and an axial bearing for naval propulsion. IEEE transactions on magnetics, 39(5), 3235-3237.

Chuhan, F. A., Kjeldstad, A., Bjørlykke, K., & Høeg, K. (2002). Porosity loss in sand by grain crushing—Experimental evidence and relevance to reservoir quality. Marine and Petroleum Geology, 19(1), 39-53.

Contrucci, I., Matias, L., Moulin, M., Géli, L., Klingelhofer, F., Nouzé, H., Aslanian, D., Olivet, J. L., Réhault, J. P., & Sibuet, J. C. 2004. Deep structure of the West African continental margin (Congo, Zaïre, Angola), between 5 S and 8 S, from reflection/refraction seismics and gravity data. Geophysical Journal International, 158(2), 529-553.

Craddock, J. P., Jackson, M., van der Pluijm, B. A., & Versical, R. T. 1993. Regional shortening fabrics in eastern North America: Far-field stress transmission from the Appalachian-Ouachita Orogenic Belt. *Tectonics, 12*(1), 257-264.

Craddock, J. P., Farris, D. W., & Roberson, A. 2004. Calcite-twinning constraints on stress-strain fields along the Mid-Atlantic Ridge, Iceland. Geology, 32(1), 49-52.

Delpomdor, F., Tack, L., & Préat, A. 2008. Microstructures in the Neoproterozoic tillites around the Congo River Basin (CRB), Democratic Republic of Congo (DRC): Comparison with the Karoo tillites from the Dekese borehole in the CRB. In 22nd Colloquium of African Geology (CAG22) & 13th Conference of the Geological Society of Africa (GSAf13) (p. 108).

Delvaux, D., Maddaloni, F., Tesauro, M., Braitenberg, C., 2021. The Congo Basin: Stratigraphy and subsurface structure defined by regional seismic reflection, refraction and well data. Global and Planetary Change 198(2), 103407.

Duan, W., Li, C. F., Luo, C., Chen, X. G., & Bao, X. (2018). Effect of formation overpressure on the reservoir diagenesis and its petroleum geological significance for the DF11 block of the Yinggehai Basin, the South China Sea. Marine and Petroleum Geology, 97, 49-65.

Ebner, M., Koehn, D., Toussaint, R., & Renard, F. 2009a. The influence of rock heterogeneity on the scaling properties of simulated and natural stylolites. Journal of Structural geology, 31(1), 72-82.

Ebner, M., Koehn, D., Toussaint, R., Renard, F., & Schmittbuhl, J. 2009b. Stress sensitivity of stylolite morphology. Earth and Planetary Science Letters, 277(3-4), 394-398.

Ebner, M., Piazolo, S., Renard, F., & Koehn, D. 2010a. Stylolite interfaces and surrounding matrix material: Nature and role of heterogeneities in roughness and microstructural development. Journal of Structural Geology, 32(8), 1070-1084.

Ebner, M., Toussaint, R., Schmittbuhl, J., Koehn, D., & Bons, P. 2010b. Anisotropic scaling of tectonic stylolites: A fossilized signature of the stress field? Journal of Geophysical Research: Solid Earth, 115(B6).

Ehrenberg, S. N., Nadeau, P. H., & Steen, Ø. 2009. Petroleum reservoir porosity versus depth: Influence of geological age. AAPG bulletin, 93(10), 1281-1296.

Erdi, A., & Jackson, C. A. L. (2021). What controls salt-detached contraction in the translational domain of the outer Kwanza Basin, offshore Angola?. Basin Research, 33(3), 1880-1905.

Etchecopar, A., 1984. Etudes des états de contrainte en tectonique cassante et simulations de déformations plastiques (approche mathématiques). Université des Sciences Techniques du Languedoc.

Frazer, M., Whitaker, F., & Hollis, C. 2014. Fluid expulsion from overpressured basins: Implications for Pb–Zn mineralisation and dolomitisation of the East Midlands platform, northern England. Marine and Petroleum Geology, 55, 68-86.

Ferrill, D. A., Morris, A. P., Evans, M. A., Burkhard, M., Groshong Jr, R. H., & Onasch, C. M. 2004. Calcite twin morphology: a low-temperature deformation geothermometer. Journal of structural Geology, 26(8), 1521-1529.

Gluyas, J. & Swarbrick, R. 2004. Petroleum Geoscience. Blackwell, Oxford.

Gradstein, F. M., Ogg, J. G., Smith, A. G., Bleeker, W., & Lourens, L. J. 2004. A new geologic time scale, with special reference to Precambrian and Neogene. Episodes, 27(2), 83-100.

Grosdidier, E., Braccini, E., Dupont, G., Moron, J.M., 1996. Biozonation du Crétacé Inférieur non marin des bassins du Gabon et du Congo. Bulletin des Centres de recherches exploration-production Elf-Aquitaine. Memoir (16), 67–82.

Green, D. H., & Wang, H. F. 1986. Fluid pressure response to undrained compression in saturated sedimentary rock. Geophysics, 51(4), 948-956.

Guiraud, R., & Bosworth, W. 1997. Senonian basin inversion and rejuvenation of rifting in Africa and Arabia: synthesis and implications to plate-scale tectonics. Tectonophysics, 282(1-4), 39-82

Guo, X.W., He, S., Liu, K.Y., Song, G.Q.,Wang, X.J., Shi, Z.S., 2010. Oil generation as the dominant overpressure mechanism in the Cenozoic Dongying Depression, Bohai Bay Basin, China. AAPG Bull. 94, 1859-1881.

Guo, X., Liu, K., Jia, C., Song, Y., Zhao, M., Zhuo, Q., & Lu, X. (2016). Constraining tectonic compression processes by reservoir pressure evolution: Overpressure generation and evolution in the Kelasu Thrust Belt of Kuqa Foreland Basin, NW China. Marine and Petroleum Geology, 72, 30-44.

Harris, N. B., 2000. TOCA Carbonate, Congo Basin: response to an evolving rift lake, in M. R. Mello and B. J. Katz, eds., Petroleum systems of South Atlantic margins: American Association of Petroleum Geologists Memoir 73, 341–360.

Heidbach, O., Rajabi, M., Reiter, K., & Ziegler, M. 2016. World Stress Map 2016. GFZ Data Services

Hrouda F., 1982. Magnetic anisotropy of rocks and its application in geology and geophysics. Geophys. Surv., 5, 37-82.

Jelinek V., 1981. Characterization of the magnetic fabric of the rocks. Tectonophysics, 79, 63–67.

Karner, G. D., Driscoll, N. W., & Barker, D. H. N. 2003. Syn-rift regional subsidence across the West African continental margin: the role of lower plate ductile extension. Geological Society, London, Special Publications, 207(1), 105-129.

Karner, G. D., & Gambôa, L. A. P. 2007. Timing and origin of the South Atlantic pre-salt sag basins and their capping evaporites. Geological Society, London, Special Publications, 285(1), 15-35.

Koehn, D., Rood, M. P., Beaudoin, N., Chung, P., Bons, P. D., & Gomez-Rivas, E. 2016. A new stylolite classification scheme to estimate compaction and local permeability variations. Sedimentary Geology, 346, 60-71.

Koehn, D., Koehler, S., Toussaint, R., Ghani, I., & Stollhofen, H. 2022. Scaling analysis, correlation length and compaction estimates of natural and simulated stylolites. Journal of Structural Geology, 104670.

Kounov, A., Viola, G., De Wit, M., & Andreoli, M. A. G. 2009. Denudation along the Atlantic passive margin: new insights from apatite fission-track analysis on the western coast of South Africa. Geological Society, London, Special Publications, 324(1), 287-306.

Kulikowski, D., & Amrouch, K. 2017. Combining geophysical data and calcite twin stress inversion to refine the tectonic history of subsurface and offshore provinces: A case study on the Cooper-Eromanga Basin, Australia. Tectonics, 36(3), 515-541.

Kulikowski, D., & Amrouch, K. 2018. 4D modelling of fault reactivation using complete paleostress tensors from the Cooper–Eromanga Basin, Australia. Australian Journal of Earth Sciences, 65(5), 661-681.

Labeur, A., Beaudoin, N. E., Lacombe, O., Emmanuel, L., Petracchini, L., Daëron, M., Klimowicz, S., & Callot, J. P. 2021. Burial-deformation history of folded rocks unraveled by fracture analysis, stylolite paleopiezometry and vein cement geochemistry: a case study in the Cingoli Anticline (Umbria-Marche, Northern Apennines). Geosciences, 11(3), 135.

Lacombe, O., Angelier, J., Laurent, P., Bergerat, F., & Tourneret, C. 1990. Joint analyses of calcite twins and fault slips as a key for deciphering polyphase tectonics: Burgundy as a case study. Tectonophysics, 182(3-4), 279-300.

Lacombe O. & Laurent P., 1992. Determination of principal stress magnitudes using calcite twins and rock mechanics data. Tectonophy., 202, 83-93

Lacombe O., Laurent P. & Angelier J., 1994. Calcite twins as a key to paleostresses in sedimentary basins: preliminary results from drill cores of the Paris basin. In "Peri-Tethyan Platforms", F. Roure Ed., Technip, 197-210

Lacombe O., 2001. Paleostress magnitudes associated with development of mountain belts: insights from tectonic analyses of calcite twins in the Taiwan Foothills. Tectonics, 20, 6, 834-849

Lacombe, O. 2007. Comparison of paleostress magnitudes from calcite twins with contemporary stress magnitudes and frictional sliding criteria in the continental crust: Mechanical implications. Journal of Structural Geology, 29(1), 86-99.

Lacombe, O. 2010. Calcite twins, a tool for tectonic studies in thrust belts and stable orogenic forelands. Oil & Gas Science and Technology–Revue d'IFP Energies nouvelles, 65(6), 809-838.

Lacombe O., Beaudoin N., Hoareau G., Labeur A., Pecheyran C. & Callot J.P. 2021b. Dating folding beyond folding, from layer-parallel shortening to fold tightening, using mesostructures : Lessons from the Apennines, Pyrenees and Rocky Mountains. Solid Earth, 12, 10, 2145-2157.

Lade, P. V., & Yamamuro, J. A. (1996). Undrained sand behavior in axisymmetric tests at high pressures. Journal of Geotechnical Engineering, 122(2), 120-129.

Lartigau, M., Kergaravat, C., Callot, J. P., Aubourg, C., & Ringenbach, J. C. (2023). Matrix deformation and fracture network in minibasins in a foreland fold and thrust belt: The Sivas Basin, Turkey. Tectonophysics, 229701.

Laurent, P., Bernard, P., Vasseur, G., & Etchecopar, A. 1981. Stress tensor determination from the study of e twins in calcite: a linear programming method. Tectonophysics, 78(1-4), 651-660.

Laurent, P., Tourneret, C., & Laborde, O. (1990). Determining deviatoric stress tensors from calcite twins: applications to monophased synthetic and natural polycrystals. Tectonics, 9(3), 379-389.

Laurent, P., Kern, H., & Lacombe, O. 2000. Determination of deviatoric stress tensors based on inversion of calcite twin data from experimentally deformed monophase samples. Part II. Axial and triaxial stress experiments. Tectonophysics, 327(1-2), 131-148.

Lehner, P., and P. A. C. De Ruiter, 1977, Structural History of the Atlantic Margin of Africa, AAPG Bulletin, vol. 61, no. 7, 961-981.

Li, C.; Zhan, L.; Lu, H. Mechanisms for overpressure development in marine Sediments. J. Mar. Sci. Eng. 2022, 10, 490.

Liu, Y., He, Z., He, S., Zhang, D., Li, T., & Wang, X. (2021). A new quantitative model and application for overpressure prediction in carbonate formation. Journal of Petroleum Science and Engineering, 198, 108145.

Makowitz, A., Lander, R. H., & Milliken, K. L. (2006). Diagenetic modeling to assess the relative timing of quartz cementation and brittle grain processes during compaction. AAPG bulletin, 90(6), 873-885.

Mark, R.P.T., Richard, R.H., Richard, E.S., Chris, K.M., Abdul, R.D., 2009. Origin of overpressure and pore-pressure prediction in the Baram province, Brunei. AAPG Bulletin. 93, 51-74.

Mastina, T., and Zerbinati, A. 2021. Rock Mechanics measurements on Cameia-1A and Cameia-3 wells. (TotalEnergies Unpublished internal report).

Marzoli, A., Melluso, L., Morra, V., Renne, P. R., Sgrosso, I., D'antonio, M., ... & Ricci, G. (1999). Geochronology and petrology of Cretaceous basaltic magmatism in the Kwanza basin (western Angola), and relationships with the Paraná-Etendeka continental flood basalt province. Journal of Geodynamics, 28(4-5), 341-356.

Mbina Mounguengui, M. and Guiraud, M. 2009. Neocomian to early aptian syn-rift evolution of the normal to oblique-rifted north gabon margin (interior and n'komi basins). Marine and Petroleum Geology, 26(6):1000-1017.

Mehrkian, K. (2016). Microfracturing in quartz grains as a measurement of effective stress evolution in sandstone reservoirs. Thèse de doctorat de l'Université de Pau et des Pays de l'Adour.

Moulin, M., Aslanian, D., & Unternehr, P. 2010. A new starting point for the South and Equatorial Atlantic Ocean. Earth-Science Reviews, 98(1-2), 1-37.

Morad, S., Ketzer, J. M., and De Ros, L. F. 2013. Linking diagenesis to sequence stratigraphy: an integrated tool for understanding and predicting reservoir quality distribution. Linking diagenesis to sequence stratigraphy, 1-36.

Nkodia, H. V., Miyouna, T., Delvaux, D., & Boudzoumou, F. 2020. Flower structures in sandstones of the Paleozoic Inkisi Group (Brazzaville, Republic of Congo): evidence for two major strike-slip fault systems and geodynamic implications. South African Journal of Geology, 123(4), 531-550.

Nkodia, H. M. D.-V., Miyouna, T., Kolawole, F., Boudzoumou, F., Loemba, A. P. R., Bazebizonza Tchiguina, N. C., & Delvaux, D. 2022. Seismogenic fault reactivation in western Central Africa: Insights from regional stress analysis. Geochemistry, Geophysics, Geosystems, 23, e2022GC010377.

Parlangeau, C., Lacombe, O., Schueller, S., & Daniel, J. M. 2018. Inversion of calcite twin data for paleostress orientations and magnitudes: A new technique tested and calibrated on numerically-generated and natural data. Tectonophysics, 722, 462-485.

Parlangeau, C., Dimanov, A., Lacombe, O., Hallais, S., & Daniel, J. M. 2019. Uniaxial compression of calcite single crystals at room temperature: insights into twinning activation and development. Solid Earth, 10(1), 307-316.

Parés J.M., Van Der Pluijm B.A. et Dinarès-Turell J., 1999. Evolution of magnetic fabrics during incipient deformation of mudrocks (Pyrenees, northern Spain). Tectonophysics, 307, 1-14.

Parés J.M. et Van Der Pluijm B.A., 2002. Evaluating magnetic lineations (AMS) in deformed rocks. Tectonophysics, 350, 283-298

Potter, H. G., & Sneag, D. B. (2008). Magnetic resonance imaging of cartilage repair. Sports Medicine and Arthroscopy Review, 16(4), 236-245.

Préat, A., Kolo, K., Prian, J. P., & Delpomdor, F. 2010. A peritidal evaporite environment in the Neoproterozoic of south Gabon (Schisto-Calcaire Subgroup, Nyanga Basin). Precambrian research, 177(3-4), 253-265.

Primmer, T.J., Cade, C.A. et al. 1997. Global patterns in sandstone diagenesis: their application to reservoir quality prediction for petroleum exploration. In: Kupecz, J.A., Gluyas, J. & Bloch, S. (eds) Reservoir quality prediction in sandstones and carbonates. AAPG, Memoirs, Tulsa, OK, 69, 61–78.

Regnet, J. B., David, C., Robion, P., & Menéndez, B. 2019. Microstructures and physical properties in carbonate rocks: A comprehensive review. Marine and Petroleum Geology, 103, 366-376.

Renard, F., Schmittbuhl, J., Gratier, J. P., Meakin, P., & Merino, E. 2004. Three-dimensional roughness of stylolites in limestones. Journal of Geophysical Research: Solid Earth, 109(B3).

Reston, T. J. (2010). The opening of the central segment of the South Atlantic: symmetry and the extension discrepancy. Petroleum Geoscience, 16(3), 199-206.

Robion P., Averbuch O. et Sintubin M., 1999. Fabric development and metamorphic evolution of lower Paleozoic slaty rocks from the Rocroi massif (French-Belgian Ardennes): new constraints from magnetic fabrics, phyllosilicate preferred orientation and illite crystalinity data. Tectonophysics, 309, 257-273.

Rocher, M., Cushing, M., Lemeille, F., Lozac'h, Y., Angelier, J., 2004. Intraplate paleostresses reconstructed with calcite twinning and faulting: improved method and application to the eastern Paris Basin (Lorraine, France). Tectonophysics 387, 1–21.

Rochette P., Jackson J. et Aubourg C., 1992. Rock magnetism and the interpretation of anisotropy of magnetic susceptibility. Rev. Geophys., 30, 209-226. Rochette P., Aubourg C. et Perrin M., 1999. Is this magnetic fabric normal ? A review and case studies in volcanic formations. Tectonophysics, 307, 219-234

Rolland, A., Toussaint, R., Baud, P., Conil, N., & Landrein, P. 2014. Morphological analysis of stylolites for paleostress estimation in limestones. International Journal of Rock Mechanics and Mining Sciences, 67, 212-225.

Rouby, D., Raillard, S., Guillocheau, F., Bouroullec, R., & Nalpas, T. (2002). Kinematics of a growth fault/raft system on the West African margin using 3-D restoration. Journal of structural geology, 24(4), 783-796

Saint-Bezar, B., Hebert, R. L., Aubourg, C., Robion, P., Swennen, R., & de Lamotte, D. F. (2002). Magnetic fabric and petrographic investigation of hematite-bearing sandstones within ramp-related folds: examples from the South Atlas Front (Morocco). Journal of Structural Geology, 24(9), 1507-1520.

Sakhaee-Pour, A., & Bryant, S. L. 2014. Effect of pore structure on the producibility of tight-gas sandstones Effect of Pore Structure on the Producibility of Tight-Gas Sandstones. AAPG bulletin, 98(4), 663-694.

Schmittbuhl, J., Renard, F., Gratier, J. P., & Toussaint, R. (2004). Roughness of stylolites: implications of 3D high resolution topography measurements. Physical Review Letters, 93(23), 238501.

Schoellkopf, N. B., and B. A. Patterson, 2000, Petroleum systems of offshore, Cabinda, Angola, in M. R. Mello and B. J. Katz, eds., Petroleum systems of South Atlantic margins: AAPG Memoir 73, p. 361–376.

Séranne, M., & Anka, Z. 2005. South Atlantic continental margins of Africa: a comparison of the tectonic vs climate interplay on the evolution of equatorial west Africa and SW Africa margins. Journal of African Earth Sciences, 43(1-3), 283-300.

Smith, R.E. and Wiltschko, D.V., 1996. Generation and maintenance of abnormal fluid pressures beneath a ramping thrust sheet: isotropic permeability experiments. Journal of Structural Geology, 18(7): 951-970.

Stricker, S., Jones, S.J., 2016. Enhanced porosity preservation by Pore Fluid overpressure and Chlorite Grain Coatings in the Triassic Skagerrak, Central Graben, North Sea, UK. Geological Society. Special Publications, London.

Swarbrick, R.E., Osborne, M.J. and Yardley, G.S., 2002. Comparison of overpressure magnitude resulting from the main generating mechanisms. In: A.R. Huffman and G.L. Bowers (Editors). A.A.P.G., pp. 1-12.

Teisserenc, P., & Villemin, J. 1989. Sedimentary basin of Gabon--geology and oil systems. In J.D. Edwards, P.A. Santogrossi (Eds.), Divergent/passive margins basins, AAPG, vol. 48 (1990), 117-199.

Terzaghi, K.v., 1933. Auftrieb und Kapillardruck an betonierten Talsperren. Wasserwirtsch, 26: 397-399.

Tian, H., Xiao, X.M., Ronald, W.T.W., Tang, Y.C., 2008. New insights into the volume and pressure changes during the thermal cracking of oil to gas in reservoirs: Implications for the in-situ accumulation of gas cracked from oils. AAPG Bull. 92, 181-200.

Tissot, B. P., Pelet, R., & Ungerer, P. H. (1987). Thermal history of sedimentary basins, maturation indices, and kinetics of oil and gas generation. AAPG bulletin, 71(12), 1445-1466.

Turner, F.J. 1953. Nature and dynamic interpretation of deformation lamellae in calcite of three marbles. American Journal of Science. 251, 276–298.

Turner, F. J., Griggs, D. T., & Heard, H. 1954. Experimental deformation of calcite crystals. Geological Society of America Bulletin, 65(9), 883-934.

Tveranger, J., Rotevatn, A., and Braathen, A. 2018. Faults, fractures ande fluid flow in the subsurface: implications for petroleum reservoir engineering. Geological Society, London, Special publications, 469(1), 1-12.

Torsvik, T. H., Rousse, S., Labails, C., & Smethurst, M. A. 2009. A new scheme for the opening of the South Atlantic Ocean and the dissection of an Aptian salt basin. Geophysical Journal International, 177(3), 1315-1333

Toussaint, R., Aharonov, E., Koehn, D., Gratier, J. P., Ebner, M., Baud, P., Rolland, A., & Renard, F. 2018. Stylolites: A review. Journal of Structural Geology, 114, 163-195.

Uncini, G., Brandao, M., & Giovannelli, A. 1998. Neocomian-Upper Aptian Pre-Salt sequence of southern Kwanza Basin: a regional view. In ABGP/AAPG International Conference and Exhibition November 8-11, 1998, Rio de Janeiro, Brazil.

Vernet, R., Assoua-Wande, C., Massamba, L., & Sorriaux, P. 1996. Paléogéographie du Crétacé (Albien-Maastrichtien) du bassin côtier congolais. Bulletin des Centres de recherches exploration-production Elf-Aquitaine. Mémoire, (16), 39-55.

Wang, G.Y., Shi, Y., Hwang, W.T. and Chen, H., 1990. Hydrogeologic processes in the Oregon -Washington accretionary complex. JGR, 95(B.6): 9009-9023.

Wang, X., Chen, Z., Chen, Z., and Zhang, L. 2019. Paleostress field and its impact on hydrocarbon accumulation in the Tarim basin. AAPG Bulletin, 103(5), 1109-1133.

Wang, L., He, Y., Peng, X., Deng, H., Liu, Y., & Xu, W. 2020. Pore structure characteristics of an ultradeep carbonate gas reservoir and their effects on gas storage and percolation capacities in the Deng IV member, Gaoshiti-Moxi Area, Sichuan Basin, SW China. Marine and Petroleum Geology, 111, 44-65.

Weil, A. B., & Yonkee, A. (2009). Anisotropy of magnetic susceptibility in weakly deformed red beds from the Wyoming salient, Sevier thrust belt: Relations to layer-parallel shortening and orogenic curvature. Lithosphere, 1(4), 235-256.

Weil, A. B., & Yonkee, W. A. (2012). Layer-parallel shortening across the Sevier fold-thrust belt and Laramide foreland of Wyoming: spatial and temporal evolution of a complex geodynamic system. Earth and Planetary Science Letters, 357, 405-420.

Weil, A. B., Yonkee, A., & Schultz, M. (2016). Tectonic evolution of a Laramide transverse structural zone: Sweetwater Arch, south central Wyoming. Tectonics, 35(5), 1090-1120.

Worden, R. H., Armitage, P. J., Butcher, A. R., Churchill, J. M., Csoma, A. E., Hollis, C., ... & Omma, J. E. 2018. Petroleum reservoir quality prediction: overview and contrasting approaches from sandstone and carbonate communities. Geological Society, London, Special Publications, 435(1), 1-31.

Wonham, J. P., Cyrot, M., Nguyen, T., Louhouamou, J., & Ruau, O. (2010). Integrated approach to geomodelling and dynamic simulation in a complex mixed siliciclastic–carbonate reservoir, N'Kossa field, Offshore Congo. Geological Society, London, Special Publications, 347(1), 133-163.

Xu, J., Deng, Y., Fu, M., Guo, R., Chen, P., Duan, G., & Ma, R. 2022. The Nonuniform Distribution of Stylolite in Bioclastic Limestones and Its Influence on Reservoir Petro-Physical Properties—A Case Study of the Mishrif Formation from the Ah Oilfield. Energies, 15(9), 3032

Yamaji, A., Sato, K., 2006. Distances for the solutions of stress tensor inversion in relation to misfit angles that accompany the solutions. Geophysical Journal International, 167, 933–942.

Yamaji, A. 2015. Generalized Hough transform for the stress inversion of calcite twin data. Journal of Structural Geology, 80, 2–15.

Yielding, G. and Freeman, B. 2011. Origin of overpressure and pore pressure prediction in a compressional tectonic regime. Journal of Petroleum science and Engineering, 77(1), 1-17.

Zang, Y., and Wang, Y. 2019. The impact of paleostress on reservoir fractures system and reservoir quality: a case study from the Permian Lucaogou Formation in the southern Junggar basin, NW China. Journal of Petroleum Science and Engineering, 178, 98-111.

# Annexes

# **Annexe n°1 :** Datation U-Pb

# Annexe n°1 : Diagramme Tera-Wasserberg des puits du bassin de Kwanza

| WELL | FORMATION | ROCK TYPE | MINERAL PHASE ANALYZED | SECTION | U-Pb SIGNAL | U-Pb AGE |
|---|---|---|---|---|---|---|
| Well-4 | Presalt | Dolostone | Replacive sucrosic, planar-E dolomite | thin | Section very thin. UPb signal OK, contamination by epoxy. Much trimming. | 111.3 ± 3.0 Ma - Dubious age |
| | Presalt | Dolostone | Pore-filling , planar-E/S dolomite | THICK | **Good signal, good isochron. Low initial Pb/Pb ratio ?** | **119.8 ± 3.4 Ma** |
| | Presalt | Dolostone | Blocky calcite | thin | No UPb signal | |
| | | | Blocky calcite | THICK | Insufficient UPb signal | |
| | | | Replacive planar-E/S dolomite | | Unstable UPb signal, no valid isochron | |
| | Presalt | Silicified dolostone | Blocky calcite | thin | No Pb signal | |
| Well-5 | Presalt | Dolostone | Planar-S dolomite | thin | **Good signal, highly radiogenic, some scatter** | **116.3 ± 3.4 Ma - Some scatter** |
| | Presalt | Dolomitic clay | Neoformed euhedral dolomite rhombs | thin | Good signal, contamination by epoxy & clays very likely. Much trimming. | 109.6 ± 3.0 Ma - Dubious age |
| | Presalt | Dolomitic clay | Neoformed euhedral dolomite rhombs | THICK | **Good signal, good isochron** | **117.1 ± 1.7 Ma** |
| | Presalt | Dolomitic clay | Neoformed euhedral dolomite rhombs | thin | Good signal, good isochron. Potential contamination by epoxy & clays | 125.4 ± 2.2 Ma - Dubious age ? |
| | | | | THICK | **Excellent signal and excellent isochron.** | **118.7 ± 3.0 Ma** |
| | Presalt | Dolomitic spherulitic limestone | Intergranular planar-S dolomite cement | thin | **Good signal, good isochron** | **107.6 ± 2.5 Ma** |
| | | | Calcite spherules | | Very weak UPb signal, no valid isochron | |
| Well-6 | Presalt | Dolostone | Massive sucrosic planar-E dolomite | thin | **Good signal, highly radiogenic, good isochron** | **114.4 ± 2.3 Ma** |
| | Presalt | Dolostone | Massive planar-E dolomite | thin | **Good signal, highly radiogenic, isochron correct with some scatter** | **110.4 ± 1.9 Ma** |
| | Presalt | Dolostone | Massive planar-E/S dolomite | thin | **Good signal, highly radiogenic, very good isochron** | **111.3 ± 1.3 Ma** |
| | | | Blocky calcite - fracture | | No U-Pb signal | |

Blocky calcite: No UPb signal, not dated…

**Dolomite**: total range of measured ages => 108-125 Ma range of ages considered as best reliable (in bold) => 108-120 Ma well average: Well-4 ~120 Ma; Well-5 ~115 Ma; Well-6 ~112 Ma

**=> Dolomitization is syn-depositional (primary?) to early diagenesis**

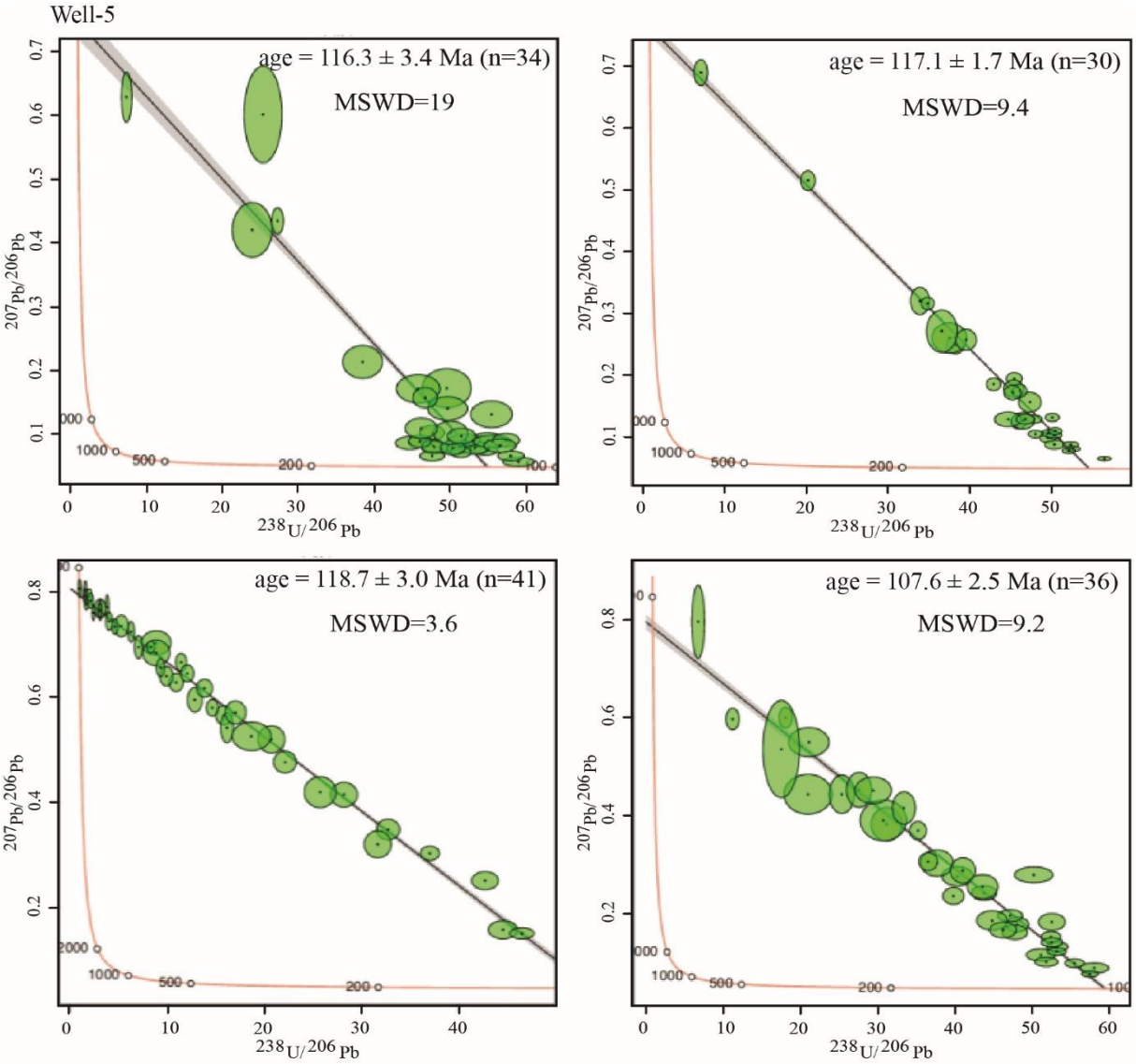
Well-5
age = 116.3 ± 3.4 Ma (n=34)
MSWD=19
age = 117.1 ± 1.7 Ma (n=30)
MSWD=9.4
age = 118.7 ± 3.0 Ma (n=41)
MSWD=3.6
age = 107.6 ± 2.5 Ma (n=36)
MSWD=9.2
207Pb/206Pb
238U/206Pb

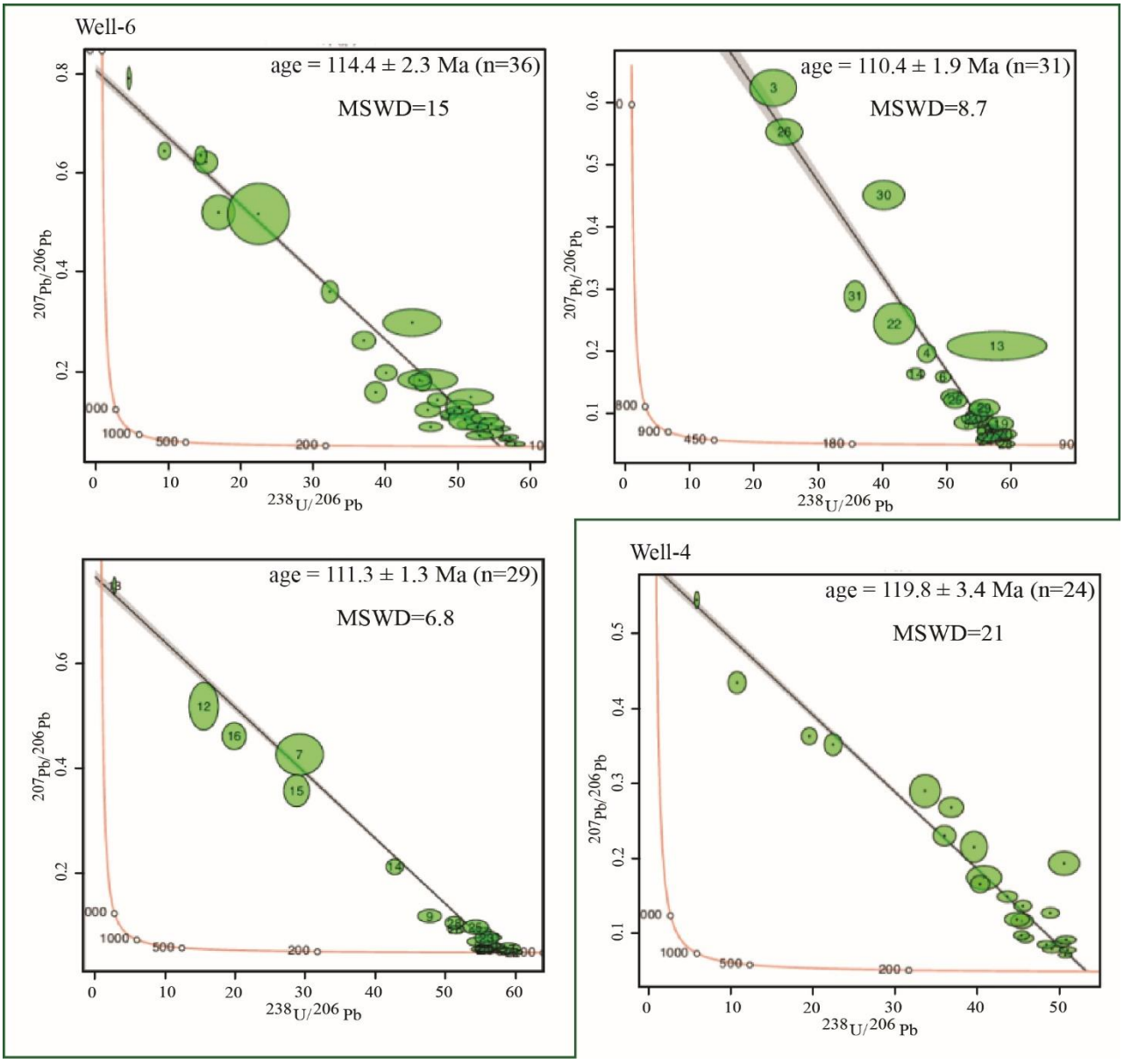
Well-6
age = 114.4 ± 2.3 Ma (n=36)
MSWD=15
age = 110.4 ± 1.9 Ma (n=31)
MSWD=8.7
age = 111.3 ± 1.3 Ma (n=29)
MSWD=6.8
Well-4
age = 119.8 ± 3.4 Ma (n=24)
MSWD=21
$^{207}Pb/^{206}Pb$
$^{238}U/^{206}Pb$

# **Annexe n°2 :** Exemple de traitement de l'inversion des macles de la calcite

# Annexe n°2 Paléopiézométrie fondée sur l'inversion des macles de la calcite

La paléopiézométrie par maclage de la calcite (par exemple, Jamison et Spang, 1976; Lacombe et Laurent, 1992; Lacombe, 2007) est une technique bien établie qui a été appliquée avec succès pour quantifier les paléocontraintes dans les bassins sédimentaires ainsi que dans les ceintures de plis et de chevauchements (par exemple, Lacombe et al., 1990, 1994, 2007; Craddock et al., 1993; Rocher et al., 1996, 2000; Lacombe et al., 2009; Arboit et al., 2015, 2017; Kulikowski et Amrouch, 2017. Voir des revues détaillées dans Lacombe, 2010 et Lacombe et al., 2021a).

L'inversion des macles de la calcite pour la contrainte a été appliquée avec succès à des carottes provenant de puits et s'est révélée appropriée pour contraindre l'histoire des paléocontraintes à partir de volumes rocheux limités (par exemple, Lacombe et al., 1994; Rocher et al., 2000; Amrouch et al., 2010; Zeboudj et al., 2023 ; Bah et al., en revision). Outre la présence de faciès pétrographique favorables (contenant de la calcite sparitique dans la matrice rocheuse ou dans les veines), la technique requiert la disponibilité évidente d'échantillons orientés dans le repère géographique. Pour les besoins de reconstitution de paléocontraintes, les carottes étudiées ont été orientées soit directement in-situ, soit a posteriori par comparaison avec les images FMS (Formation Micro-Scanner) du puits.

### *1.1.Acquisition des données de macles*

Les échantillons utilisés pour les mesures de jumeaux de calcite (Fig. 3 & 5) étaient orientés spatialement comme suit : axe X parallèle à la génératrice orientée par rapport au nord, axe Y parallèle au pendage de la carotte et axe Z perpendiculaire au plan XY. Trois sections minces orthogonales ont été coupées pour chaque échantillon (une dans le plan XY, une dans le plan XZ et une dans le plan YZ) (Fig.1).

Dans chaque lame mince, les orientations des lamelles jumelées ont été mesurées à partir de ~30 cristaux à l'aide d'un microscope optique équipé d'une platine universelle (U-stage), en notant la direction et le pendage de chaque famille de maclage dans le référentiel de la U-stage. Le logiciel développé par Tourneret et Laurent (1991) permet de déterminer l'orientation de l'axe optique et des plans non maclés à partir de la mesure de deux autres plans maclés ou de clivage sur la base des relations angulaires et symétriques établies entre les plans cristallographiques et l'axe optique dans le cristal de calcite.

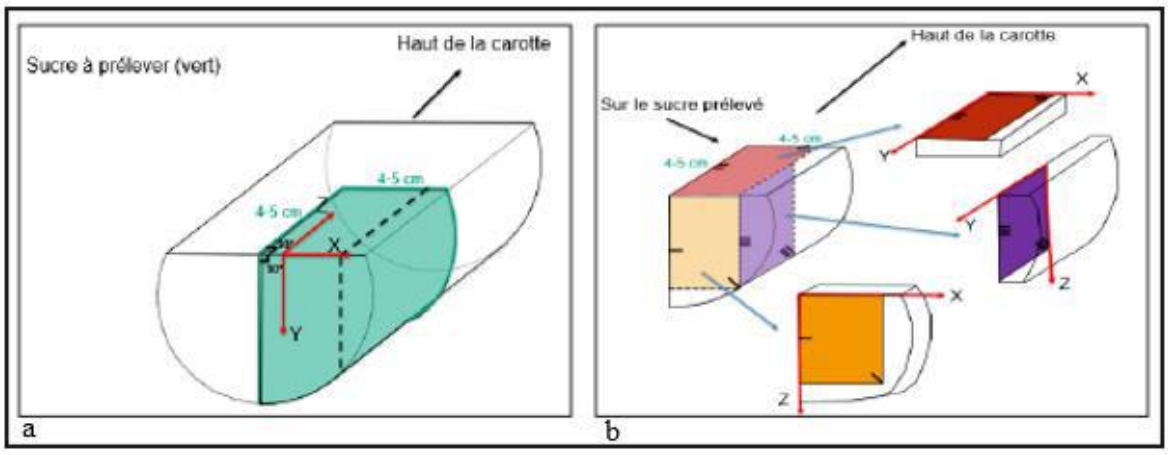


**Figure 8**: Schéma de prélèvement de sucre et de taille des lames minces orientées, a) l'encart vert correspond au sucre à prélever sur la carotte ; b) sucre prélevé et les différentes lames orientées réalisées dans les 3 plans indiqués sur le sucre.

Une fois que tous les axes optiques déterminés pour les cristaux de chaque lame, on calcule les rotations nécessaires à appliquer à chacune des lames, afin de remettre les données dans le repère géographique (Fig. 2). Pour cela, la première rotation s'effectue selon l'axe vertical, la deuxième selon l'axe Nord-Sud et en regardant vers le Nord et la troisième est à nouveau selon l'axe vertical avec une convention de signe (Fig.2). Chaque cristal analysé est numéroté, cela permet d'y revenir en cas de doute sur la réelle (in)existence d'un ou plusieurs plans non maclés car la taille des grains, la limite de l'angle d'observation et les impuretés peuvent rendre difficile la caractérisation d'un plan maclé ou non maclé. On crée ensuite des fichiers répertoriant les données de macles pour toutes les lames de chaque échantillon, et on applique ensuite le programme d'inversion de Parlangeau et al. (2018).

Il faut noter que la platine universelle présente quelques limites concernant les mesures, vu que les plans qui présentent un pendage supérieur à 60° sont difficiles à mesurer. Il arrive que l'on ne puisse pas voir si le plan est maclé ou non. C'est pour cette raison que dans le programme utilisé (Tourneret et Laurent, 1991), on donne à chaque fois un pourcentage de confiance au caractère maclé ou non maclé d'un plan; l'utilisation de trois lames minces perpendiculaires permet de vérifier la distribution aléatoire des axes optiques afin d'identifier tout biais potentiel lié à une orientation préférentielle liée à la croissance ou à la déformation du cristal (Fig. 3a). Nous nous sommes assurés que les mesures de macles de calcite étaient collectées sur des grains de la même phase diagénétique en nous basant sur les images de cathodoluminescence.

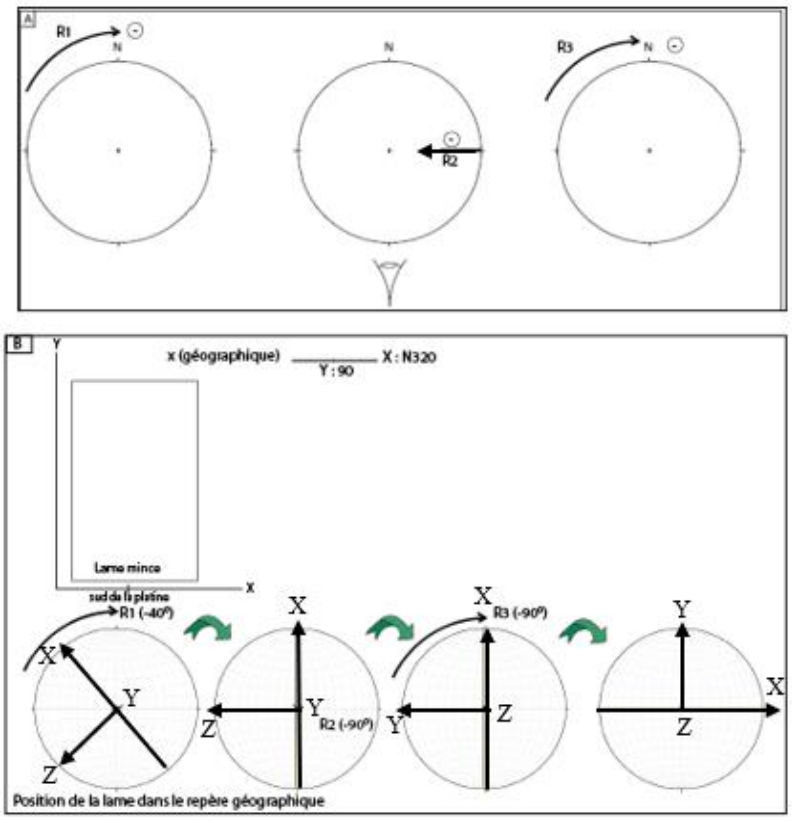


**Figure 9:** A)Représentation schématique de la manière dont on retrouve les trois rotations à effectuer pour remettre les données dans le repère géographique. B) Un exemple concret de rotations pour remettre la lame dans le repère géographique. Les rotations sont ici de - 40°/- 90°/- 90° pour aller du repère géographique au repère de la platine (dans lequel les mesures ont été faites). On doit donc appliquer les rotations de sens inverse et dans l'ordre inverse pour restituer les données mesurées dans le repère géographique : + 90°/+ 90°/+ 40°.

Pour obtenir une estimation approximative de la déformation de la calcite accommodée par le maclage, nous avons additionné la largeur de chaque lamelle de macle d'un ensemble de maclage donné dans un grain et divisé cette valeur par la largeur du grain mesurée perpendiculairement aux macles. Nous avons également déterminé la taille du grain 2-D dans chaque lame mince en additionnant les axes long et court et en divisant par 2 pour chaque grain, l'histogramme de taille de grain résultant nous permettant d'éliminer les cristaux les plus petits et/ou les plus gros, qui sont sous-représentés dans chaque échantillon (Fig. 8b). La déformation interne et la taille moyenne des grains ont ensuite été utilisées pour contraindre la valeur de la contrainte de cisaillement résolue critique (CRSS) pour le maclage à utiliser dans le processus d'inversion (Parlangeau et al., 2019 ; Lacombe et al., 2021a).

### *1.2.Principe de l'inversion des données de macles pour la reconstitution des paléocontraintes (CSIT-2)*

Plusieurs méthodes d'inversion des macles de calcite pour les contraintes ont été proposées (par exemple, Laurent et al., 1981; Etchecopar, 1984; Laurent et al., 1990; Yamaji, 2015; Parlangeau et al., 2018; voir la revue dans Lacombe et al., 2021a). Elles reposent sur des principes différents mais partagent les mêmes conditions d'application, à savoir une faible déformation, ce qui justifie la coaxialité entre contrainte et déformation, et un champ de contrainte homogène à l'échelle du grain/agrégat. La déformation par maclage est considérée comme irréversible, et le maclage se produit si la contrainte cisaillante résolue appliquée, appelée $\tau_s$, est égale ou supérieure à la contrainte de cisaillante résolue critique pour le maclage (CRSS), appelée $\tau_a$ (Jamison et Spang 1976; Tullis, 1980; Lacombe et Laurent, 1996; Ferrill, 1998; Laurent et al., 2000; voir la revue et la discussion sur l'existence et la signification de la CRSS dans Lacombe et al., 2021a). Ainsi, on suppose que pour les plans maclés : $\tau_s \geq \tau_a$ et pour les plans non maclés : $\tau_s < \tau_a$.

Il a été démontré que le développement de macles de la calcite dépend fortement de la taille des grains (Rowe et Rutter, 1990) et de la déformation (Turner, 1953; Turner et al., 1954; Laurent et al., 2000). Le maclage de la calcite est plus facile (CRSS plus faible) dans les gros grains et plus difficile (CRSS plus élevé) dans les petits grains. De plus, comme la calcite se durcit une fois maclée, le CRSS augmente lorsque la contrainte pour le maclage augmente, ce qui rend plus difficile la poursuite du maclage (Lacombe, 2010; Parlangeau et al., 2019; Lacombe et al., 2021a). Dans cette étude, nous avons utilisé la technique d'inversion des macles pour les contraintes (CSIT-2) développée par Parlangeau et al., (2018) pour déterminer les tenseurs de paléocontraintes successifs à partir des ensembles de macles mesurés. Le principe de l'inversion est de trouver un tenseur de contrainte (ou plusieurs tenseurs de contraintes) qui vérifie les inégalités (2) pour le plus grand nombre de plans maclés et l'ensemble des plans non maclés. La solution a la forme d'un tenseur de contrainte réduit avec 4 paramètres: les orientations des axes de contraintes principaux ($\sigma_1$, $\sigma_2$, $\sigma_3$) et le rapport de forme ($\Phi$) :

$$1 \geq \Phi = \frac{\sigma 2 - \sigma 3}{\sigma 1 - \sigma 3} \geq 0 \quad \text{with} \quad \sigma_1 \geq \sigma_2 \geq \sigma_3 \ (2)$$

La méthode CSIT-2 permet de détecter automatiquement la présence d'un ou plusieurs tenseurs. En considérant le jeu de données complet (plans maclés et non maclés), la première étape du processus consiste en une recherche systématique dans l'espace 3-D de trois angles d'Euler (définissant les orientations des axes des tenseurs de contraintes) avec un intervalle

régulier de 10°, le rapport de forme étant fixé à 0,5, afin de sélectionner les tenseurs de contrainte réduits représentant au moins 20% des plans maclés. Pour chaque tenseur, la fonction de pénalisation f est définie comme suit:

$$f = \sum_{j=1}^{j=n}(\tau_s^j - \tau_s^{min}) \quad (3)$$

avec $\tau_s^j$ la contrainte cisaillante résolue appliquée sur les plans non maclés j tels que $\tau_s^j \geq \tau_s^{min}$ et $\tau_s^{min}$ la plus petite contrainte cisaillante résolue appliquée sur les plans maclés compatibles avec le tenseur, est calculée. D'un point de vue théorique, la fonction de pénalisation devrait être égale à 0 pour un jeu de données parfait et elle augmente si des plans non maclés incompatibles sont incorporés dans la solution. Les tenseurs de contraintes dont la fonction de pénalisation est inférieure à 0,5 sont retenus après cette première étape et chacun d'entre eux est pondéré par le nombre de ses plus proches voisins en fonction d'un critère de similarité (c'est-à-dire la distance angulaire entre les tenseurs telle que définie dans Yamaji et Sato, 2006). Cela permet la détection simultanée et automatique de différents groupes de tenseurs qui partagent un pourcentage élevé de plans maclés compatibles et sont associés à de faibles valeurs de la fonction de pénalisation (voir Parlangeau et al., 2018, pour plus de détails). Le tenseur de contraintes réduit de référence de chaque groupe est ensuite appliqué à l'ensemble des plans maclés et non maclés tandis que le pourcentage de plans maclés à expliquer est progressivement augmenté. Le tenseur optimal est obtenu lorsque 1) le nombre maximum de plans maclés est pris en compte; 2) le nombre minimum de plans non maclés est pris en compte; 3) la valeur de la fonction de pénalisation est minimale.

Ce processus d'inversion donne pour chaque tenseur l'orientation des axes principaux des contraintes ($\sigma_1$, $\sigma_2$, $\sigma_3$), le rapport de forme ($\Phi$) et un différentiel de contrainte adimensionné $\frac{(\sigma_1 - \sigma_3)}{\tau a}$ qui est liée à la valeur finale de $\tau s^{min}$:

$$\frac{(\sigma_1 - \sigma_3)}{\tau a} = \frac{1}{\tau s^{min}} \quad (4)$$

À la suite de Rocher et al., (2004) et Amrouch et al., (2010), Parlangeau et al., (2019) ont proposé des courbes empiriques reflétant l'évolution de la valeur du CRSS en fonction de la taille des grains (règle de Hall-Petch) et de la déformation, à partir desquelles nous avons estimé la valeur appropriée du CRSS $\tau_a$ pour nos échantillons. En utilisant la valeur $\tau s^{min}$ dérivée du processus d'inversion, nous avons déterminé les valeurs des différentielles de contraintes ($\sigma_1$-

$\sigma_3$) et ($\sigma_2$-$\sigma_3$) en utilisant l'équation (4), qui donne les 5 paramètres du tenseur des contraintes déviatoriques.

La capacité de cette technique à détecter, séparer et déterminer les tenseurs de contraintes à partir d'ensembles de données de macles monophasées et polyphasées, incluant les erreurs de mesures ou les différentes tailles de grains, a été démontrée par de multiples tests sur des ensembles de données de macles générées numériquement ainsi que sur des échantillons polyphasés déformés naturellement (Parlangeau et al., 2018). L'incertitude méthodologique associée est de ± 10° pour les orientations des contraintes principales, ± 0,1 pour le rapport de contraintes et ±30% pour les valeurs des contraintes différentielles.

### *1.3.Exemple de traitement d'un échantillon*

#### 1.3.1. Caractérisation préliminaire des ciments de calcite par la cathodoluminescence

La cathodoluminescence est un phénomène optique et électrique que l'on observe lorsqu'un faisceau d'électrons produit par un canon à électrons (par exemple un tube à rayons cathodiques) bombarde un échantillon sous vide, conduisant à l'émission de lumière visible. La longueur d'onde de la luminescence est un indicateur sur le type de minéral présent, et elle peut être proportionnelle à la concentration du minéral porteur de l'élément activateur dans la roche. La cathodoluminescence est avant tout un outil très utilisé pour les analyses diagénétiques en sédimentologie, mais l'idée de la combiner avec d'autres méthodes d'analyse microtectonique comme l'analyse des macles de calcite pourrait s'avérer très bénéfique. L'objectif de la cathodoluminescence est de discriminer les différentes phases de précipitation de la calcite dans la matrice ou dans la veine. Si différentes phases de calcite sont identifiées, il sera nécessaire d'effectuer des mesures des macles au microscope optique pour chaque famille et de les traiter différemment, car ces familles de calcite peuvent ne pas être affectées par les mêmes événements de maclage et donc ne pas avoir enregistré la même phase de déformation. Le fait de ne pas les séparer entraînerait un biais potentiel dans la restitution et l'interprétation des résultats de l'analyse des données de macle de la calcite.

Les observations faites par cathodoluminescence optique ont permis de distinguer dans nos échantillons deux types de ciment dans la matrice, conformément aux études diagénétiques plus détaillées sur la carotte d'où proviennent nos échantillons. L'acquisition des données de macles de la calcite ont été effectuées dans un seul ciment (C1) montrant de belles plages de calcite sparitiques.

### 1.3.2. Exemple de traitement d'un l'échantillon

Pour illustrer la méthode de traitement d'analyse des macles de la calcite, j'ai choisi de développer l'échantillon 8 du puit Well-2.

Je décris ici étape par étape la méthode d'inversion utilisée.

**Etape 1 :** Cette étape consiste à l'acquisition des données de macles à l'aide d'un microscope muni d'une platine universelle (Fig.1) et du programme informatique de Tourneret et Laurent (1990). Sur chacune des 3 lames d'un échantillon, 30 cristaux sont mesurés pour obtenir un total de 90 cristaux. Chaque cristal conporttant 3 plans qui sont soit tous maclé ou non. Le programme de Tourneret et Laurent (1990) permet de calculer les positions des 3 plans de plans de macles et l'axe optique du cristal qui peuvent être activés ou non à partir de deux plans : macles/macles, macles/clivages ; clivages/clivages. Cette étape est longue et fastidieuse.

**Figure 10:** Photo de microscope muni d'une platine universelle

A titre d'exemple une personne expérimentée et efficace passera une journée sur une lame si elle l'échantillon n'est pas trop difficile à observer. A noter qu'avant de commencer toute mesure il est recommandé à l'utilisateur de prendre des photos de son échantillon et de numéroter les cristaux mesurés au fur et à mesure. Ces images permettront de revenir sur un cristal douteux à des fins de vérification d'une part et de pouvoir quantifier grossièrement la quantité de déformation intra cristalline qui est nécessaire pour les estimations des grandeurs des contraintes.

**Etape 2 :** Lorsque les échantillons ont été acquise, la seconde phase est d'effectuer les rotations décrites ci-dessus pour passer du repère de la platine au repère géographique. Ensuite les fichiers sont mis en forme dans un format qui est pris en charge par le programme d'inversion proprement dite de Parlangeau et al., (2018). Avant de commencer l'inversion tous les 90 cristaux de l'échantillon sont mesurés pour avoir la gamme de taille sous forme d'histogramme (Fig.5). Sur cet exemple, 90 cristaux comportant 205 plans maclés et 65 plans non maclés ont été mesurés dans la matrice, dont la taille dominante est comprise entre 50 µm et 250 µm avec un mode autour de 150µm (Fig. 9). Pour l'inversion nous nous assurerons que seul les cristaux ayant une taille comprise entre 50 et 250 µm seront utilisées pour l'inversion et le reste des cristaux sont écartés définitivement. Un moyen d'éviter de perdre des cristaux est de s'assurer de mesurer des cristaux d'à peu près de même temps si cela est toutefois possible.

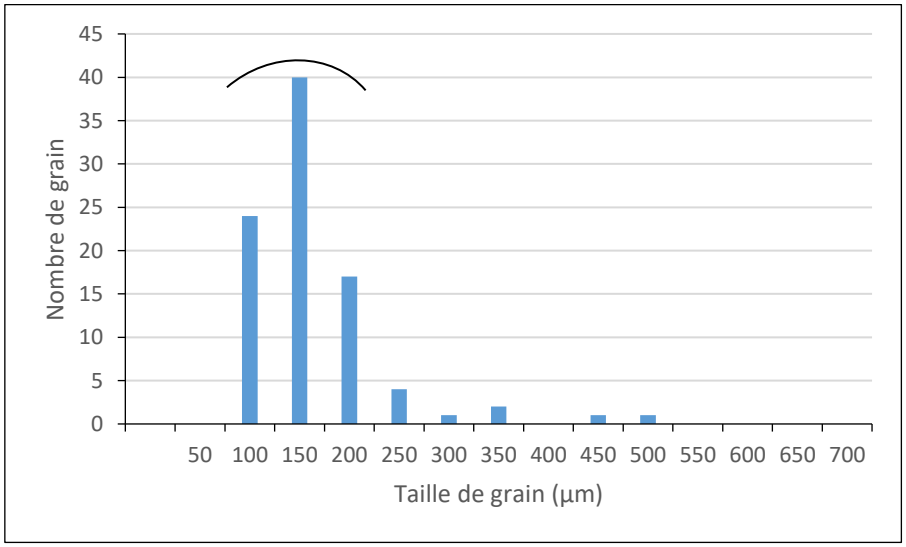


**Figure 11:** Histogramme du nombre de grains en fonction de la taille

Pour repérer et numéroter les cristaux on utilise une photographie de la lame pour pouvoir revenir en cas d'erreur. L'histogramme permet de discriminer une gammes de taille de grains > 50 µm et <250 µm. Une fois acquises, les mesures sont restituées dans leur position réelle par

rapport au Nord géographique ce qui permet de vérifier le caractère aléatoire de l'orientation des axe optiques afin d'éviter que la recherche de tenseurs soit biaisée par une orientation préférentielle de croissance des cristaux ou une trop forte déformation.

**Etape 3 :** lorsqu'on lance le programme, un message nous demandant de choirsir le type de données que nousvoulons utiliser, Tois choix possible (capture)

```
Initialisation :
  Chargement de l'environnement de travail

--> exec('C:\Users\bahb2\Documents\En_Cours\Programmes\Macles\[CSIT-2]_09-10-2021.sce', -1)

  "(1) : Universal stage"

  "(2) : Dipazimuth Dip Pitch"

  "(3) : EBSD"
KIND OF ENTER FILE : (1, 2 or 3)
```

Pour l'inversion des macles de la calcite, on rentre 1 et on choisit le nombre de lames pour cet échantillon : 3 dans mon cas et j'entre le chemin pour mes données

```
--> exec('C:\Users\bahb2\Documents\En_Cours\Programmes\Macles\[CSIT-2]_09-10-2021.sce', -1)

  "(1) : Universal stage"

  "(2) : Dipazimuth Dip Pitch"

  "(3) : EBSD"
KIND OF ENTER FILE : (1, 2 or 3) 1

NUMBER OF THIN SECTIONS : (1 to infinity!) 3

WAY ACCESS : (in inverted commas) "C:\Users\bahb2\Documents\En_Cours\DDKM-1\Scilab\8Y.txt"

WAY ACCESS : (in inverted commas) "C:\Users\bahb2\Documents\En_Cours\DDKM-1\Scilab\8X.txt"

WAY ACCESS : (in inverted commas) "C:\Users\bahb2\Documents\En_Cours\DDKM-1\Scilab\8Z.txt"
```

Ensuite je choisi le pourcentage minimum de plan de macles que je souhaiterai expliquer la formation, la valeur recommander par Parlangeau est 20

Le programme nous renvoie le nombre de plans et non maclés dans le set de données utilisé. La valeur limite pour la fonction de pénalization est de 0. ; 0.5 ; 1. De mon expérience d'utilisateur de la méthode je recommande 0.5

Ensuite le programme demande à quel angle en degré il recherche, Il est recommandé de choisir 30 et un pourcentage de similarité de 70 % pour la suite

Dans le cas de l'échantillon 1, la fabrique des axes optiques est assez homogène dans le stéréogramme (Fig.10).

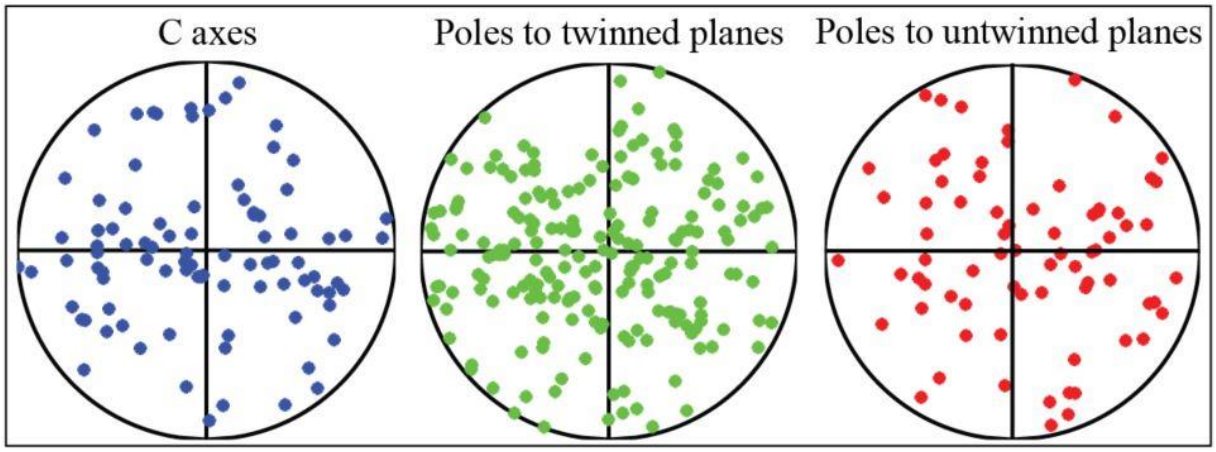


**Figure 12:** Représentation stéréographique des axes optiques, pôles des plans maclés et non maclés pour l'échantillon 8.

Le programme renvoie le nombre de tenseur compatible avec nos paramètres d'entrée et nous demande lesquels nous voulons optimiser

Sur cet exemple il a trouvé 17 tenseur c'est l'utilisateur de voir s'il n'y a pas des tenseurs qui soient super proche et on entre le nombre de tenseur que nous voulons optimiser le numéro du tenseur et le nom que l'on souhaite lui donner en sortie.

```
  "Percentage 20"

  "Number of twins : 205 Number of untwins : 65 Incorporated twins : 41"

  "Percentage of twins number : 31.707317"
Give a limitation to penalization function value (0, 0.5 or 1 are recommended)0.5


  "THERE ARE 562 TENSORS COMPATIBLES ON 5832 TESTED TENSORS"
ANGLE GAP FOR SETS TENSORS (°) : 30

CHOOSE THE PERCENTAGE OF SIMILARITY BETWEEN TENSOR (%) 70


  "17 TENSORS ARE BROUGHT OUT"

  "SIGMA 1 DIRECTION : 269.56869 DIP : 6.4086463"

  "SIGMA 2 DIRECTION : 0.4324611 DIP : 7.6442701"

  "SIGMA 3 DIRECTION : 140 DIP : 80"

  "SHAPE RATIO : 0.5"

  "SIGMA 1 DIRECTION : 278.25563 DIP : 12.700006"

  "SIGMA 2 DIRECTION : 11.763297 DIP : 15.188924"

  "SIGMA 3 DIRECTION : 150 DIP : 70"

  "SHAPE RATIO : 0.5"

  "SIGMA 1 DIRECTION : 290.43131 DIP : 6.4086463"

  "SIGMA 2 DIRECTION : 199.56754 DIP : 7.6442701"

  "SIGMA 3 DIRECTION : 60 DIP : 80"

  "SHAPE RATIO : 0.5"

  "SIGMA 1 DIRECTION : 70 DIP : 0"

  "SIGMA 2 DIRECTION : 340 DIP : 30"

  "SIGMA 3 DIRECTION : 160 DIP : 60"

  "SHAPE RATIO : 0.5"
```

Ensuite on récupère les données et on observe les graphiques sur Excell pour le choix de la solution optimale

Le choix du tenseur survient à la suite de la recherche d'une solution stable par rapport aux différents paramètres calculés par le logiciel. Le tenseur doit être celui dont le maximum de plans maclés est incorporé pour le moins de plans non-maclés tout en essayant de privilégier une certaine stabilité dans les autres paramètres autour du pourcentage de macles expliquées choisi. La valeur de la fonction de pénalisation ne doit pas dépasser 1 car cela signifie que l'on incorpore beaucoup trop de plans non maclés (ou quelques plans non maclés bien orientés recevant une forte contrainte cisaillante résolue, et qui donc auraient dû être maclés, et qui peuvent correspondre à des erreurs de mesure ou une impossibilité de vérification du caractère maclé). Donc on est revenu aux données et on a vérifié le caractère maclé ou non de certains plans, on a changé quelques-uns dans le fichier de données et on a procédé à nouveau au traitement. Le traitement à conduit à 3 tenseurs différents pour cet échantillon. Pour le premier tenseur, on a décidé de retenir un pourcentage de plans maclés expliqué de 36%. Ce pourcentage correspond à une fonction de pénalisation élevée 0,9.

Les courbes d'orientation des contraintes principales sont très stables avec des valeurs autour de N260 pour $\sigma_1$, et N130 pour $\sigma_3$. Le pendage des axes, sont aussi très stables avec des valeurs entre 1° et 8° pour $\sigma_1$ et entre 80° et 90° pou $\sigma_3$. Mais c'est surtout la valeur du seuil interne et de la fonction de pénalisation qui aident à faire un choix de la solution adéquate.

Pour valider le choix nous pouvons aussi regarder les courbes de la contrainte cisaillante associées à la solution (Fig.11). La courbe montre le classement des plans maclés en fonction de la contrainte cisaillante décroissante. On a ainsi le pourcentage de plans maclés incompatibles avec le tenseur. Ici, on prend en compte 23% de plans non maclés dans la solution du tenseur ce qui correspond à 15 plans non maclés sur un total 65. Afin de calculer le différentiel de contrainte ($\sigma_1 - \sigma_3$), il est nécessaire de faire une estimation de la quantité de déformation de l'agrégat comme décrit ci-haut. Ce travail fait sur toutes les lames a permis d'estimer un faible pourcentage de déformation (< 1%). Donc la valeur de 1 % a été retenue pour le choix de la valeur du seuil de maclage ($\tau_a$).

La taille de grains retenue pour ce traitement se situe entre 50 μm et 200 μm comme l'indique l'histogramme (Fig.15). En se servant des courbes de Parlangeau et al., (2019) Fig. 3, on voit que pour un faible pourcentage de taux de déformation comme notre cas (1 %), la valeur seuil ($\tau a$) varie entre 6 MPa et 8 MPa.

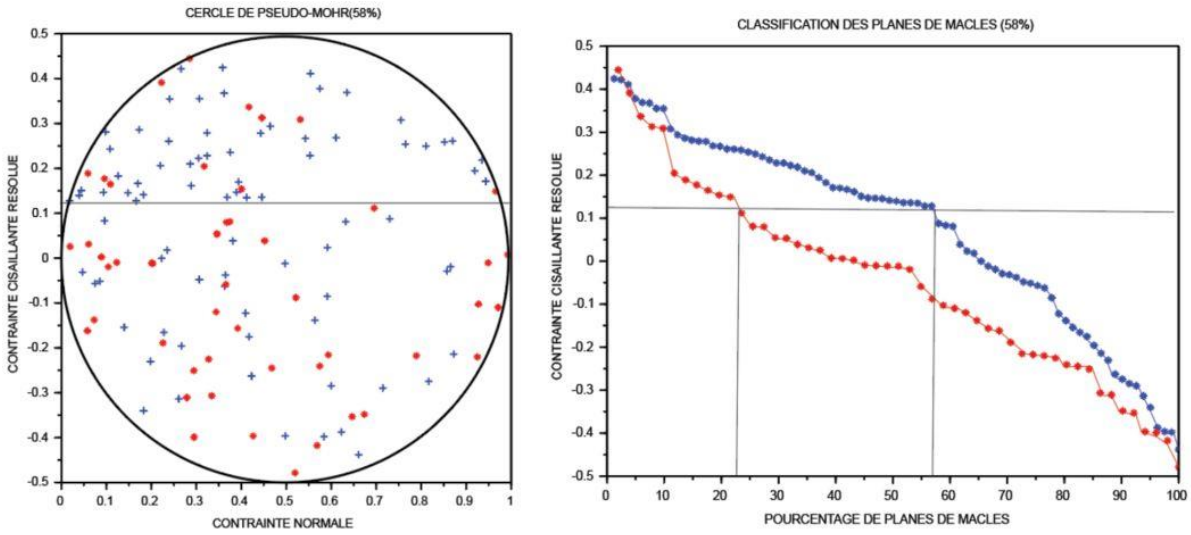


**Figure 13:** Deux diagrammes de représentation de la contrainte cisaillante résolue en fonction du pourcentage des plans maclés. Les points rouges et bleus correspondent respectivement aux plans non maclés et aux plans maclés. a) Pseudo-cercle de Mohr ; b) classification des plans de macles dans le tenseur solution selon la contrainte cisaillante résolue.

Ce tenseur a une contrainte principale maximale $\sigma_1$ : N261-4, une contrainte intermédiaire $\sigma_2$ : N352-6 et une contrainte minimale $\sigma_3$ : N137-83 (Fig.12a) pour un rapport de forme de 0,3, une fonction de pénalisation de 0,9 et une contrainte cisaillante résolue ($\tau_c$) de 0,127.

Connaissant la valeur seuil ($\tau_a$), la contrainte cisaillante résolue ($\tau c$) et le rapport $\Phi$ on peut calculer les valeurs des différentiels : ($\sigma_1 - \sigma_3$) et ($\sigma_2 - \sigma_3$) à partir de l'équation (4). On obtient les valeurs des différentiels pour cet échantillon de l'ordre de 47 MPa pour ($\sigma_1 - \sigma_3$) et 14 MPa pour $\sigma_2 - \sigma_3$).

Le second tenseur a été choisi pour une valeur de 34 % des plans maclés, la fonction de pénalisation est de 1.0, le rapport de forme est de 0,6 et la contrainte cisaillante résolue de 0.163. Les orientations des contraintes principales sont : $\sigma_1$ : N171-45, $\sigma_2$ : N35-36 et $\sigma_3$ : N287-24 (Fig. 12b). Les valeurs des différentiels sont 37 MPa pour ($\sigma_1 - \sigma_3$) et 21 MPa pour ($\sigma_2 - \sigma_3$).

Le troisième tenseur a été choisi pour une valeur de 29 % des plans maclés, la fonction de pénalisation est de 0,8, le rapport de forme est de 0,5 et la contrainte cisaillante résolue de 0.167. Les orientations des contraintes principales sont : $\sigma_1$ : N348-15, $\sigma_2$ : N79-3 et $\sigma_3$ : N180-74 (Fig. 12c). Les valeurs des différentiels sont 36 MPa pour ($\sigma_1 - \sigma_3$) et 18 MPa pour ($\sigma_2 - \sigma_3$).

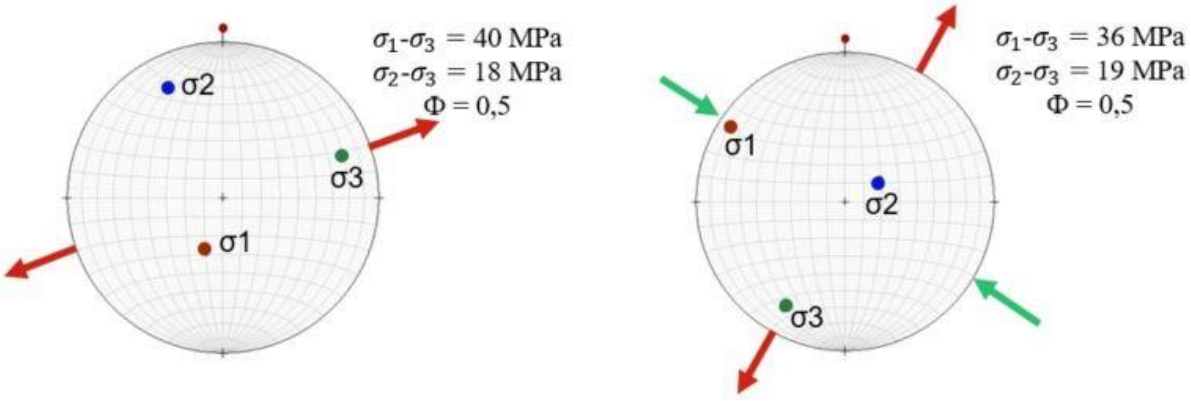


**Figure 14:** Représentation stéréographique des deux tenseurs trouvés à l'aide de l'inversion des macles de la calcite pour une taille de grains comprise entre 150 µm et 350 µm. Les flèches rouges et vertes indiquent les directions d'extension et de compression respectivement.

# **Annexe n°3 :** Core photos


1 cm


1 cm


1 cm

Calcite twins